CORA Cork Open Research Archive
Cartlann Taighde Oscailte Chorcaí

Title	Applications of finite element computer modelling and thermal infrared remote sensing to the study of geothermal anomalies
Authors	Cosgrave, Robert J.
Publication date	2000
Original Citation	Cosgrave, R. J. 2000. Applications of finite element computer modelling and thermal infrared remote sensing to the study of geothermal anomalies. PhD Thesis, University College Cork.
Type of publication	Doctoral thesis
Link to publisher's version	http://library.ucc.ie/record=b1315270~S0
Rights	© 2000, Robert J. Cosgrave - http://creativecommons.org/licenses/by-nc-nd/3.0/
Download date	2026-10-31 07:26:08
Item downloaded from	https://hdl.handle.net/10468/1665

UCC
University College Cork, Ireland
Coláiste na hOllscoile Corcaigh

DP2000 COSG

Applications of Finite Element Computer Modelling and Thermal Infrared Remote Sensing to the study of Geothermal Anomalies.

Robert J. Cosgrave

Supervisor: Dr. Bettie Higgs
Department: Department of Geology, Faculty of Science, University College Cork
Date: June 2000

Table of Contents

ACKNOWLEDGMENTS ix
ABSTRACT xi

CHAPTER 1: INTRODUCTION **1**
1.1 OUTLINE OF THESIS 5
1.2 THE PHYSICAL SYSTEM 8
1.3 THERMAL INFRARED REMOTE SENSING 11
1.4 FINITE ELEMENT MODELLING 13

CHAPTER 2: THERMAL INFRARED REMOTE SENSING **16**
1.1 THEORY OF THERMAL INFRARED REMOTE SENSING 17
1.2 GEOLOGIC THERMAL INFRARED REMOTE SENSING 24

CHAPTER 3: THE PHYSICAL MODEL **35**
3.1 GEOLOGICAL THERMAL PROCESSES 36
3.2 SURFACE THERMAL PROCESSES 51

CHAPTER 4: MATHEMATICAL MODELS **69**
4.1 ANALYTIC MATHEMATICAL MODELS 75
4.2 NUMERICAL MODELS 82

CHAPTER 5: AN INTRODUCTION TO THERMAL MODELING USING ANSYS **88**
5.1 STEADY STATE PURE CONDUCTIVE MODELS 90
5.2 TRANSIENT MODELS 96
5.3 RADIATIVE MODELS 98
5.4 SURFACE CONVECTION 100
5.5 SUBSURFACE CONVECTION MODELS 101
5.6 PHASE CHANGE MODELS 103
5.7 ELEMENTS 104
5.8 VALIDATION 107

CHAPTER 6: STEADY STATE MODELS **112**
6.1 THE ALPHA MODEL 115
6.2 ALPHA MODEL RESULTS 123
6.3 THE BRAVO MODEL 146
6.4 BRAVO MODEL RESULTS 155
6.5 CONCLUSIONS 184

CHAPTER 7: TRANSIENT MODELS **188**
7.1 MODELS 189

CHAPTER 8: PHASE CHANGE MODEL **202**
8.1 STEADY STATE PHASE CHANGE MODELS 204

8.2 TRANSIENT PHASE CHANGE MODELS 208

CHAPTER 9: THE WARM SPRINGS OF SOUTHERN IRELAND 211
9.1 REMOTE SENSING ANALYSIS 213
9.2 NUMERICAL MODELLING 222
9.3 CONCLUSIONS 223

CHAPTER 10: THE KILAUEA LAVA FLOW 225
10.1 REMOTE SENSING DATA 227
10.2 QUANTITATIVE RESULTS 244
10.3 FINITE ELEMENT MODELLING OF LAVA TUBES 258
10.4 LAVA TUBE MODEL RESULTS 270
10.5 CONCLUSIONS 273

CHAPTER 11: LUNAR THERMAL MODELLING 275
11.1 THE THERMAL GEOLOGY OF THE MOON 276
11.2 THERMAL MODELS OF THE LUNAR SURFACE 285
11.4 CONCLUSIONS 304

CHAPTER 12: MARS 306
12.1 THE THERMAL GEOLOGY OF MARS 308
12.2. PHYSICAL PROPETIES OF MARTIAN GEOLOGIC MATERIALS 314
12.3 THERMAL MODELS OF THE MARTIAN SURFACE 316
12.4 CONCLUSIONS 326

CHAPTER 13: CONCLUSIONS 327
13.1 EFFECT OF GEOTHERMAL HEAT SOURCES ON SURFACE TEMPERATURE 329
13.2 DERIVING INFORMATION ABOUT GEOTHERMAL HEAT SOURCES FROM THEIR SURFACE THERMAL ANOMALY 331
13.3 DISCRIMINATION AND IDENTIFICATION OF GEOTHERMAL HEAT SOURCES 332
13.4 THE UTILITY OF THE FINITE ELEMENT METHOD 334
13.5 THE EFFECT OF THE PHYSICAL SYSTEM ON THE MODELED RESULTS 337
13.6 FURTHER WORK 339

APPENDICES 351
A: SYMBOLS USED IN THE TEXT 351
B: ABBREVIATIONS AND ACRONYMS 352
C: PROPERTIES OF SELECTED MATERIALS 354
D: DESCRIPTION OF INSTRUMENTS 358
E: THE ALPHA AND BRAVO MODELS 363
F: IDL PROGRAMME SCRIPTS 379
G: THE FINITE ELEMENT METHOD 387

BIBLIOGRAPHY 394

Figures

1.1	Thermal Infrared Images	2
1.1	The Physical System	8
3.1	Temperature dependence and thermal conductivity dependence of basalt	41
3.2	Enthalpy for solid basalt as a function of temperature	45
3.3	Enthalpy curve of water, rock and water/rock mixes for varying porosity	46
3.4	Net Pyradiometer over grassland	56
3.5	A 3-d sonic anemometer and fine wire thermocouples	61
3.6	Mast for the measurement of surface fluxes by the profile method.	64
4.1	Simplest case mathematical model for the physical system	70
4.2	Explicit finite difference method for one-dimensional heat flow using a lumped mass approximation	85
5.1	Linear Approximation of radiant flux	92
5.2	Comparison between linear and quartic expressions for radiant flux	93
5.3	Convective heat transfer from a heated surface	101
5.4	Element symmetry modes	104
5.5	Generalised structure of the Plane 55 thermal finite element	105
5.6	Generalised structure of the Plane 77 thermal finite element	105
5.7	Generalised structure of the Surf 19 thermal finite element	106
5.8	Steady State Validation Geometry	108
5.9	Comparison of Finite element and Analytic results	110
6.1	The Alpha Model Geometry	115
6.2	Alpha Model Mesh	118
6.3	Relationship between peak temperature for different mesh densities for the Alpha Model	119
6.4	Nodal Temperature Solution for the Alpha Model	121
6.5	Surface Temperature Distribution for a typical Alpha model run	121
6.6	Thermal Flux for a typical Alpha model run	122
6.7	Variation in the Gross Thermal Gradient	124
6.8	Peak Temperature vs. Gross Thermal Gradient	124
6.9	Peak Temperature variations as a function of thermal storage properties	126
6.10	The relationship between the anomaly peak temperature and the atmospheric thermal conductivity	129
6.11	The relationship between thermal anomaly size and the thermal conductivity of the Atmospheric Boundary Layer	129
6.12	The relationship between anomaly peak temperature and SBL thermal conductivity	131
6.13	Thermal anomaly peak temperature vs. thermal conductivity of the SBL, for different values of the ABL	131
6.14	Thermal anomaly size vs. Surface Boundary Layer thermal conductivity	132

6.15	Rock thermal conductivity vs. peak temperature	133
6.16	Rock thermal conductivity and the thermal anomaly size	134
6.17	Source temperature vs. peak temperature	135
6.18	Source temperature vs. thermal anomaly size	135
6.19	Source depth vs. peak	137
6.20	Dependence of anomaly size on thermal anomaly size	137
6.21	Peak temperature vs. thermal conductivity for different source depths	139
6.22	Peak temperature vs. thermal conductivity for different source depths	139
6.23	Slope and offset of the lines for depth and anomaly size	140
6.24	Anomaly size vs. peak temperature for different anomaly size	142
6.25	Peak anomaly temperature/anomaly size ratio vs. log of the depth	143
6.26	Generalised geometry of the Bravo model (not to scale)	146
6.27	Final Bravo Model Mesh	150
6.28	The left hand side of the Bravo mesh enlarged	150
6.29	Peak temperatures derived from an equivalent series of Alpha and Bravo model runs	153
6.30	Thermal anomaly size derived from an equivalent series of Alpha and Bravo model runs	153
6.31	Background temperature vs. emissivity	156
6.32	Space node temperature vs. background temperature	156
6.33	Background temperature vs. convection film coefficient	157
6.34	Bulk temperature vs. background temperature	157
6.35	Net thermal anomaly vs. emissivity	159
6.36	Surface thermal anomaly size vs. emissivity	159
6.37	Space node temperature vs. net thermal anomaly	162
6.38	Net thermal anomaly vs. convection film coefficient	162
6.39	Net thermal anomaly size vs. convection film coefficient	163
6.40	Net thermal anomaly vs. rock thermal conductivity	165
6.41	Thermal anomaly size vs. rock thermal conductivity	166
6.42	Net thermal anomaly due to vesicularity controlled, temperature dependant thermal conductivity	167
6.43	Thermal anomaly size due to vesicularity controlled, temperature dependent thermal conductivity	167
6.44	Net thermal anomaly vs. source depth	169
6.45	Thermal anomaly size as a function of source depth	169
6.46	Net thermal anomaly vs. source temperature	171
6.47	Thermal anomaly size as a function of source temperature	171
6.48	Net thermal anomaly vs. vertical thermal conductivity	174
6.49	Thermal anomaly size vs. vertical thermal conductivity	175
6.50	Net thermal anomaly vs. source size and geometry	176
6.51	Thermal anomaly size vs. source size and geometry	177
6.52	Net thermal anomaly vs. thermal conductivity for various depths	178
6.53	Thermal anomaly size vs. thermal conductivity for different depths	179
6.54	The slope and offset of the lines for net thermal anomaly and thermal anomaly size plotted as a function of thermal conductivity	179
6.55	Net thermal anomaly vs. source temperature for various source depths	180
6.55	Net thermal anomaly vs. source temperature for various source depths	180
6.56	Thermal anomaly size vs. source temperature and depth	181

6.57	Variations in the slope of the Figures 6.54 and 6.56 vs. source depth	181
6.58	Offset of the trends in Figures 6.48 and 6.47	182
6.59	Net thermal anomaly/thermal anomaly size ratio vs. depth	182
6.60	Synthetic surface temperature distribution for an idealised lava tube	187
7.1	Evolution of the temperature distribution for a lava tube of 2m diameter at a depth of 3m in basalt (basalt type 3)	180
7.2	The evolution of the net thermal anomaly for two realistic end members, a lava tube set in 3m depth of high conductivity basalt (Basalt Type 3), and a lava tube set in 10m depth of low conductivity basalt (Basalt Type 4)	181
7.3	The Brick model mesh	94
7.3	The variation in surface temperature for a material subjected to varying diurnal loads	195
7.4	Variation in temperature as a function of depth for the times of maximum and minimum temperatures during the diurnal cycles	196
7.5	The variation in the surface temperature as a function of depth for the maximum and minimum temperatures in the diurnal cycle	196
7.6	The variation in the surface temperature as a function of time for three different depths of the brick model	197
7.7	Variation in temperature across four diurnal cycles for different depths	198
7.8	Variation in temperature as a function of depth the maximum temperature and minimum temperature curves	198
7.9	Variation in the surface temperature for identical surface loads and varying basal fluxes	201
7.10	The maximum and minimum daily surface temperatures as a function of increasing basal flux.	201
8.1	Net thermal vs.source temperature for phase change enabled and Phase change disabled material	205
8.2	Anomaly size vs. source temperature for temperature dependant thermal conductivity and fixed thermal conductivity	206
8.3	Peak surface temperature over time for a lava tube embedded in Type 2 Basalt for phase change enabled and phase change disabled models	210
9.1	Location of Mallow Warm Springs	212
9.2	The Mallow Town region in a false colour, visible image	214
9.3	A pixel value histogram (unstretched) for the thermal infrared band	214
9.4	A contrast stretch to the thermal infrared band image	215
9.5	A 3x3 high pass filter of the thermal image	215
9.6	Low pass filter thermal image of Mallow town	216
9.7	Directional Filtering	216
9.8	Average temperature for with pixel fraction with 373K hotspot, 292K background	218
10.1	TIMS image map of part of the east rift zone area of Kilauea	226
10.2	Precipitation in mm at the HVNP HQ weather station	228
10.3	Radiant temperature image of the lava tube region	230
10.4	Geometric distortion present in the images	231

10.5	An example of geometric distortion	232
10.6	Figure 10.6 The effect of atmospheric absorption	234
10.7	The difference between the Band 1 and Band 6 radiant temperatures	236
10.8	The emissivity curve used in deriving the kinetic temperature maps	238
10.9	A 3-D plot of the derived surface kinetic temperature	238
10.10	Kinetic temperature images	240
10.11	Image histograms	241
10.12	Band 1 minus band 6 radiant temperatures	242
10.13	Image histogram for temperature difference image of September 6th	243
10.14	Net thermal anomaly along the length of the lava tube	245
10.15	Evolution of the peak temperature value along the lava tube	245
10.16	Location of the peak temperature value along the lava tube	246
10.17	Width of the thermal anomaly (west)	246
10.18	Width of the thermal anomaly (east)	247
10.19	Difference between the thermal anomaly size to the west and east	247
10.20	Total anomaly size for the first five images, and average value	248
10.21	Variation in the total anomaly size for the selected points in the images	248
10.22	Radiant flux integrated for each row	251
10.23	Convective flux integrated for each row	251
10.24	Conductive Heat Transfer from a lava tube	260
10.25	Convective heat transfer for a lava tube in a media of various permiabilities	263
10.26	Vertical (convective plus conductive) heat transfer from a lava tube	264
10.27	Binned frequency distribution of measured peak temperature values	265
10.28	Binned frequency distribution of measured radiative flux values	266
10.29	Acceptable ranges of values for the horizontal and vertical effective thermal conductivity	269
10.30	Approximate curves for the maximum and minimum tube profiles	271
10.31	A virtual thermal image of a lava tube	272
11.1	Variation in the specific heat capacity for lunar basalt	278
11.2	The variation in density of lunar regolith as a function of depth	279
11.3	Thermal conductivity of lunar regolith as a function of temperature	281
11.4	Variation of Specific Heat Capacity of near surface fines	283
11.5	Clementine LWIR image of a lunar Rille	284
11.6	Variations in the temperature across four lunar days for various depths	286
11.7	Temperature-depth profiles maximum and minimum surface temperature	286
11.8	Disagreement between modelled and measured depth-temperature profiles	287
11.9	Basalt and regolith surface temperature variation across diurnal cycle	288
11.10	Basalt depth-temperature variation for maximum and minimum values across the diurnal cycle	289
11.11	Temperatures of mixed surface pixels	289
11.12	Variation in maximum and minimum surface temperatures for increasing geothermal flux	291
11.13	Pre-dawn Virtual Thermal Image of a region of 60% rock outcrop	292
11.14	Pre-dawn Virtual Thermal Image of a region of anomalous geothermal heat flow	293
11.15	Noon Virtual Thermal Image of a region of 60% rock outcrop	294

11.16	Noon Virtual Thermal Image of a region of anomalous $30Wm^{-2}$ geothermal heat flow	295
11.17	Apparent temperature of a lunar lava tube skylight	300
11.18	Radiative equilibrium model	301
11.19	Apparent radiant temperature of a lava tube skylight for a lava tube	301
11.20	Summary of the diurnal variation	305
12.1	A section of a typical TERMOSKAN thermal infrared image	310
12.2	Visible band TERMOSKAN image of the candidate volcanic activity	311
12.3	Thermal infrared image of the region shown in Figure 12.1	312
12.5	Temperature variation at various depths below the Martian surface across several diurnal cycles	319
12.6	Diurnal temperature variations at various depths for solid basalt	320
12.7	Martian surface temperature variations for different surface materials	320
12.7	Temperature range versus thermal inertia for the materials in Figure 12.6.	321
12.8	Surface temperature variation for increasing basal geothermal flux	322
12.9	Depth to the base (DTB) of Cryolithosphere	323
12.10	Effect of a basal heat flux on the DTB of Cryolithosphere	324
13.1	A hemispherical view of Io, showing visible and thermal infrared views	341
13.2	Fractured ice surfaces on Europa	342
13.3	ASTER image of Mauna Loa, Hawaii	343
13.4	Photo of Ape Cave, Washington. Empty lava tube with skylight	344

Acknowledgements

At the Department of Geology, University College Cork, I would like to thank my supervisor, Dr. Bettie Higgs, for her assistance, guidance, and patient reviewing of my work and Professor P.M. Bruck, Head of Department. I would also thank Joanne Clarke for tips on Ansys and IDL and Jim Smith for general IT support and assistance. I would also like to thank the rest of the staff and postgraduates of the department for helping to make my time there a pleasant one.

At the Jet Propulsion Laboratory, I would like to thank Dr. Anne Kahle for facilitating and hosting my visit to JPL. Also at JPL, Dr. Simon Hook, for driving me halfway across America, and Dr. John P. Schieldge for driving me the other half, and teaching me about surface boundary layers, Sonia Chernobieff at JPL for patient help with provision of TIMS datasets, Ron Alley for provision of TIMS calibration data, I would also like to thank Howard L. Tan, Dr Andrew Morrison, Dr. Elsa Abbott, and Dr. Frank Palluconi.

Also of assistance in the in the course of my US study visit was Dr. Laszlo Keszthelyi, who leading the way in the thermal properties of basalt, and Professor Bruce Murray for introducing me to Dr. Keszthelyis' work. Dr. Hugh H. Kieffer and Dr. Bruce Jakosky for taking the time to meet with me, Dr. B.H. Betts for providing me with the TERMOSKAN dataset, and Dr. Neal Fujii, Hawaii State Climatologist, for provision of meteorological data.
At the Open University, Dr. Dave Rothery, Robin Wright and Dr. Stephan Blake who provided assistance and advice in the course of a study visit.

This project was financially supported by a Higher Education Grant from Kerry Co. Council, and Forbairt/Enterprise Ireland basic Research Grant (BR/1995/015), and a postgraduate studentship from the Department of Geology, University College Cork, I would also like to thank Dr. Pat Meere for various and nefarious assistance in seeking further funds, and Antoin O'Slatara for showing him how.

The student himself was supported by the patience and gainful employment of Coca-Cola Bottlers, Ireland (with thanks to Mary Breen) and Dan O'Keeffe B.Agr.Sci, and the unending patience of Catherine Sheehan at Bank of Ireland.

I would also like to thank my Family, Ruth, Una and Mike, my housemates, Annette O'Herlihy M.A., and Aimi Baker B.Sc. for washing dishes and putting up with me.
And, finally, Edith O'Regan, for everything.

This thesis is dedicated to Dr. Edith O'Regan

Abstract

Buried heat sources can be investigated by examining thermal infrared images and comparing these with the results of theoretical models which predict the thermal anomaly a given heat source may generate. Key factors influencing surface temperature include the geometry and temperature of the heat source, the surface meteorological environment, and the thermal conductivity and anisotropy of the rock.

In general, a geothermal heat flux of greater than 2% of solar insolation is required to produce a detectable thermal anomaly in a thermal infrared image. A heat source of, for example, 2-300K greater than the average surface temperature must be at depth shallower than 50m for the detection of the anomaly in a thermal infrared image, for typical terrestrial conditions. Atmospheric factors are of critical importance. While the mean atmospheric temperature has little significance, the convection film coefficient is a dominant factor, and can act to swamp the thermal signature entirely.

Given a steady state heat source that produces a detectable thermal anomaly, it is possible to loosely constrain the physical properties of the heat source and surrounding rock, using the surface thermal anomaly as a basis. The success of this technique is highly dependent on the degree to which the physical properties of the host rock are known. Important parameters include the surface thermal properties and thermal conductivity of the rock.

Modelling of transient thermal situations was carried out, to assess the effect of time dependant thermal fluxes. One-dimensional finite element models can be readily and accurately applied to the investigation of diurnal heat flow, as with thermal inertia models. Diurnal thermal models of environments on Earth, the Moon and Mars were carried out using finite elements and found to be consistent with published measurements. The heat flow from an injection of hot lava into a near surface lava tube was considered. While this approach was useful for study, and long term monitoring in inhospitable areas, it was found to have little hazard warning utility, as the time taken for the thermal energy to propagate to the surface in dry rock (several months) is very long..

The resolution of the thermal infrared imaging system is an important factor. Presently available satellite based systems such as Landsat (resolution of 120m) are inadequate for detailed study of geothermal anomalies. Airborne systems, such as TIMS (variable resolution of 3-6m) are much more useful for discriminating small buried heat sources. Planned improvements in the resolution of satellite based systems will broaden the potential for application of the techniques developed in this thesis. It is important to note, however, that adequate spatial resolution is a necessary but not sufficient condition for successful application of these techniques.

The finite element method is a useful technique for investigations of geothermal processes. The principle advantages over older finite difference or analytical approaches are the speed, ease of use, flexibility in the model geometry, and precision. The limitations to the application of such numerical models to real world processes lie in the uncertainties of the physical parameters of real world systems, and not with any uncertainties in the modelling process.

Chapter 1: Introduction

This thesis asks the question: What can we learn about buried geological heat sources from examining their effect on surface temperature. To address this question, this thesis uses two technologies that have not been previously brought together, Thermal Infrared Remote Sensing (TIRS) and Thermal Finite Element Modelling (TFEM). Thermal Infrared Remote Sensing provides a capacity to detect and measure surface temperature patterns, and Thermal Finite Element Modelling provides a tool to model the geologic heat flow which may cause such patterns, without requiring custom software to be developed.

The principle question can be conveniently divided into three separate problems:

1. Under what circumstances will a geothermal heat source produce a detectable temperature change at the surface?

2. Given a known surface temperature distribution derived from a thermal infrared image, can the properties of the geothermal heat source be constrained by modelling the predicted surface temperature distribution and comparing it with the known surface temperature distribution?

3. Can the heat source be clearly discriminated from surrounding surface clutter?

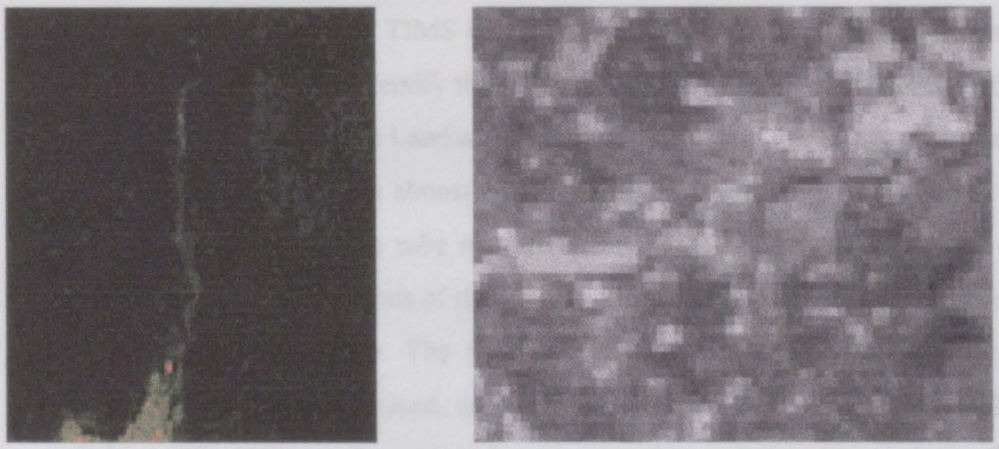


Figure 1.1 Above left: Thermal Infrared Mapping Spectrometer (TIMS) image of a lava tube and skylight from the Pu'U'Oo lava flow field, Kilauea. Spatial resolution ~ 5m per pixel. Above right: Landsat Thematic Mapper Band 6 (Thermal Infrared) image of Mallow, Co. Cork. Spatial resolution ~ 120m per pixel.

The two thermal images in Figure 1.1 demonstrate some of the principle issues in thermal infrared (TIR) detection of heat sources. In the image on the left, the linear bright patch represents a buried lava tube, carrying active lava to feed a flow that begins at the bottom of the image. The image on the right also contains a buried heat source expressed at the surface as a warm spring system. However, the bright patches in the image can all be easily correlated and explained by surface features, and the geothermal heat source has no measurable effect on the image.

There are three key differences between the two images, which explain why the geothermal heat source is visible in one, and not in the other. These are the geometry of the heat source, the resolution of the sensor system, and the nature of the surface.

The Geometry of the Heat Source: In the image on the left of Figure 1.1 (TIMS image) the heat source is strong and shallow, at a depth of less than 10m. The heat source contains active basaltic lava at over 1400K, which increases the temperature of the surface by approximately 10K over normal background levels. In the image on the right of Figure 1.1 (Landsat TM image) the heat source is a flow of warm (c. 20°C) groundwater. There is approximately 1000K of a difference in the temperature of the heat sources under consideration.

The Image Resolution: The TIMS image has a surface resolution of approximately 5m, sufficient not only to identify the heat source, but to acquire information about its' shape and structure. The Landsat TM image has a resolution of 120m, thus each pixel samples a surface area almost 600 times larger than a TIMS pixel. Even if a source as strong as the lava tube were to be present in a Landsat TM image of a uniform surface, the limitations of the sensor resolution may render it undetectable.
The Nature of the Surface: The surface material in the TIMS image is almost completely uniform, unvegetated, dark coloured pahoehoe lava flow surface. There is little significant spectral, structural or topographic variation across the surface, and this is evident in the parts of the image not affected by the geothermal heat source where little temperature variation is present. This is because all the factors controlling the surface thermal response to non-geological effects like solar radiation and convective cooling are similar across the image.

In contrast, the Landsat Thematic Mapper Band 6 (TM6) image of Mallow Town shows a great deal of variation. All the visible structure in the Landsat TM6 image can be correlated with variations in the surface. The bright areas correspond with freshly cropped fields, where stubble grass and bare earth are several degrees warmer than adjacent grassy fields, even though both are subjected to essentially the same meteorological conditions. The cropped fields have absorbed much more solar heat during the day than the grassy field, and are less capable of losing that heat by radiation and convection to the surrounding atmosphere. Even if a thermal source similar to the lava tube in the TIMS image were present in the Landsat TM image, and even if it had sufficient spatial extent to overcome image resolution effects, it may not be readily discriminated from a large, closely cropped field or hot urban surfaces.

Thus, from a consideration of the two contrasting images, the principle problems facing detection of geothermal heat sources using TIRS can be described qualitatively. What remains to be answered is where exactly the boundary between the obvious and the invisible lies, between the extremes of the images on the left and right of Figure 1.1. Quantitative analysis to define the limits of detectability of a given anomaly is not straightforward and will require numerical and mathematical modelling. Quantifying the factors that affect the surface thermal signature and

detectability of a buried geothermal heat source is the principle objective of this thesis.

1.1 OUTLINE OF THESIS

This work can be conveniently subdivided into three main sections: Chapters 2 to 5 review existing work in the field, and summarises the underlying theory of the techniques used in the study. Chapters 6, 7 and 8 describe a series of theoretical models of geological thermal processes, not applied to specific real world examples. These chapters lay an essential foundation for the subsequent application of these finite element models to specific case studies.

Chapters 9 to 12 describe various applications of the theoretical models to real world problems, and how the results may be helpful in interpreting thermal infrared images. A series of case studies are examined, to reflect as wide a variety of physical environments as possible. Chapter 13 concludes the thesis.

Chapter 2 reviews the theoretical background of thermal infrared remote sensing and methods for extracting radiant temperatures, measuring sub-pixel thermal anomalies and performing atmospheric correction. Previous work on applications of thermal infrared remote sensing to geological problems such as volcanic thermal sources and thermal inertia are also reviewed here.

Chapter 3 introduces the principal thermophysical properties of geological materials, and the factors affecting them are discussed and reviewed. The chapter then examines in more detail the physical processes outlined in *1.3 The Physical System*, geological heat transfer and surface thermal processes. These topics are, where possible, discussed quantitatively and their governing equations described.

Chapter 4 moves on to discuss more detailed mathematical and numerical models of the overall system. Previous analytic and numerical models of geologic processes are also discussed, and the mathematics of the finite element method are introduced.

Chapter 5 describes the finite element analysis software, Ansys, which is used for this study. The procedure for constructing a finite element model using Ansys is briefly described, as are the various adaptations required to accommodate radiative and convective heat transfer, transient processes and phase changes.

Chapter 6 describes two models for a simple physical system, a near surface lava tube. The first, the Alpha model, uses a simplified upper boundary condition, and the second, The Bravo Model, fully utilises the convective and radiative analysis capacities of *Ansys* to describe the upper boundary condition. Many sets of models are solved for different values of the variable parameters and the results of the Alpha and Bravo Models are compared, to assess the advantages of the more complex model, and to quantify the relative importance of the various parameters. All these individual runs are steady state, that is, they assume an unchanging, stable environment.

Chapter 7 examines time varying problems. The heating of the rock surrounding a freshly refilled lava tube is modelled. A second model considers the effect of diurnal heating and cooling on the surface temperature for different materials, and demonstrates that thermal inertia modelling can be conducted using the finite element method.

Chapter 8 investigates models of systems whose component materials undergo a phase change in the temperature range of the model. A cooling, crystallising lava tube is considered as one example. A second example considers the melting of ice in pore spaces in permafrost (cryolithosphere).

Chapter 9 examines the warm springs system of Mallow, and considers the usefulness of finite element modelling, and mathematical modelling in general, in assisting the detection of such low temperature spring systems in the thermal infrared.

Chapter 10 considers an almost ideal case study, an active lava tube. Here, a geothermal heat source is clearly visible in a set of high quality thermal infrared images, and a detailed information can be extracted from the images about the surface temperature distribution and thermal budget of the lava tubes. Using an enhanced version of the Bravo model, the depth and size of the lava tube, and the physical properties of the surrounding basalt can be constrained.

Chapter 11 discusses the application of the technique to lunar geology. A number of different problems are considered, including the extent to which a buried heat source may be detectable using thermal infrared imaging systems, whether an evacuated lava tube could be detected by means of thermal inertia, and the thermal stability of ice in the lunar regolith. Existing thermal infrared datasets are discussed

in light of these models, and means of extracting further information from them in light of numerical modelling is also considered.

Chapter 12 considers applications in Martian Geology. Finite element models of cryolithosphere melting due to endogenetic heat are described, and their consequences for the existence and detection of hydrothermal biomes are considered.

Finally, Chapter 13 discusses the implications of all this material and summarises the principle findings. Directions for potentially useful future work are also outlined.

1.2 THE PHYSICAL SYSTEM

The physical system under consideration extends from the geothermal heat source buried deep beneath the planetary surface, to the satellite sensor system high above it (see Figure 1.2). The system can be conveniently broken up into three parts, the sensor system and atmosphere, the surface boundary, and the underlying geology.

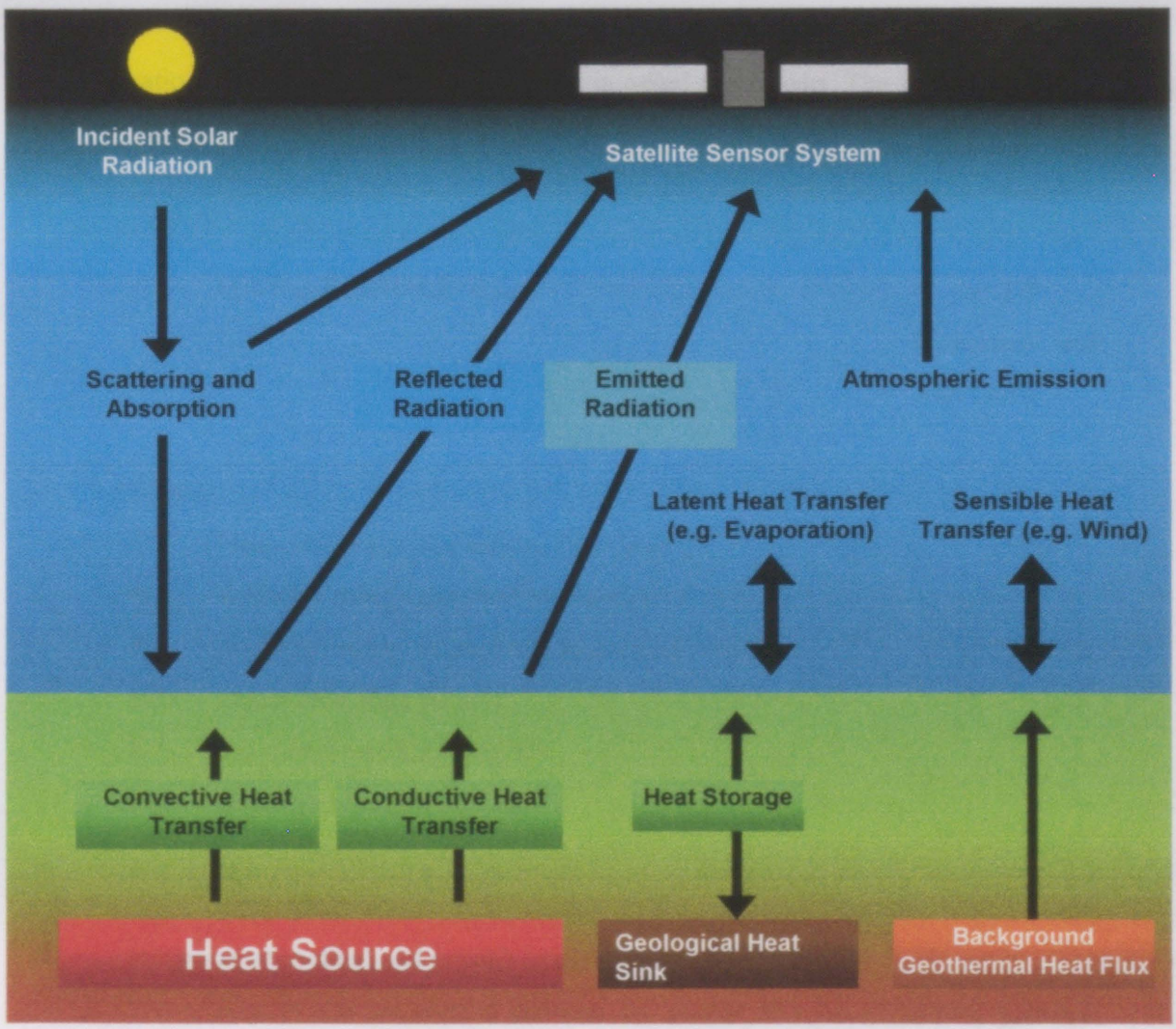


Figure 1.2 The Physical System. Arrows shows the direction of the principal energy .

In the physical system outlined in Figure 1.2, the energy fluxes vary in scale across 5 orders of magnitude, from incident solar energy with an order of

magnitude of 10^3 Wm^{-2} to geothermal fluxes with magnitudes of approximately 10^{-2} Wm^{-2}. The principle factor affecting surface temperature is solar radiation, with an incident flux of 1342 Wm^{-2} at the top of the atmosphere (Oke 1978). During interaction with the atmosphere, some of this radiation is scattered by various processes such as Mie Scattering, Rayleigh Scattering and Non-Selective Scattering. Some of the radiation is absorbed by atmospheric molecules (principally CO_2 and Water Vapour). Between 50% and 95% of the radiation incident at the top of the atmosphere reaches the surface.

At the surface a certain fraction of the incident radiation is reflected. The ratio of incident to reflected radiation is called the albedo. The remainder of the radiation is absorbed by the surface.

The energy flow at the surface can be described by a heat balance equation.

$$Q = R_{abs}-R_{rad}+H+LE+E_{geot} \qquad 1.1$$

(Cracknell and Xue 1996)

Where:

Q	Heat change per unit surface area (Wm^{-2})
R_{abs}	Radiative energy absorbed by the material (Wm^{-2})
R_{rad}	Radiative energy emitted by the material (Wm^{-2})
LE	Latent Heat Flux (Wm^{-2})
H	Sensible Heat Flux (Wm^{-2})
E_{geot}	Geothermal Heat Flux (Wm^{-2})

Heat will be lost from the surface to the atmosphere by latent heat transfer (evaporative cooling) and sensible heat transfer (wind-chill).

Heat is also transferred between the surface and the underlying geology. Background geothermal heat flow contributes only marginally to the surface energy balance. Heat is also conducted away from the surface into subsurface layers (during the day) and stored, to flow back up at night to the surface. Heat flow in subsurface layers by conduction is governed by Fouriers' Law of Heat Conduction:

$$\frac{dE}{dt} = KA\frac{dT}{dx} \qquad 1.2$$

(Halliday et al 1996)

Where:

K Thermal conductivity of the material ($Wm^{-1}K^{-1}$)

A Cross Sectional Area (m^2)

dE/dt Energy transfer as a function of time (Js^{-1})

dT/dx Temperature gradient (Km^{-1})

For high temperature gradients heat transfer may also occur by convection. The balance of all these fluxes at the surface and near surface gives an energy change at the surface per unit time, which affects the surface temperature.

The surface will emit radiation as a function of its temperature. The surface temperature and surface emissivity controls the amount of radiation emitted. For a greybody:

$$R_{net} = \varepsilon\sigma T_s^4 \qquad 1.3$$

(Halliday et at 1996)

Where:

R_{net} Net heat transfer between the surface element and the space node (Wm^{-2})

ε Emissivity

σ Stefan-Boltzmann Constant ($5.669 \times 10^{-8} Wm^{-2}K^{-4}$)

T_s Surface temperature (K)

This radiation will again undergo scattering and absorption in its passage up through the atmosphere. The satellite sensor detects this radiation (together with reflected radiation and radiation scattered from other sources) and quantifies it as a digital number. The sensors spatial resolution, spectral resolution and sensitivity will affect the recorded digital number value.

The overall physical system is quite complex, and its various components are described in more detail in *Chapter 3: The Physical Model*.

1.3 THERMAL INFRARED REMOTE SENSING

A thermal infrared image is in effect an indirect measure of the temperature of a body. Objects emit radiation as a function of their temperature and emissivity, and at temperatures encountered in most planetary environments the peak of this emitted radiation will lie in the region of the electromagnetic spectrum known as the thermal infrared. Thus a thermal infrared image of a surface can be used to derive a temperature map of the surface. The details of this process are discussed further and in detail in *Chapter 2: Thermal Infrared Remote Sensing*.

The first thermal infrared remote sensing ever conducted was carried out by Lord Rosse, from Birr Castle, Co. Offaly, Ireland, in 1868. Lord Rosse made the first measurement of radiated heat from the moon.

Imaging remote sensing systems had to wait for the development of modern electronic and coolant systems. The first thermal infrared studies of volcanic regions were conducted by aircraft in Iceland in the 1960s (Friedman et al 1969). The first satellite infrared observation of a volcanic hot spot took place in 1966, using the Nimbus II High Resolution Infrared Radiometer and was of Surtsey, Iceland (Williams and Friedman 1970).

Thermal infrared remote sensing began to reach an operational level with the launch of the Heat Capacity Mapping Mission (HCMM), which explored the utility of using day-night thermal image pairs to map surface properties. Landsat 4 and 5, with a thermal infrared channel 6 on the Thematic Mapper instrument ('TM6' for short), made high-resolution (120m) satellite thermal infrared images available for the first time. Low-resolution data (1.1 km) images also became widely available at this time from the Advanced Very High-Resolution Radiometer (AVHRR) instrument, aboard polar orbiting weather satellites. As satellite thermal imaging systems evolved, so did airborne systems, for example, the 6 channel Thermal Infrared Mapping Spectrometer (TIMS) operated by the U.S. Department of Energy (DoE).

Meanwhile, thermal infrared imaging systems have found application in planetary exploration. Thermal imaging systems have been flown to the Moon

aboard Apollo 17 and Clementine, and to Mars, aboard the Viking and Phobos orbiters, and the Mars Global Surveyor.

At the present time Landsat TM remains the highest resolution satellite based thermal infrared imaging system commercially available. Data from airborne platforms are available at much higher resolution, but only for limited areas. The Advanced Spectroscopic Thermal Emission Radiometer (ASTER) instrument, launched in December 1999 aboard the much delayed EOS AM1 Terra platform will improve availability somewhat by providing data in 6 thermal channels at 90m resolution.

1.4 FINITE ELEMENT MODELLING

The Finite Element Method (FEM) is a numerical technique for solving complex physical problems in continuous media by breaking up the domain into small, discrete finite parts. This idea is very old, and is conceptually similar to the ancient Greek method for calculating Pi by inscribing a polygon of many sides into a circle. The more sides the polygon has the closer an approximation to a circle it becomes.

In its modern form as an engineering method for structural analysis, it was first described by Hrenikoff (1941) who subdivided planer objects into collections of bars and beams. The method continued to evolve in the 1940's and 1950's. The term 'Finite Element' was first used to describe the method by Clough in 1960. The mathematics of the finite element method are briefly reviewed in *Chapter 5: An Introduction to Thermal Modelling Using Ansys* and in Appendix F. The textbooks Zienkiewicz (1971), Zienkiewicz (1985) or Reddy (1993) may serve as a starting point in the extensive literature of the finite element method.

The increasing availability of computers from the 1960's onwards made available the processing power required by the finite element method and it soon found widespread application in the aerospace industry. Initially, programs solving finite element problems had to be custom written for each application, but by the 1980's, generic software became available which allowed solution of various problems using the finite element method without the need for extensive custom written code or detailed theoretical knowledge of the method. By the 1990's, the software had evolved to a stage where numerical models could be rapidly constructed and solved on computer using the finite element method essentially as a 'black box'. Only a general familiarity with its principles is required to generate useful results rather than a detailed grounding in the mathematics. It is one of these finite element analysis software packages, *Ansys*, which is used for the work in this thesis, and it is described in more detail in *Chapter 5: An Introduction to Thermal Modelling Using Ansys*

WHAT IS A MODEL?

This thesis makes extensive use of various kinds of model, and it is worth pausing to consider the meaning of the term. According to the Oxford English Dictionary (OED) a model is:

"A simplified or idealised description or conceptions of a particular system, situation, or process (often in mathematical terms: so mathematical model) that is put forward as a basis for calculations, predictions or further investigation"

(Simpson and Weiner 1989)

It is telling that the OED also contains two pages of definitions for various other meanings of the word model. Even in strictly scientific usage, there are many different varieties of model and modelling techniques.

An analogue model is a physical experiment to simulate an actual process, for example, using hot wax to simulate flowing lava or using an electrical circuit to model a mechanical process.

A physical model is a description of a system and its constituent processes. Before proceeding to numerically model a system, one must first have a concise physical model of the system. A physical model may also include quantitative information, such as the material properties of components in the system or physical laws governing their behaviour, for example, Fourier's Law of Heat Conduction would be part of the physical model for geothermal heat flow.

Mathematical models go slightly further than physical models and attempt to describe the system in purely mathematical terms, as a set of interconnected governing equations. All the models in this thesis are fundamentally mathematical in nature.

Analytic models go further still, and attempt to solve these equations to generate useful results. For simple systems this is a relatively straight forward matter of solving the equations, but as systems become more complex, it may become necessary to include more and more approximations to an analytic model so that the equations remain soluble. Complex analytic models often include 'constants' whose values vary from case to case, and are not easily derivable. These

'constants' can often only be quantified by empirical measurements of a real physical system and models based on such terms are called Empirical Models. Many of the 'models' for Sensible Heat Transfer at the earth's surface are empirical in nature.

When systems become too complex or large for analytic models to be of use, one must turn to numerical modelling techniques. The core idea of numerical modelling is that, instead of trying to describe a system as one large complex equation, one describes the system as many small, simple equations. This is a far more straightforward approach, but not without its own difficulties. Unless one wishes to deal with systems on an atomic scale, it is necessary to break down large systems into a number of arbitrary, discrete, components (or *elements*), the behaviour of which can be described by a simple equation or set of equations. This process of discretisation of a continuous system into discrete units itself introduces uncertainties, but these can be minimised by designing the model carefully.

Two broad types of numerical model are referred to in this thesis. The bulk of geological thermal modelling, which has been published to date, uses the Finite Difference method. This thesis considers a more complex method, the Finite Element Method, and considers its usefulness in the geological context. The details of these methods and previous published applications are reviewed in *Chapter 4: Mathematical Models*

To avoid confusion, the catch all term 'model' should usually be grammatically chaperoned by a pronoun. The word 'model' is generally only used in isolation in this thesis to refer to a specific finite element model of given geometry. The process of solving a single model for a given set of variable parameters is referred to as a run, and a number of related runs with varying parameters is referred to as a *series*.

Chapter 2: Thermal Infrared Remote Sensing

The purpose of this chapter is to provide a background in the principles and applications of geological Thermal Infrared Remote Sensing, and to introduce and review relevant background material that is utilised later in the text. Individual techniques, such as radiant temperature calculation are described as required as background for subsequent chapters. Sensor systems referred to or used in the work are described separately in *Appendix D: Description of Instruments.*

2.1 THEORY OF THERMAL INFRARED REMOTE SENSING

BLACKBODY RADIATION

Thermal Infrared remote sensing is made possible because all object emit radiation as a function of their temperature. This emission obeys Planck's radiation formula:

$$M_\lambda = 2\varepsilon_\lambda \pi h c^2 / \lambda^5 [\exp(hc/\lambda kT) - 1]^{-1} \quad 2.1$$

(Plank 1901)

Where

M_λ Spectral Radiance ($Wm^{-2}\mu m^{-1}$)

ε_λ Emissivity of the surface at wavelength λ

h Planck's constant (6.626×10^{-34} Js)

c Speed of light in vacuum (2.99792×10^{8} ms^{-1})

λ Wavelength (m)

k Boltzmanns' constant (1.38054×10^{-34} $J K^{-1}$)

T Temperature (K)

CONVERSION OF DIGITAL NUMBERS TO RADIANT TEMPERATURES

Thermal infrared imaging systems do not measure surface temperature directly. Like imaging systems in other bands, they measure received radiance at the sensor and convert this into a Digital Number (DN).

Corrections for sensor distance can be omitted as:

$$R_{inst} = R_{emm}(A)/(x^2) \quad 2.2$$

Where:

R_{inst} Radiance measured by the instrument ($Wm^{-2}\mu m^{-1}$)

R_{emm} Radiance emitted per unit area ($Wm^{-2}\mu m^{-1}$)

x^2 Distance to emitter squared (m^2)

A Area of Emitter = $((IFOV)(x))^2$ 2.3

IFOV Instantaneous Field of View (radians)

When the expression 2.3 is substituted into equation 2.2 the range x between the sensor and the source cancels, leaving only the instrument field of view (IFOV). This is a fixed property and thus is usually already accounted for in the calculation of radiance to digital number conversions for the instrument.

In theory, spectral radiance can be calculated from temperature by inversion of equation 2.1 and then the result can be converted into a digital number by means of a lookup table derived from the sensor gain and offset. In practise, this is not as straightforward as it sounds. Sensors are not sensitive to a single wavelength only but have a response function (e.g. *Appendix D:* Figure D2*)*.

Equation 2.1 should be integrated across the sensor response curve to give the observed radiance value:

$$R_{inst} = \frac{\int \psi(\lambda)\, M_\lambda(T,\lambda) d\lambda}{\int \psi(\lambda)\, d\lambda} \qquad 2.4$$

(Jentoft-Nilson and Alley 1996)

Where:

ψ Instrument response function

M_λ Spectral Radiance emitted by object ($Wm^{-2}\mu m^{-1}$)

λ Wavelength (m)

R_{inst} Observed Total Radiance ($Wm^{-2}\mu m^{-1}$)

These equations cannot be inverted explicitly (Jentoft-Nilson and Alley 1996). Numerical approximations of the calculation are inaccurate, and explicitly integrating equation 2.4 for each pixel is very time consuming.

In practise, this procedure is done in reverse. For a source at a given temperature, the resultant DN is calculated (assuming that the source is a blackbody) and a lookup table is generated, giving radiant temperatures and

corresponding digital numbers (*Appendix D*: Figure D2 is generated from such a lookup table). Thus when wishing to extract radiant temperatures or generate radiant temperature maps, the pixel values can be converted directly into radiant temperature with little difficulty, provided that the lookup table is available for the instrument.

In some cases, the DN-Temperature curve can be readily approximated by an equation, for example, for Landsat TM6:

$$R_{inst} = [209.831+(0.834*DN)]-[(DN)^2*0.00133] \qquad 2.5$$

(Malaret *et al* 1985)

Where

DN Digital Number

R_{inst} Observed Total Radiance ($Wm^{-2}\mu m^{-1}$)

SUBPIXEL RADIANCE CALCULATION

The radiant temperature observed by an imaging system is an area weighted average of the radiant temperatures of the different surfaces within the target pixel. The sensor cannot resolve objects smaller than its resolution, but will amalgamate them into a single return value for a pixel. For a thermal anomaly smaller than the sensor resolution to be detectable in a remote sensing image the increase in average pixel temperature must be sufficient to increase the measured digital number by an amount greater than sensor noise.

For data with multiple thermal bands it is possible to quantify subpixel thermal anomalies. Using Dozier's method (Dozier 1981) it is possible to calculate the size and temperature of a subpixel thermal anomaly given the sensor spectral response curve and the background surface temperature. For a given spectral band:

$$R_A(t_A)=(1-P)\,R_A(t_b)+PR_A(t_{anom}) \qquad 2.6$$

(Dozier 1981)

Where:

$R_A(t_A)$ The observed radiance in Band A ($Wm^{-2}\mu m^{-1}$)

$R_A(t_b)$ The expected radiance in band A from a full pixel of background temperature ($Wm^{-2}\mu m^{-1}$)

$R_A(t_{anom})$ The expected radiance in band A from a full pixel of anomalous temperature ($Wm^{-2}\mu m^{-1}$)

P Proportion of Pixel occupied by the Thermal Anomaly

Since the radiance is often a complex function of the temperature and spectral channel response (see equation 2.1) equation 2.6 cannot always be easily solved simultaneously for multiple spectral bands to give solutions for P, t_b and t_{anom}. In theory at least three spectral bands are required to allow solution of the equation without 'guessing' any of the variables. In practice, even with multiband data such as TIMS, it is often easier to approach the problem in reverse, by calculation of the expected radiance in a given band from a pixel of given background temperature, anomaly size and anomaly temperature. This generates a lookup table giving values for the observed radiance and corresponding anomaly characteristics. However this approach presents further difficulties. Such an array for 16 bit TIMS radiance range over 6 bands would occupy $(32767*2)^6$ bytes of memory (approximately $8x10^{28}$ bytes, enough to fill $1.3x10^{20}$ CD-ROMS).

This problem could be circumvented using a greatly abbreviated lookup table to give approximate values, and then using an iterative algorithm to give a more precise result.

MINIMUM DETECTABLE ANOMALY

To calculate the minimum anomaly size and temperature that will be detectable for a given system, equation 2.6 can be rearranged to calculate the subpixel anomaly which will increase the received Digital Number by one.

$$1+ DN_a[R_a(t_a)]= DN_a[(1-P)\, R_a(t_b)+R_a(t_{anom})] \qquad 2.7$$

(Rothery et al 1995)

Where:

$DN_a[x]$ The digital number returned by radiance X in channel A.

$R_a(t_a)$ The observed radiance in Band A ($Wm^{-2}\mu m^{-1}$)

$R_a(t_b)$	The expected radiance in band A from a full pixel of background temperature ($Wm^{-2}\mu m^{-1}$)
$R_a(t_{anom})$	The expected radiance in band A from a full pixel of anomalous temperature ($Wm^{-2}\mu m^{-1}$)
P	Proportion of Pixel occupied by the Thermal Anomaly

Note that data from multiple channels will still be required to quantify the size and temperature of the thermal anomaly. This technique can be useful for determining if a geothermal source of a given size will be detectable in a given imaging system, particularly when the anomaly size is less than or equal to the sensor resolution.

ATMOSPHERIC CORRECTION

Measured radiance, either by airborne or satellite sensor system, can be affected significantly by atmospheric factors, which can either increase or decrease the received radiance. Principle atmospheric processes affecting the passage of radiation are Rayleigh scattering, Mie scattering, non-selective scattering, atmospheric absorption and atmospheric emission. For airborne surveys absorption and emission by near surface water vapour and aerosol scattering are the principle sources of atmospheric noise. Satellite and extreme high altitude surveys must also consider atmospheric ozone and carbon dioxide absorption effects. Satellite surveys are the most sensitive to atmospheric effects, due to the greater atmospheric thickness between target and sensor. For satellite sensors atmospheric effects tend to be more uniform, whereas airborne systems are subject to 'limb darkening' due to longer path lengths at the edge of the image swath.

The radiance reaching the sensor is in fact the sum of two components, the target radiance and the path radiance. The path radiance can be defined as the sum of the emitted radiation from the atmosphere along the path viewed by the sensor:

$$R_{path}=\int_0^h \sigma(t(z))^4\tau(z-h) \qquad 2.8$$

(Schott 1982)

Where:

R_{path}	Path radiance ($Wm^{-2}\mu m^{-1}$)
h	Height of sensor (m)
$Pl(\lambda,T(z))$	Planck function (of wavelength and temperature)
σ	Stefan-Boltzmann constant ($5.669x10^{-8}Wm^{-2}K^{-4}$)
t(z)	Atmospheric temperature at height z (K)
$\tau(z-h)$	Atmospheric transmissivity of the segment of atmosphere between the radiating element of atmosphere and the sensor.

Methods for the correction of atmospheric factors fall into two general categories, numerical techniques such as LOWTRAN7 and analytic techniques, such as the Split Window technique.

Numerical Techniques

Numerical techniques use complex models of the atmosphere to calculate the path radiance, absorption and scattering of light, and generate correction factors. Techniques vary, but the most popular system, LOWTRAN7 (Kneizys 1987) uses a multilayer atmospheric model to calculate these terms on a layer by layer basis. These techniques, while computationally not very intensive, generally require comprehensive meteorological data, usually in the form of an airsonde profile of temperature, pressure and humidity.

Atmospheric correction of TIMS data using LOWTRAN7 is problematical, and in tests at Kilauea (Warner and Levandowski 1992) LOWTRAN7 correction often simply inverts limb darkening effects over sea surfaces, while over land surfaces it creates very little improvement over uncorrected data.

Analytic techniques

The split window technique is useful where data exists for multiple infra red channels. The surface temperature is derived using the expression:

$$t_s=C_1+C_2 t_1+C_3 t_2 \qquad 2.9$$

(Schott 1982)

Where:

t_s Surface Temperature (K)

t_1, t_2 Observed radiant temperature in two instrument channels (K)

C_1,C_2,C_3 Derived constants.

The constants C_1,C_2,C_3 can be derived in a number of ways. If ground truth is available for two locations and atmospheric effects are assumed to be uniform for the whole scene, the constants can be calculated by simple substitution. The constants can also be derived empirically from known 'standard atmospheres'.

The split window method has limitations, it requires a known surface emissivity close to unity, a flat uniform surface and a stable atmosphere, with relatively low aerosol and water vapour contents. It was developed primary for determining accurate sea surface temperatures (SST) and is thus of reduced accuracy over land, due to emissivity variations (Givri 1997). Application of the Split Window technique to TIMS data was moderately successful in tests (Matsunaga, et al 1992) where ground truth is available.

Warner and Levandowski (1992) describe another analytical technique for atmospheric correction. For an image swath containing a sea surface, it can be assumed that the sea surface is at constant temperature and emissivity. Thus, limb darkening effects can be readily quantified from a sea surface image swath. They then proceeded to make the same assumption for vegetated surface on land to facilitate correction of terrestrial TIMS images. The method was found to be somewhat more accurate and robust than other techniques.

Even with comprehensive radiosonde data, atmospheric correction techniques are problematic. Testing of various techniques (Kalluri and Dubayah 1995) with AVHRR data showed mixed results, often with the 'corrected' data being less accurate than uncorrected data. Similarly, studies of Landsat TM data (Goetz et al 1995) found that Landsat 5 band 6 systematically overestimated the surface temperature by approximately 3.3°C. They attributed the problem to drifting of the parameters of the DN-Radiance conversion, but similar difficulties have been found in other studies. Studies of atmospheric correction of HCMM data (Schott 1982) noted that empirical correction techniques gave results within 1.1°C of the correct surface kinetic temperature whereas atmospheric propagation models such as LOWTRAN7 gave errors of up to 7°C.

2.2 GEOLOGICAL THERMAL INFRARED REMOTE SENSING

Use of thermal infrared imaging of emitted radiation for geological purposes can be subdivided into two categories, Remote Sensing of volcanic thermal sources and studies of Thermal Inertia.

REMOTE SENSING OF VOLCANIC THERMAL SOURCES

A great deal of work has been done on using remote sensing techniques in the study of volcanology. Principally this is due to the fact that many active volcanoes are difficult to study on the ground, both due to the hazardous environment, remote location and irregular timing of eruption. It is often not possible for researchers to get to an erupting volcano, or safe to work when they arrive. Remote Sensing provides relatively low cost data on active volcanoes irrespective of location.

Early Studies

Thermal infrared systems have been used for the detection of volcanic heat sources for over 30 years. Some of the earliest airborne infrared studies were carried out over Iceland (Friedman et al 1969). Night-time and twilight thermal infrared images were acquired at Surtsey, Reykjanes, Krisuvik, Hekla, Myvatn, Askja and Vatnajokull. These surveys revealed complex thermal anomalies, many previously unknown and clearly due to the volcanic activity.

The first satellite infrared observation of a volcanic hot spot was an observation of the eruptions of Surtsey in 1966, by the Nimbus II High resolution Infrared Radiometer, (Williams and Friedman 1970).

HCMM and Endogenetic Heat Sources

Attempts were made to use the Heat Capacity Mapping Mission instrument (launched in 1978, see below) for the study of geothermal sources. These attempts met with little success, probably due to the relatively low resolution of the system (Short and Stuart 1982), although an image taken one month after the eruption of Mount St. Helens did show a strong post-eruptive thermal anomaly.

Thermal Infrared Studies of Mt. St. Helens.

Some of the earliest work conducted using thermal infrared imaging to study volcanic activity was carried out at Mt. St. Helens. Thermal infrared surveys were undertaken as early as 1966 (Moxham 1970) and identified regions of geothermally elevated temperature, as did later surveys in the 1970's (Friedman and Frank 1978).

An extensive set of surveys was carried out in 1980, prior to the May 18th eruption (Kieffer et al 1982). These surveys, using a wide variety of instruments, identified multiple thermal anomalies and elevated heat fluxes both at the main crater and at associated fissures. Thermal anomalies of up to 50°C and total power outputs of up to 3MW were observed prior to May 18th eruption. Two clusters of thermal anomalies, which were identified on May 16th, occurred on surfaces that subsequently failed in the May 18th landslide. However:

"There was no major change in the pattern of thermal emission from Mount St. Helens during the last 50hr prior to the major eruption that would have signalled its immediate occurrence."

(Kieffer, *et al* 1982).

Thermal Infrared Studies of Mt. Etna.

Thermal infrared studies have been carried out of Mt. Etna volcano, in Sicily. An analysis of four night-time NOAA polar orbiter scenes acquired between October 1981 and January 1982 by Bonneville et al (1984) revealed some possible anomalies. After processing for atmospheric and elevation effects they noted a small thermal anomaly at the peak, and a major 6-8°C anomaly on the north flank of the volcano in the region of the 17th March 1983 eruption. This anomaly was too large to be accounted for by remnant heat from the surface lava flow, and was thought to indicate an underlying magma body.

Subsequent study by the same team (Bonneville and Kerr, 1987) using more complex processing techniques and a larger dataset, noted similar anomalies on the south and north east flank of the volcano prior to the 28th March 1983 eruption, which occurred in the vicinity of the southern anomaly. Bonneville and Kerr concluded that the anomaly was due to convective heat transfer from an

underlying magma body. Precise correlation of the eruption and the anomaly is difficult due to the low resolution of the data. Further work (Bonneville and Gouze 1992) detected similar anomalies, prior to the 9th December 1991 eruption, which again occurred in the region of the observed anomaly. This suggests a potential for thermal infrared imaging, even of relatively low resolution, to detect buried heat sources and serve as a predictive tool, but with limitations. In their own words:

"...these anomalies cannot readily be distinguished from others which are not directly related to actual volcanic activity."

(Bonneville and Kerr, 1987)

Other studies of Mt. Etna have been carried out using Landsat TM datasets to study the thermal budget of the June 1984 lava flow (Pieri *et al* 1990). Studies carried out using AVHRR data (e.g. Harris *et al* 1997) estimated the active lava area, thermal flux, effusion rates and total flow volume.

High resolution studies of Mt. Etna and Stromboli have been carried out using the Airborne Visible/Infrared Spectrometer (AVIRIS) system (Oppenheimer *et al* 1993). Multiple hot spots due to active lava were detected, but as AVIRIS is a short wave infrared system it was not useful for the detection of subsurface anomalies.

Other Volcano Monitoring.

Techniques of volcano monitoring using relatively low resolution systems have been developed (e.g. Harris *et al* 1997). The systems utilise relatively low-resolution satellite systems such as Landsat TM and the Advanced Very High Resolution Radiometer (AVHRR). Harris et al made use of AVHRR images to detect volcanic activity and monitor lava flow temperatures, areas and effusion rates at Krafla, Cerro Negro, Fogo, Erebus, Lascar and Mt. Etna (Harris *et al* 1997). The utility of the AVHRR system for the detection of active lavas of 1000°C with surface areas of greater than $60m^2$ has been clearly demonstrated (Mouginis-Mark *et al* 1994)

Landsat TM and AVHRR data have also been used to constrain the post 1974 activity of the Erta' Ale volcano, in Ethiopia, which has not been effectively monitored on the ground since that time (Oppenhiemer and Rothery 1997). Using

satellite data, they were able to compile a history of volcanic activity, lava effusion rates and lava lake levels through the time period 1974-1996.

TIMS Studies.

Studies of active volcanism and lava flows have been carried out using the TIMS instrument (Thermal Infrared Mapping Spectrometer).

Using a TIMS dataset acquired on the morning of October 1st 1988 over the Kupaianaha flow field, Kilauea volcano, Hawaii, the principle lava tubes feeding the main flow were identified by linear 10°C thermal anomalies (Realmuto et al 1992). Variations in the intensity of the thermal anomaly could be associated with the changes in the depth of the lava tube in the 3-8m range. Smaller thermal anomalies in the 3-5 °C range were identified associated with lava emplaced up to 10 months prior to image acquisition. Extensive thermal anomalies were also noted in the seawater at the point of lava entry.

Emissivity studies using the same data set successfully delineate older, inactive, lava tube systems by means of surface emissivity contrast due to mineral alteration by fumarolic sulphates. Different lava flows could also be delineated and assigned relative ages by variations in the emissivity spectra. TIMS data has also been used to discriminate and map Aa and S and P type Pahoehoe surfaces. (Rowland, 1992).

An extensive TIMS field campaign was conducted over the volcanoes of the Kamchatka peninsula in the summer of 1995 (Pieri et al 1997). A total of 29 volcanoes were imaged in the study, and multiple geothermal anomalies associated with the volcanics were identified.

Geothermal Systems

Thermal infra red systems have also been used to study and monitor geothermal systems associated with volcanics. Studies of geothermal fields in Japan (Sekioka 1985) using helicopter borne imaging systems have yielded heat flow estimates. Work in New Zealand, (Deroin *et al* 1995) used Landsat TM to study the distribution of geothermal systems. Deroin *et al* (1995) successfully detected many

of the larger geothermal systems in the region, but were limited by the low resolution of the imaging system.

Conclusions

In summary, work on volcano monitoring using thermal infrared techniques has been chiefly effective in the detection and monitoring of active lavas. Volcano monitoring programmes using AVHRR and GOES data are in operational use to monitor otherwise inaccessible or rarely visited volcanoes. The 1998 Galapagos eruption was first detected by this means. The information which can be gleaned from such monitoring is limited by the low resolution of the data to the detection of active volcanism only.

Thermal anomalies precursory to eruptions have been detected on several occasions, most probably due to magma driven groundwater circulation. Direct application of thermal infrared data to eruption prediction has proved problematic, and on no occasion has thermal infrared data proved to be as useful as other techniques for early warning of impending eruption. Detection of precursory thermal anomalies has been restricted by the need for high-resolution data, usually from airborne platforms such as TIMS. This is both costly and cumbersome, as an aircraft may not be available on short notice. Satellite data are not usually of sufficient resolution to give conclusive information for such studies.

There is potential for future improvement. The ASTER instrument, scheduled to fly aboard the EOS AM-1 platform in early 2000, is a multi-spectral instrument which, in addition to visible and short wave infrared data, will supply data on 6 thermal bands at a resolution of 90m. This will begin to narrow the cost-resolution gap and provide a potentially vast dataset for thermal studies of volcanology.

THERMAL INERTIA MAPPING

All surface geological materials are subjected to diurnal heating and cooling due to solar thermal forcing. The extent to which different materials heat and cool is controlled by their thermal inertia. The thermal inertia is defined as:

$$I = \sqrt{\rho k C} \qquad 2.10$$

(Cracknell and Xue 1997)

Where:

I Thermal Inertia ($Jm^{-2}s^{-1/2}K^{-1}$)

ρ Density (kgm^{-3})

k Thermal Conductivity ($Wm^{-1}K^{-1}$)

C Specific Heat Capacity ($Jkg^{-1}K^{-1}$)

The thermal inertia can be thus derived from measured physical properties or can also be measured directly from measurements of the surface temperature at different points in the diurnal cycle:

$$I=2J/\omega^{1/2}(T_{max}-T_{min}) \qquad 2.11$$

(Cracknell and Xue 1997)

Where:

T_{max} Maximum Surface Temperature (K)

T_{min} Minimum Surface Temperature (K)

J Maximum heat flux at the surface (Wm^{-2})

ω Phase angle of the Earths rotation ($7.292x10^{5}rads^{-1}$)

Thermal inertia and thermal inertia modelling are discussed in more detail in *Chapter 4: Mathematical Models.*

Early Work

Pohn et al (1970) carried out thermal inertia studies of a region in Oman using low-resolution (8km) data from the Nimbus III and VI weather satellites. They were able to readily distinguish multiple different mapped geological units, and were able in some cases to correct the existing (somewhat sketchy) geological maps by means of successfully identifying high thermal inertia regions and correlating them with probable quartzite belts. Later thermal inertia models were developed to take account of various atmospheric and meteorological effects on the surface temperature (Price 1977, Kahle 1977).

The Heat Capacity Mapping Mission

The main advances in thermal inertia mapping were made due to studies of the results of the Heat Capacity Mapping Mission (HCMM). The HCMM was launched on April 26th 1978 into a high inclination (97.6°) polar sun synchronous orbit, with local overflight times of 02.30 and 13.30 at northern mid-latitudes (NASA 1978). HCMM was a single experiment platform designed to study day-night temperature changes. Its onboard sensor operated on 2 bands, Near infrared 0.5-1.1μm and Thermal Infra Red 10.5-12.5μm. Sensor resolution was 600m. The project produced maps of Apparent Thermal Inertia (ATI), defined as

$$ATI=NC(1-\alpha)/\delta t \qquad 2.12$$

(NASA 1978)

Where:

N Scaling factor, to bring result into 1-255 range. N=1000.

C Normalising factor for latitude and solar declination.

α Albedo, measured by the NIR channel.

δt Temperature difference between day and night images (K)

HCMM data was successfully utilised in a number of publications to produce thermal inertia maps that showed strong correlation with known surficial geology in arid regions (e.g. Schieldge *et al* 1980). Thermal inertia maps were found to be of use in discriminating different lithologies with similar reflectivity but dissimilar thermal properties (Abrams *et al* 1984). Studies undertaken using HCMM data for Sardinia (Cassinis *et al* 1984) identified that apparent thermal inertia data was very sensitive to lithological and tectonic boundaries, probably due to alteration and soil moisture along contacts. They also noted difficulty in discriminating rocks with apparent thermal inertia contrast of <30-35%, although in the HCMM anthology Short and Stuart (1982) noted that Thermal Inertia maps were capable of discriminating thermal inertia contrast of 10-15%, even in regions of poor exposure.

HCMM data was also widely applied for mapping soil moisture and soil type (Pratt and Ellyett 1979), measuring plant canopy temperature, sea surface

temperatures and studies of urban heat islands. Its geological utility was however, limited to arid regions with low evaporation due to the large influence of difficult to calculate evaporation effects. Quantitatively accurate surface thermal properties could not be readily extracted from the using the HCMM data, meteorological data and assumed surface properties (Price 1982).

Post HCMM Thermal Inertia Studies.

Nash (1988) identified a buried caliche horizon in the Mojave desert due to the temperature difference in a NS001 image (Airborne Landsat TM Simulator).

Xue and Cracknell (1992, 1993 and 1996) have carried out more recent work on thermal inertia using AVHRR data. While of lower resolution than the HCMM data, Xue and Cracknell have applied more sophisticated meteorological processing and developed a system of extracting thermal inertia data from AVHRR images using the phase angle of the diurnal temperature change. Thus, Xue and Cracknells' method requires only the time of day of the maximum surface temperature in addition to the image to produce a second order approximation of the thermal inertia in areas with widely variable surface cover and soil moisture. This was necessary, as AVHRR does not provide data at maximum and minimum surface temperatures as is required by traditional thermal inertia mapping techniques. However, operational applications of thermal inertia techniques for monitoring of other properties such as soil moisture and vegetation are still very much in developmental stages.

Planetary Applications

Extensive work has been carried out in creating thermal inertia maps based on the Viking IRTM dataset. (e.g. Kieffer et al 1977). These models generally use less complex atmospheric boundary conditions and greatly simplified solar insolation, and produce estimates of thermal inertia ranging from 40-600$Wm^{-2}sec^{-1/2}$ K^{-1}, consistent with particulate materials in the upper 1-10cm of the soil (Xue and Cracknell 1996).

These estimates may be too high due to atmospheric dust effects, and more recent models (Haberle and Jakosky 1992) give values up to 26% smaller, consistent with a tenfold decrease in grain size. In all cases mapping of thermal inertia showed a

strong correlation between thermal inertia and surficial geological units (Spudis and Greeley 1976). Thermal inertia studies have also been carried out using thermal cooling in the shadow of Phobos instead of the diurnal cooling cycle (Betts 1994). Thermal infrared studies of Mars are discussed further in *Chapter 11:Mars*.

Thermal inertia mapping has also been applied to Phobos (Ksanfomality et al 1989), but has not as yet been applied extensively to other planetary bodies due to lack of suitable data.

Conclusions

Thermal inertia mapping techniques have found little operational use. In geological applications, it was limited to relatively arid areas with little or no vegetative cover and low soil moisture, as soil moisture effects dominate the thermal inertia signal. Thermal inertia proved to be useful in these regions for identifying lithological contrasts beneath thin (cm scale) layers of surficial material.

The expense of acquiring Day-Night image pairs of suitable resolution and the complex processing required has restricted the wider application of thermal inertia. The potential applications in soil moisture mapping have been overtaken, while still in developmental stages, by more effective techniques using active microwave remote sensing. Similarly, multi- and hyper-spectral imaging have superseded the use of thermal inertia for geologic mapping. Only in planetary environments such as Mars, with no evaporative effects and highly limited datasets, has thermal inertia mapping remained useful, providing data on surface properties and grain sizes unavailable from any other source.

OTHER APPLICATIONS OF THERMAL INFRARED IMAGERY

Coal Mine Fires

Thermal anomalies due to coal mine fires have been noted on thermal infrared images. In Landsat TM images of the Jharia coalfield, in Bihar state, India, thermal anomalies of 2-5 DN were detected (Saraf et al 1995). These were correlated with shallow coal fires. Estimations of fire depth were carried out based on the known

outcrop, dip and strike of the coal seam. Upwards of 45 fires were detected in this manner, at depths of up to 30m.

Landfill

Some studies have been carried out to utilise thermal infrared images of landfill to differentiate between solid waste and waste sections where methane generation was ongoing (Zilioli et al 1992). They observed a 1.2 K thermal contrast between inert waste and waste undergoing methanisation, which they interpret as being due to heat generation, rather than thermal inertia contrast, as it remained constant throughout the diurnal cycle.

Seismoactivity Surveys.

Thermal changes in groundwater have been noted as precursory to seismic activity for many years. Little work has been done in the detection of such changes using thermal infrared remote sensing. One study examined a set of approximately 10,000 AVHRR images of the region to the east of the Caspian sea (Tronin 1996) and detected regional thermal anomalies, tens of hundreds of kilometres in size, along structural lineaments and hydrothermal spring lines. Tronin found a statistically significant correlation between thermal anomaly frequency and size and subsequent seismicity. The arid, dry clear conditions of the study area present almost ideal conditions for the detection of subsurface geothermal anomalies, and Tronin conjectured that the scale of such anomalies could only be explained by enhanced hydrothermal circulation.

Mineralogic Mapping

During the day, the reflected thermal infrared radiation signal dominates over any emitted signal. Daytime thermal infrared images are thus a measure of the infrared reflective spectra of materials. Such techniques have been successfully and widely applied for mapping lithology in arid climates (Kahle and Goetz 1983, Hook et al 1994) and for mapping fresh lava flows (Crisp et al 1990). Such techniques, while useful and interesting, rely on reflected radiation rather than emitted radiation and as such are beyond the scope of this review.

Chapter 3: The Physical Model

The physical system considered in this thesis spans 150 million kilometers and several scientific disciplines. The extreme limits of the system range from the mammoth energies at the heart of the sun, where the vast majority of the energy fluxes at the earth's surface originate, to the depths of the earth, from which the geothermal sources draw their energy. The exotic environments where the energy comes from are of little direct interest to this work. The physical system being considered here is effectively the borderland between these two energy domains, solar and geothermal. Below a few metres depth, solar energy is a largely irrelevant issue, only affecting average temperatures over long time periods. A few meters above the earth's surface, all but the most dramatic expressions of geothermal heat (e.g. explosive volcanism) have little effect on the atmospheres' temperature. The most complex part of this vast physical system, the turbulent frontier between the geothermal and solar realms, is the element that we are most familiar with in our day to day experience, the earth's surface. It is important that we understand the processes going on in this region before proceeding to discuss how to numerically model the system.

The physical system and some of its key equations were briefly introduced in *Chapter 1: Introduction*. This chapter will consider, component by component, the two parts of the physical system, above and below the surface. Section 3.1 discusses Geological Heat Transfer, and the thermophysical properties of geological materials, and how they affect the transport and storage of heat. Section 3.2 discusses Surface Thermal Processes, such as heat transfer to and from the atmosphere, and radiative heat transfer processes active at the earth surface. These topics are, where possible, discussed quantitatively, and the equations describing their behavior are introduced at this stage. The assembly of these quantitative, mathematical descriptions of physical components into cohesive mathematical models of the complete physical system is discussed in *Chapter 4: Mathematical Models*.

3.1 GEOLOGICAL THERMAL PROCESSES

The extent to which heat permeates geological material and is stored by them is controlled by three primary physical properties: Density, Thermal Conductivity and Specific Heat Capacity. A number of secondary material properties are also commonly considered, chiefly thermal inertia and diffusivity. Typical values for thermophysical properties of geological materials are given in *Appendix C: Properties of Selected Materials.*

Property	Symbol	S.I. Unit	Other Unit	Conversion Factor
Density	ρ	kgm^{-3}	Gcm^{-3}	1000
Specific Heat Capacity	C	$Jkg^{-1}K^{-1}$		
Thermal Conductivity	k	$Wm^{-1}K^{-1}$	$Cal\ cm^{-1}sec^{-1}K^{-1}$	41.86
Thermal Diffusivity	κ	m^2s^{-1}		
Thermal Inertia	I	$Jm^{-2}s^{-1/2}K^{-1}$	$Cal\ cm^{-2}s^{-1/2}K^{-1}$	$41.86x10^3$

Table 3.1 Thermal Properties and their S.I. Units.

DENSITY

The density of a material is defined as the mass per unit volume of the material. The density of a sample of material can be readily measured by a variety of well-established techniques. Note that the porosity and permeability of a material may affect the measured density, depending on the measurement technique used. The density of most materials is temperature dependent, as the materials will expand when heated. For geological materials, the thermal expansion coefficients are relatively low. In the case of basalt, the linear thermal expansion at 1200K is approximately 0.5-0.6% (Touloukian et al 1989) and so this effect is negligible and need not be considered in this study. In this work, the densities of geological materials will be assumed to be constants as a function of temperature.

SPECIFIC HEAT CAPACITY

The specific heat capacity of a material (C) is defined as the amount of energy required to raise the temperature of 1kg of the material by 1K.

The specific heat capacity of material can be temperature dependant. For example Touloukian et al (1989) give expressions to describe the temperature dependence of thermal conductivity of basalt:

$C_p = 1100 Wm^{-2}K^{-1}$ For T>1010K 3.1

$C_p = 1211 - (1.12X10^5/T)$ For T≤1010K

Where

C_p Specific Heat Capacity at Constant Pressure

For some materials, the specific heat capacity can also be pressure dependent, however, references in the literature generally discuss changes due to very high pressures as might be encountered in the deep crust. Variations in the pressure ranges encountered in this study are negligible. The specific heat capacity used in this study, unless explicitly stated otherwise, is the specific heat capacity at constant pressure (C_p).

THERMAL CONDUCTIVITY

The thermal conductivity of a material is defined as the heat flux across a 1m thick layer of material per degree Kelvin (or Celsius) of temperature difference across the layer, per square metre of material, per second. The thermal conductivity of a material may be affected by a number of factors, for geological materials, the principle factor being the size and extent of internal fractures and pores, and the nature and pressure of any vapour or fluid phase within them.

Thermal Conductivity of Porous media

The thermal conductivity of material can be significantly influenced by pores and fractures and by fluid or vapour within the pores. Gas pressure variations can be significant if the dominant pore size is smaller than the mean free path for the gas (Woodside and Messmer, 1961b). This is not usually a factor in terrestrial environments, but in environments such as Mars, (mean free path ≈10m) it can play a significant role (see below).

The effect of pores on the thermal conductivity of a material is described by Maxwell's formula for a homogeneous matrix with randomly distributed spherical inclusions:

$$k = \frac{k_{bas}[2(1-\phi)k_{bas}+(1+2\phi)k_{gas}]}{[(2+\phi)k_{bas}+(1-\phi)k_{gas}]} \qquad 3.2$$

(Maxwell, 1892)

Where:

k Thermal conductivity of the bulk rock ($Wm^{-1}K^{-1}$)

k_{gas} Thermal conductivity of the gas filled vesicles ($Wm^{-1}K^{-1}$)

k_{bas} Thermal conductivity of the solid rock ($Wm^{-1}K^{-1}$)

ϕ Vesicularity of rock

This formula gives effective maximum values. For a more detailed discussion of the intricacies of thermal conductivity in basalt, the reader is referred to Hoorai (1991).

Keszthelyi (1994) discusses the effects of porosity on the thermal conductivity of basalt, and notes that radiative and convective heat transfer across pores in basalt is negligible at most temperatures.

Gas Pressure and Thermal Conductivity

Where the material in the pore spaces is a gas, the gas pressure can have a significant effect on the thermal properties of the rock. The physics of this effect are such that it is of little relevance in terrestrial studies. The gas pressure does have major effects on the calculation of thermal properties of the surface of Mars, where the atmospheric pressure dependence leads directly to a reduction in thermal inertia as a function of elevation (Keiffer 1977).

The kinetic theory of gases gives an expression for the thermal conductivity of a gas:

$$k_g = A\rho c_v v \zeta \qquad 3.3$$

(Mandl 1991)

Where:

k_g Thermal conductivity of a gas ($Wm^{-1}K^{-1}$)

A Constant

ρ Density (kgm^{-3})

c_v Specific heat capacity of the gas at constant pressure ($Jkg^{-1}K^{-1}$)

v Mean molecular velocity (ms^{-1})

ζ Mean free path (m)

The thermal conductivity of a gas is normally independent of pressure as the density is in proportion to the pressure and the mean free path is in inverse proportion to the pressure, thus effect on the component variables cancel. However, when the gas is in a confined space, this arrangement breaks down because the maximum possible mean free path is the mean pore space diameter (Woodside and Messmer 1961a).

The mean free path decreases as a function of pressure. Once the mean free path is less than the pore size, further increases have no effect on the thermal conductivity of a gas filled porous medium. When the mean free path equals or exceeds the mean pore size, gas in pore spaces begins to have an increasingly dominant effect on heat transfer in porous media.

For a vapour in a pore space of diameter d, the effective thermal conductivity is:

$$k_f = A\rho c_v v\zeta[d/(\zeta+d)] \qquad 3.4$$

(Woodside amd Messmer, 1961a)

Where:

k_f Effective thermal conductivity of a gas ($Wm^{-1}K^{-1}$)

A Constant

ρ Density (kgm^{-3})

c_v Specific heat capacity of the gas at constant volume ($Jkg^{-1}K^{-1}$)

v Mean molecular velocity (ms^{-1})

ζ Mean Free Path (m)

d Mean pore space diameter (m)

This value for the thermal conductivity of the included vapour can then be combined with the values for the surrounding rock by a variety of means, dependent on the shape and connectivity of the pore space (for example, equation 3.2). For further discussion of this effect the reader is referred to (Woodside and Messmer, 1961a).

Temperature Dependent Thermal Conductivity

The thermal conductivity of the rock and pore fluid are often in themselves temperature dependent. The temperature dependent thermal conductivity of gases are relatively well understood, and can be derived from the gas laws:

$$k_{gas}=\eta_{gas}(Cpgas+5R_m/4M_g) \qquad 3.5$$

(Mandl, 1991)

Where:

η_{gas} Viscosity of gas ($kgs^{-1}m^{-1}$)

Cp Specific Heat Capacity of gas at constant pressure ($Jkg^{-1}K^{-1}$)

R_m Molar gas Constant (8.314 $Jmol^{-1}K^{-1}$)

M_g Mean Atomic Mass of the gas

Many geological materials are also known to have temperature dependent thermal conductivity but the principle sourcebook on the matter states:

"Except for a limited number of cases it has not been possible to recommend temperature dependant property values due to the extreme scatter in the data and the lack of adequate specimen characterisation"

(Touloukian et al, 1989).

However, Keszthelyi (1994) gives the equation:

$$k_{bas}=0.427+(772/t)+-(8.72x10^4/t^2) \qquad 3.6$$

Where:

k_{bas} Thermal conductivity of Basalt ($Wm^{-1}K^{-1}$)

t Temperature (K)

As an empirical fit to the laboratory data from Touloukian et al (1989), and, in the absence of alternative formulations, this equation will be used in this thesis.

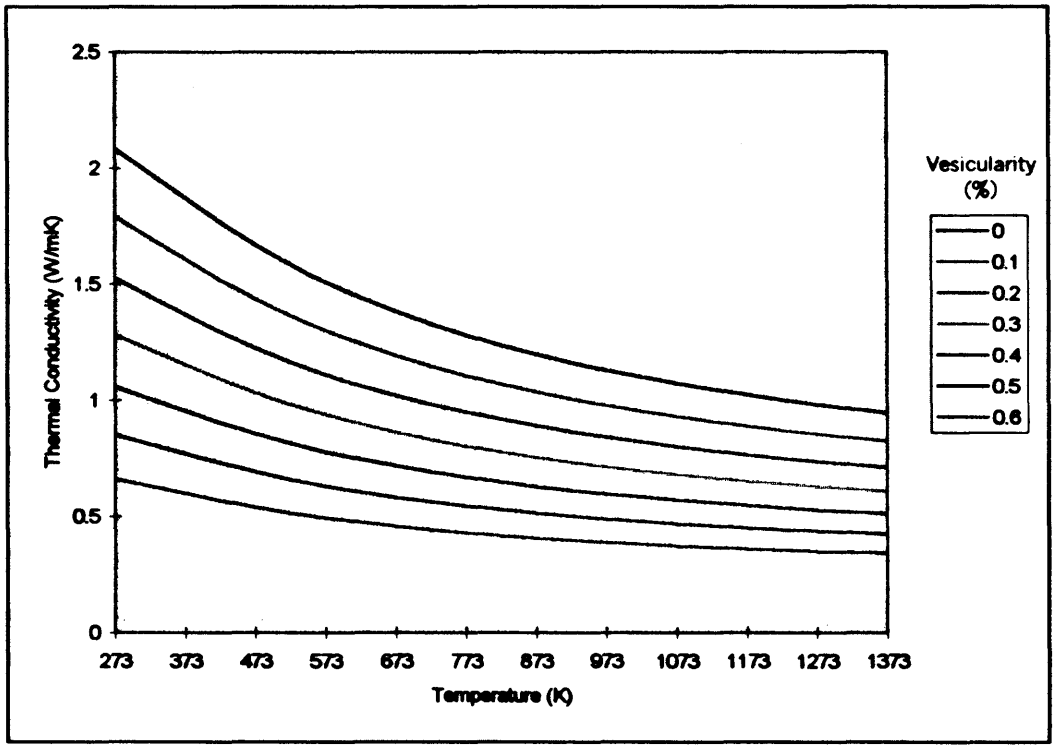


Figure 3.1 shows the temperature dependence and thermal conductivity dependence of basalt. (After Touloukian et al 1989 and Keszthelyi 1994).

Measurement

A wide variety of methods exist for the measurement of thermal conductivity of materials, some of which contain a numerical model implicit to the stated result, for example, if used to calculate heat loss from a heated probe embedded in the material to be measured. Measurements are often very specific to a given particular sample, Touloukian et al (1989) for example, cites Sass and Munroe (1974) who gives 72 values for the thermal conductivity of basalt from the Colombia River Plateau, ranging from 1.1-2.4 $Wm^{-1}K^{-1}$.

THERMAL INERTIA

Thermal inertia is a measure of how quickly the temperature of a surface will respond to changes in the surface heat balance. It is defined as:

$$I = \sqrt{\rho k C} \qquad 3.7$$

(Cracknell and Xue 1996)

Where:

I Thermal Inertia ($Jm^{-2}s^{-1/2}K^{-1}$)

ρ Density (kgm^{-3})

k Thermal Conductivity ($Wm^{-1}K^{-1}$)

C Specific Heat Capacity ($Jkg^{-1}K^{-1}$)

Thermal Inertia can also be derived directly from measurements of the surface temperature across a diurnal cycle:

$$I=2J/\omega^{1/2}(t_{max}-t_{min}) \qquad 3.8$$

(Cracknell and Xue 1996)

Where:

I Thermal Inertia ($Jm^{-2}s^{-1/2}K^{-1}$)

t_{max} Maximum diurnal surface temperature (°C or K)

t_{min} Minimum diurnal surface temperatures (°C or K)

J Maximum heat flux at the surface (Wm^{-2})

ω Phase angle of Earth rotation ($7.292x10^{-5}$)

The study of thermal inertia for remote sensing is a large field in itself and has already been discussed briefly in *Chapter 2: Thermal Infrared Remote Sensing*.

Thermal inertia can be strongly affected by the porosity of the materials, for example, the thermal inertia of basalt shows a strong inverse linear dependence on

its porosity (Zimbelman 1986), because an increase in porosity act to reduce all three of the factors affecting thermal inertia.

THERMAL DIFFUSIVITY

Thermal diffusivity is a derived property describing the rate at which a temperature change propagates through a medium. It is defined as:

$$\kappa_d = k / \rho C_p \qquad 3.9$$

(Halliday et al 1996)

Where:

κ_d Thermal Diffusivity of the rock (m^2s^{-1})

k Thermal Conductivity ($Wm^{-1}K^{-1}$)

ρ Density ($kg\ m^{-3}$)

C_p Constant pressure specific heat ($Jkg^{-1}K^{-1}$)

LATENT HEAT OF PHASE CHANGE

The latent heat of a phase change is defined as the amount of heat that is absorbed (or released) per kilogram of material when a phase change occurs. It is often referred to as the Latent Heat of Crystallisation (for solid-liquid phase changes) or the latent heat of vapourisation (for liquid vapourisation). It is of importance in phase change processes. The latent heat of crystallisation of basalt is quoted variously as $400kJkg^{-1}$ (Kesthelyi 1994), $334\pm41kJkg^{-1}$ (Peck 1978), and $209kJkg^{-1}$ (Höskuldsson and Sparks 1997).

ENTHALPY

The Enthalpy of a material is calculated from the specific heat capacity, density and temperature by the expression:

$$H_e = \int \rho C dT \qquad 3.10$$

(Heald Johnson and Roth 1995)

Where:

H_e Enthalpy of the material (Jm^{-3})

ρ Density (kgm^{-3})

C Specific Heat Capacity ($Jkg^{-1}K^{-1}$)

Enthalpy is utilised in Ansys phase change modeling (See *Chapter 5: An Introduction to Thermal Modeling Using Ansys* and *Chapter 8 Phase Change Models*) as a measure of thermal energy density, in place of density and specific heat capacity. Note that it is not an absolute property, but an energy change per unit temperature change across a given temperature range. Thus for calculation of enthalpy the enthalpy at arbitrary temperature below that expected in any model is arbitrarily set at zero, and enthalpy values generated from there.

Enthalpy of Basalt

The melting point of basalt is approximately 1343K (at one atmosphere). The latent heat of crystallisation of basalt is approximately $400kJkg^{-1}$ (Keszthelyi 1995). Given these values and the expressions for the density and specific heat capacity of basalt cited above, the enthalpy of basalt can be calculated as a function of temperature, as shown in Figure 3.2.

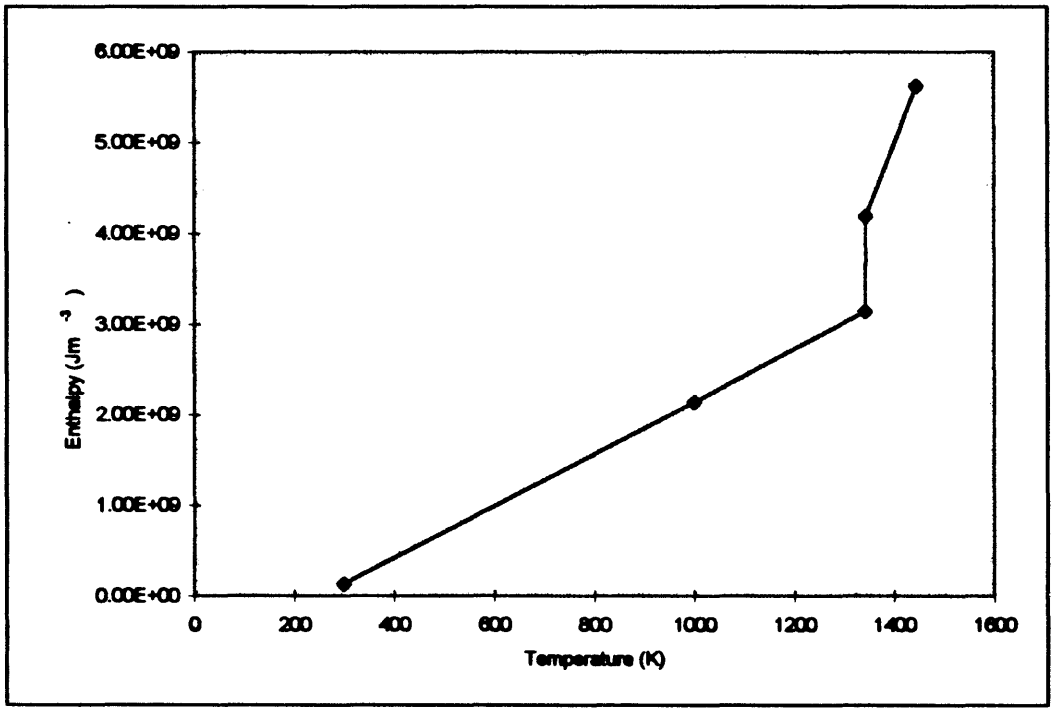


Figure 3.2 shows the enthalpy for solid basalt as a function of temperature. Enthalpy effects of exsolution of dissolved gases, vesicle formation etc. are not included in this estimate.

Enthlapy of Water Ice

Consider the melting point of ice to be 273.15K, and the latent heat of fusion to be $0.335 mJkg^{-1}$, and temperature dependant properties of ice from Raznjevic (1976), the enthalpy of water ice and water ice/rock mixes can be calculated, as shown in Figure 3.3.

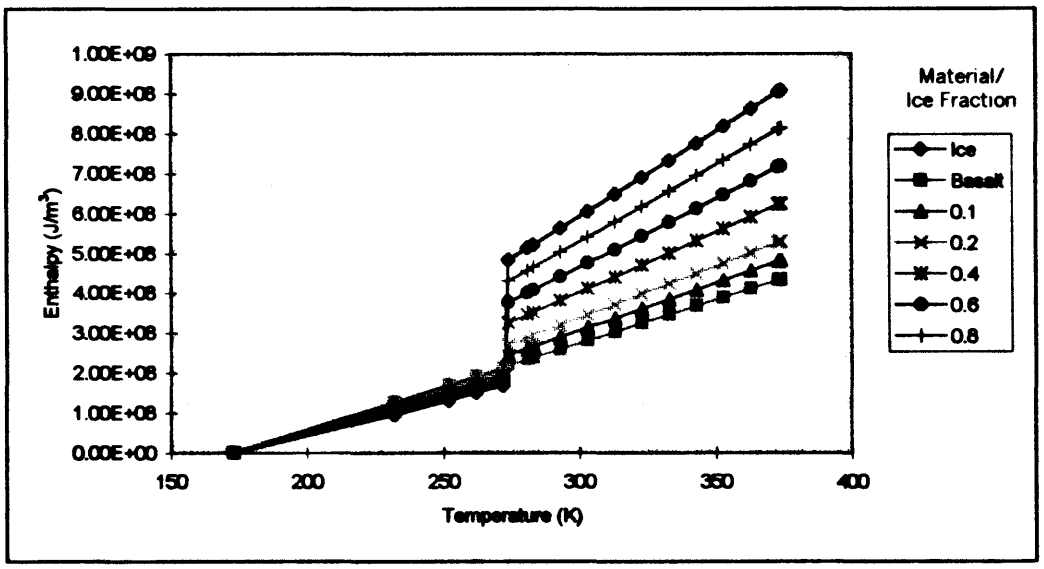


Figure 3.3 shows the enthalpy curve of water, rock and water/rock mixes for varying porosity. The rock values used are for basalt.

The thermal properties of materials, specifically geological materials, are quite variable as can be seen from the table in *Appendix C: Thermal Properties of Selected Materials*, and even within a specific rock type properties can vary significantly. Fortunately the thermal properties are relatively easy to measure and where possible it is advisable to sample the rocks and measure the thermal properties directly.

CONDUCTIVE HEAT TRANSFER

Heat transfer by thermal conduction can be described quantitatively by Fouriers Law:

$$\frac{dQ}{dt} = kA\frac{dT}{dx} \qquad 3.11$$

(Halliday et al, 1996)

Where:

k Thermal conductivity of the material ($Wm^{-1}K^{-1}$)

A Cross Sectional Area (m^2)

dQ/dt Heat Transferred as a function of time (Js^{-1})

dT/dx Temperature gradient (Km^{-1})

All mathematical models of geological heat transfer are fundamentally based on this equation. Mathematical models are described in detail in *Chapter 4: The Mathematical Model.*

CONVECTIVE HEAT TRANSFER

Convection is a much more effective heat transfer mechanism than conduction. In the context of this thesis, it occurs in two environments, above the earth's surface, and in pore spaces and fissures within the rock. There are two distinct modes of convection, forced and free convection. Forced convection occurs where heat is transferred into a fluid which is being forced across a surface by external means, for example, air pumped by a fan cooling a computer processor. Free convection occurs when heating of a fluid initiates convection currents without external assistance. In cases of geological fluid heat transfer, free convection is the relevant case.

Free convection occurs when the dimensionless Rayleigh number exceeds a critical value (Ra_c) for the fluid. The value Ra_c is dependent on the geometry of the problem. The Rayleigh (Ra) number is the product of the dimensionless Grashof (Gr) and Prandtl (Pr) numbers:

$$Ra=Gr.Pr \qquad 3.12$$

(Çengel, 1997)

The Grashof number is a dimensionless number that expresses the ratio of the buoyancy forces and the viscous forces acting on a fluid:

$$Gr= g\beta\Delta TV/\nu^2 \qquad 3.13$$

(Çengel, 1997)

Where:

Gr Grashof Number

g Acceleration due to gravity ($9.81 ms^{-1}$)

β Coefficient of volume expansion (K^{-1})

ΔT Temperature difference (K)

V Volume (δ^3)

δ Characteristic length, dependant on the geometry of the problem (m)

ν Kinematic Viscosity of the fluid (m^2s^{-1})

The Prandtl (Pr) Number is a dimensionless number that expresses the ratio of the molecular diffusivity of momentum and the molecular diffusivity of heat for the fluid:

$$Pr=\mu C_v/\chi \qquad 3.14$$

(Çengel, 1997)

Where:

Pr Prandtl number

μ Dynamic viscosity of the fluid ($kgm^{-1}s^{-1}$)

χ Specific heat ratio (C_p/C_v)

C_v Specific heat at constant temperature ($Jkg^{-1}C^{-1}$)

C_p Constant pressure specific heat ($Jkg^{-1}C^{-1}$)

The quantity of heat transferred by free convection from a surface is expressed by a heat transfer coefficient h from Newtons Law of cooling:

$$H = h\,A(T_1-T_2) \qquad 3.15$$

(Halliday et al 1996)

Where:

H Heat Transfer across the surface (Wm^{-2})

A Surface Area (m^2)

T_1-T_2 Temperature difference (K)

h Heat transfer coefficient ($Wm^{-2}K^{-1}$)

For free convection the heat transfer coefficient h is expressed as a non-dimensional heat transfer coefficient, the Nussult (Nu) number, defined as:

$$Nu = h\delta/\chi = CRa^n \qquad 3.16$$

(Çengel, 1997)

Where:

C,n Constants dependant on the problem geometry (determined experimentally for each geometry)

χ Specific heat ratio C_p/C_v

V Volume (δ^3)

δ Characteristic length, dependant on the geometry of the problem (m)

GEOTHERMAL HEAT

The geothermal heat flux is generally the unknown variable in this equation, and its effect on surface temperature must be modelled numerically. Generally the geothermal heat flux will be split between 2 components.

Firstly, the diurnal heat storage represents the heat stored in subsurface layers. This term may be negative, in the case of heat underlying material absorbing heat from the surface during the day, or positive as underlying material cools during the night. Integrated across a full day cycle this term will sum to approximately zero. The quantity of heat stored in this way is controlled by the thermal inertia of the underlying material.

Secondly, the true geothermal heat flow, which represents the heat flow from deeper regions of the earth, will be constant, uninterrupted and normally very small, on continental areas averaging approximately $0.059Wm^{-2}$ (Armstead and Tester, 1987). Regions of elevated heat flow such as Steamboat Springs, Nevada, may have rates in the order of $0.34Wm^{-2}$ (Thompson and White, 1964). To provide a measurable effect on the surface heat flow the geothermal heat flux will have to be greater than the uncertainty range of the other conditions. This specific problem is addressed in model series 7.1.3, in *Chapter 7: Transient Models*.

OTHER GEOTHERMAL PROCESSES

Other thermal processes that take place include phase changes, chemical reactions within the rock such as combustion and radiative heat transfer within the pore spaces.

Phase changes consume or produce a quantity of heat called the Latent Heat of Phase Change (through vapourisation, crystallisation etc.) This can be a relevant process in the near surface in a number of ways, such as crystallisation of lava or melting/freezing of interstitial fluid such as occurs in permafrost regions.

Chemical reactions are not usually thermally significant in the near surface, with the exception of burning. Coal Mine fires are a common problem in coal mining regions, and can burn for months or years, and leave readily detectable thermal signatures at the surface (Saraf et al 1995).

Radiative heat transfer within pore spaces is also possible, but has been determined to be insignificant under most normal regimes. Only for materials with very large pore spaces or porosities and very high thermal gradients does radiative heat transfer become significant (Keszthelyi 1994).

3.2 SURFACE THERMAL PROCESSES

Surface and near surface processes control the flow of heat between a surface and the atmosphere and space above it. The study of these surface thermal processes is a large field of meteorology in itself, and this review aims to be functional for the purposes of the background required by the thesis rather than a complete review. A fully comprehensive review of boundary layer meteorology lies far beyond the scope of this work, but this brief review of the field should be more than adequate for the purposes of this thesis. Material in this review is drawn from a wide variety of sources, chiefly from Xue and Cracknell (1995), Pratt et al (1980), Brutsaert (1982), Price (1977), Kahle (1977) and Oke (1978), Garrett (1992). The interested reader may refer to these as an introduction to the vast field of boundary layer meteorology.

Three meteorological factors dominate the surface thermal signature:

- Radiation: Both incident on the surface from the sun and emitted from the surface by thermal emission.
- Sensible Heat Transfer: Heat transfer to and from the atmosphere.
- Latent Heat Transfer: Heat lost from the surface due to evaporative cooling.

RADIATION

Radiative energy absorbed by the Surface

The radiation incident on the surface is the sum of the direct and indirect solar radiation.

$$R_{net}=R_{dir}+R_{sky} \qquad 3.17$$

Where:

R_{net} Energy absorbed at surface (Wm^{-2})

R_{dir} Direct Radiance absorbed (Wm^{-2})

R_{sky} Background sky radiance absorbed (Wm^{-2})

In areas of low relief a third term representing reflection and emission of radiation from nearby surfaces can be safely omitted as it is negligible (see equation 3.19, below for related aspect correction). The ratio of direct to indirect radiation is strongly a function of local meteorology and cloud cover. In cases of very high atmospheric scattering direct radiation will be negligible, all radiation being completely absorbed and scattered by the atmosphere.

Direct Radiation

The direct radiation from the sun can be described by the equation:

$$R_{dir} = S\tau(\varepsilon)(Sin\delta sin\varphi + Cos\delta Cos\varphi Cos\omega t) \qquad 3.18$$

(Duffie and Beckman 1974)

Where:

S Solar Constant at the top of the Atmosphere ($1367 \pm 7 Wm^{-2}$)

τ Atmospheric transmissivity

ε Emissivity

δ Solar Declination (Rad)

φ Local Latitude (Rad)

ω Phase angle of Earth rotation ($7.292 \times 10^{5} rad\ s^{-1}$)

t Number of seconds after local solar noon (s)

In areas of complex topography it may be necessary to correct for surface aspect:

$$R_{dir}^{*} = R_{dir} Sin\beta \qquad 3.19$$

Where:

R_{dir}^{*} Radiance corrected for Aspect (Wm^{-2})

R_{dir} Radiance Incident on a horizontal surface (Wm^{-2})

β Angle between the surface and the sun on the plane containing the sun (Rad)

Indirect Radiation

Indirect radiation is due to general background sky radiance. It is comprised of radiation emitted by the atmosphere (generally long wave) and scattered radiation (generally short wave, due to wavelength dependant scattering). It should be noted that terrestrially, most long wave indirect radiation incident on a surface is from thermal emission in the lower 100m of the atmosphere and thus most long-wave radiation formulae use values at the meteorological screen height, circa 1.5m (Oke, 1978).

A number of empirical relationships exist to describe the net longwave radiation flux at the surface under cloudless skies as a function of other variables. Most are derived by statistical regression and are useful for daily averages only, not as a precise calculation. A typical relation would be:

$$R_{sky} = -170.9 + 1.2\sigma T_a^4 \qquad 3.20$$

(Swinbank, 1963)

Where:

R_{sky} Indirect radiation (Wm^{-2})

σ 5.669×10^{-8} ($Wm^{-2}K^{-4}$)

T_a Air Temperature (K)

This particular expression is only valid for temperatures greater than 0°C. It is unlikely to be valid for non-terrestrial environments such as Mars, where secondary emission from dust is a major factor. The importance of secondary emission from the atmosphere will need to be considered on a case by case basis.

Integrated Approach

A more integrated approach is described in Kahle (1977) from Joseph (1966, 1971). This approaches includes approximates for scattering and absorption in the atmosphere.

Assuming that wavelengths <9μm are subjected to Rayleigh Scattering and wavelengths >9μm are subjected to absorption, for a horizontal surface:

$$E_{abs} = \varepsilon_s(1-(0.271u^* \sec z)^{0.303})(0.349)(S \cos z) \quad 3.21$$

$$+ \varepsilon_s((1-\alpha_0)/(1-\alpha_0\alpha_g))(0.651)(S \cos z) \qquad \text{(Kahle, 1977)}$$

Where:

E_{abs} Energy Absorbed at surface (Wm^{-2})

ε_s Shortwave emissivity

u^* Effective Water vapour content of the atmosphere. Total precipitable water in a cloudless atmosphere (gcm^{-2})

z Zenith angle of the sun as a function of time of the day and date of year (Rad)

α_0 Atmospheric Albedo

α_g Ground Albedo

Radiative flux can also be calculated numerically by inputting the full parameters of the atmospheric column over the study region into an atmospheric model such as LOWTRAN which will calculate in detail scattering and absorption at each wavelength. However, such models are highly data intensive and require detailed radiosonde and atmospheric composition data, to an extent which would render them of little utility in this study.

For a given study area which is largely cloud free and of an aerial extent small enough that latitude and time of day variations are not likely to be significant, it is safe to assume that the longwave and shortwave radiation incident on the area is uniform

Light or scattered clouds at the time of image acquisition or prior to that time are also unlikely to be significant sources of uncertainty. Clouds present at the time of image acquisition can be readily identified in the visual band and their

shadows and 'Cold tracks' can be detected. Assuming that the clouds are random and being moved along by the wind it can safely be assumed that the net solar radiation during the time previous to the observation is still uniform across the study area. Such artifacts could also be readily removed by stacking, if sufficient images across a time series were available. Cloud thermal artifacts could also be readily removed by stacking, if sufficient images across a time series were available.

Variations in incident solar radiation across the study area due to solar time or latitude variations will be linear and uniform in nature, and are likely to be apparent only on regional scales ($>5x10^4$m). Stacking of images acquired at the same time of day would however, accentuate such clines in the data, but this would make them easier to identify and remove by filtering.

The only other effect which may cause some local increase in incident thermal radiation would be a local greenhouse effect due to locally higher concentrations of water vapour or carbon dioxide. These may be of interest as sources of endogenetic heat such as coal mine fires and volcanic activity would also be expected to emit such gases. Modelling their exact effect would require research in micrometeorology and is far beyond the context of this work. Equipment for the quantitative monitoring of such plumes is expensive and difficult to come by. If such regions of local greenhousing were stable over time, stacking would amplify them. All that can be done is to watch out for visible sign of such sources such as increased vegetation or steam plumes, in the field.

The most accurate way to acquire the incident radiation flux is by measurement, using a device such as a net pyradiometer, as shown in Figure 3.4, if available. Indirect radiation may be measured less effectively by monitoring background sky radiation with a hand held radiometer.



Figure 3.4 shows a Net Pyradiometer over grassland.

Radiation Emitted by the material

Thermal emission is a relatively simple process to describe quantitatively, but some complexities do occur.

A surface will emit energy as a grey-body radiator according to Planks law. The total heat loss due to radiation (E_{rad}) can be described as:

$$E_{rad}=\sigma\varepsilon T_{surf}^{4} \qquad 3.22$$

(Halliday 1996)

Where:

σ Stefan-Boltzmann Constant ($5.669x10^{-8}$ $Wm^{-2}K^{-4}$)

ε Emissivity

T_{surf} Surface Temperature (K)

This expression is accurate but describes an ideal case of a smooth Lambertian surface radiating into a half space.

Roughness in non-ideal surfaces also increases the emissivity, as radiation from any given point is likely to be reabsorbed by an immediately adjacent surface and re-emitted. Again, the total radiation from a surface can be measured using a Net Pyradiometer and the emissivity of a given surface in the field can be readily derived using a radiometer and an independent measure of temperature.

Discussion

Radiative thermal fluxes are the best defined and easiest to calculate of the surface fluxes, although their strong non-linearity makes incorporation into numerical modeling more difficult. Net uncertainties in the radiant flux will be in the order of 10^{-2} (1%) in most circumstance, unless radiometric measurements are available. Accurate field measurement with radiometers and/or net pyradiometers could reduce the uncertainty to 10^{-3} or 10^{-4}, depending on the quality of equipment

SENSIBLE HEAT TRANSFER

Sensible Heat Transfer is the transfer of energy between the air and the surface due to heat transfer directly into the overlying air. It is the most complex and elaborate part of the surface boundary condition. In practice, it is a combination of free convection due to heated surfaces generating convection currents, and forced convection due to wind movement.

Theoretically, the heat loss due to free convection from a flat surface can be calculated by:

$$Nu = h\delta/k = 0.225Ra^{1/3} \qquad 3.23$$

(Keszthelyi 1994)

Where:

Nu Nussult number.

h Heat transfer coefficient (Wm^{-2})

δ Characteristic dimensions, in this case the height of the plume of warm air (m).

And:

$$Ra = \rho g \beta \Delta T \delta^3 / \eta \kappa_a \qquad 3.24$$

(Keszthelyi 1994)

Where:

Ra Rayleigh number

ρ Density of air (kgm^{-3})

g Acceleration due to gravity ($9.81ms^{-1}$)

β Thermal expansion coefficient of air (K^{-1})

ΔT Temperature difference (K)

η Viscosity of air

κ_a Thermal Diffusivity of Air (m^2s^{-1})

δ Characteristic dimensions, in this case the height of the plume of warm air (m).

In air, the Rayliegh number must exceed a critical value of 1000 for free convection to occur.

For forced convection the Nussult (Nu) number equals:

$$Nu = CRe^{m} Pr^{n} \qquad 3.25$$

(Çengel 1997)

Where:

Re Reynolds Number

Pr Prandtl Number

C,m,n, Constants

The calculation of C,m and n, and hence utilisation of this theoretical approach, is complex and not readily applicable to the practical calculation of surface thermal fluxes.

Two main methods exist for the field measurement and calculation of Sensible Heat Flux: Eddy correlation methods and Profile methods.

Eddy Correlation

Eddy correlation methods are based on the measurement of vertical wind speeds and the temperature of the air, which will directly yield the amount of heat transfer in the area. It is only applicable in areas of uniform surface type. The turbulent sensible heat flux can be written as:

$$H=\rho_a C_p WT \qquad 3.26$$

(Oke 1978)

Where:

H Sensible heat Flux (Wm^{-1})

ρ_a Density of Air (kgm^{-3})

C_p Specific heat of Air at constant pressure ($Jkg^{-1}°C^{-1}$)

W Instantaneous vertical windspeed (ms^{-1})

T Instantaneous temperature (K or °C)

Measurement of latent heat flux by the eddy correlation method can be precise to within a few Wm^{-2} (Schieldge pers. comm. 1997) but require elaborate and precise equipment to measure the vertical windspeed and temperature with great accuracy. Examples of this equipment are shown in Figure 3.5. The method is described in more detail in Weaver (1990).



Figure 3.5. Shows a 3-d sonic anemometer for the measurement of vertical windspeed and fine wire thermocouple for the measurement of temperature. Readings are taken at high frequency, usually every 10th of a second, and recorded in the data storage unit (at base) for subsequent download and processing. For accuracy, Eddy correlation systems should be deployed on level ground downwind of a large, homogenous area (Hieser and Seller 1995).

Profile Methods

A variety of techniques exist under the heading of 'Profile methods' chiefly Aerodynamic and Bowen ratio type solutions. The simplest of these schemes requires an assumption of steady state non-turbulent conditions, and similarity of all transfer coefficients (diffusion coefficients of water vapour, heat, momentum etc). More complex approaches allow for turbulent conditions. One such approach is described in Oke (1978):

$$H = -\rho_a c_a k_v^2 z^2 ((\Delta u/\Delta z)(\Delta T/\Delta z)(\Phi_m \Phi_x)^{-1} \quad 3.27$$

Where:

k_v Von Karmans Constant (0.4)

z Vertical distance (m)

u Horizontal windspeed (ms^{-1})

T Temperature (K)

z Thickness of layer (m)

c_a Specific Heat of Air at constant pressure ($kJkg^{-1}K^{-1}$)

$$(\Phi_m \Phi_h)^{-1} = (1-5Ri)^2 \quad \text{(Stable case where } Ri>0) \quad 3.28.1$$

$$(\Phi_m \Phi_h)^{-1} = (1-16Ri)^{3/4} \quad \text{(Unstable case where } Ri<0) \quad 3.28.2$$

Ri is the Richardson number, an expression which quantifies the stability and degree of turbulence in the atmospheric boundary layer. It is described by the expression:

$$Ri = \frac{(g/T)(\Delta T/\Delta z)}{(\Delta u/\Delta z)^2} \quad 3.28.3$$

(Oke, 1978)

Where:

g Acceleration due to gravity ($9.81 ms^{-1}$)

T Mean temperature in the layer Δz (K)

u Horizontal windspeed (ms^{-1})

g Acceleration due to gravity ($9.81 ms^{-1}$)

T Mean temperature in the layer Δz (K)

u Horizontal windspeed (ms^{-1})

In general, Richardson numbers are linked to convection type:

Ri>1	No Convection	
1>Ri>0.01	Damped Forced Convection	
0.01>Ri>-1	Mixed Convection	
-1>Ri	Free Convection	(Oke 1978)

This method is relativity simple to use and is suitable for averaging over approximately half-hour intervals, thus reducing its sensitivity to uncertainty. Measurement requires a tower or mast of height (see Figure 3.6) equivalent to the lower atmospheric boundary layer: 1-3 m depending on the degree of surface roughness, with a number of anemometers and fine wire thermocouples at different levels to measure the required data.



Figure 3.6 shows a mast for the measurement of sensible and latent heat flux by the profile method. Note the five conventional anemometers along the left side of the mast, and four Krypton hygrometers along the right hand side. Fine wire thermocouples for temperature measurement are also present but not visible. The white box attached to the base of the mast is a data recorder. Power is supplied by the solar array over the data recorder.

Other Methods

A number of other systems exist for the calculation of sensible heat flux, for example, the methods used by Pratt et al (1980), Kesthelyi (1994) and Kahle (1977) are outlined. In most cases these systems of calculations require surface variables or parameters that are not available in the absence of detailed field measurements.

Other techniques exist for calculation of sensible heat fluxes, both over simple surfaces ('Single Source models' and vegetated surfaces 'Dual-Source models'), often using satellite derived radiometric temperatures (for reviews see Zhan et al, 1996). Such techniques are complex, and may only be useful on a site-specific basis (Cooper and Smith, 1995).

Many other methods exist for the approximation and measurement of sensible heat transfer, but are all more or less variations on the methods outlined above. Diak and Whipple (1995) estimate the sensible heat flux using satellite derived surface temperatures and an elaborate Planetary Boundary Layer model.Alternatively, sensible heat fluxes can be estimated by using geostropic wind speed (Crago et al, 1995). Other methods derive sensible heat fluxes based on the rate of change of surface temperature (Anderson et al, 1997). Sensible heat flux can also be estimated based on a single surface temperature measurement and maximum air temperature (Lagourde and McAneney, 1991). An extensive body of literature exists describing other techniques for deriving sensible heat fluxes, and for estimating the other parameters of the surface thermal balance equation from various combinations of surface and satellite datasets. While many of these techniques are useful and innovative, their complexity and data requirements place them beyond the scope of this review.

LATENT HEAT TRANSFER

Sensible heat transfer represents energy loss due to evaporative cooling at the surface. At its simplest it can be described as:

$$LE = L_v m \qquad 3.29$$

(Garrett, 1992)

Where:

LE Latent heat flux of vapourisation (kJ)

L_v Latent heat of vaporisation of water (2260kJkg^{-1})

m Mass of water evaporated or condensed (kg)

The volume of water evaporated or condensed is a complex function of many variables. Techniques for the measurement of latent heat flux again fall into two categories, Eddy Correlation methods and Profile methods.

Eddy Correlation

This method follows the same principle and limitations as the eddy correlation method for sensible heat flux, except that humidity is the measured parameter instead of temperature. The expression is:

$$LE=\rho L_v wq \qquad 3.30$$

(Oke 1978)

Where:

LE Latent Heat transfer

ρ Density of dry air (kgm^{-3})

L_v Latent heat of vaporisation of water (2260kJkg^{-1})

w Instantaneous vertical windspeed (ms^{-1})

q Specific Humidity (kg kg^{-1})

As with specific heat, it can be determined with high accuracy using similar equipment, substituting a krypton hygrometer for the fine wire thermocouple in the apparatus in Figure 3.5.

Profile Methods

These techniques are similar to those described for Sensible Heat Flux above. The equivalent expression for latent heat transfer (LE) is:

$$LE=-\rho_a L_v k^2 z^2((\Delta u/\Delta z)(\Delta q/\Delta z)(\Phi_m \Phi_x)^{-1} \qquad 3.31$$

(Oke 1978)

Where:

L_v Latent Heat of Vapourisation ($kJkg^{-1}$)

k Von Karmans Constant (0.4)

z Vertical distance (m)

u Horizontal windspeed (ms^{-1})

q Humidity of air (kgm^{-3})

T Temperature (K)

This can be measured by a system equivalent to that described for measurement of sensible heat flux (see Figure 3.4), with the addition of instruments for measurement of humidity, such as krypton hygrometers.

OTHER SURFACE THERMAL PROCESSES

Rain

Rain will affect not only the latent heat flux by altering the atmospheric and soil humidities by mass transfer of water, but will also have a massive effect on the temperature balance by heat transfer. Cold rain may chill the surface. Dissipation of mechanical energy due to the rain impact may heat the surface. Wetness may change the emissivity of the surface. Rain will alter the thermal properties of the surface layer, and as it seeps away and will transfer heat by fluid flow. These complexities are, again, well beyond the scope of this project, and will not be considered in this work. Study areas should not be assessed at times of precipitation. Such a condition is unlikely to restrict choice of areas as high soil moisture due to rain will increase the uncertainties due to latent cooling (see above) to intolerable ranges, and, in any event, rainfall will imply cloud cover which will prevent thermal imaging of the study area.

Advection

Where major variation in surface properties occur within a study area heat transfer due to advective winds may occur. Calculation of advective heat transfer is non-trivial and would probably require large-scale numerical models of the lower atmosphere. Difficulties with advection may be limited by choosing study areas without strong terrain type contrasts across the area of interest. In such cases

regional winds will probably dominate advective winds. Where surface material contrasts occur, however, care should be taken with the interpretation of thermal images close to the boundary, and, in the event of field studies, flux measurement equipment should not be sited within 50-100m of the boundary (Schieldge, 1997)

Plant Effects

Plant layers have extensive thermal effects. Transpiration from leaf stomata can have major effect on surface boundary layer temperatures. Plant canopies can strongly effect the surface albedo, and cause surfaces to differ significantly from ideal Lambertian performance. Plants can trap relatively large volumes of air close to the surface to effectively create an additional insulator to sensible heat flux, and creating an additional heat sink. By modifying near surface humidity gradients plants can radically affect latent heat transfer. Estimation of thermal fluxes across plant canopies is a thus a complex business, but can be simplified by placing sensors for flux measurement, either by eddy correlation or profile methods, a reasonable height above the plant layer. Where possible, study areas with heavy plant cover should be avoided. In practice this is not as arbitrary a judgement as it may seem, regions with strong endothermic heat sources will have high thermal gradients in the soil, which tends to discourage heavy plant growth. In geothermal areas with plant cover, the thermal source is much more likely to be identifiable by its effect on the vegetation than by direct measurement (for example, Deroin et al, 1995)

Chapter 4: Mathematical Models

This chapter sets out to review mathematical models for calculating the surface temperature using the components of the physical system already outlined in *Chapter 3: The Physical Model.* It is important to review existing mathematical models of the physical system, and the mathematics of the finite element method, before attempting to carry out any finite element modelling.

There are two principle approaches to the calculation of surface temperature, or, indeed, for modelling any complex physical problem. The first approach involves trying to generate a 'big equation' into which the relevant variables may be fed. This is referred to as an analytic approach. Such approaches are often quite mathematically elaborate and, in their efforts to create an equation that is not hopelessly unwieldy, may introduce considerable simplifications. A second approach is to break the problem up into a number of small, simple and easily soluble equations, each representing an element of the physical system. This approach, while conceptually less complex, may require solution of a very large number of equations, and because of this these computationally intensive numerical techniques did not come into common use until the advent of digital computers. These numerical modelling techniques can be subdivided into two categories, Finite Difference Methods and Finite Element Methods.

Section 4.1 discusses analytic approaches to mathematical modelling of the physical system under investigation. Numerical approaches to mathematical modelling of the system are then described in section 4.2.

Before moving on to the details of modelling techniques, it is illustrative to consider the simplest possible mathematical representation of the physical system as a whole, as illustrated schematically in Figure 4.1.

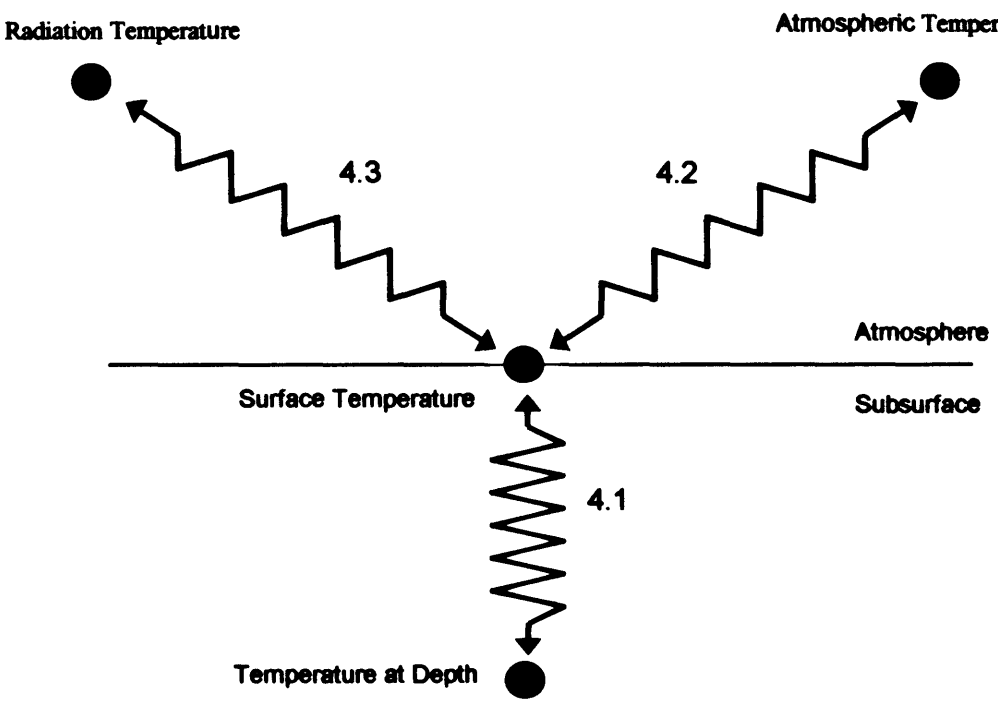


Figure 4.1 shows the simplest case mathematical model for the physical system, consisting of equations for conduction (4.1) convection (4.2) and radiation (4.3)

At its simplest level, the physical system can be mathematically described as three linked equations for conduction into the ground, and convection and radiation at the surface, as represented in Figure 4.1.

From Fouriers Law of Heat Conduction:

$$Q_1 = k(t_{surf} - t_d) \qquad 4.1$$

Where:

Q_1 Net heat transfer (Wm^{-2})

k Thermal conductivity ($Wm^{-1}K^{-1}$)

t_{surf} Surface temperature (K)

t_d Temperature at depth (K)

From Newtons Law of Cooling:

$$Q_2 = hA(t_{surf} - t_o) \qquad 4.2$$

Where:

Q_2 Net heat transfer (Wm^{-2})

h_f Film Coefficient ($Wm^{-2}K^{-1}$)

A Surface Area (m^2)

t_{surf} Surface temperature (K)

t_o Atmospheric temperature (K)

And from Planks Greybody radiation formula:

$$Q_3 = \sigma\varepsilon(t_s^4 - t_e^4) \qquad 4.3$$

Where:

Q_3 Net heat transfer (Wm^{-2})

σ Stefan-Boltzmann Constant (5.669×10^{-8} $Wm^{-2}K^{-4}$)

ε Emissivity

t_e Surface temperature (K)

t_s Radiation temperature (K)

From the heat balance equation (1.1) and the heat capacity of the surface material the surface temperature can be readily calculated for a given set of stable conditions.

$$\Delta t = (Q_1 + Q_2 + Q_3)/C \qquad 4.4$$

Where:

Δt Temperature change of the surface (K)

$Q_1 \ldots Q_3$ Net thermal fluxes (Wm^{-2})

C Specific Heat Capacity of surface material ($Jkg^{-1}K^{-1}$)

Equation 4.4 involves a number of simplifications, concerning latent heat transfer, radiative heat transfer and geologic heat transfer.

i) Latent Heat Transfer:

Comparison of the figure with equation 1.1, the surface energy balance equation, shows that the term for latent heat capacity has been eliminated. This has the effect of greatly reducing the number of variables. In most of the case studies considered in this thesis, latent heat transfer is not significant (see Chapters 9 to 12).

ii) Radiation Heat Transfer

The two radiation terms from equation 1.1, representing energy absorbed and remitted by the material, can be summed:

$$R_{net}=R_{dir}+R_{sky}-R_{rad} \qquad 4.5$$

Where:

R_{net} Net flux due to radiative processes (Wm^{-2})

R_{dir} Direct radiant flux (Wm^{-2})

R_{sky} Indirect Flux from atmospheric emission (Wm^{-2})

R_{rad} Emitted Flux (Wm^{-2})

Using equation 3.17, this can be recast as:

$$R_{net}=\sigma t_{sky}^{4}+a+b\sigma t_{a}^{4}-\sigma\varepsilon t_{surf}^{4} \qquad 4.6$$

Where:

t_{sky} Effective radiant temperature of the sky (K)

t_{a} Atmospheric Temperature (K)

t_{surf} Surface Temperature (K)

a,b Empirical constants describing atmospheric emission.

σ Stefan-Boltzmann Constant ($5.669x10^{-8}$ $Wm^{-2}K^{-4}$)

ε Emissivity

t_{sky} can be either measured directly or calculated indirectly from the solar constant. Equation 4.6 can be rearranged such that:

$$R_{net}=a+\sigma(t_{sky}^4+bt_a^4)-\sigma\varepsilon(t_{surf}^4) \quad 4.7$$

$$R_{net}=a+\sigma(t_{space}^4)-\sigma\varepsilon(t_{surf}^4) \quad 4.8$$

$$R_{net}=a+\sigma(t_{space}^4-\varepsilon t_{surf}^4) \quad 4.9$$

Where:

$$T_{space}^4=(t_{sky}^4+bt_a^4) \quad 4.10$$

iii) Geological Heat Transfer

The description of geological heat transfer is reduced to a single equation. In reality, what is represented here as a finite line element is, for all practical purpose, infinite in length, with a complex, time varying, temperature distribution near the surface. The simplification of the model here is extreme, and it is here that most of the mathematical complexities of existing models occur. Approaches for modelling the true heat distribution at and near the surface can be broadly subdivided into two categories. First, there are techniques which replace the finite line element represented by equation 4.1 with a semi-infinite half line or half space, an analytic approach. The second approach strings a large number of small, finite elements, each represented by an individual equation, together to approximate a solution, a numerical approach.

This simplified mathematical model illustrates the salient features of mathematical models of the surface temperature. Processes at or above the surface boundary layer can be described as single equations and simplified as appropriate to the conditions. For a simple boundary layer, without vegetative canopies such 'Single Source models' can be used. More complex, vegetated surfaces require 'Dual-Source models' incorporating factors like heat storage in plant canopies, latent heat transfer, and transpiration (for reviews see Zhan et al 1996). Such

techniques are complex, and may only be useful on a site-specific basis (Cooper and Smith 1995).

The key variable coupling the processes above and below the surface is the surface temperature. What goes on above the surface is difficult to measure, but can be expressed as simple equations, what goes on below the surface, as heat diffuses, requires more complex analytic or numerical solution techniques.

4.1 ANALYTIC MATHEMATICAL MODELS

The principle source of analytic mathematical thermal models is from the field of thermal engineering. Prior to the advent of high-speed computers, which facilitated numerical analysis, an analytic solution was required for complex engineering problems. Thus many geological applications of the analytic models are engineering applications in disguise. Analytic thermal modelling has been used by geologists in two principal fields, thermal inertia modelling and heat flow modelling.

THERMAL INERTIA MODELS

Most analytic modelling of geological thermal processes to date has been concerned with thermal inertia and the cyclic heating and cooling of the earth surface.

The temperatures of geological materials are controlled by their thermal properties and total heat flux. The principle source of heat in the near surface is the sun, the heat flux from which varies diurnally (See *Chapter 3: The Physical Model*). This results in cyclic heating and cooling of materials on the surface of the earth. Materials with a higher thermal inertia will tend to heat and cool more slowly.

From the conservation of energy, the temperature change in a given body of material is dependent on the net heat fluxes in and out of the material, assuming no change of state occurs:

$$dT/dt = \Sigma_t H/\rho CV \qquad 4.11$$

Where:

T	Temperature (K)
t	Time (s)
$\Sigma_t H$	Sum of heat fluxes in the time interval t (Wm^{-2})
ρ	Density of material (kgm^{-3})
C	Specific Heat Capacity ($Jkg^{-1}K^{-1}$)
V	Volume of material (m^3)

Using equation 4.11 and 1.2 it can be shown that:

$$dT(z,t)dt = \kappa_d \, d^2T(z,t)/dz^2 \qquad 4.12$$

(Cracknell and Xue,1996)

Where:

T(z,t) Temperature at time t (s), depth z (m).

κ_d Thermal diffusivity (m^2s^{-1})

Heat flow into the ground as a function of time can be expressed in simplified form by applying a sinusoidal temperature forcing at z=0 (Van Wijk, 1963, Hillel 1982), Thus:

$$T(z,t) = T_{avg} + A_z \, Sin(\omega t + n) \qquad 4.13$$

Where:

T_{avg} Average daily temperature (K)

A_z Cycle temperature amplitude at depth $z = Ae^{-z/d}$

A Cycle temperature amplitude at surface (i.e. $T_{max}-T_{min}$)

z Depth (m)

n z/d

d Thermal Skin Depth ($\sqrt{(\kappa_d P/\pi)}$

P Period ($8.44x10^4$seconds diurnal for earth, $3.15x10^5$ seconds annual for earth)

κ_d Thermal diffusivity (m^2s^{-1})

Applying this:

$$T(z,t) = T_{avg} + Aexp(-z/d)Sin(\omega t - z/d) \qquad 4.14$$

(Cracknell and Xue, 1996)

The thermal skin depth d is also known as the diurnal thermal wave penetration depth or the damping depth and is the depth at which no temperature

variation occurs due to diurnal thermal variation. For a dry sandy soil of κ_d= $0.23x10^{-6}m^2s^{-1}$, d is 0.079m. For annual variations d is about 1.5m.

Equation 4.14, while useful, has limitations. It does not incorporate geothermal heat flow. It cannot easily accommodate variations in the thermal properties of the material, and most seriously, it assumes that the surface temperature follows a simple sinusoidal curve. In fact the upper boundary condition is far more complex than that. A more elaborate analytic technique involves expressing the upper boundary condition by means of Fourier series. One such approach (Carslaw and Jaeger 1959) produced the equation:

$$T(0,t)= -\frac{A_c}{B} + \frac{(1-\alpha)\, S_0 \tau A_1 \cos(\omega t-\delta)}{I^2+\sqrt{2}\omega BI+B^2} \qquad 4.15$$

A_c,B Complex constants representing atmospheric factors

α Albedo

S_0 Solar Constant at top of the Atmosphere (Wm^{-2})

τ Atmospheric transmissivity (Average 0.75)

A_1 Coefficient of Fourier Series

δ Solar Declination (rad)

I Thermal Inertia ($Jm^{-2}s^{-1/2}K^{-1}$)

ω Phase angle of the earth's rotation

This model also has its limitations. It contains an approximation, as the Fourier series expression is truncated. The constants A and B are also approximated from meteorological data by means of highly complex equations, themselves subject to uncertainty and approximation. Significantly for this thesis, this analytic model also does not allow for geothermal heat flow, or variation in the underlying materials.

Elaboration of this basic technique has been carried out (Xue and Cracknell 1995) using sophisticated expressions for the calculation of the surface boundary condition, which enable production of thermal inertia maps directly from a single AVHRR image and the time of peak surface temperate.

Library CORK

A wide variety of other sophisticated approaches to the analytic calculation of surface temperature as a function of surface fluxes and soil properties exist, such as the force-restore method (Lin 1980). Other approaches address the fact that in moist soils, heat transfer by diffusion of water vapour can occur. While this is relevant for heat flow calculations in soil moisture studies, where the study areas are by definition of high and of variable humidity, it is considered not relevant to this work, as the case studies considered in this thesis are generally dry.

HEAT FLOW MODELS

An extensive literature of analytic solutions exists for thermal conduction problems involving heat sources. For example, Carslaw and Jaeger (1959) give a solution for a cooling lava flow:

$$T(z,t) = T_1/2\{2\mathrm{erf}(z/(2\sqrt{\alpha t})) - \mathrm{erf}((z-e)/(2\sqrt{\alpha t})) - \mathrm{erf}((z+e)/(2\sqrt{\alpha t}))\} \quad 4.16$$

Where:

$T(z,t)$ Temperature at depth z, time t

T_1 Initial Temperature (K)

z Depth (m)

t Time (s)

e Flow thickness (m)

Many of these models are mathematically quite elaborate and attempt to describe very complex physical systems in a single 'big equation'. While providing useful initial insight into a problem, using this technique, many aspects of the system are lost. Equation 4.16, for example, does not incorporate variables to allow for phase changes in the lava leading to crust formation or differences in heat flow regime between solid and liquid sections. It simply describes the cooling of a solid slab of material. As more variables and processes are added to the system, the complexity of the resulting equation increases greatly, and it becomes more time consuming to customise and adapt for a particular situation. In many cases there may be no known solution for the equations involved.

CONVECTIVE HEAT TRANSFER MODELS

The discussion above describes mathematical models with 'dry' conduction only. In real world environments many geological materials have pore spaces which may contain fluid or gas. This will affect the bulk thermal properties of the material, as described in *Chapter 3, The Physical Model.*

If the fluid or gas in the pore spaces is subjected to a hydraulic pressure gradient, and if they are interconnected to allow flow between them, then an additional dimension is added to the problem, heat transfer by mass transfer. Movement of fluid from a warm region to a cooler region of the system will bring with it a quantity of heat. Given a known, stable, fluid flow regime this quantity of heat transfer can be calculated and expressed as a function of the temperature difference and a heat transfer coefficient, which can be incorporated into the value for thermal conductivity. In this way heat transfer due to steady state fluid flow can be indirectly incorporated into finite element models. This technique is discussed further in *Chapter 5: Finite Element Modelling using Ansys.*

In a geological context, the relatively straightforward theoretical formulation of convective heat transfer (outlined in section 3.1.10) is complicated by a number of factors such as the permeability of the medium and the geometry of the heat source. The following examples of heat transfer processes in porous media are quoted from Çengel (1997) and Cheng (1985), and Bonneville and Kerr (1987).

Horizontal Hot Surface.

For a flat, hot surface with an overlying cold fluid (e.g. an intrusion under an aquifer) the form of the equation is, from Çengel 1997:

For: $10^4 \leq Ra \leq 10^7$

$$Nu=0.54Ra^{1/4} \qquad 4.17$$

For: $10^7 \leq Ra \leq 10^{11}$

$$Nu=0.15Ra^{1/3} \qquad 4.18$$

The characteristic length for this geometry is area of plate/perimeter of plate.

Rectangular Enclosure

For a rectangular enclosure heated at the bottom the matter is more complex.

Range of Pr	Range of Ra	Nussult number
1-5000	$1.7x19^3$-$6x10^3$	$Nu=0.012Ra^{0.4}$
1-5000	$6x10^3$-$3.4x10^4$	$Nu=0.375Ra^{0.2}$
1-20	$3.7x10^4$-10^8	$Nu=0.13Ra^{0.3}$
1-20	$Ra>10^8$	$Nu=0.057Ra^{1/3}$

Table 4.1 Rayleigh and Nussult numbers as a function of the Prandtl number for different enclosures (after Çengel 1997).

The characteristic dimension is the thickness of the enclosure.

Horizontal Intrusion

Bonneville and Kerr (1987) give an example of an analytic convection model over a horizontal intrusion. They use this model to demonstrate a requirement for convective heat transfer from an underlying intrusion to explain observed thermal anomalies on Mt. Etna.

Assuming fissure porosity at the contact, and a saturated water fluid phase, for natural convection in an unenclosed aquifer overlying a hot body the Rayleigh number (Ra) is given as:

$$Ra= g\beta\, \Delta THC\rho_f^2 k_p/Kn_f \qquad 4.19$$

(Bonneville and Kerr, 1987)

Where:

g Acceleration due to gravity ($9.81 ms^{-1}$)

ΔT Temperature difference between intrusion and background temperature (K)

T_m Mean temperature, the average of intrusion and background temperature (K)

β Thermal expansion coefficient of steam at given temperature = $1/T_m$ (K^{-1})

ρ Density of steam at T_m (kgm^{-3})

C Specific heat capacity of water vapour at T_m ($Jkg^{-1}K^{-1}$)

n_f Diffusivity of water vapour ($kgs^{-1}m^{-1}$)

k_p Permeability of the medium

K Thermal conductivity of the medium ($Wm^{-1}K^{-1}$)

H Thickness of the overlying layer (unenclosed aquifer) (m)

The critical value for the Rayleigh number in this geometry in $4\pi^2$ (≈ 40). Convection will take place when the Rayleigh number exceeds this value. The convective heat flux can be calculated as a function of the Nusselt number.

Not all problems can be expressed in a geometrically simple form. In any event, analytic solutions often carry implicit assumptions and approximations.

Convection in porous media is, as the examples given above serve to demonstrate, a major specialty of thermal physics. The analytic cases shown should be considered as the 'simplest cases' of a very complex field.

4.2 NUMERICAL MODELS

Numerical modelling of physical systems is a vast field, encompassing myriad different techniques, from chaotic models of non-linear systems to cellular automata models of lava flow dynamics. In modelling of heat transfer, however, two methods of numerical modelling have principally been used, the Finite Difference method, and the Finite Element method.

The discussion of these methods in this chapter restricts itself to conductive heat transfer only. An extensive body of work exists in the field of thermal engineering concerning the use of numerical methods, including the Finite Element method, for the integrated calculation of heat and mass transfer in porous media (e.g. "Free Convection about a vertical flat plate embedded in a porous medium" Cheng and Minkowycz, 1977). While some of these models are quite sophisticated, most are custom written for specific applications and are not readily applicable to the problems considered in this thesis. Generation of such models would easily be the work of a complete Ph.D. in itself, and in the absence of a Commercial Off The Shelf (COTS) modelling system, heat transfer by pore fluids will be approximated analytically in this thesis, as outlined later.

THE FINITE DIFFERENCE METHOD

Finite difference techniques have been extensively used for the study of thermal inertia and geothermal heat flow. There are two broad types of finite difference methods, implicit and explicit. The explicit finite difference method iteratively calculates the temperature at each space and time interval as a function at the previous time interval. This procedure is described graphically in Figure 4.2. The implicit finite difference method solves the same equations simultaneously, and is mathematically more exact. The finite difference system allows for variable physical properties of underlying materials and basal heat fluxes. While finite difference methods can be used three dimensionally, they have generally only been applied in one spatial dimension for geological thermal problems. The finite difference method is computationally intensive compared with analytic methods, and this has deterred many workers.

The first finite difference technique widely applied to thermal inertia problems was devised by Kahle (1977). This explicit finite difference technique modelled the upper 50cm of soil in 1cm elements. The upper boundary condition is complex, incorporating solar radiation and atmospheric effects, and sensible heat transfer (See *Chapter3: The Physical Model*). The heat conduction equation is rewritten in the form:

$$H=k(T_1-T_g)/\Delta z \qquad 4.20$$

Where:

H Heat Flux (Wm^{-2})

T_1 Temperature of element (K)

T_g Ground temperature (K)

Δz Vertical step size (m)

k Thermal Conductivty ($Wm^{-1}K^{-1}$)

Time intervals must be carefully selected to ensure accurate solutions. Kahle (1977) applied the convergence criteria to determine a time interval of less than 50 seconds.

$$\kappa_d(\Delta t/\Delta z^2)<0.5 \qquad 4.21$$

(Carnahan et al 1969)

Where:

κ_d Thermal diffusivity of the rock (m^2s^{-1})

Δt Temperature difference (K)

Δz Interval (element) size (m)

Some authors (Clifford et al 1987) prefer to use 0.25 as a convergence criterion, which results in a more stable, rapidly converging solution.

This model was considered to be reasonably accurate and was extensively used by workers, but its limitations include the requirement for extensive meteorological data not readily derivable from remotely sensed data, thus, ground truthing is required. This limitation is, however, common to any model attempting

to predict surface temperatures. This model and derivatives thereof, have been used in subsequent work on thermal inertia. Some studies (Wood et al, 1990) have indicated that the model may overestimate the thermal inertia by up to 25%, and that it is overly sensitive to variations in surface albedo and diurnal temperature.

One-dimensional finite differences have also been applied to non-terrestrial environments. The Viking thermal model (Keiffer et al, 1977) and later MARSTHERM model (Clifford et al, 1987) use an explicit finite difference technique with layers and time intervals successively increasing with depth to speed computation time. The surface boundary condition is adjusted to allow for the effects of CO_2 frost formation.

Simple three-dimensional finite difference modelling has been carried out (Tosi, 1983) for the Island of Sardinia using 20x10x0.5m blocks. The model produced thermal inertias somewhat lower than expected, as it did not take into account the energy balance at the soil surface. However, from the model Tosi concluded that a thermal inertia difference of 30-35% was required to discriminate different materials in the Sardinian environment.

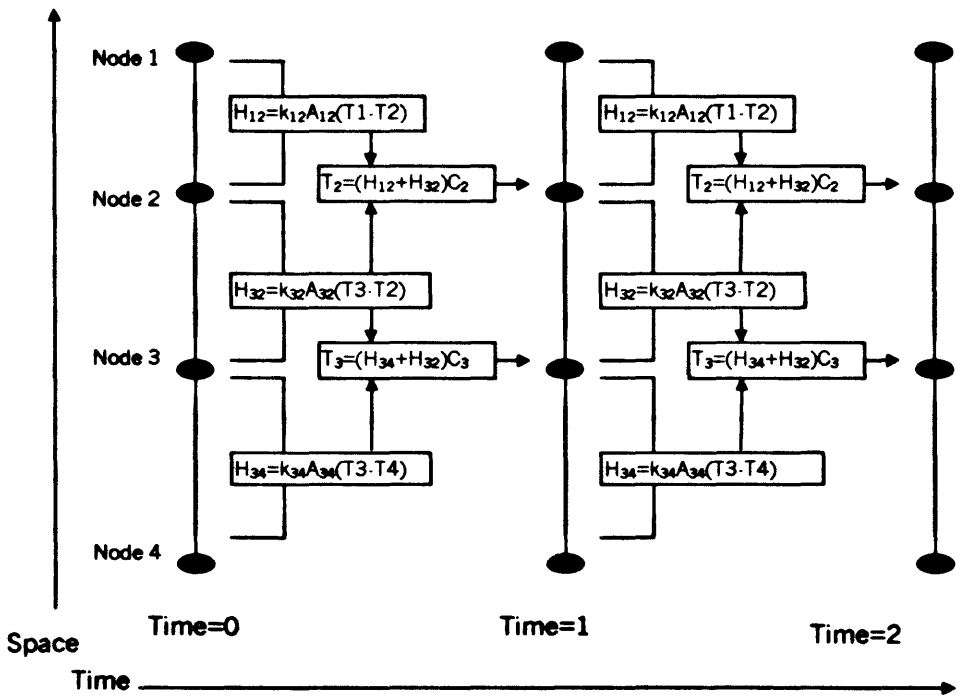


Figure 4.2 describes explicit finite difference methods for one-dimensional heat flow using a lumped mass approximation. Given an initial temperature distribution T at time = 0, (i.e. T1,T2,T3,T4) the heat transfer (H_{nm}) between adjacent nodes (subscripts n and m representing numbered nodes) is solved using the heat conduction equation (where k_{nm} is the thermal conductivity between the two nodes, and A_{nm} is the cross sectional area of contact) in the form:

$$H_{nm} = k_{nm}A_{nm}(T_n - T_m)$$

The new temperature for each node o (T_o) is then calculated based on the net heat change at that node due to flow between the adjacent nodes n,m, and the heat capacity (C_o) of a node with an equation of the form:

$$T_o = (H_{no} + H_{om})C_o$$

Thus, a new temperature distribution for the nodes at a time = 1 is generated and the process is repeated.

An extensive body of literature exists dealing with modelling of surface temperatures, heat fluxes and moisture fluxes as function of complex near surface boundary conditions (see *Chapter 4: The Physical Model*). Almost without exception the methods outlined above, or slight variations, are used to address heat storage in the near surface material in these models.

THE FINITE ELEMENT METHOD

Finite element modelling is a mathematical method for solving very large or complex problems numerically. Since the development of computerised methods in the 1950's it has been applied in nearly every field of science, from engineering and microelectronics to fluid flow physics and geology. Computer software is now available in both the public and commercial domains to solve generalised finite element problems. Computer software and specific techniques for its use are described in *Chapter 5: Introduction to Finite Element Modelling with Ansys*. Solving Finite Element models on computer requires only a cursory familiarity with the mathematics of the technique. However, one must describe the geometry, properties and boundary conditions of the model in the form of a user designed program script, and the software reads this script and solves the model. However, it is still worth reviewing broadly what happens in the 'black box'.

Briefly, by writing the governing equations of the physical model in their integral form, and utilising matrix methods a steady state thermal problem can be expressed as a large matrix equation of the form:

program script, and the software reads this script and solves the model. However, it is still worth reviewing broadly what happens in the 'black box'.

Briefly, by writing the governing equations of the physical model in their integral form, and utilising matrix methods a steady state thermal problem can be expressed as a large matrix equation of the form:

$$[K]\,(a) = (f) \qquad 4.22$$

(Heald et al, 1995)

Where:

[K] Stiffness matrix.

(a) The set of the values of the free variable at each nodal point.

(f) Forcing functions, the external forces driving the system.

For a Transient model the equation is:

$$[C](t)+[K]\,(a) = (f) \qquad 4.23$$

(Heald et al, 1995)

Where:

[C] Capacitance Matrix

(t) Time derivative of temperature.

This can then be solved by a number of computation methods such as Gauss-Siedel algorithms.

Finite Element techniques have not been extensively used in the study of thermal inertia or analysis of geothermal heat transfer. This is probably due to the general lack of readily available off-the-shelf finite element software packages, and the complexity of writing finite element programs from scratch compared with developing finite difference programs. Software like Ansys has been, until recently, relatively expensive and rare.

Hughes et al (1993) describes the use of the finite element method for geologic thermal modelling. The Hughes model uses an upper boundary condition similar to that used in Kahle (1977), but somewhat more elaborate, incorporating

model with a finite element scheme replacing Kahle's finite difference scheme. Hughes et al found the method to be accurate given sufficient meteorological information.

The mathematical procedures of the finite element method are outlined briefly in Appendix F. For a more detailed review, a wide variety of excellent textbooks are in print describing the method and its subtleties, for example Reddy 1993.

Chapter 5: An Introduction to Thermal Modelling Using Ansys

The geological numerical models described in subsequent chapters of this thesis make use of the Ansys Software package. It is important to have a basic understanding of the software before proceeding to consider applications to theoretical and practical problems in subsequent chapters.

Ansys is an off-the-shelf commercial software package used for Finite Element Analysis (FEA). A number of other FEA software packages are commercially available, (e.g. Abacus). Ansys was considered most suitable for a number of reasons, principally its relative ease of use and cost effectiveness.

Ansys is used extensively in industry, particularly in engineering, and is capable of performing finite element analysis of mechanical, thermal, electromagnetic, vibrational and fluid dynamics problems for steady state or transient cases. The Ansys interactive Graphical User Interface (GUI) allows programs or 'scripts' for various models to be written and saved. The GUI creates an illusion of simplicity for what is in fact, a complex task. Models must be generated in a rigorously logical order to produce a valid solution. Ansys, in practice, operates more like a procedural programming language than a conventional Windows application that it at first appears to be.

Ansys can be operated from the menu system, but in general, it is more time efficient and flexible to create models using scripts. A script is a text file listing the sequence of commands, which Ansys will follow. It may be easily modified and has many characteristics of a procedural programming language, such as Fortran or C. Loops or subroutines may be used to facilitate systematic variation of the model parameters.

The purpose of this chapter is to describe the Ansys Finite Element Analysis software, and the techniques for applying it to conduct numerical modelling of geologic heat flow. Particular element types and analysis techniques to be used in later chapters are introduced and described here. Methods for validation of the results of Ansys thermal models are also outlined, with some examples.

In subsequent chapters describing work carried out using Ansys a specific terminology is used to describe the hierarchy of problems addressed. The word Model is used to refer to a specific problem geometry and the Ansys script used to carry out an analysis of that problem. Each particular model contains a number of parameters, such as material properties and boundary conditions, which can be easily varied, with little alteration to the script. The process of generating a single solution of a specified model with given parameters is called a Run. Runs are generally organised into Series, where given parameters are varied systematically to ascertain their influence on the results.

Ansys does not use a single specified system of units. It is necessary to define all material properties and physical constants in an internally consistent system of units. In this work SI units are used, unless explicitly stated otherwise.

5.1 STEADY STATE PURE CONDUCTIVE MODELS

Steady state problems are relatively straightforward to investigate using Ansys. Some modifications must be made to incorporate more complex aspects of the problem, such as non-linear radiative processes and convective heat transfer, into a 'simple' purely conductive model.

MODELLING PROCEDURE

In general, the following procedure is used to generate a non-transient model:

1) Set-up: Establish the problem as a thermal problem, and select element types to be used. It may be necessary to generate physical constants associated with the element types and system of units in use.
2) Establish Material Properties and Variables: Variables (or 'parameters') can subsequently be altered in the text of the script. This allows lengthy series of similar models to be run with relative ease, once the initial script has been generated.
3) Define a Work-plane. Establishes a co-ordinate system to be used in the model.
4) Establish Model Geometry: This must be done by defining a series of keypoints using the co-ordinates system in the work-plane. These are then used to define lines, and hence areas and volumes. Areas and volumes can be created directly, but such a shortcut approach can create unforeseen problems with heat flow across area boundaries if not managed correctly.
5) Assign attributes to areas: Material Properties must be assigned to specific areas.
6) Mesh Model: The model must be discretised into a Finite Element mesh. Discretisation must be handled with care to ensure that the elements are correctly shaped, as elements with very high length/width ratios or extreme corner angles will increase final uncertainty. The mesh must also be fine enough to ensure an accurate solution (see Validation, below). Each element has a number of nodes (see element descriptions below) for which a precise solution is obtained.

7) Load Model: Temperature or heat flow loads are applied to nodes on the mesh. The computer generates the finite element matrices for the model (see *4.2.2 The Finite Element Method*).

8) Solve Model. The computer generates a nodal solution for the model and interpolates values for points between the nodes using the appropriate element shape functions.

ATMOSPHERIC BOUNDARY CONDITIONS

A purely conductive model cannot directly describe radiation and convection at its boundaries. This issue can be addressed in one of two ways. Either additional radiative and convective boundary conditions are applied, which complicates the model, or by using a conductive layer of unit thickness at the upper boundary of the model to simulate heat loss to the atmosphere from the surface by radiation and sensible heat transfer, a virtual atmospheric boundary layer. The thermal conductivity of this layer is set as a function of the atmospheric and radiative conditions. This is similar to an approach mentioned in Bonneville and Kerr (1987) who refer to the method as a 'Global Transfer Coefficient'. This technique is used for the Alpha model, described in *Chapter 6: Steady State models*. In later models, more sophisticated techniques of applying the radiative and convective loads directly are used. From Fouriers Law:

$$\frac{dE}{dt} = kA\frac{dT}{dx} \qquad 5.1$$

Where:

k Thermal conductivity of the material ($Wm^{-1}K^{-1}$)

A Cross Sectional Area (m^2)

dE/dt Heat transferred as a function of time (Js^{-1})

dT/dx Temperature gradient (Km^{-1})

Using a layer of unit thickness and unit area, and calculating the flux per unit area this reduces to

$$Q = k\Delta T/x \qquad 5.2$$

Where:

Q Heat flux across the surface (Wm^{-2})

k Thermal conductivity of the material ($Wm^{-1}K^{-1}$)

ΔT Temperature Difference (K)

x Thickness of the layer, kept at unity (m)

The Virtual Thermal Conductivity (VTC) of the Atmospheric Boundary Layer can be defined as:

$$VTC = k = h_f(\Delta T)+K_{rad}(\Delta T) \qquad 5.3$$

Where:

h_f Convection Film coefficient of Surface ($Wm^{-2}K$)

K_{rad} Linearised Radiation Coefficient ($Wm^{-2}K$)

Again, the layer thickness is 1m, so the right hand side of the equation is divided by 1m.

Latent Heat Loss cannot readily be approximated using this technique, as it is not a simple function of the temperature difference between the surface and the atmosphere. Latent heat fluxes should be neglected or treated separately, as described below.

Linearising Radiation

For equation 5.3, a Linearised Radiation coefficient must be calculated. For a system in a relatively steady state without endogenetic fluxes the radiative heat balance at the surface will sum to zero. This means that the surface will be in radiative equilibrium with its environments. Adding in an endogenetic heat source creates an additional source of energy, some of which will be lost by radiation. Thus, for a blackbody, from Planks Law:

$$\text{Additional radiative heat loss} = \sigma T_s^4-\sigma(T_s+T_d)^4 \qquad 5.4$$

Additional radiative heat loss $\approx K_{rad}(T_d)$ 5.5

Where:

T_s Steady state temperature of the Surface (K)

T_d Elevation of temperature of surface due to endogenetic heat (K)

K_{rad} Linearised radiative heat transfer coefficient ($Wm^{-2}K$)

σ $5.669x10^{-8}$ ($Wm^{-2}K^{-4}$)

By assuming that the average atmospheric temperature is the same as the steady state temperature of the surface (a reasonable assumption at long timescales) a linearised radiative heat transfer coefficent K_{rad} can be approximated for a given temperature range.

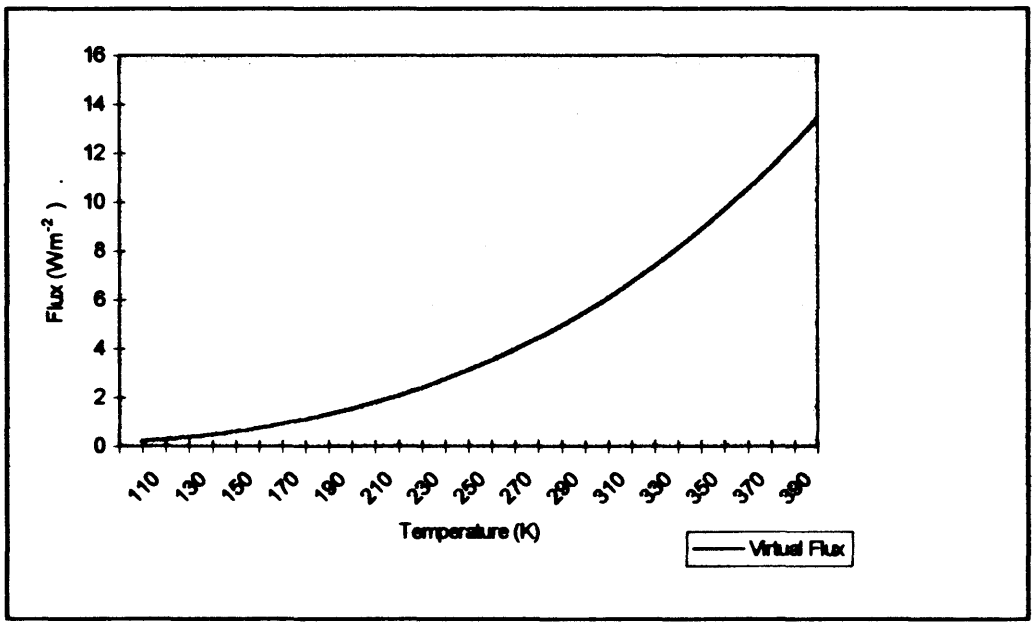


Figure 5.1 shows a linearised radiation heat flux coefficient for a range of surface temperatures using equation 5.4 and 5.5. For a blackbody, a linear approximation of 5.4 $Wm^{-2}K^{-1}$ gives a reasonable approximation of radiant flux for temperatures within 15K of 273K (see Figure 5.2).

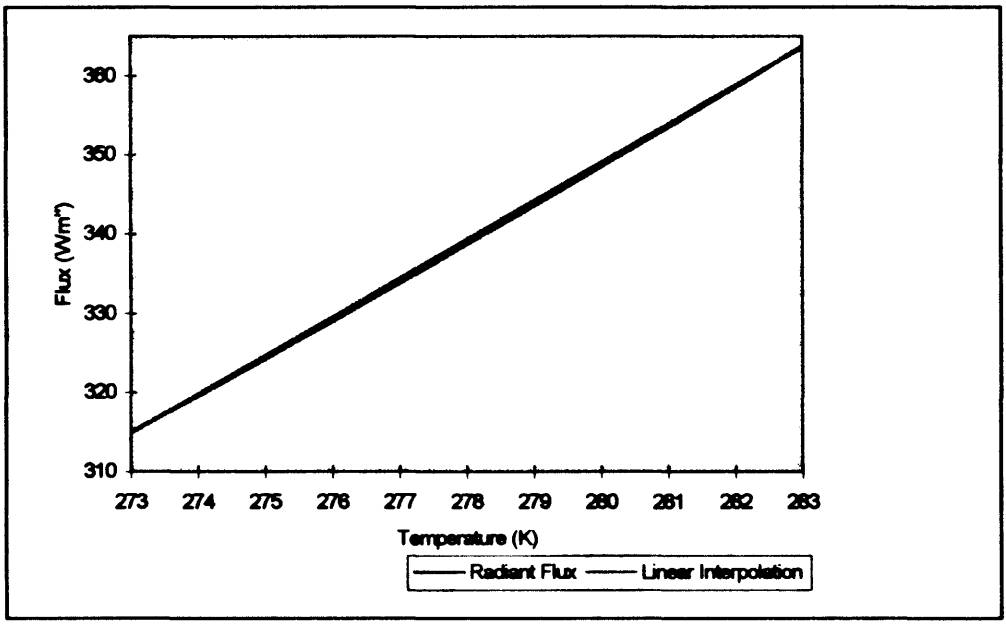


Figure 5.2 Comparison between linear approximation and quartic expressions for radiant flux, for typcial earth surface temperature rnages.. The linear and quartic expressions can be seen to be in very good agreement across narrow temperature regimes. The 'zero flux' value, the temperature at which the radiative flux emitted and the flux incident would be equal, is set at 263K. Total percentage uncertainty across the entire 10K range is 7.3×10^{-15}%.

This technique is suitable for steady state analyses where the net flux across the surface due to diurnally varying meteorological parameters is zero. If the net flux were not zero, this would imply a long term heating or cooling of the earth. This does not occur significantly within the time scales in question. Thus only transfer of endogenetic heat to the atmosphere need be considered.

This technique is suitable for long duration transient analyses i.e. across many modelled days, where diurnal variations in the boundary layer properties and radiative environments can be averaged out. This approach is not suitable for transient analyses at diurnal or near-diurnal time scales due to the linearisation of the radiation term. It is also unsuitable for surfaces with large temperature variations, for the same reason.

Approximating Convective Heat Transfer

Sensible Heat Loss formulae take the general form of the Newtonian cooling formula:

$$Q = hA\,(T_{surf} - T_{air}) \qquad 5.6$$

Where:

h Convective heat loss coefficient of the surface ($Wm^{-2}K^{-1}$)

A Cross Sectional Area (m^2)

Q Heat Flux (Wm^{-2})

T_{surf} Surface Temperature (K)

T_{air} Air Tempeature (K

Assuming unit area, the coefficient h can be calculated from the formulae for sensible heat transfer as outlined in *Chapter 3: The Physical Model.*

LATENT HEAT TRANSFER

Latent heat transfer is difficult to incorporate into Ansys. Latent heat transfer cannot readily be approximated as a function of the temperature difference between the surface and. the atmosphere, in the same way as convective or radiative heat transfer can. This difficulty may be readily avoided by using the following formula:

$$\text{Latent Heat Transfer} = L_v\,(W_{int} - W_{final})/t \qquad 5.7$$

Where:

L_v Latent Heat of Vapourisation (Jkg^{-1})

W_{int} Mass of water in the surface at start of modelling time interval (kgm^{-2})

W_{final} Mass of water in the surface at end of modelling time interval (kgm^{-2})

t Duration of modelling time interval (s)

This gives a heat loss per unit area per unit time due to latent heat transfer. This can be applied to the model where required as a negative heat generation load on the region subjected to latent heat loss, just below the surface boundary.

5.2 TRANSIENT MODELS

MODELLING PROCEDURE

For transient models the solution procedure is more complex than that described in section 5.1 and step 8 of the procedure breaks up into several substeps:

8a) Deactivate time integration (Ansys command: TIMINT, 0) and run the model as a transient model for a single, very small timestep size. This is to allow the initial conditions to be propagated onto the model.

8b) Specify initial loads for load step 1 and apply to model. Specify the size of timestep 1 (*see below*).

8c) Solve the current load step

8d) Repeat steps 8b and 8c as necessary (loop).

TIMESTEP SIZES

It has already been stated (*Chapter 4: Mathematical Models*) that timestep sizes for finite difference models must be selected with care to ensure the stability and convergence of the model. The same is true for finite element models. The maximum timestep size can be estimated using the Biot and Fourier numbers:

$$Fo=k(\Delta t)/\rho c(\Delta x)^2 \qquad 5.8$$

$$Bi=h(\Delta x)/k \qquad 5.9$$

(Heald et al 1995)

Where:

Fo Fourier Number

Bi Biot Number

Δx Average element length (m)

k Thermal Conductivity of material, or average of mixed materials ($Wm^{-1}K^{-1}$)

ρ Density of the material, or average of mixed materials (kgm^{-3})

C Specific Heat Capacity of the material, or average of mixed materials ($Jkg^{-1}K^{-1}$)

The timestep interval for conduction only can be derived by inverting equation 5.8:

$$\Delta t=\beta\rho c(\Delta x)^2/k \qquad 5.10$$

If film convection is taking place the product of 5.8 and 5.9 is used:

$$\Delta t=\beta\rho c\Delta x/h \qquad 5.11$$

Where β is an optional scaling factor ($1\leq\beta\leq100$, default value 1)

INITIAL CONDITIONS

Transient models also require the specification of initial conditions, which are of importance for model convergence. In many cases the initial conditions will be well known and straightforward, but not always. In a diurnal model, the initial temperature distribution will be complex function of depth and time of day, and thus will not be easily specified at the start of the model run. It is more efficient to apply an approximated initial condition and then subject the model to a number of cycles of the diurnal load. The temperature distribution as a function of time will rapidly converge to reasonable values (see *Chapter 7: Transient Models*). The more accurate the estimate of initial conditions, the more rapidly the model will converge to stable temperatures. Diurnal transient models should then be subjected to typical diurnal loads for several day cycles before attempting further modelling.

5.3 RADIATIVE MODELS

True radiative models, without using conductive approximations, require a number of further steps and introduce new complexities, not least of which is the greatly increased processing time required due to the non-linear nature of radiative processes.

Ansys models incorporate radiation in one of three ways, using special radiation link elements, using surface effect elements and using a radiation matrix. In this study only the second method, using surface effect elements is applied. The first method, using radiative link elements, is more appropriate where only a limited number of elements are losing heat through radiation. The third technique, using a radiation matrix, is most appropriate for models with complex surfaces, such as cooling fins, interacting radiatively with each other. In this method radiative loads are applied as a function of the temperature difference between the surface and a defined 'space node' at a given temperature:

$$H=\phi\varepsilon(T_n^4-T_s^4) \qquad 5.12$$

(Heald et al,1995)

Where:

H	Net heat transfer between the surface element and the space node (Wm^{-2})
ϕ	Radiation shape factor
ε	Emissivity
T_s	Surface temperature (K)
T_n	Space Node temperature (K)

The radiation shape factor (ϕ) is usually a function of the distance between two objects and their relative aspect and area. This value should be left at unity if modelling radiation to and from the sky (a half space), so that the surface elements will radiate correctly. Radiation is a two way process, so careful selection of the space node temperature will allow modelling of incident solar radiation also. It should also be noted, that as a non-linear process, radiation may increase processing time considerably, and, when combined with non-linear temperature dependent

material properties, as might occur in phase change models, serves to increase processing time by an order of magnitude, and makes generating a converged solution prohibitively time consuming.

MODELLING PROCEDURE

The general procedure for carrying out radiative modelling is:

1) Proceed as for a conductive model steps 1 to 6 in section 5.1. Ensure that an emissivity is specified
2) Create a single free node outside the main model region (a 'space node')
3) Create the surface effect elements (Menu path Preprocessor> Create> Elements> On Free Surface). Ensure that element type has been set to a suitable surface effect element (e.g. SURF19 or SURF22, described below)
4) Specify the space node number to which the elements will be radiatively coupled
5) Delete non-essential elements. Note that the options to generate the surface effect elements tend to create them on all surfaces, including the sides and base of the model. Check and ensure that radiative elements exist only on surfaces that will be radiating and delete the surplus elements as required
6) Set initial temperature. A zero temperature at a radiating element generates an error in Ansys and terminates the solution process. Due to the iterative approach which Ansys takes to solving radiative problems, an initial non-zero uniform temperature (Ansys command: TUNIF) must be specified for the model. This temperature is used for otherwise unloaded nodes in the initial iterative step. The value of the initial temperature has little effect on the final solution to the problem, when tested a 250K variation in the initial temperature produced a <0.1K variation in the solution
6) Proceed and solve as normal. Note that the non-linear nature of radiative problems increases the required solution time.

5.4 SURFACE CONVECTION

Convective heat transfer from a surface can be directly handled using Ansys, by applying a convective load to a line or surface. Ansys calculates the heat transfer using the Newtonian cooling equation 5.6 above, and setting values for the convective heat transfer coefficient and the bulk temperature of the convecting medium.

This approach has some limitations. Convective cooling on the surface of a material may be highly variable as a function of surface temperature if the surface temperatre ranges are such as to span different convective regimes. If necessary, this may be reflected in finite element models by defining the convective heat loss coefficient h as being dependent on the surface temperature. However, this would require that the convection regime for the system be very well understood. In most cases examined in this thesis, the temperature ranges will not be such as to move the system between different convective regimes, so this will not be a factor.

5.5 SUBSURFACE CONVECTION MODELS

Ansys does not explicitly support convective heat transfer in porous media. Thus, where this process is of importance, it will be necessary to 'bootstrap' the complexities of convective heat transfer into a conductive model. This can be achieved by approximating convective heat transfer as a 'convective heat transfer coefficient' added to the dry thermal conductivity.

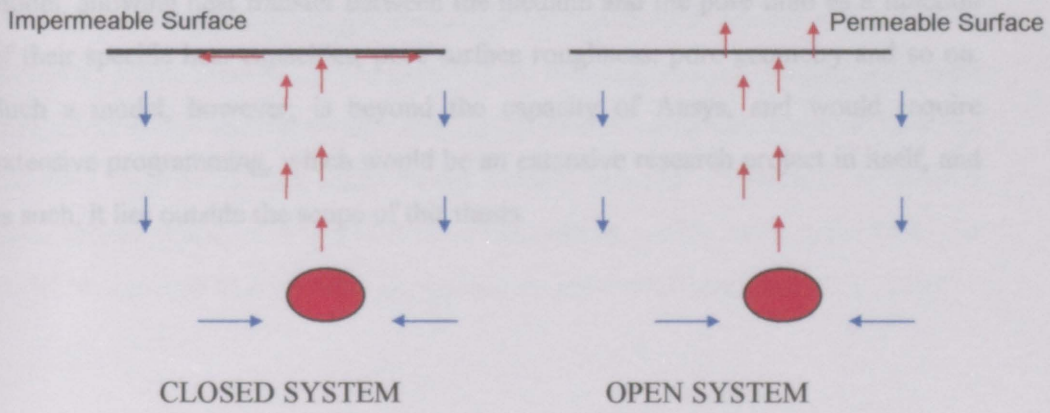


Figure 5.3 shows convective heat transfer from a heated region (red) in a two dimensional case with air as the pore fluid. In a closed system air around the heat source is heated becomes less dense and rises (red arrows) as cooler air displaces it (blue arrows). In a closed system i.e. with an impermeable 'lid', like a room with a heater, lateral heat transfer will occur at the upper boundary as the warm air move laterally, cools, and sinks. However, for an open system, like convection around a lava tube, the heated air will simply escape into the atmosphere. Thus the net convective heat transfer is in the vertical direction only.

It is possible to calculate the Nussult number of such a system analytically. In an open system, we can assume that all convective heat transfer lies in the vertical direction (see Figure 5.3) This assumption cannot be made for a closed system, as lateral heat transfer from fluid constrained at the upper boundary may be important. From this assumption and the Nussult number, one can then calculate a convective heat transfer coefficient for a given set of physical parameters (e.g. temperature differences, rock properties). This can be added to thermal conductivity in the vertical direction when required to approximate convective heat transfer for various systems being investigated.

The Nussult number is calculated from analytic expressions that are difficult to verify and often contain many implicit assumptions. As a real physical process, convective heat transfer in porous media is difficult to quantify. Thus, modelling convective heat transfer in porous media by assuming a vertical thermal anisotropy is not an unreasonable simplification in this context.

Theoretically, one could generate a parallel finite element model of thermal convection within a pore system. This could then be coupled to a purely conductive model, allowing heat transfer between the medium and the pore fluid as a function of their specific heat capacities, pore surface roughness, pore geometry and so on. Such a model, however, is beyond the capacity of Ansys, and would require extensive programming, which would be an extensive research project in itself, and as such, it lies outside the scope of this thesis.

5.6 PHASE CHANGE MODELS

Modelling of phase change is done by specifying temperature dependent thermal conductivity and enthalpy of the material as a function of temperature. The relationship between enthalpy values and primary thermophysical properties is outlined in *Chapter 3:The Physical Model*. The density and specific heat capacity of the material are not specified- the enthalpy property effectively replaces them.

Solution of phase change models can be expedited by choosing lower order elements such as Plane55 (see section 5.7) for meshing, and using a backward time integration rather than a central time integration formulation. Caution must be exercised when conducting phase change models, however. Model runs in which a phase change occurs at or near a radiative element invariably result in failure of the model to converge to a solution. Such cases should not be attempted using Ansys.

5.7 ELEMENTS

Ansys discretises the continuous problems into a number of Finite Elements. The Ansys element library contains over one hundred different element types suitable for various analyses. However, only a few are specific to thermal analysis.

TWO-DIMENSIONAL ELEMENTS

Two-dimensional elements are used for the majority of thermal models. They can be used to represent three-dimensional models by means of applying appropriate symmetry modes. The Ansys planar elements can be set to one of two symmetry modes axi-symmetric, appropriate for point heat sources, and planar symmetric, appropriate for linear heat sources, as shown in Figure 5.4.

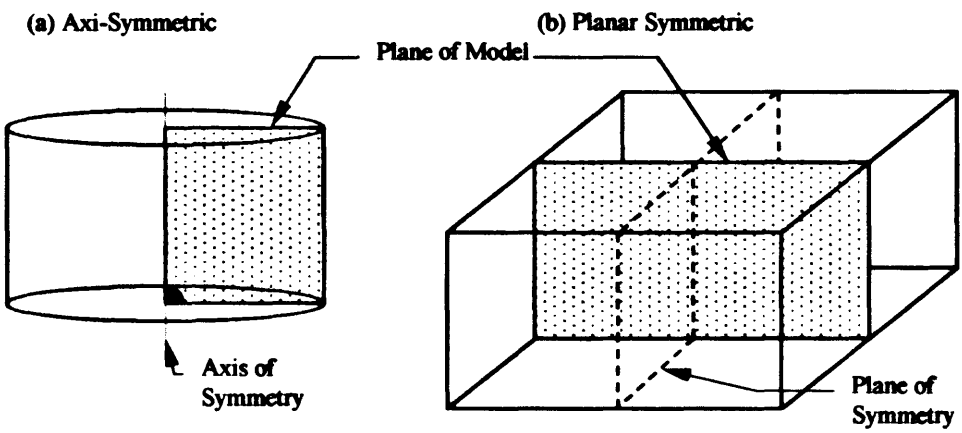


Figure 5.4 Element symmetry modes.

Two different two-dimensional thermal elements are available in Ansys, named Plane55 and Plane77, shown in Figures 5.5 and 5.6 respectively.

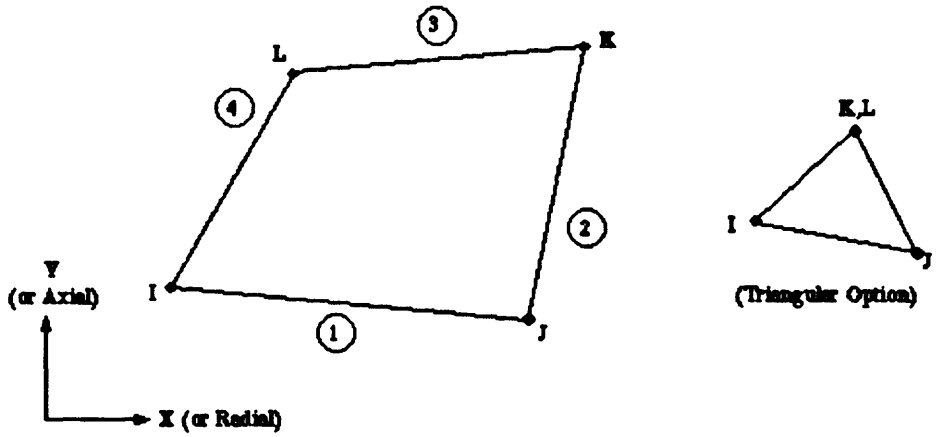


Figure 5.5 Generalized structure of the Plane 55 thermal finite element, with letter codes indicating the nodes, and numbered edges. The triangular variant is shown on the right. The Plane 55 element has no mid-side nodes and so is less processing time intensive than more complex elements. It is ideal for computationally intense problems such as transient analyses. (After Ansys *Elements Manual*)

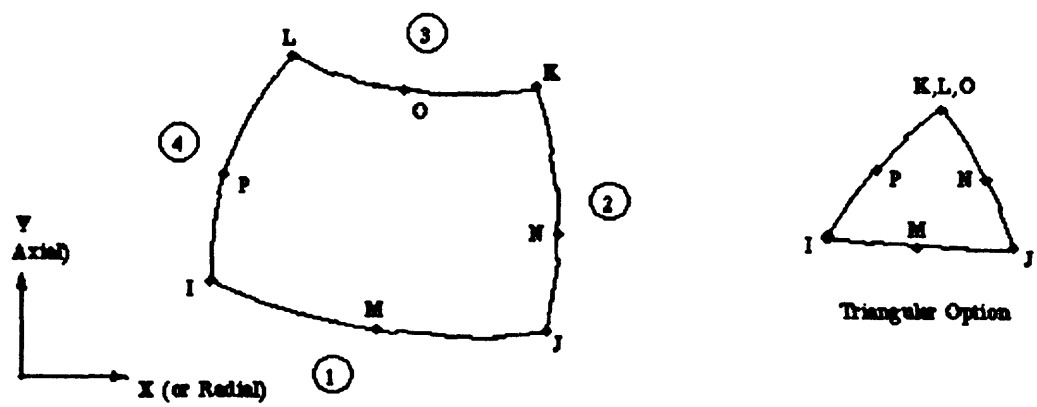


Figure 5.6 shows the generalized structure of the Plane 77 thermal finite element, with letter codes indicating the nodes. The triangular variant is shown on the right. The Plane 77 element has mid-side nodes and so is more processing time intensive, and more accurate than simpler elements. It is not suitable for computationally intense problems such as transient analyses. (After Ansys *Elements Manual*)

SURFACE EFFECT ELEMENTS

Radiation loads cannot be applied directly to the element types specified above. Surfaces involved in radiative heat transfer must be covered with surface effect elements which are capable of radiative behaviour. The principle surface effect element used in this work is Surf 19, shown in figure 5.7. This is also used to handle convective loads on surfaces.

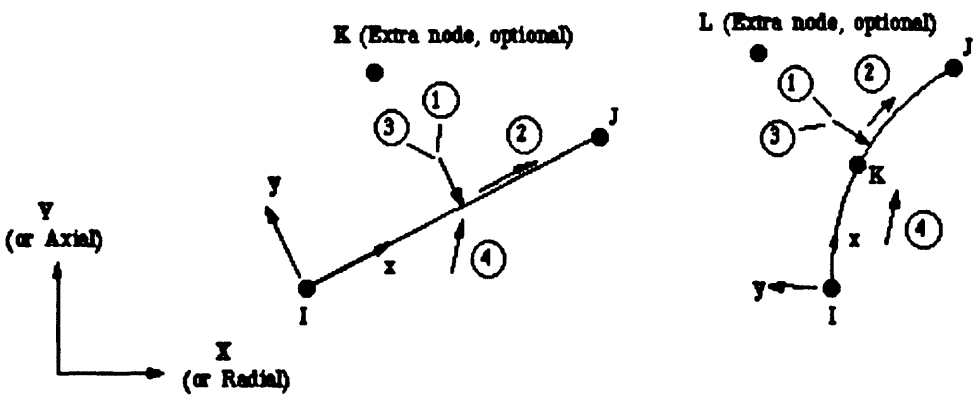


Figure 5.7 shows the element geometry and node numbering system, with the right hand option containing a midside node. The element nodes must match up with the nodes of the underlying planar elements, so a midside node will be required for use with Plane 77 elements, and no midside node is required for use with Plane 55 elements. (After Ansys *Elements Manual*)

5.8 VALIDATION

All results from numerical modelling are approximations. It is necessary wherever possible to validate the models produced using Ansys by direct comparison with analytic solutions. Validation acts as a check to ensure that the numerical models are being carried out correctly, and to ensure that they give meaningful results. This is only possible for simple models where analytic solutions are available. As models increase in complexity past the stage where analytic solutions exist for comparison, this is no longer possible. However, if meaningful results for simple models can be generated numerically, the results of more complex numerical models can be accepted with more confidence.

STEADY STATE MODEL VALIDATION

The aim of this model was to compare analytic solutions with numerical solutions for a simple pseudo-one dimensional geometry.

Model Geometry

A two dimensional rectangular area was used for this analysis, as shown in Figure 5.8, with a height, width ratio such that the problem was effectively one dimensional, to facilitate comparison with an analytic solution.

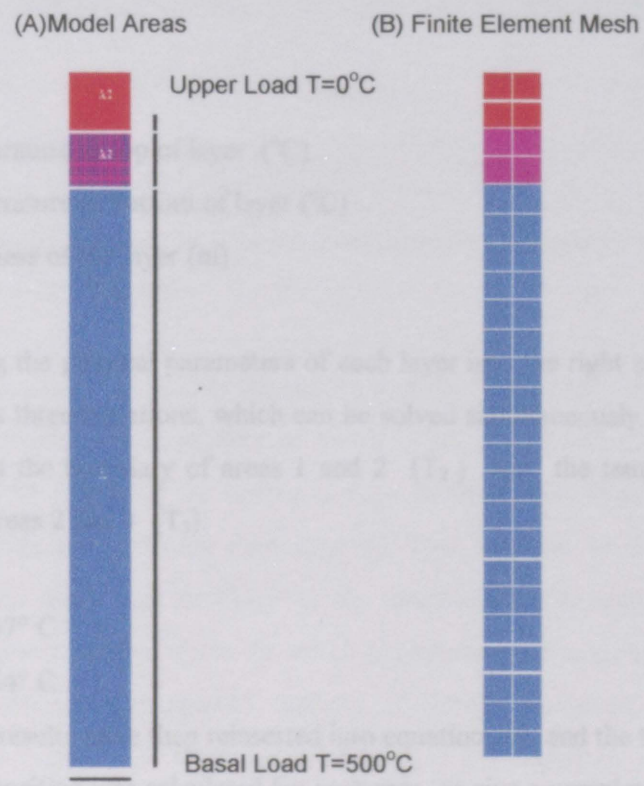


Figure 5.8 shows Steady State Validation Model Geometry

The three areas were assigned the physical properties:

Layer	Thickness (m)	Thermal Conductivity ($Wm^{-1}K^{-1}$)
1	10	1.5
2	1	1
3	1	7

The applied boundary conditions were fixed temperatures of 500°C at base of layer 3 and 0°C at top of layer 1.

The problem could also be solved analytically using Fourier's law:

$$\frac{dE}{dt} = -KA\frac{dT}{dx} \qquad 1.2$$

$$\frac{dE/dt}{A} = \text{Constant} = \frac{K}{X}(T_a - T_b) \qquad 5.13$$

Where:

T_a Temperature at top of layer (°C)

T_b Temperature at bottom of layer (°C)

X Thickness of the layer (m)

Putting the physical parameters of each layer into the right side of equation 5.13 generates three equations, which can be solved simultaneously. This gives the temperature at the boundary of areas 1 and 2 (T_2) and the temperature at the boundary of areas 2 and 3 (T_3):

T_2 73.1707° C

T_3 9.14634° C

These results were then reinserted into equation 1.2, and the temperature as a function of position was calculated for each area, to give a complete temperature distribution.

To derive a Finite Element Solution for the same problem, simple finite element mesh of plane 55 elements was defined (see Figure 5.8) and the model solved in the steady state for the given loads and physical parameters.

Figure 5.9 shows a comparison of the results from the numerical and analytic solutions. They can be seen to be in agreement to within a twentieth of a degree. Subsequent runs of the same model with different variables, and comparison

with analytic solutions gives an equally close correlation, indicating that Ansys is generating reasonable and meaningful results for steady state thermal problems.

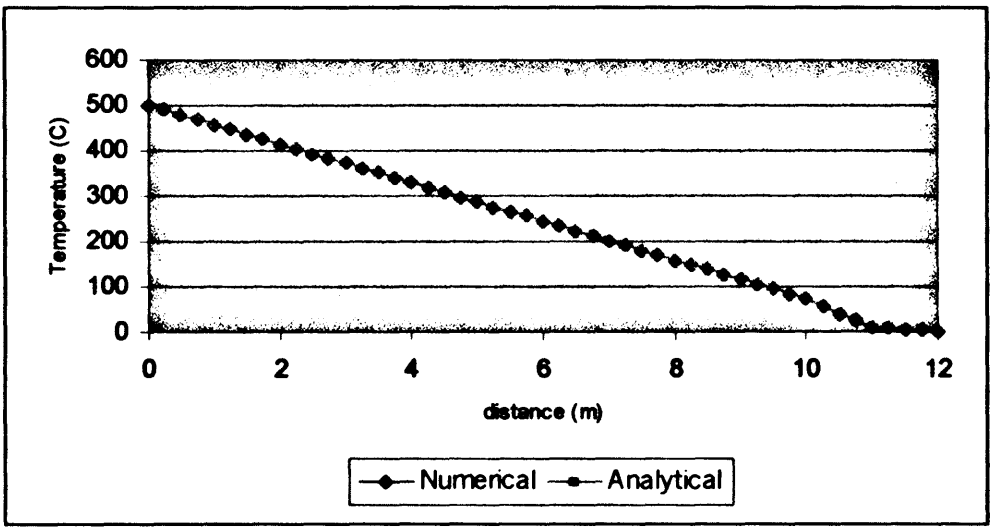


Figure 5.9 Comparison of Finite element and Analytic results for temperature as a function of distance along rectangular section.

For more complex models the accuracy of the Ansys Finite Element solution is dependent chiefly on the number of nodes in the model and the element size. Accuracy can be increased by having a finer mesh density thus increasing the number of nodes and reducing their spacing. This however results in increased processing time. Repeated increases of the element density may also result in generation of poorly shaped elements, which contribute to uncertainties.

In the absence of comparable analytic solutions convergence testing must be carried out on each model. Convergence testing is conducted by establishing the model mesh and steadily increasing the density of elements and solving until the results have stabilised to a steady value. The mesh density can be increased uniformly, but it is usually more computationally efficient to increase it in areas of interest and regions of high thermal gradients. Examples of convergence testing of complex models can be seen *in Chapter 6: Steady State Models.*

TRANSIENT MODEL VALIDATION

Transient models require a somewhat different approach to validation and testing. Care should be taken to ensure that a small enough timestep size is being used (see section 5.2) In addition to this, the mesh must also be tested. Steady state convergence testing of a model mesh prior to its use in a transient model is advisable. For models with rapidly changing transient loads, it is necessary to ensure that thermal energy is accurately 'flowing' between nodes in the model. Fortunately, this is handled automatically by Ansys. Within each model substep, the software solves a number of equilibrium iterations to ensure that the solution for that substep converges to a stable value. Conservative mesh design may reduce the number of iterations required, but will not effect the accuracy of the solution over that of a steady state model.

Transient models also require the specification of initial conditions, which influence the rate of model convergence. In many cases the initial conditions will be well known and straightforward, but not in all cases. In a diurnal model, the initial temperature solution will be complex function of depth and time of day, and thus will not be easily specified at the start of the model run. Initial conditions need to be approximated as outlined in section 5.2.

Chapter 6: Steady State Models

This chapter considers the question of what factors affect the size of the surface thermal signature of an idealised geothermal heat source. This is investigated by considering an idealised linear heat source of 2m diameter. The source type and overall geometry of the system was selected to broadly reflect an active lava tube.

This study will principally investigate the effect of ten principle variables (six physical properties and four boundary conditions) on the size and temperature of a surface thermal anomaly due to a linear, cylindrical heat source. The principle variable physical properties are the Density, Specific Heat Capacity and Thermal Conductivity of the rock and the overburden (if any). The principle boundary condition variables are the temperature of the source (Thot), the mean atmospheric temperature (Tair) and the properties of the atmospheric boundary layer, expressed as a virtual thermal conductivity (The Alpha Model) or the film coefficient and emissivity (The Bravo Model). Changes in the source geometry and effects of convective heat transfer are also briefly examined.

The chapter divides broadly into two section. First, 6.1 *The Alpha model*, a relatively simple conductive multilayer model is investigated with a systematic variation of its material properties. Secondly, *6.2 The Bravo model*, examines the results of a model with more sophisticated upper boundary conditions. In each section the geometry and design of these models is discussed, and a number of different model series are conducted for each geometry to assess the variables independently. A comparison of the results is then conducted.

Model series are selected with a view to being thorough and comprehensive rather than specifically interesting. As a result a great many of the model series are demonstrating numerically what is intuitively obvious, and are included both for the sake of thoroughness as well as model validation.

Ansys generates a very large results set for each model run, including a complete temperature solution and heat flux solution. However, for comparison with thermal infrared images, only the temperature distribution at the surface is of interest. Two principle pieces of data are extracted from the results:

(i) The Peak Temperature: This is the maximum temperature of the surface thermal anomaly, as observed over the centre of the anomaly. The Net Thermal Anomaly, referred to in the Bravo Model, is equivalent, but as the Bravo Model generates a non-zero background temperature, the Net Thermal Anomaly is the difference between the peak temperature and the background temperature.

(ii) Thermal anomaly size: This is the distance from the peak surface anomaly temperature to the point where the surface temperature is only elevated by one degree from the original (background) temperature.

General Assumptions

- The models are non-transient. The Finite Element equation is solved for a minimum value, representing the steady state case where all loads are constant. This assumes that the thermal properties of the model are constant over a fairly long time-scale. Internal heat sources remain fixed at the same temperature. The validity of this assumption will need to be addressed on a case by case basis for real-world models. For most geological examples this is a valid assumption, for example, constant effusion lava tubes (Keszthelyi 1994) and coal mine fires remaining active for months or years.
- The diurnal temperature variations are not significant. This means that the atmospheric temperature is assumed to oscillate about an average value, and that the net heat flow in or out of the model across the diurnal cycle is zero, and thus will have no effect on the final temperature distribution. It should be noted that in most terrestrial cases the depth of penetration of the diurnal thermal wave is less than 1m, and so below this, diurnal thermal change will have negligible effect. At a depth above that of the diurnal thermal wave, the diurnal temperature distribution will be superimposed on the steady state case solution due to the endogenetic heat source, and the temperature distributions may be added. Surface temperatures elevated above the average will, during the day, reduce the thermal gradient and thus the endogenetic heat flow to the surface, but below average surface temperatures at night will have the opposite and negating effect. Numerical analysis of diurnal thermal cycles has been considered extensively for thermal inertia modelling, and existing models are reviewed in *Chapter 3: The*

Physical Model and *Chapter 4: Mathematical Models.* Finite Element thermal models of diurnal cycles will be examined in detail *Chapter 7: Transient Thermal Modelling.*

- All materials and surfaces are assumed to be isotropic and homogeneous unless specified otherwise, as in the case of model series addressing the effect of thermal convection.
- All internal heat transfer is by thermal conduction only. Where thermal convection takes place it is simulated by the addition of a conductive heat transfer coefficient.

THE ALPHA MODEL

A basic model has been devised which will allow independent variation of the principle parameters of the system i.e:

- Source temperature
- Average atmospheric temperature,
- Density of the rock and surface material
- Thermal conductivity of the rock and surface material
- Specific heat capacity of the rock and surface material
- Heat transfer through the atmospheric boundary layer.

The model will allow independent variation of these 9 variables to assess which are the most important in stable, steady state processes.

Relevant surface thermal processes are described using the Atmospheric Boundary Layer technique outlined in *Section 5.1*, where a single virtual thermal conductivity is used to approximate heat transfer to the atmosphere.

The complete model program script file can be found in Appendix E.

GEOMETRY

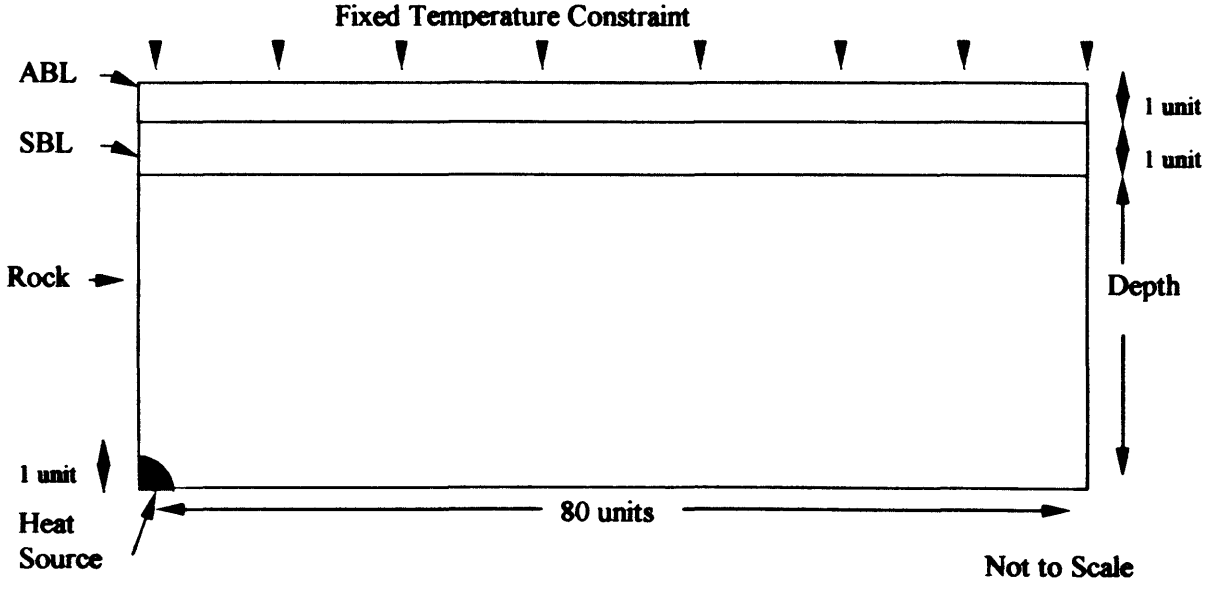


Figure 6.1 The Alpha Model Geometry.

The basic model is two-dimensional and consists of three different regions. This two dimensional model can be specified as being axisymmetric about the y axis or planar symmetric, depending on the nature of the heat source. This therefore allows modelling of linear or point sources without extensive rewriting of the model script (see *Chapter 5: An Introduction to Thermal Modelling Using Ansys)*. Unless specified otherwise the models will be in the planar symmetry mode, representing a linear heat source.

The three model layers represent the rock, surface boundary layer, and atmospheric boundary layer respectively:

(i) Rock

This lowermost region is 80 units across and of variable depth (normally 10 units, unless otherwise specified). This represents a body of rock. A temperature load is applied to the nodes in a region of 1 unit radius in the lower left hand corner. This loading represents a 2 unit wide cylindrical heat source in a linearly symmetric model. The density, specific heat capacity and thermal conductivity of the material can be easily varied.

(ii) Surface Boundary Layer (SBL)

The Surface Boundary Layer (SBL) is a one unit thick, 80m long rectangle (Figure 6.1). It represents overburden, vegetative cover and/or weathered surfaces on the rock. Where no cover is being modelled, this layer can be set to the same thermal properties as the underlying rock. As it is unit thickness, the thermal properties are entered per m^2 rather than per m^3. Thus they can be adjusted to model any thickness of material without adjusting the geometry of the model.

Note that caution needs to be exercised in the use of the surface boundary layer. While it may be used to approximate heat transfer in surface material, it should be noted that the type and nature of the surface material must be considered carefully. Taking the extreme example of a surface cover of dense vegetation, it would be unwise to give it thermal properties simply on the basis of it being a thickness X of mean density of a material with given thermal properties. Vegetation does not occupy the complete volume, and air will have a dominant effect. Surface

roughness will be affected and thus sensible heat transfer, which is dealt with in the Atmospheric Boundary Layer (ABL) approximation, will be altered. The increased surface area due to foliage will affect the emissivity of the surface and radiative heat loss, also dealt with in the ABL approximation. Material more complex than a simple layer of overburden will require much care and consideration in selection of thermal properties.

(iii) Atmospheric Boundary Layer (ABL)

The Atmospheric Boundary Layer (ABL) is a one unit thick, 80 unit long rectangle (Figure 6.1). It is used to model heat transfer from the surface by giving the layer a thermal conductivity equal to the virtual thermal conductivity for an atmospheric boundary layer as described *in Chapter 5: An Introduction to Thermal Modelling using Ansys*. The top of this layer is fixed at a temperature of zero units (degrees), to simulate the average atmospheric temperature (The justification of this is addressed in model Series 6.2.1). This layer models additional heat lost to the atmosphere due to endothermic heating. The net heat transfer due to diurnal processes is assumed to be zero in the steady state. In all cases the atmospheric density is held at: $1.172 kgm^{-3}$, and the specific heat capacity is held at $1006 Jkg^{-1}K^{-1}$.

ASSUMPTIONS

A number of assumptions and linearisations are implicit in the methodology of the Atmospheric Boundary Layer. These are discussed at length in *Chapter 5:An Introduction to Thermal Modelling using Ansys.*

It is assumed for this model that no net heat transfer occurs as a result of diurnal processes in the steady state case. If this assumption was false, it would imply a net heating or cooling of the earth across long time scales. While this does occur on seasonal and decadal time scales, these variations are not significant or relevant to the scale of the problem at hand.

MODEL MESH

The Plane 77 Element is used exclusively in this model. This element and its advantages are described in *Chapter 5:An Introduction to Thermal Modelling using Ansys.*

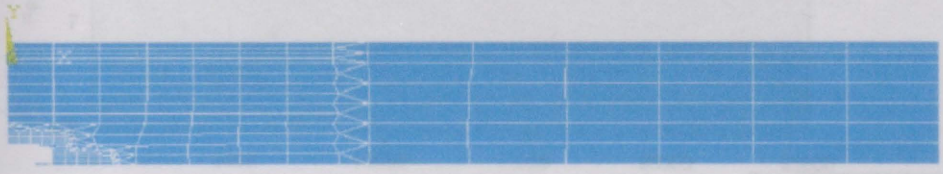


Figure 6.2 Alpha Model Mesh. Note the increased mesh density in the lower left hand corner close to the heat source.

CONVERGENCE TESTING

Increasing the density of the model mesh improves the accuracy of the final results. However, this also increases the processing time. Figure 6.3 shows the relationship between the peak temperature and mesh density. It can be seen that for a uniform increase in mesh density across the entire area of the model, the model converges towards a value of approximately 8°C reaching it at 20,000 nodes. However, by selectively refining the mesh in areas of highest thermal gradient, this stable value can be achieved for much lower mesh densities. It can be seen that increasing the mesh density beyond that point fails to significantly reduce the uncertainties. In fact, difficulties with selective enhancement of the mesh at these scales can introduce new errors due to poorly shaped elements. The final (non uniform) mesh chosen has 2662 nodes which gives the best trade off between accuracy and processing time. Based on a comparison between this mesh and the results from the rectilinear meshes generated by uniform mesh refinement, the Alpha model is accurate to two significant figures.

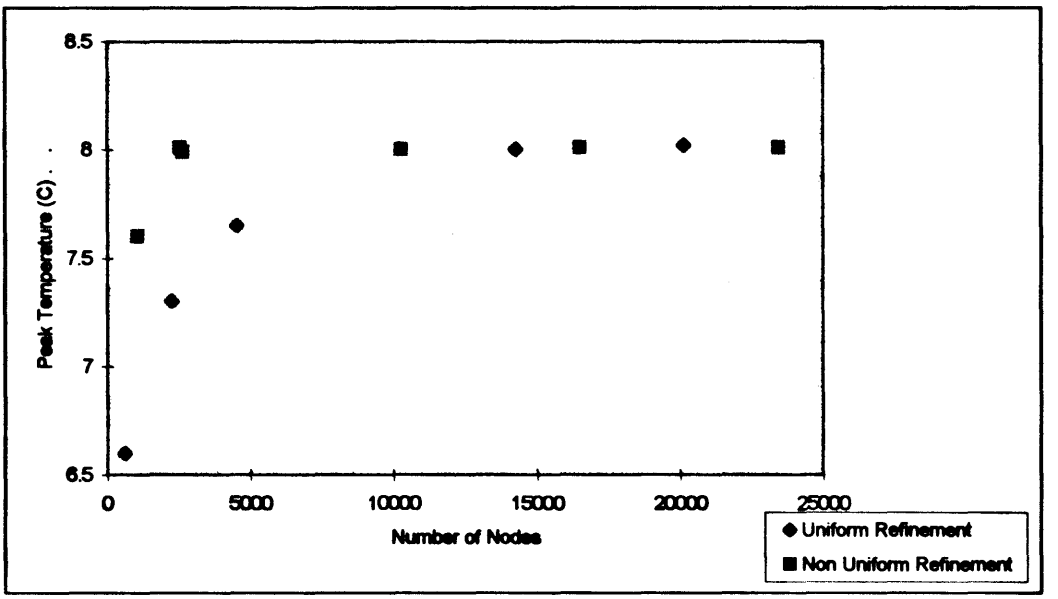


Figure 6.3 The relationship between peak temperature for different mesh densities for the Alpha model. In all cases model parameters are as listed in Table 6.1

Parameter	Value	Unit
Thickness	10	m
Thot	1000	°C
Tair	0	°C
ABL Thermal Conductivity	13	$Wm^{-1}K^{-1}$
SBL Thermal Conductivity	2	$Wm^{-1}K^{-1}$
SBL Density	2700	kgm^{-3}
SBL Specific Heat Capacity	800	$Jkg^{-3}K^{-1}$
Rock Thermal Conductivity	2	$Wm^{-1}K^{-1}$
Rock Density	2700	kgm^{-3}
Rock Specific Heat Capacity	800	$Jkg^{-3}K^{-1}$

Table 6.1 Alpha Model Test Parameters.

UNCERTAINTIES

(i) Peak Temperature

From convergence testing (above) the temperature values can be taken as accurate to two significant figures.

(ii) Thermal Anomaly Size

Uncertainties in the thermal anomaly size are managed by assuming the values at the nodal points on the surface of the model to be precise. The distances from the y axis to the nodes with values just above and just below 1°C are taken as the upper and lower limits of the uncertainty, respectively.

Assuming the nodal solutions to be precise may appear to present a risk of further error, but in practice, this does not occur. The nodal results usually bracket the 1°C contour by a temperature range greater than the error in the nodal solution. For example, if the node at 18.666m has a value of 1.13 degrees and the node at 20m has a value of 0.87, the 1°C contour must still lie between the two, even if the results of both are inaccurate by 0.1°C. For the Alpha model surface line nodes are spaced at a distance of 1.333m and so this gives the uncertainty in the thermal anomaly size value of ±0.7m.

SAMPLE MODEL RUN

A typical model run is capable of producing a wide variety of detailed results, including nodal temperature solutions, internal energy solutions and heat flux vectors. The following figures show examples of some of these results for a model with the parameters:

Parameter	Value	Unit
Thickness	10	M
Thot	1000	°C
Tair	0	°C
ABL Thermal Conductivity	13	$Wm^{-1}K^{-1}$
SBL Thermal Conductivity	2	$Wm^{-1}K^{-1}$
SBL Density	2700	kgm^{-3}
SBL Specific Heat Capacity	800	$Jkg^{-3}K^{-1}$
Rock Thermal Conductivity	2	$Wm^{-1}K^{-1}$
Rock Density	2700	kgm^{-3}
Rock Specific Heat Capacity	800	$Jkg^{-3}K^{-1}$

Table 6.2 Sample Run Parameters

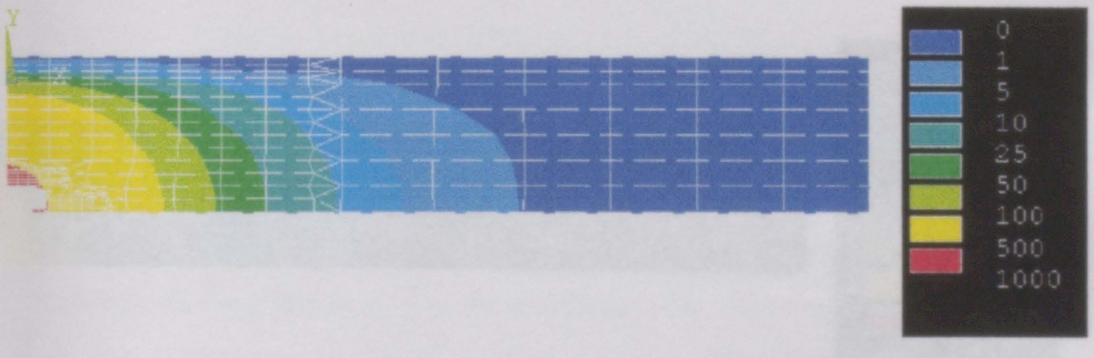


Figure 6.4 Nodal Temperature Solution for a typical model run. Temperature scale is in degrees centigrade.

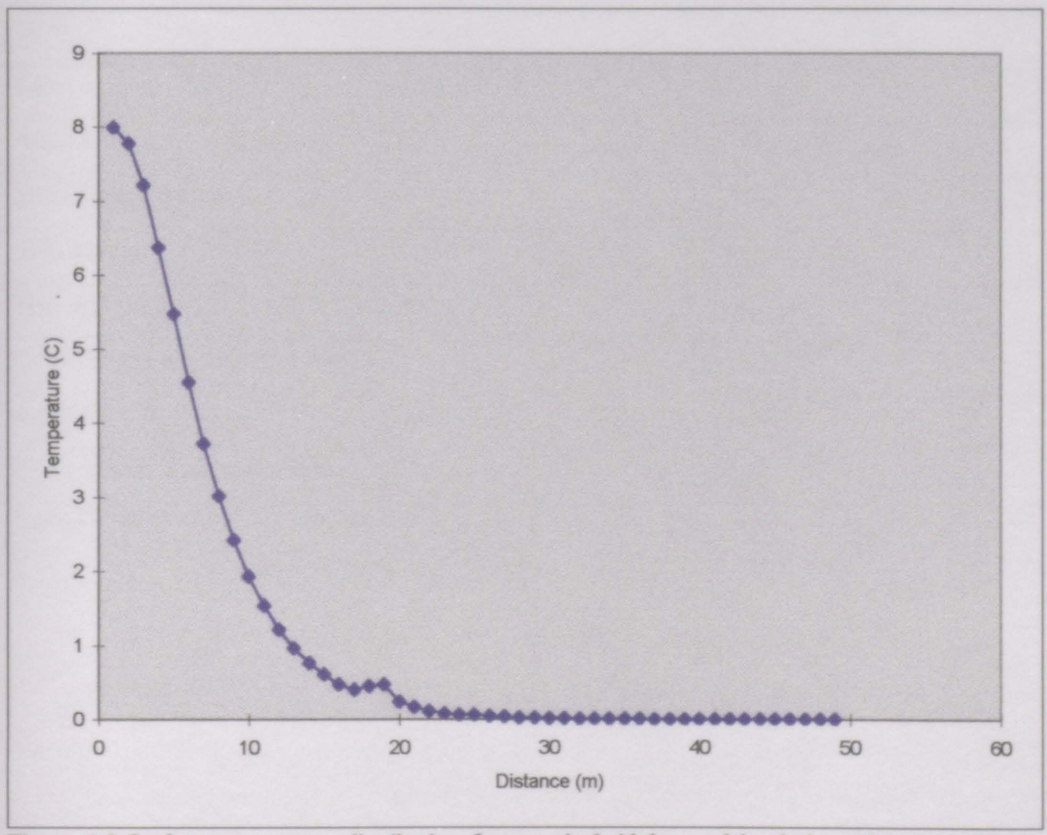


Figure 6.5 Surface temperature distribution for a typical Alpha model solution. Note how the change in mesh geometry at 20m generates a "hiccup" in the plot, without actually disturbing the overall curve.

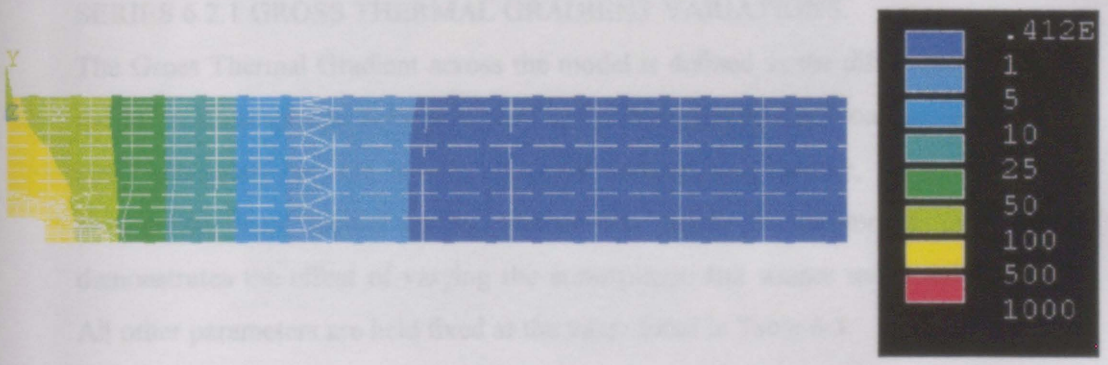


Figure 6.6 Thermal Flux for a typical Alpha model run. Legend in Wm^{-2}.

6.2 ALPHA MODEL RESULTS

Series 6.2.1 to 6.2.8 systematically investigate the effect of variations on the physical parameters and boundary conditions of the system.

SERIES 6.2.1 GROSS THERMAL GRADIENT VARIATIONS.

The Gross Thermal Gradient across the model is defined as the difference between the Mean Atmospheric Temperature, T_{air}, the fixed temperature load applied to the upper boundary of the model, and the source temperature, T_{hot}, the fixed temperature load applied to the bottom left region of the model. Series 6.2 demonstrates the effect of varying the atmospheric and source temperatures only. All other parameters are held fixed at the value listed in Table 6.3.

Parameter	Value	Unit
Thickness	10	M
Thot	Varied	°K
Tair	Varied	°K
ABL Thermal Conductivity	13	$Wm^{-1}K^{-1}$
SBL Thermal Conductivity	2	$Wm^{-1}K^{-1}$
SBL Density	2700	kgm^{-3}
SBL Specific Heat Capacity	800	$Jkg^{-3}K^{-1}$
Rock Thermal Conductivity	2	$Wm^{-1}K^{-1}$
Rock Density	2700	kgm^{-3}
Rock Specific Heat Capacity	800	$Jkg^{-3}C^{-1}$

Table 6.3 Model Series 6.2.1 Parameters

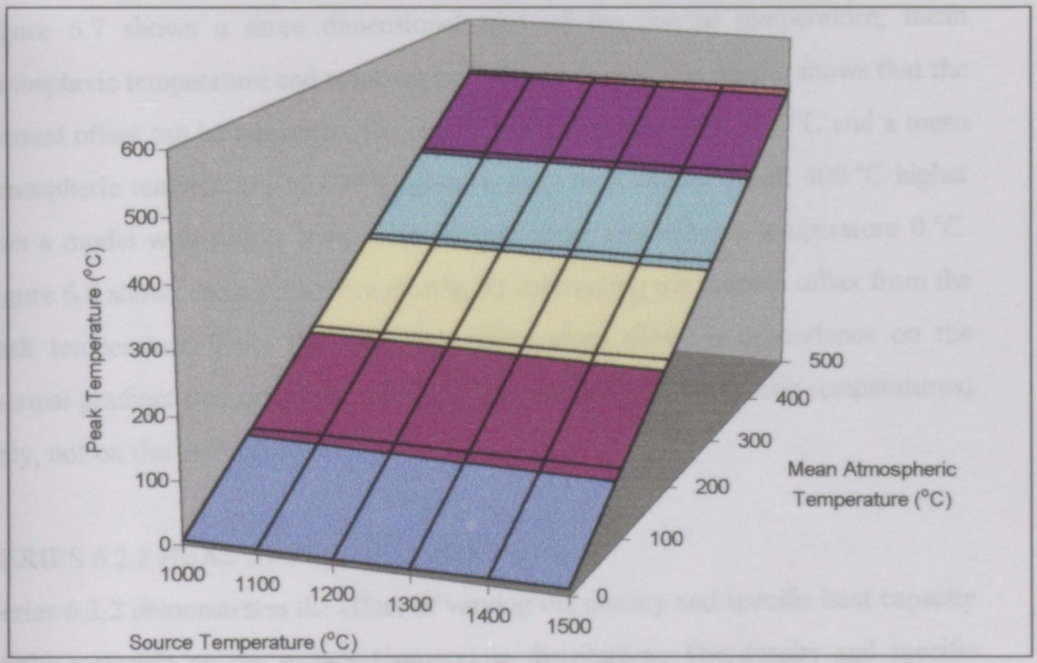


Figure 6.7 Variation in the Gross Thermal Gradient This shows how increasing the mean atmospheric temperature increases the peak temperature by the same amount, whereas increasing the source temperature has a much lesser effect.

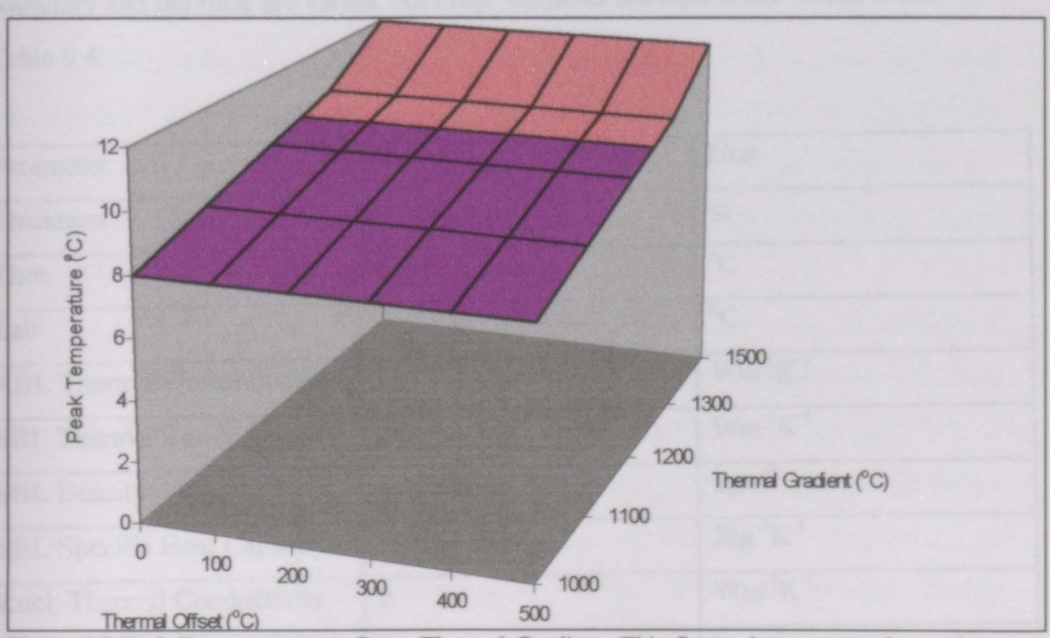


Figure 6.8 Peak Temperature vs. Gross Thermal Gradient. This figure demonstrates how a heat sources at 1400°C (T_{hot}) and an atmosphere at 400°C (T_{air}) will generate the same increase in surface temperature above background as a heat sources at 1000°C (T_{hot}) and an atmosphere at 0°C (T_{air}).

Figure 6.7 shows a three dimensional plot of the source temperature, mean atmospheric temperature and resultant peak temperature. The results shows that the thermal offset can be neglected, for example, a source temp of 1400°C and a mean atmospheric temperature of 400 °C gives a peak temperature result 400 °C higher than a model with source temp 1000 °C and mean atmospheric temperature 0 °C. Figure 6.8 shows the results more clearly, by subtracting the thermal offset from the peak temperature. Note that the peak temperature shows a dependence on the thermal gradient (the difference between the source and atmospheric temperatures) only, not on the thermal offset.

SERIES 6.2.2 HEAT STORAGE VARIATIONS

Series 6.2.2 demonstrates the effect of varying the density and specific heat capacity of the materials on the surface temperature distribution. The density and specific heat capacity are referred to as the thermal storage properties as they control the extent to which heat may be stored in the model. The values of the surface boundary and the rock are varied. All other variables are held at the values shown in Table 6.4.

Parameter	Value	Unit
Thickness	10	m
Thot	1000	°C
Tair	0	°C
ABL Thermal Conductivity	13	$Wm^{-1}K^{-1}$
SBL Thermal Conductivity	2	$Wm^{-1}K^{-1}$
SBL Density	1-1000	kgm^{-3}
SBL Specific Heat Capacity	1-100	$Jkg^{-3}K^{-1}$
Rock Thermal Conductivity	2	$Wm^{-1}K^{-1}$
Rock Density	1-1000	kgm^{-3}
Rock Specific Heat Capacity	1-100	$Jkg^{-3}K^{-1}$

Table 6.4 Series 6.2.2 Model Parameters.

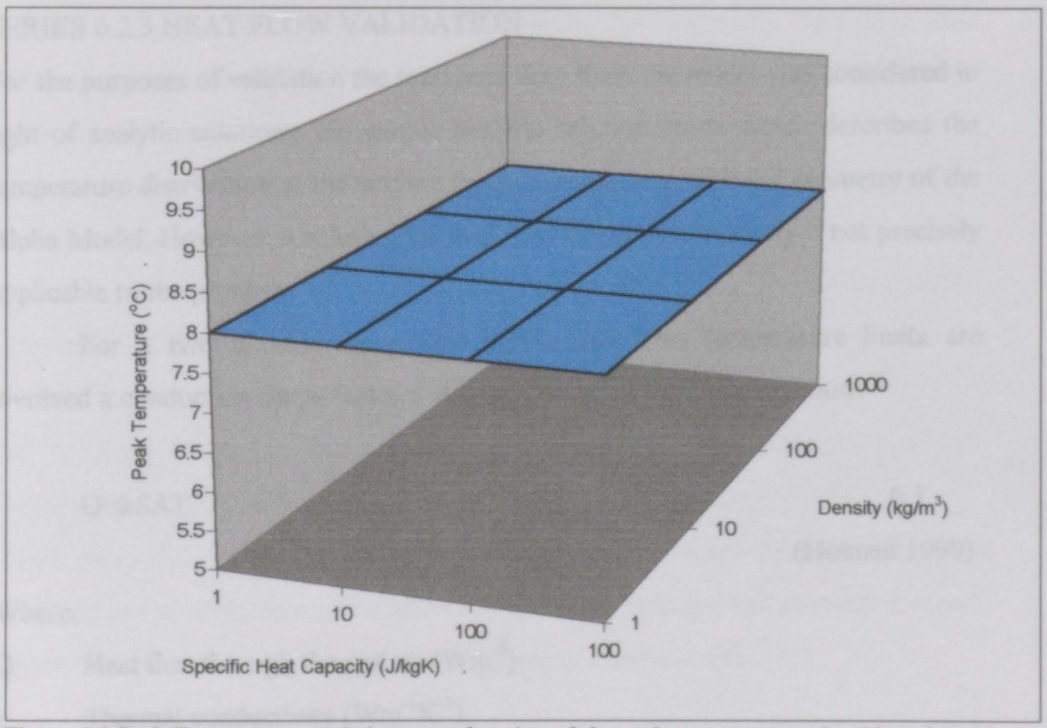


Figure 6.9 Peak Temperature variations as a function of thermal storage properties. Note that the density and specific heat capacity have no effect on the peak tempeature.

The results of series 6.2.2 are plotted in Figure 6.9. A number of further model runs were conducted varying the thermal properties of all layers both independently and together, for both integer and non-integer values of the parameters. In all cases the complete temperature distribution returned by Ansys was identical.

Given the physics of the problem and the steady state mode of solution, it was not expected that variations in the four thermal storage properties would affect the temperature distribution in any way. This was observed to be the case. This is because in a steady state solution, there is no change in the internal energy of the system, and the capacitance matrix is thus not considered (see *Chapter 5: An Introduction to Thermal Modelling using Ansys*). The four thermal storage variables will not be considered in future steady state analyses.

SERIES 6.2.3 HEAT FLOW VALIDATION

For the purposes of validation the total heat flow from the model was considered in light of analytic solutions. No simple analytic solution exists which describes the temperature distribution at the surface for an arrangement with the geometry of the Alpha Model. However, a solution for heat flow exists which closely if not precisely applicable to the problem.

For a two dimensional system where only two temperature limits are involved a conduction shape factor S may be described from the equation:

$$Q=kS\Delta T \qquad 6.1$$

(Holman 1990)

Where:

Q Heat flux through the system (Wm^{-2})

k Thermal conductivity ($Wm^{-1}K^{-1}$)

S Conduction Shape Factor

ΔT Gross Thermal Gradient. (Km^{-1})

Kesthelyi (1994) citing (Incropera and DeWitt 1990) gives the equation for the conduction shape factor for a cylindrical heat source in an infinite half space:

$$S = 2\pi/\cosh^{-1}(2d/D+1) \qquad 6.2$$

Where:

d Depth of cylinder roof (m)

D cylinder radius (m)

Results of test models indicate that the total heat flow calculated from the finite element model is consistently 10-15% higher than the heat flow from the analytic solution, as would be expected. This discrepancy was expected for two reasons:

(i) Adaptation of the conduction shape factor to a slightly different geometry. The quoted shape factor is for a complete geometry, and the finite element model only

describes the upper right quadrant of the system. Proportionally more heat loss could reasonably be expected in the upper quadrants than in the lower, due to higher thermal gradients.

(ii) Approximations implicit in both the finite element method and the conduction shape factor calculations.

The fact that the two techniques do not yield major (order of magnitude scale) differences would suggest that no serious errors exist.

SERIES 6.2.4 VARIATIONS IN THE ATMOSPHERIC BOUNDARY LAYER THERMAL CONDUCTIVITY.

Model series 6.2.4 seeks to determine the importance of atmospheric effects as expressed in the ABL thermal conductivity on the surface thermal anomaly size and distribution. The variables used in this series are as shown in Table 6.5

Parameter	Value	Unit
Thickness	10	M
Thot	1000	°C
Tair	0	°C
ABL Thermal Conductivity	Varied	$Wm^{-1}K^{-1}$
SBL Thermal Conductivity	2	$Wm^{-1}K^{-1}$
Rock Thermal Conductivity	2	$Wm^{-1}K^{-1}$

Table 6.5 shows model series 6.2.4 model parameters

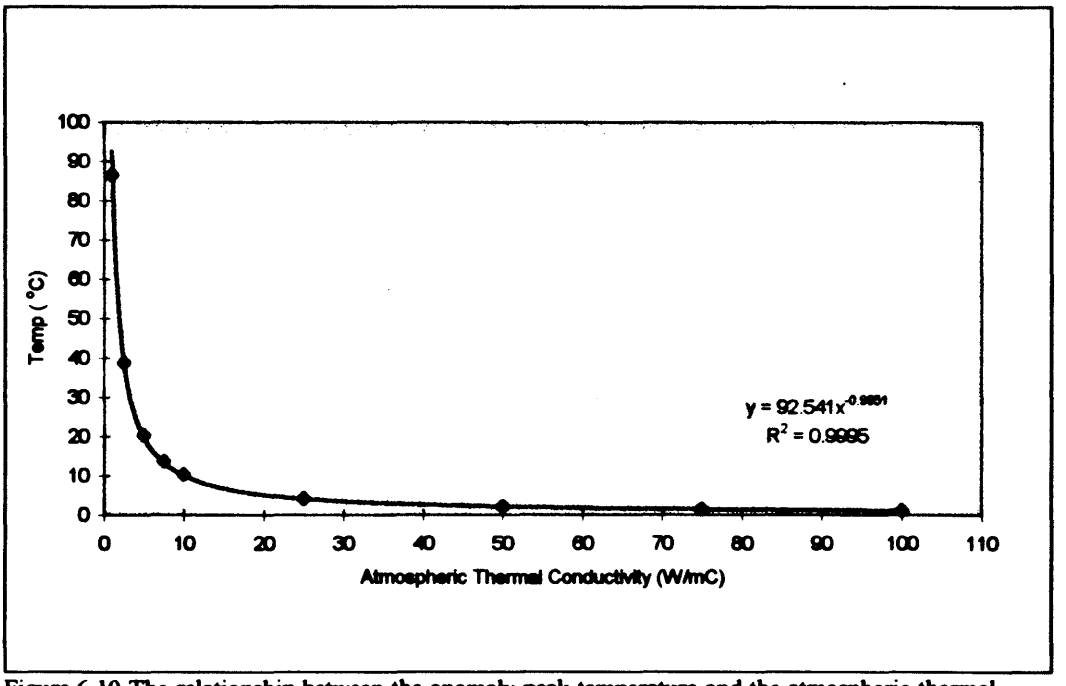


Figure 6.10 The relationship between the anomaly peak temperature and the atmospheric thermal conductivity. Note the inverse power decay in the values of the peak temperature as the ABL conductivity increases. Also note that the peak temperature is greatly increased at values of the ABL thermal conductivity of less than 10 $Wm^{-2}K^{-1}$

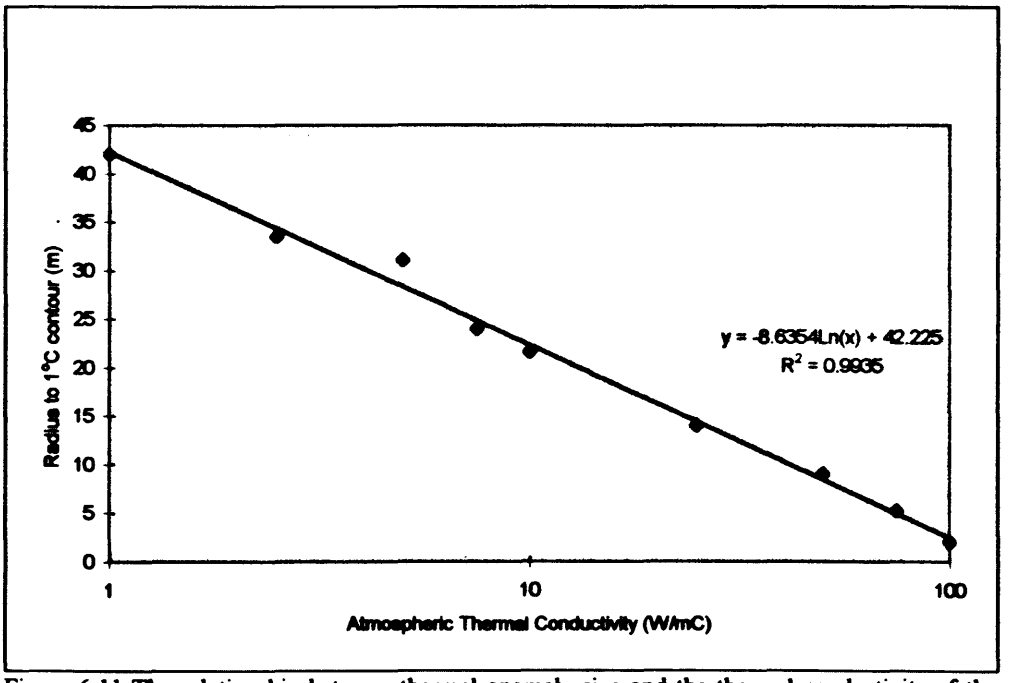


Figure 6.11 The relationship between thermal anomaly size and the thermal conductivity of the Atmospheric Boundary Layer. Note the steady decay in the size of the thermal anomaly as the thermal conductivity of the atmospheric boundary layer increases. Also note that the graph is more ragged due to broader uncertainty ranges in this data.

The anomaly peak temperature has an inverse power relationship to the thermal conductivity of the ABL as can be seen in Figure 6.10. The thermal anomaly size is in an inverse logarithmic relationship with the to the thermal conductivity of the ABL.

SERIES 6.2.5 VARIATIONS IN THE SURFACE BOUNDARY LAYER THERMAL CONDUCTIVITY

Model series 6.2.5 seeks to determine the importance of surface cover material in determining the size and magnitude of a surface thermal anomaly. The variables used in this series are as shown in Table 6.6

Parameter	Value	Unit
Thickness	10	m
Thot	1000	°C
Tair	0	°C
ABL Thermal Conductivity	13	$Wm^{-1}K^{-1}$
SBL Thermal Conductivity	varies	$Wm^{-1}K^{-1}$
Rock Thermal Conductivity	2	$Wm^{-1}K^{-1}$

Table 6.6 Model series 6.2.5 Parameters

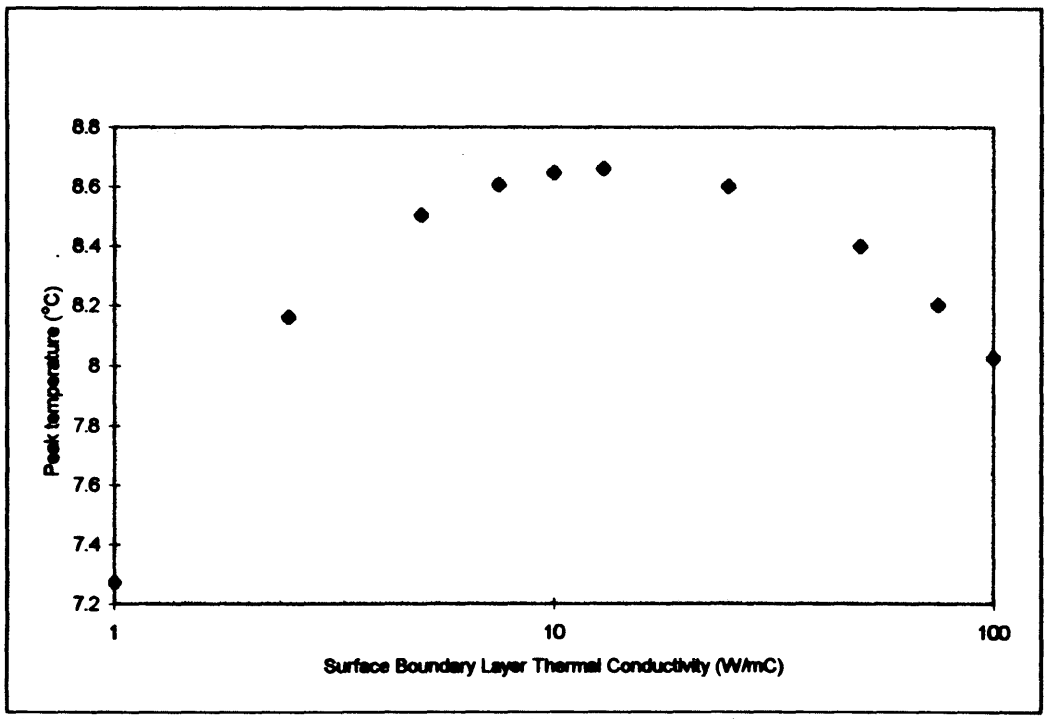


Figure 6.12 The relationship between anomaly peak temperature and SBL thermal conductivity. Note that the anomaly peak temperature peaks at the point where the SBL thermal conductivity equals the ABL thermal conductivity (13 $Wm^{-1}K^{-1}$)

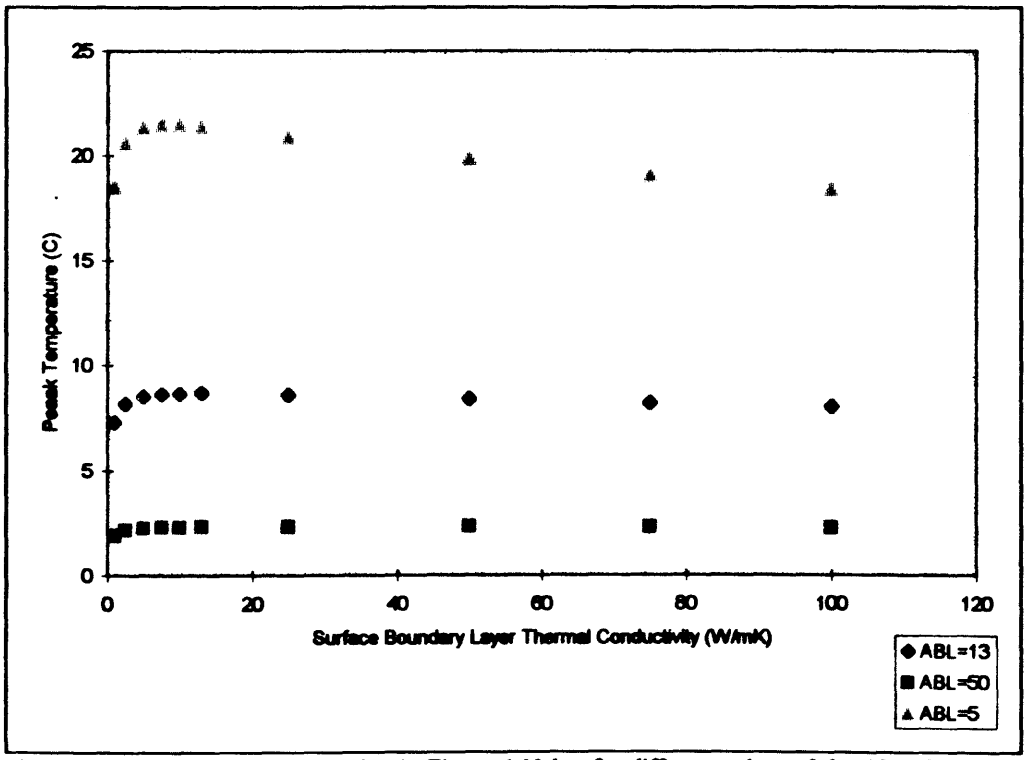


Figure 6.13 shows similar plot to that in Figure 6.12 but for different values of the ABL thermal conductivity (is $Wm^{-1}K^{-1}$).

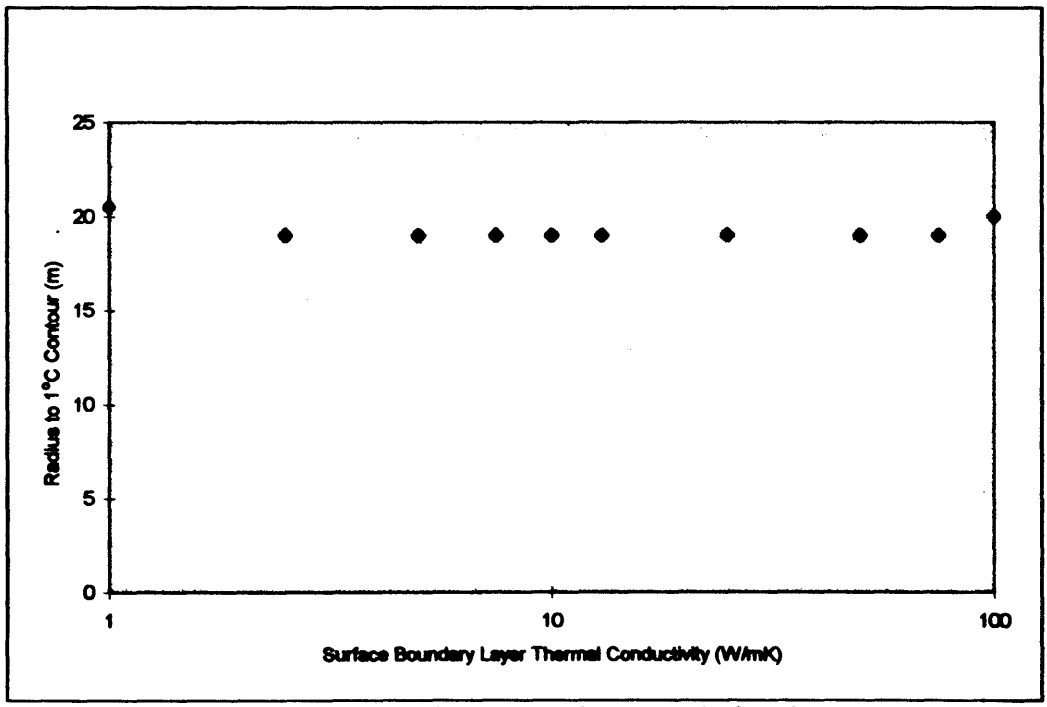


Figure 6.14 The relationship between the thermal anomaly size and the SBL thermal conductivity. Note that the thermal anomaly size is relatively stable, indicating that it is not strongly affected by the SBL thermal conductivity.

The thermal conductivity of the Surface Boundary Layer has a small effect on the peak temperature, as shown in Figure 6.12 and 6.13. Note that in Figure 6.12 the temperature appears to peak when the SBL thermal conductivity equals the ABL thermal conductivity. This would at first glance appear to suggest a linkage. Further tests (Figure 6.13) were conducted using different values of the Atmospheric Boundary Layer thermal conductivity to test this theory. These would seem to support a linkage but it can be noted that the dependence of peak temperature on surface boundary thermal conductivity is not very strong in any case, having an effect of no more than 1.5°C across two orders of magnitude.

The thermal conductivity of the Surface Boundary Layer seems to have no effect at all on the physical extent of the geothermal anomaly. In general, the surface boundary layer, having only a slight influence on the peak temperature, and no influence on the anomaly size, is not a significant factor in the physical system.

SERIES 6.2.6 VARIATIONS IN THE ROCK THERMAL CONDUCTIVITY

Model series 6.2.6 seeks to determine the importance of the thermal conductivity of the rock on the peak temperature and size of the thermal anomaly.

Note that the range of values for the thermal conductivity of rock is much smaller than the ranges for the other two thermal conductivities in the system. The wide ranges for the other two layers are due to highly variable heat transfer processes (ABL) and variable real world thickness (SBL). Real world values for rock thermal conductivities lie in the range 1-5 $Wm^{-1}K^{-1}$ (see *Appendix C*)

Values used in this model series are as shown in Table 6.7

Parameter	Value	Unit
Thickness	10	m
Thot	1000	°C
Tair	0	°C
ABL Thermal Conductivity	13	$Wm^{-1}K^{-1}$
SBL Thermal Conductivity	2	$Wm^{-1}K^{-1}$
Rock Thermal Conductivity	Varies	$Wm^{-1}K^{-1}$

Table 6.7 Model series 6.2.6 Parameters

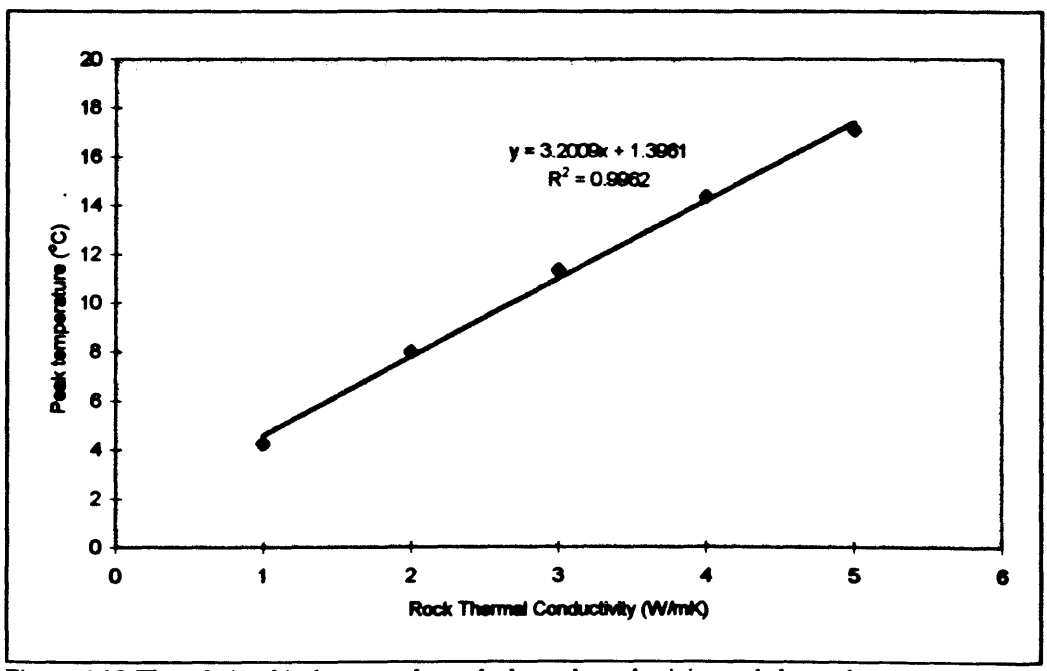


Figure 6.15 The relationship between the rock thermal conductivity and the peak temperature. Note the strongly linear relationship.

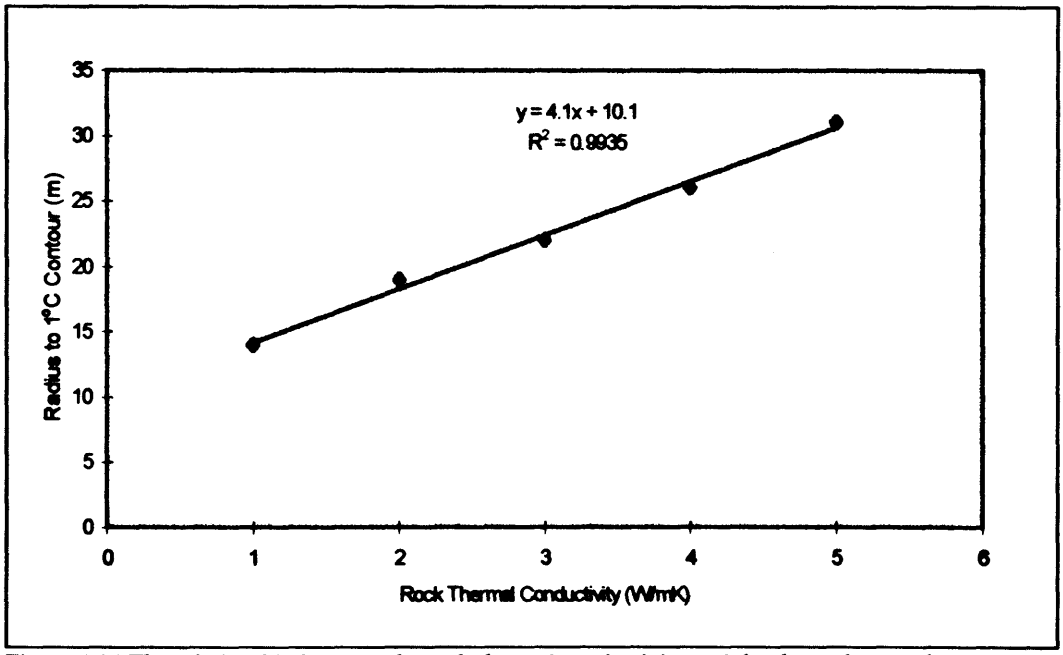


Figure 6.16 The relationship between the rock thermal conductivity and the thermal anomaly size. Note again the strongly linear relationship.

The linear relationship between peak temperature, thermal anomaly size and thermal conductivity suggests a simple linear correlation, as we might expect. A further subseries of models was run varying the rock thermal conductivity and the source depth, to assess the dependence of the slope of the graphs in Figures 6.15 and 6.16 on these variables. These are described in the Series 6.2.8

SERIES 6.2.7 VARIATIONS IN THE SOURCE TEMPERATURE

Model series 6.2.7 seeks to determine the importance of variations in the source temperature. Values used are in this model series are shown in Table 6.8

Parameter	Value	Unit
Thickness	10	m
Thot	varies	°C
Tair	0	°C
ABL Thermal Conductivity	13	$Wm^{-1}K^{-1}$
SBL Thermal Conductivity	2	$Wm^{-1}K^{-1}$
Rock Thermal Conductivity	2	$Wm^{-1}K^{-1}$

Table 6.8 Model series 6.2.7 parameters.

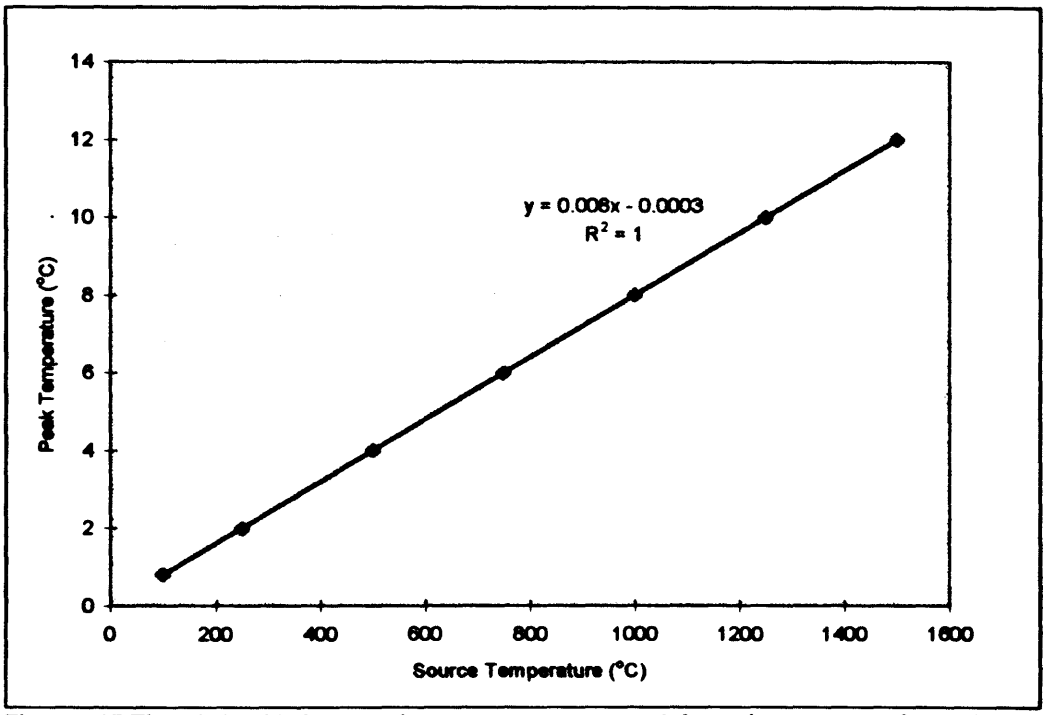


Figure 6.17 The relationship between the source temperature and the peak temperature for model series 6.2.7 . Note the definite linear, positive correlation.

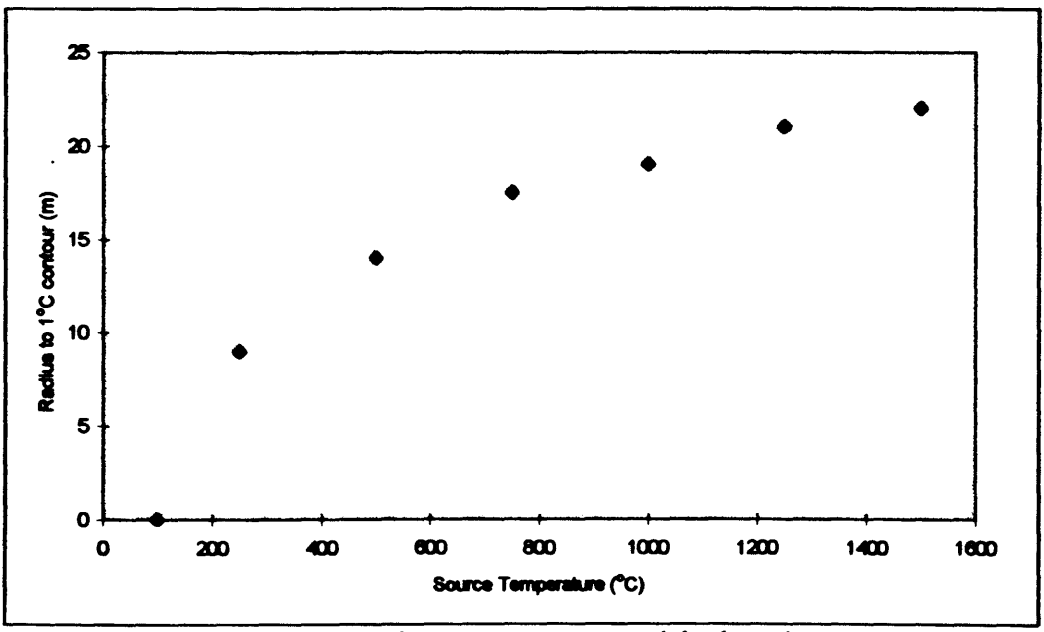


Figure 6.18 The relationship between the source temperature and the thermal anomaly size. Note again the positive, near linear correlation.

A strong positive linear or near linear correlation occurs between the source temperature and both the peak temperature and thermal anomaly size. Further

models will be required to identify if a useable empirical relationship underlies this trend, expressing the slope and offset of these linear trends in terms of the other variables. This is examined in detail below.

SERIES 6.2.8 VARIATIONS IN THE SOURCE DEPTH

Model series 6.2.8 seeks to determine the importance of variations in the source depth. Special care must be taken with this model series. Variations of the depth parameter change the overall geometry and require remeshing. Thus each individual run at a different depth must be rechecked for convergence. In practice this is handled by continually refining the mesh until a stable solution is found.

Parameter	Value	Unit
Thickness	varies	m
Thot	1000	°C
Tair	0	°C
ABL Thermal Conductivity	13	$Wm^{-1}K^{-1}$
SBL Thermal Conductivity	2	$Wm^{-1}K^{-1}$
Rock Thermal Conductivity	2	$Wm^{-1}K^{-1}$

Table 6.9 Model series 6.2.8 parameters.

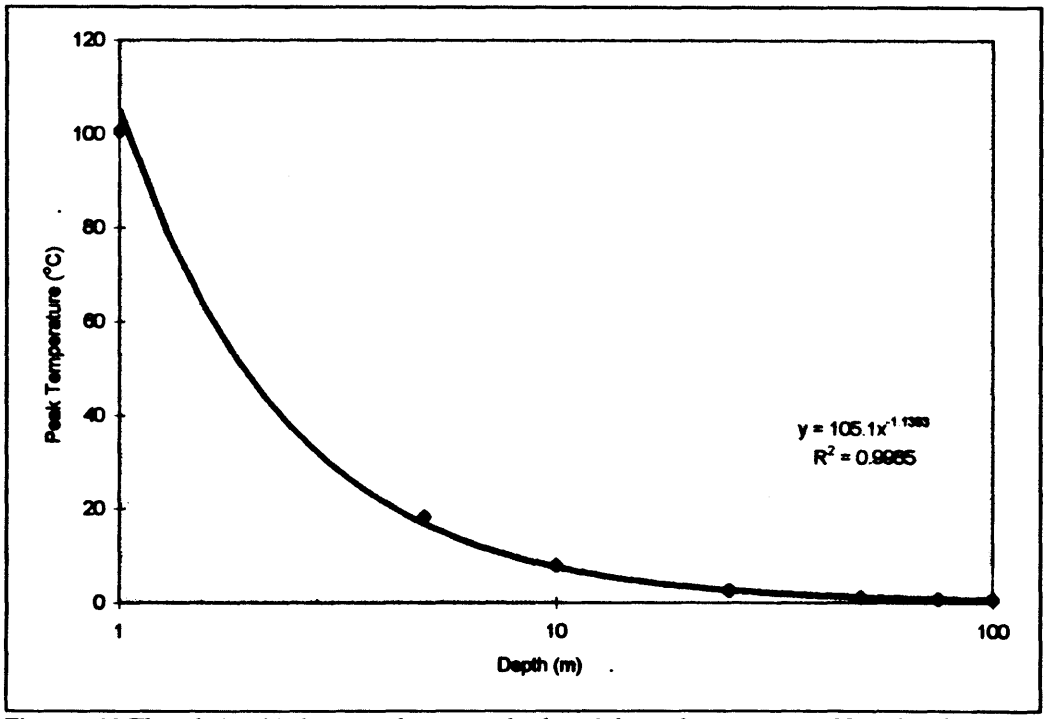


Figure 6.19 The relationship between the source depth and the peak temperature. Note that the x-axis is logarithmic. An inverse power relationship is seen to relate the two terms. Note that this data is essentially an orthogonal section across the data shown in Figure 6.18 for a fixed source temperature.

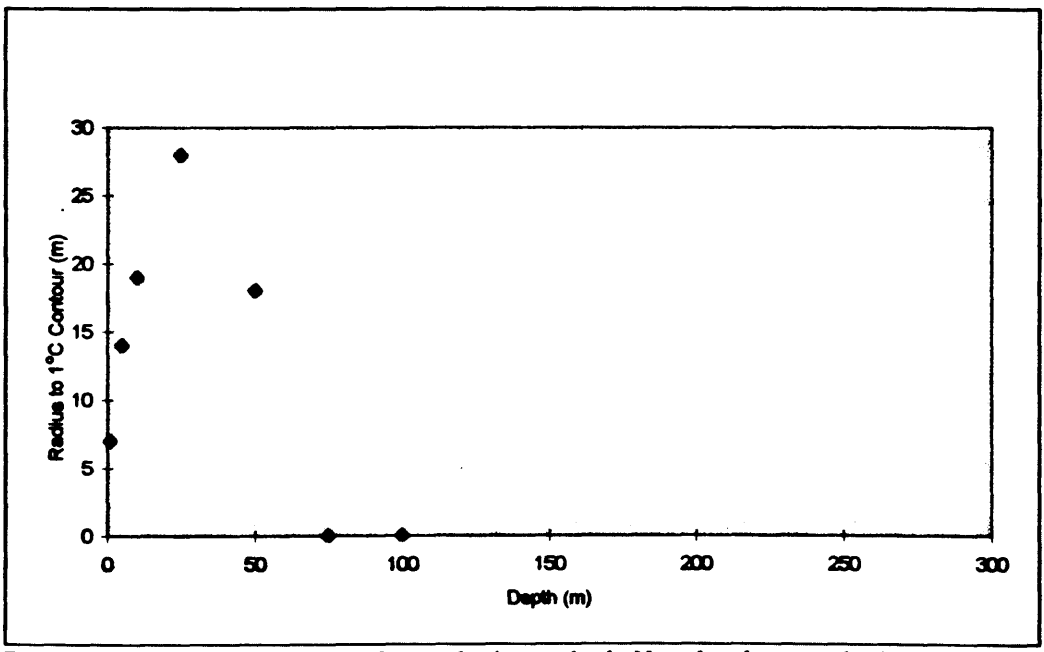


Figure 6.20 shows the dependence of anomaly size on depth. Note that the anomaly size initially increases to depths of up to 28m and them rapidly begins to decay.

The peak temperature and the source depth as shown in Figure 6.19 are in inverse power relationship governed by the function:

$$T_{max} = 105.1(D)^{-1.1365} \qquad 6.7$$

Where:

T_{max} Peak Temperature (C)

D Source Depth (m)

The thermal anomaly size shows no such clear relationship with the source depth. The anomaly becomes more extensive until about 28m in size, and then rapidly collapses, when the peak temperature decays below 5°C. A third order polynomial expression can be derived to fit the modelled curve but the function returns nonsense values for large depths and serves only to illustrate the hazards of seeking direct empirical relationships where none may exist.

SERIES 6.2.8 VARIATION OF MULTIPLE PARAMETERS

Some variables, particularly those with very linear slopes, suggest that they may be controlled or related to other variables which were held constant in the series examined so far. By combining existing datasets for the models described above and running additional models as necessary, simultaneous analysis of multiple parameters can be carried out to assess if the slopes of figures such as 6.16 or 6.17 are controlled in this way.

(i)Conductivity and Depth

Series 6.2.6 and 6.2.7 show strongly linear trends suggesting a governing function for the slope of these figures. Combining the data from these series and running further models, the following graphs can be constructed, using the same surface and atmospheric boundary layer parameters as is series 6.2.6 and 6.2.7.

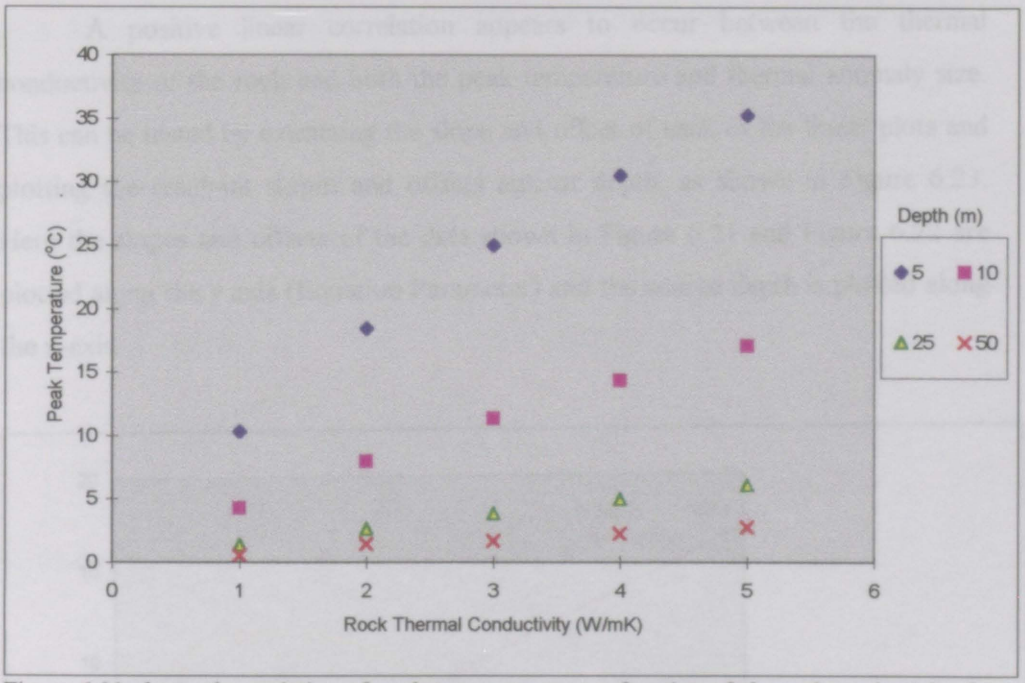


Figure 6.21 shows the variation of peak temperature as a function of thermal conductivity for different source depths in m, as identified in the legend. This graph is an extension of the data set shown in Figure 6.16, for different source depths. Note the linear trends.

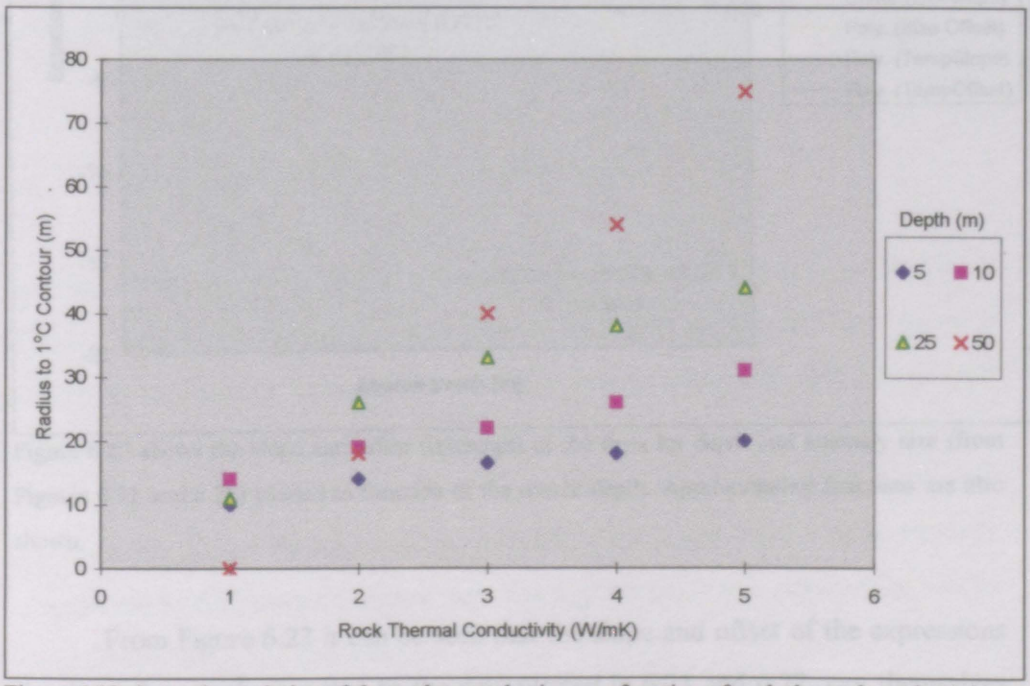


Figure 6.22 shows the variation of thermal anomaly size as a function of rock thermal conductivity for different source depths. Note the linear trends.

A positive linear correlation appears to occur between the thermal conductivity of the rock and both the peak temperature and thermal anomaly size. This can be tested by extracting the slope and offset of each of the linear plots and plotting the resultant slopes and offsets against depth, as shown in Figure 6.23. Here the slopes and offsets of the data shown in Figure 6.21 and Figure 6.22 are plotted along the y axis (Equation Parameter) and the source depth is plotted along the x-axis.

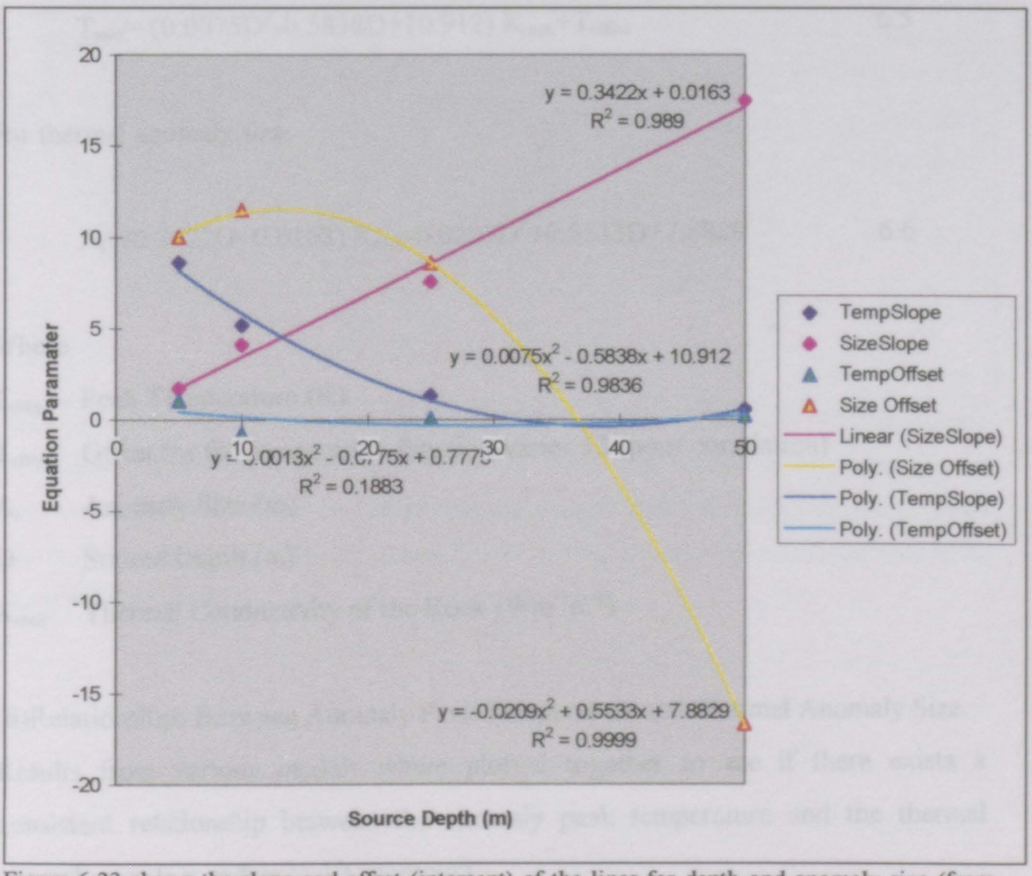


Figure 6.23 shows the slope and offset (intercept) of the lines for depth and anomaly size (from Figures 6.21 and 6.22) plotted as function of the source depth. Approximating functions are also shown.

From Figure 6.23 it can be seen that the slope and offset of the expressions for thermal anomaly size that fit the data plotted in 6.21 and 6.22, can themselves both be readily approximated as functions of depth (in red, and yellow on figure 6.23). The slope of the peak temperature functions can also be plotted as a function of the depth (blue line, Figure 6.23), but the offset of these expressions (green line,

Figure 6.23) shows little or no correlation with depth, and must therefore be dependant on some other parameter.

Combining the expressions for the slope and offset as a function of the source depth from Figure 6.23 into expression to describe the lines in figures 6.21 and 6.22 suggests the following empirical relationships:

For peak temperature

$$T_{max} = (0.0075D^2 - 0.5838D + 10.912)\, K_{rock} + T_{offset} \qquad 6.5$$

For thermal anomaly size:

$$A_s = (0.3422D + 0.0162)\, K_{rock} - 0.0209D^2 + 0.5533D + 7.8829 \qquad 6.6$$

Where

T_{max} Peak Temperature (K)

T_{offset} Offset for the temperature function-varies ±2 (poor correlation)

A_s Anomaly Size (m)

D Source Depth (m)

K_{rock} Thermal Conductivity of the Rock ($Wm^{-1}K^{-1}$)

(ii)Relationships Between Anomaly Peak Temperature and Thermal Anomaly Size.

Results from various models where plotted together to see if there exists a consistent relationship between the anomaly peak temperature and the thermal anomaly size (i.e. radius to 1°C contour).

Figure 6.24, shows data with a wide variety of other parameters, shows that the geometry is the principle factor controlling the ratio of the peak anomaly temperature to the thermal anomaly size. For a given depth this ratio can be readily approximated using the expression:

$$Ratio = 13.457(Depth)^{-1.4546} \qquad 6.7$$

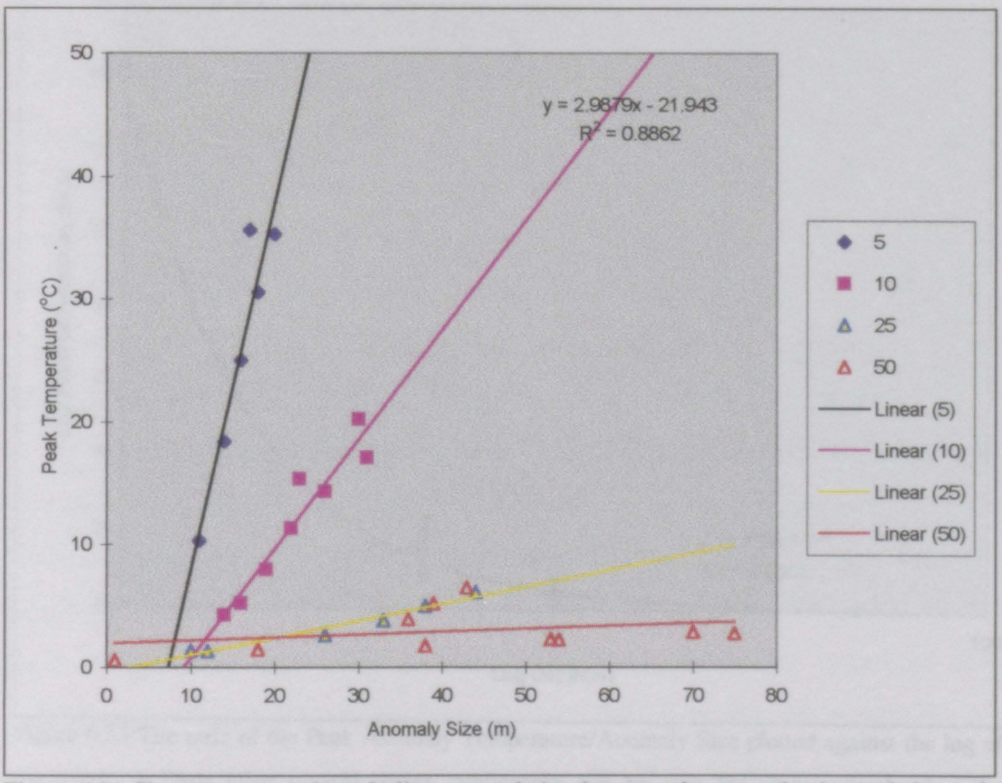


Figure 6.24 Shows an approximately linear correlation between the anomaly size and the peak temperature for different anomaly size. The data is drawn from multiple models using different values of the other parameters. The fact that the data clusters readily along lines determined by the source depth indicates that the relationships between the two variables are chiefly controlled by the geometry of the model.

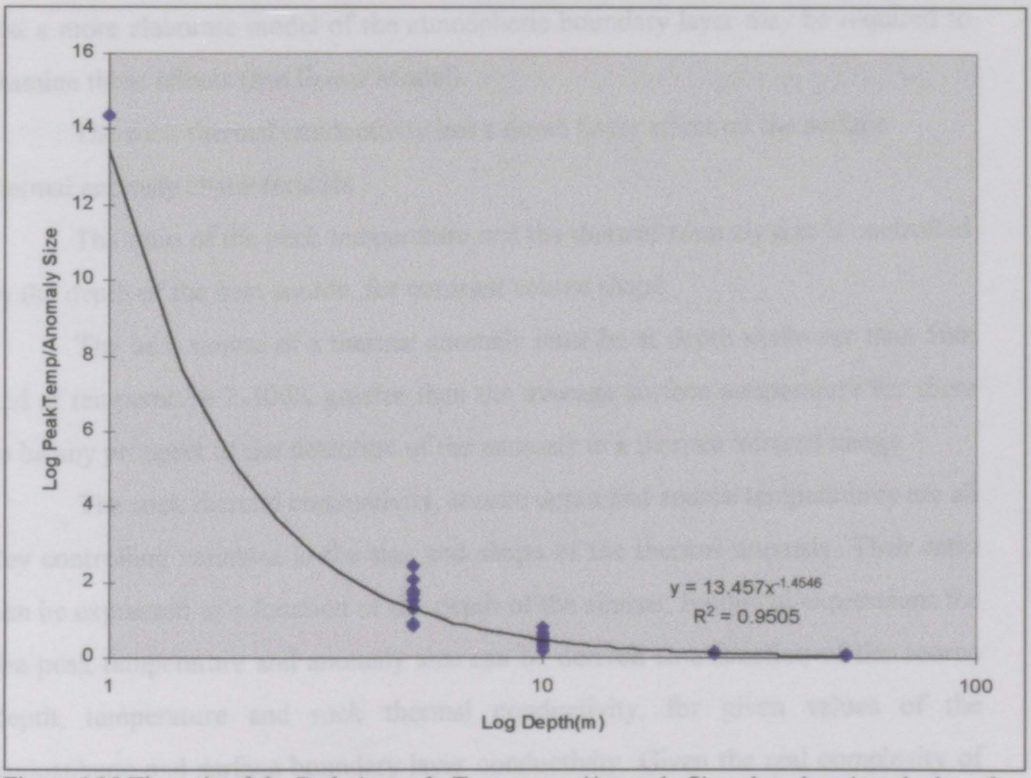


Figure 6.25 The ratio of the Peak Anomaly Temperature/Anomaly Size plotted against the log of the depth. A fairly clear inverse power relationship can be seen for greater depths, but the correlation weakens for shallow depths.

CONCLUSIONS

A number of conclusions can be drawn from these models.

The density and specific heat capacity of the materials are irrelevant in steady state analyses.

The effect of a surface boundary layer of unit thickness is not significant. This is a surprising result and suggests that the underlying approximation of the surface boundary layer, that a layer of unit thickness can be used to approximate a layer of variable thickness, is incorrect. The result however, can be taken at face value for layers of 1m thickness, and suggests that the thermal effect of such layers, and of layers of less than 1m thickness, is negligible. Thus the surface boundary layer can be dispensed with as unnecessary in future models, unless specifically required by the case study.

The thermal properties of the atmospheric boundary layer are significant. Very high virtual thermal conductivities swamp the thermal anomaly. This suggests

that a more elaborate model of the atmospheric boundary layer may be required to examine these effects (see Bravo Model).

The rock thermal conductivity has a direct linear effect on the surface thermal anomaly characteristics.

The ratio of the peak temperature and the thermal anomaly size is controlled by the depth of the heat source, for constant source shape.

The heat source of a thermal anomaly must be at depth shallower than 50m and at temperature 2-300K greater than the average surface temperature for there to be any prospect of the detection of the anomaly in a thermal infrared image.

The rock thermal conductivity, source depth and source temperatures are all key controlling variables in the size and shape of the thermal anomaly. Their ratio can be expressed as a function of the depth of the source. Empirical expressions for the peak temperature and anomaly size can be derived as a function of the source depth, temperature and rock thermal conductivity, for given values of the atmospheric and surface boundary layer conductivity. Given the real complexity of the atmospheric boundary layer and its strong variation in reality, these expressions are of limited utility.

In general, the uncertainty ranges established by means of convergence testing are too small. By inspection of the graphs and R^2 values of the approximating functions, it can be seen that the uncertainty in the modelled temperature values is itself variable, in some places values falling precisely along a linear trend, in others, values lying 3-4 degrees centigrade off the trend. In all cases, however, any observed trends are quite clear and uncertainties in the data, while larger than those suggested by the convergence testing, are not large enough to call any of the conclusions into question.

With little difficulty the Alpha model can be readjusted and additional model series can be run virtually *ad infinitum*. Potentially interesting variations include:

- Variation of the heat source size and shape.
- Testing the effect of anisotropic conduction, for example, introducing a vertical anisotropy to simulate convective heat transfer.

However, considering some of the limitations of the Alpha model, it would be more appropriate to leave such elaboration to a more sophisticated model, the Bravo Model.

6.3 THE BRAVO MODEL

The purpose of the Bravo model is to investigate the size and intensity of surface geothermal anomalies as a function of the variable parameters of surface emissivity, incident radiant flux, convection transfer coefficient, bulk atmospheric temperature, source temperature, source depth, and rock thermal conductivity.

The Bravo model is an evolution of the Alpha model using more sophisticated surface boundary layer techniques to model radiation and convection as independent processes. A number of operational improvements, outlined below, were made on the basis of experience gained in developing and using the Alpha model.

GEOMETRY

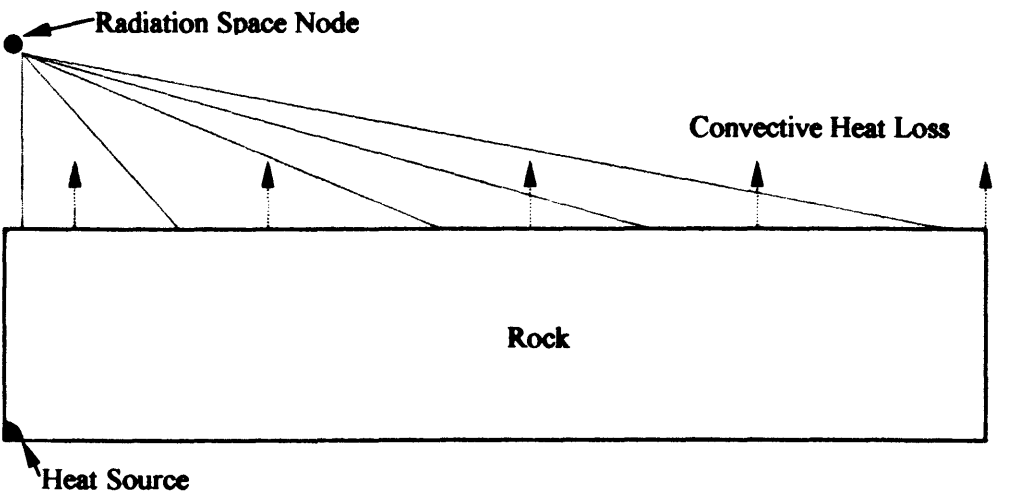


Figure 6.26 Generalised geometry of the Bravo model (not to scale).

The Bravo model geometry (Figure 6.26) is simpler than that used by the Alpha model. The Atmospheric Boundary Layer has been removed, its function having been superseded by the surface effect elements for radiation and the convective heat transfer loads. The Surface Boundary Layer (SBL) used in the Alpha model has also been eliminated, on the basis that considering its relatively small effect on the surface temperature distribution, its effects are not significant.

MODEL DESIGN

A number of improvements were made to the modelling design based on the experience gained in working with the Alpha model. These were directed towards increasing the model accuracy, ease of use, restraining processing time, and facilitating planned adaptation of the model to transient and other cases.

The mesh is improved (see below) to give more accurate results and be easier to adjust for different model depths.

In addition, the model script has been broken up into two elements, one *Bravoshell*, sets up the model geometry and the second, *Bravol*, applies the various boundary conditions and loads, and solves the model equations (See *Appendix E*). This eliminates the need to regenerate the same mesh anew for each problem, which, for such a large mesh, is very time consuming. This also facilitates the adaptation of the model to a transient case by modifying *Bravol* appropriately and encasing it within a DO loop in *Bravoshell*.

MESH DESIGN AND CONVERGENCE

Meshing was carried out using the Plane 55 and Surf 19 elements (see *Chapter 5: An Introduction to Thermal Modelling using Ansys*) without element midside node options selected. This was to optimise processing time.

Convergence testing of the model mesh was carried out as the mesh was being developed. This was done by starting out with a basic mesh and refining it, uniformly or selectively, until a satisfactorily stable solution was achieved. The results of this process are interesting, and are tabulated in table 6.11.

A set of standard values for the variable parameters was used for convergence testing and validation models, which are as tabulated in table 6.10.

Parameter	Value	Unit
Thickness	10	m
Thot	1000	K
Bulk Temperature	273	K
Convection Film Coefficient	10	$Wm^{-1}K^{-1}$
Space Node Temperature	250	K
Initial Temperature	283	K
Rock Thermal Conductivity	2	$Wm^{-1}K^{-1}$
Rock Density	2700	kgm^{-3}
Rock Specific Heat Capacity	800	$Jkg^{-3}K^{-1}$
Emissivity	1	

Table 6.10. Parameters for convergence testing models.

No.	Description	Nodes	Max (K)	Min (K)	Difference (K)
1	BravoBasic	647	272.6	266.5	6.1
2	Basicx2	2475	269.3	263.1	6.2
3	Basicx4	9683	266.1	259.6	6.6
4	Basicx2,left halfx2	9114	266.1	263.1	3.0
5	Tube refined	2013	272.6	266.5	6.1
6	Surface refinedx2	830	269.2	263.1	6.1
7	Surface refinedx4	1496	266.1	260	6.1
8	Surface refinedx8,rad	2521	272.6	266.4	6.2
9	Ultimate	5724	270.5	266.4	3.6

Table 6.11 Results of the mesh refinement and design process. Max indicates the maximum temperature (K) directly over the thermal anomaly, min indicates the minimum temperature at the node furthest from the anomaly, difference is the amplitude of the thermal anomaly.

The evolution of the final mesh sheds light on the subtleties of the modelling software. Initial refinements focused on increasing the overall mesh density. This had little effect on the anomaly amplitude, which remained in the region of 6K, but had the effect of decreasing both the maximum and minimum temperatures by 3K

each time. This approach rapidly ran into difficulties due to computer memory limitations before showing any sign of convergence.

Refinement 4 involved doubling the overall mesh density and doubling again the mesh density on the left-hand side of the model, where the thermal anomaly is sited. This had the effect of halving the anomaly amplitude, indicating that selective refinement was affecting the final temperature. A refinement of the region around the heat source was carried out, to rule out any effect from that quarter (No. 5), which led to the conclusion that the surface temperature variation was strongly affected by the mesh density of near surface elements. Further tests refining only these elements (No. 6, 7) confirmed this effect.

At this point it was noted that the element refinement procedure is not automatically applied to the surface effect elements, and that these elements were remaining at the original size. The steady decrease in temperature was probably due to the size discrepancy between the radiating surface effect elements and the underlying conducting elements, which was introducing approximations to the solution procedure. This had a more pronounced effect in areas of higher thermal gradient (over the source) than in areas of low thermal gradient, and resulted in inaccurate radiative heat fluxes.

In test No. 8 the surface effect elements were added last, so that they would 'coat' the refined element properly. The resultant values returned to the values generated in the initial mesh for the 'cold end' and generated a cooler value (due to more precise calculation of the radiation) at the hot end.

A final revision was carried out to increase the mesh density close to the surface. This was both to improve accuracy in the region and facilitate adoption of the model to transient problems, where near surface thermal propagation is of greater significance. Near surface elements were successively refined to give a minimum size of 0.2 units (20cm).

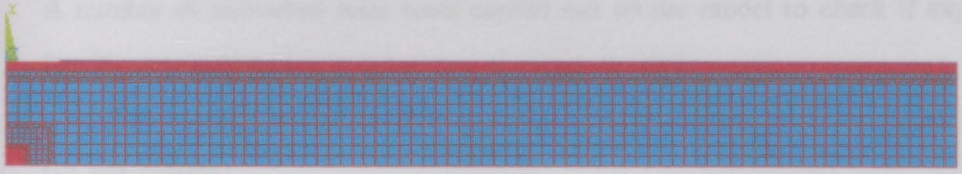


Figure 6.27 Final Bravo Model Mesh.

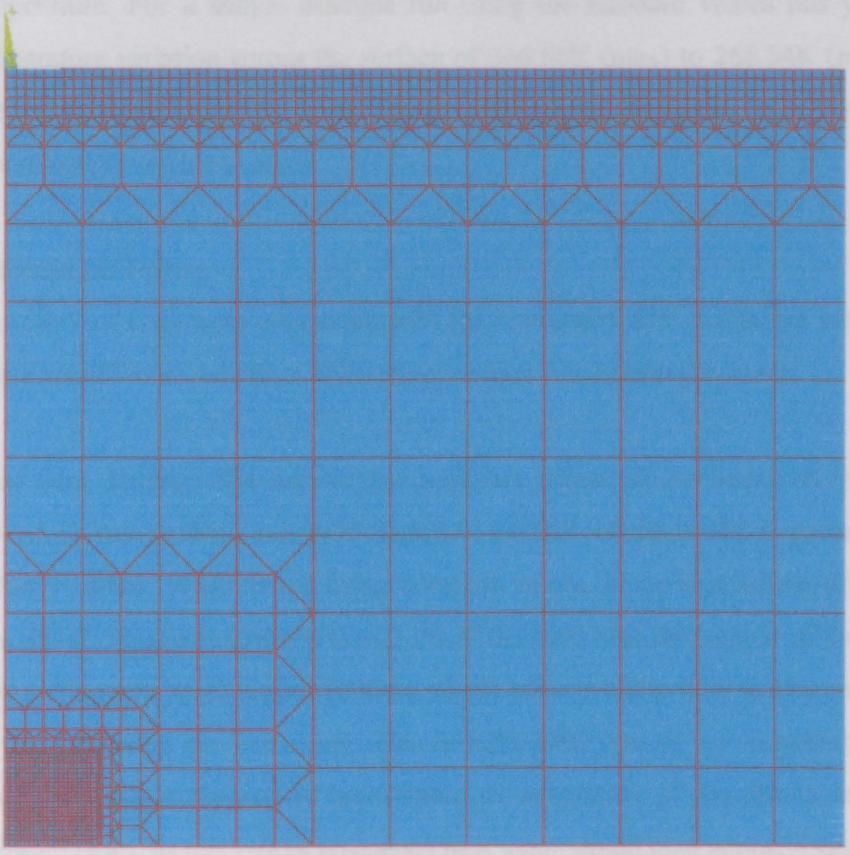


Figure 6.28 The left hand side of the Bravo mesh from Figure 6.29 enlarged. Note the increased mesh densities in the region of the thermal anomaly and close to the surface.

MODEL TESTING

A number of individual tests were carried out on the model to check if expected results were achieved.

(i)Cold Testing

The model was set with the heat source temperature set at the same value as the uniform, background temperature. This should generate a uniform surface temperature. For a simple example run using the standard values this yielded a temperature variation across the surface of 266.56K (max) to 266.54K (min). The maximum value occurred over region where the mesh had been refined to accommodate the heat source.

(ii)Radiation Testing:

A number of tests were conducted with the convection film coefficient set at zero, which should have the effect of disabling surface convection processes.

Heat Sum Testing: The sum of the heat flux across all the nodes of the model should be zero in this case, as all heat lost by bulk of the model is gained by the radiation space. When tested using standard values, a net heat inflow of 0.154W was found. This represent less than 0.1% of the total heat throughput of the system. (Note: Since the model is solved for a steady state the heat flow can be considered as that occurring per unit time). This is sufficiently low to not contribute to any error, nor will it present an impediment to adaptation of the Bravo model for transient cases, as this rate of erroneous heat input would take almost 4 centuries to increase the total model temperature by 1K. Transient modelling will be not carried out on that time scale in this study.

Incident radiation testing: By setting the space node (see Figure 6.28) at a relatively hot temperature, the model should itself heat to that temperature due to radiative transfer from the space node. On testing, this was found to be the case, verifying that radiation to the space node is functioning as a two way process.

No radiative transfer: By setting the model initial temperature to equal that of the space node, and shutting off the internal heat source, no heat transfer should occur in the model, thus maintaining a uniform heat distribution. This was found to be the case, and the model remained at the initial temperature.

(ii) Convection Layer Testing:

By setting the surface emissivity to zero, radiative processes can be deactivated. This should yield a zero net heat flux for the radiation space node, and this was observed to be the case.

Bulk temperature testing: By setting the bulk temperature to a higher value than the initial temperature for the problem, the model should itself heat to that temperature due to convective transfer from the fluid. On testing, this was found to be the case.

TEST COMPARISION OF ALPHA AND BRAVO RESULTS

The results of the Alpha and Bravo models are not directly comparable because:

- The absence of a distinct surface boundary layer in the Bravo model geometry, thus the heat source focus is 1m shallower than in the Alpha model.
- Less precise 4 noded elements were used in the Bravo model mesh instead of more computationally intensive 8 noded elements.
- Different surface boundary layer handling techniques are employed.

The models are, however, models of the same process and so should be similar. A comparison can be made by making the following adjustments:

- Setting the bulk temperature to 273K (0°C), equal to the mean atmospheric temperature used in the Alpha model.
- Setting the source temperature (Thot) to 1273K (equivalent to 1000°C).
- Setting the convective heat transfer coefficient equal to the ABL thermal conductivity.
- Seting the material properties to be the same as in Series 6.2.4 of the Alpha model, in which the ABL thermal conductivity was varied.

Thus an approximate comparison of the results can be made, as is shown in Figure 6.29 and 6.30.

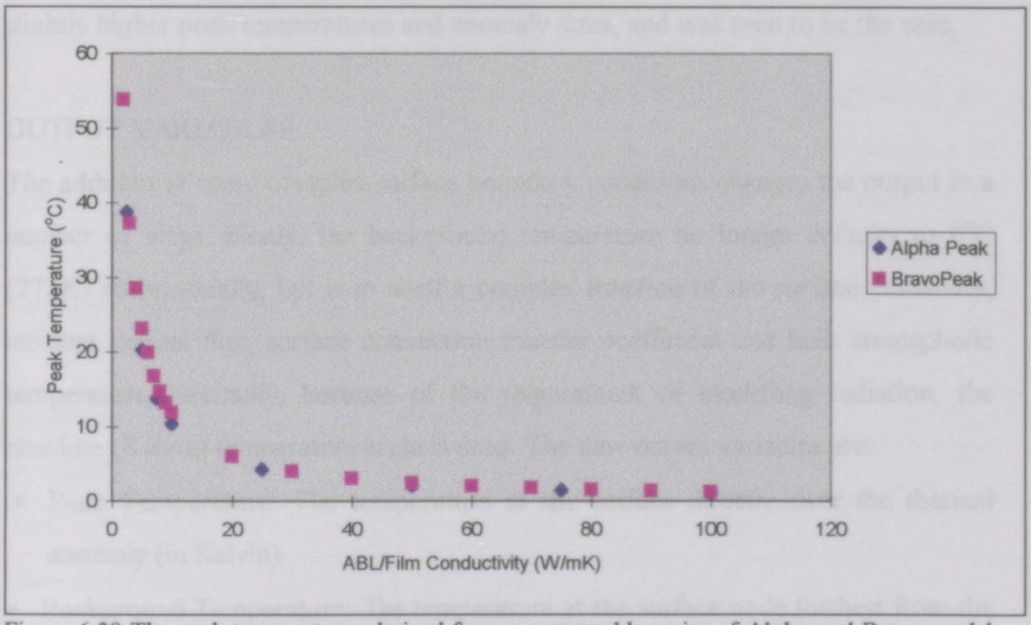


Figure 6.29 The peak temperatures derived from a comparable series of Alpha and Bravo model runs.

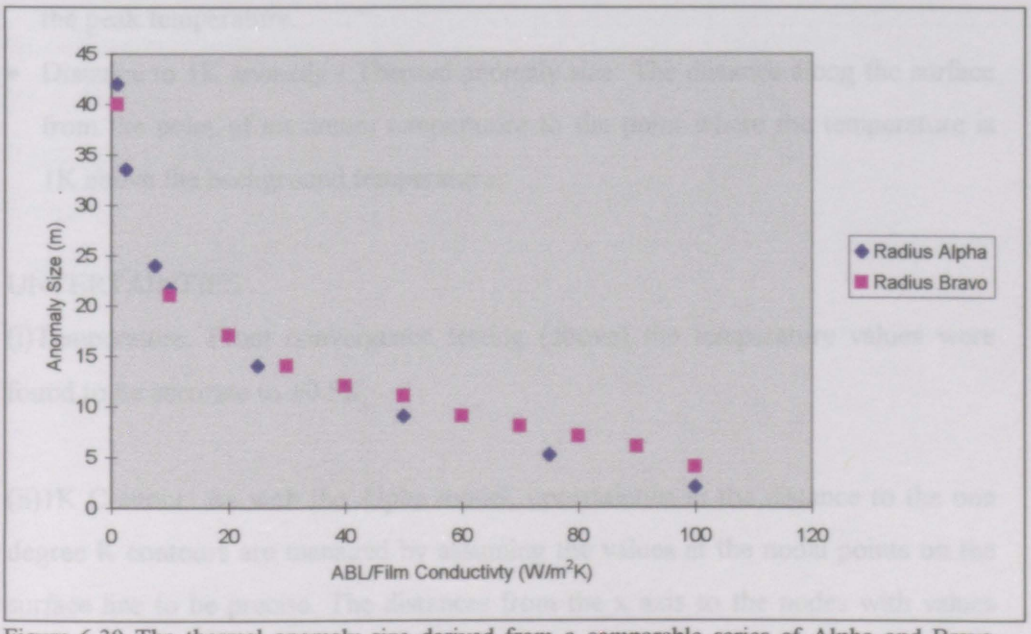


Figure 6.30 The thermal anomaly size derived from a comparable series of Alpha and Bravo model runs.

The comparison of results shows that the two models yield broadly similar trends, but are as expected, not identical. The Bravo model was expected to give slightly higher peak temperatures and anomaly sizes, and was seen to be the case.

OUTPUT VARIABLES

The addition of more complex surface boundary conditions changes the output in a number of ways. Firstly, the background temperature no longer defaults to 0°C (273K) automatically, but is in itself a complex function of the surface emissivity, incident radiant flux, surface convection transfer coefficient and bulk atmospheric temperature. Secondly, because of the requirement of modelling radiation, the absolute (Kelvin) temperature scale is used. The new output variables are:

- Peak Temperature: The temperature at the surface directly over the thermal anomaly (in Kelvin).
- Background Temperature: The temperature at the surface node furthest from the heat source.
- Net Thermal Anomaly: The difference between the background temperature and the peak temperature.
- Distance to 1K anomaly / Thermal anomaly size: The distance along the surface from the point of maximum temperature to the point where the temperature is 1K above the background temperature.

UNCERTAINTIES

(i)Temperature: From convergence testing (above) the temperature values were found to be accurate to ±0.5K.

(ii)1K Contour: As with the Alpha model, uncertainties in the distance to the one degree K contours are managed by assuming the values at the nodal points on the surface line to be precise. The distances from the x axis to the nodes with values just above and just below 1°C are taken as the upper and lower limits of the error, respectively. As the nodes are evenly spaced in this case, this gives an uncertainty of ±0.5units (0.5m). Distances will be given to the nearest metre.

6.4 BRAVO MODEL RESULTS

SERIES 6.4.1 FACTORS AFFECTING THE BACKROUND TEMPERATURE

The purpose of model series 6.4.1 is to quantify the factors affecting the background temperature, namely, the surface emissivity, incident radiant flux (a function of the space node temperature), convection transfer coefficient, bulk atmospheric temperature and rock thermal conductivity. Each of these factors are varied in turn, and otherwise held at the values in Table 6.12.

Parameter	Value	Unit
Thickness	10	m
Thot	Off	K
Bulk Temperature	273	K
Convection Film Coefficient	10	$Wm^{-2}K^{-1}$
Space Node Temperature	270	K
Initial Temperature	283	K
Rock Thermal Conductivity	2	$Wm^{-1}K^{-1}$
Rock Density	2700	kgm^{-3}
Rock Specific Heat Capacity	800	$Jkg^{-3}K^{-1}$
Emissivity	1	

Table 6.12 Parameter Values

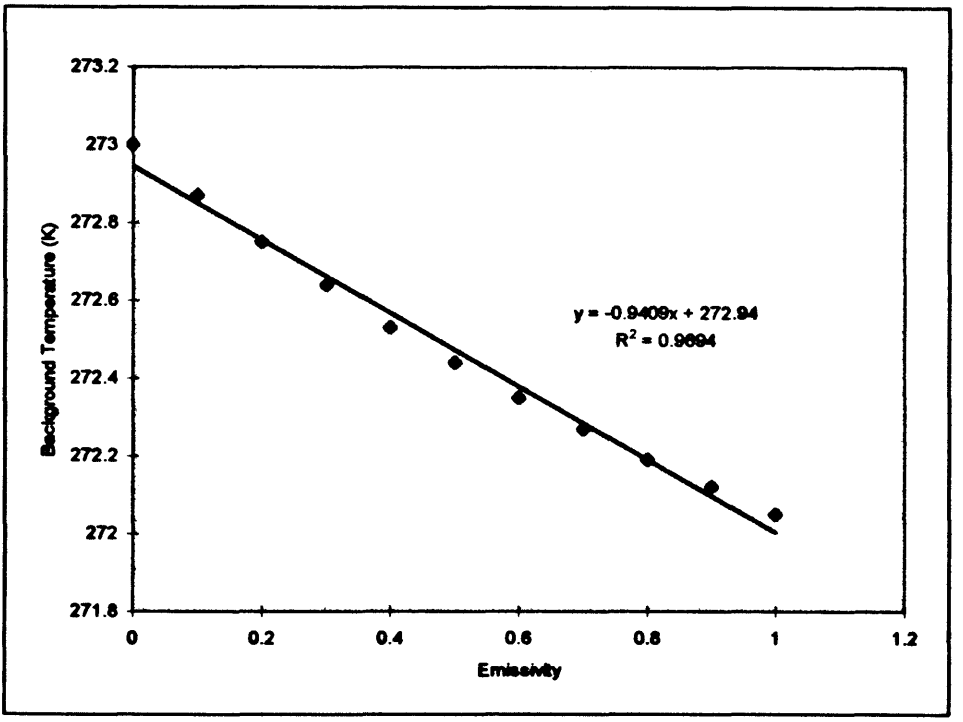


Figure 6.31 Background temperature plotted against variations in the emissivity. Note the inverse linear correlation between the background temperature and the emissivity.

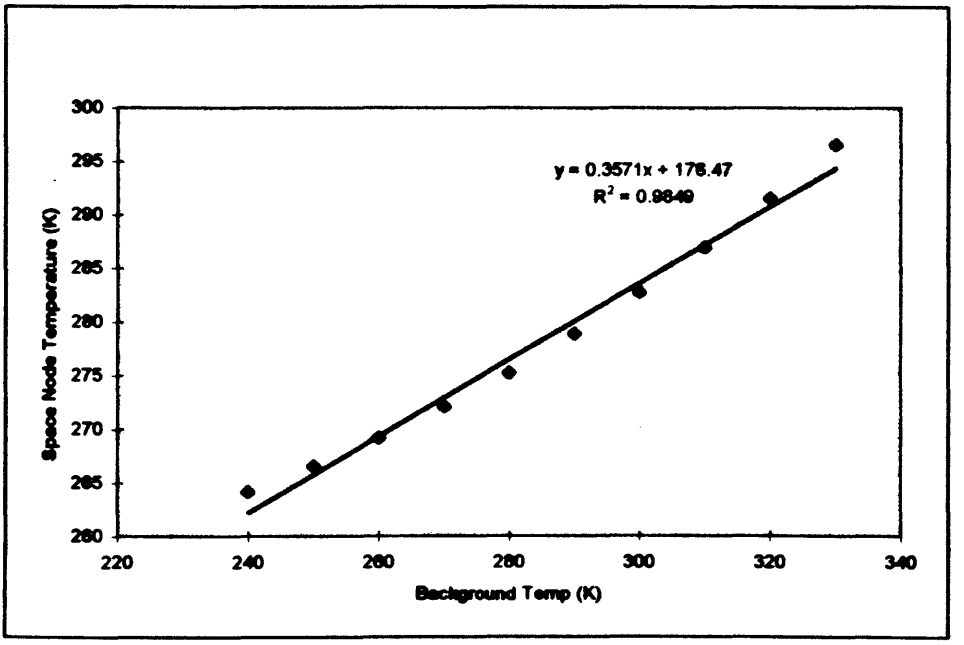


Figure 6.32 Space node temperature plotted against background temperatures. Note the linear correlation.

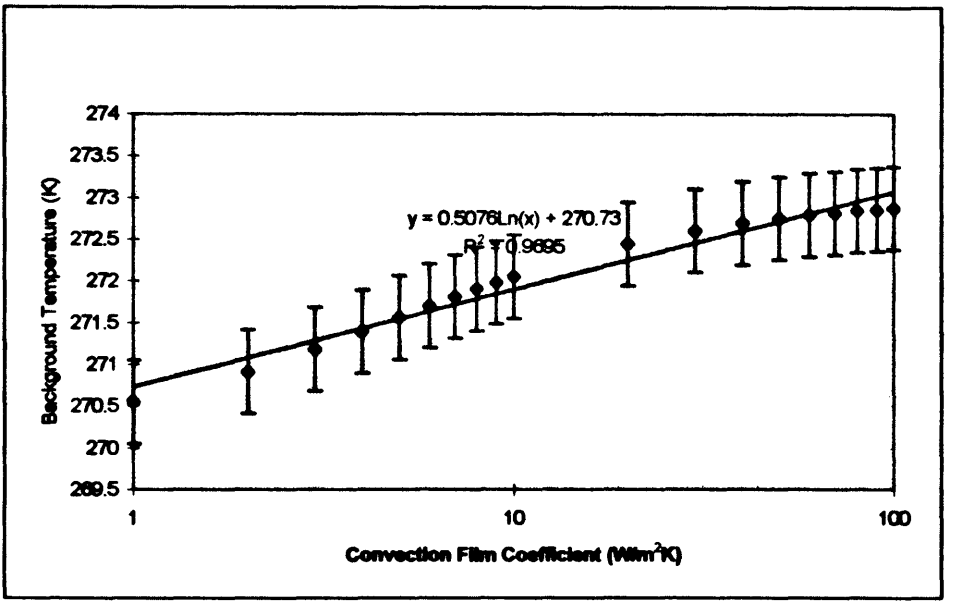


Figure 6.33 Relationship between the background temperature and the convection film coefficient. Note that the convection film coefficient axis is logarithmic.

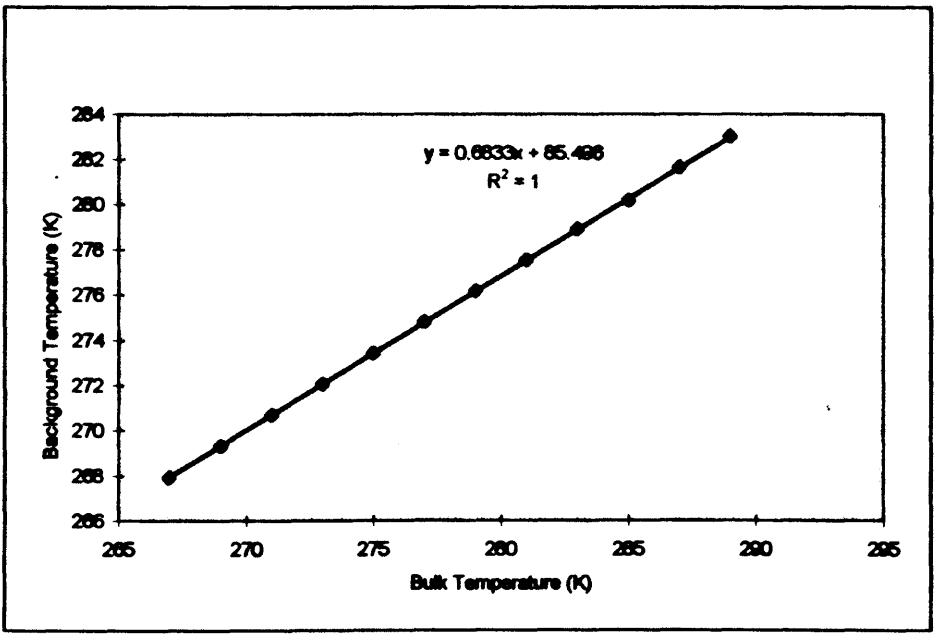


Figure 6.34 The relationship between the bulk temperature (i.e. atmospheric temperature) and the background temperature. Note the linear correlation.

Variations in the rock thermal conductivity across normal geological ranges (1-5 $Wm^{-1}K^{-1}$) were also investigated and found to have no effect on the background temperature.

From Figures 6.30 to 6.34 it can be seen that the two dominant factors were found to affect the background temperature, incident radiation (expressed via the space node temperature) and the mean atmospheric temperature (expressed as the bulk temperature). Both show strong positive linear correlations, with slopes of 0.3571 and 0.6833 respectively as shown in figures 6.32 and 6.34 respectively.

The 'controlling' coefficient of these two terms i.e. the convective heat transfer coefficient and the emissivity, showed much weaker influence on the surface temperature. At the standard ranges they both affected the background temperature by only a degree or two, negatively, in the case of the emissivity, due to increased radiative cooling, and positively in the case of the convection film coefficient.

SERIES 6.4.2 EMISSIVITY VARIATIONS

Model series 6.4.2 sets out to outline the effect of emissivity variations on the thermal anomaly size and temperature. Values used in the model series are listed in Table 6.13.

Parameter	Value	Unit
Thickness	10	m
Thot	1000	K
Bulk Temperature	273	K
Convection Film Coefficient	10	$Wm^{-2}K^{-1}$
Space Node Temperature	270	K
Initial Temperature	283	K
Rock Thermal Conductivity	2	$Wm^{-1}K^{-1}$
Emissivity	Varies	

Table 6.13 Series 6.4.2 Model Parameters

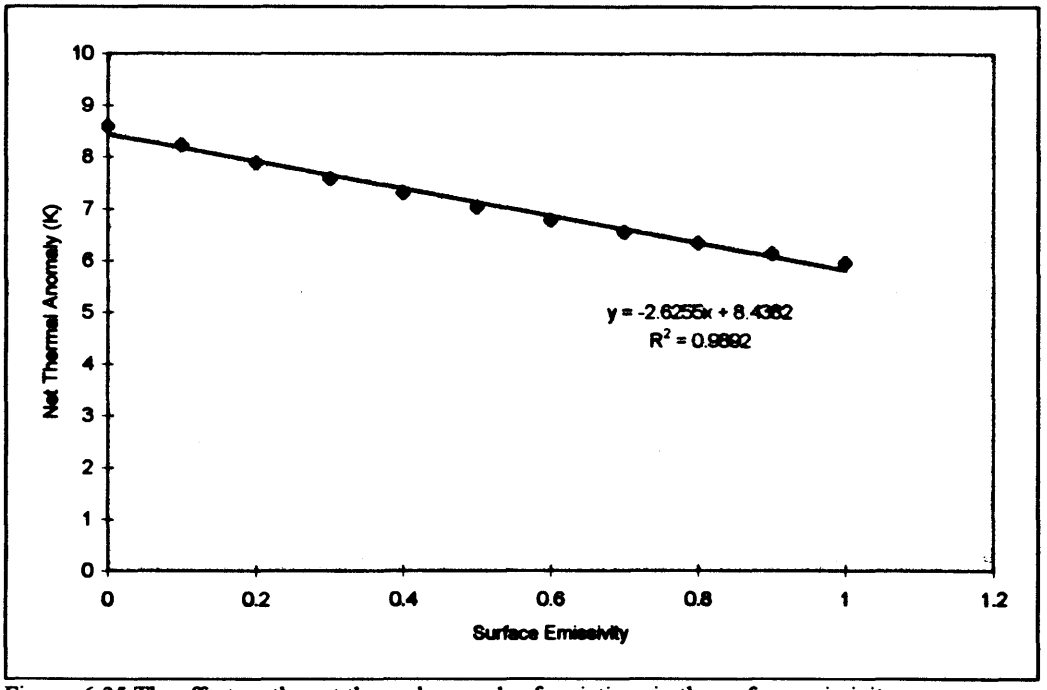


Figure 6.35 The effect on the net thermal anomaly of variations in the surface emissivity.

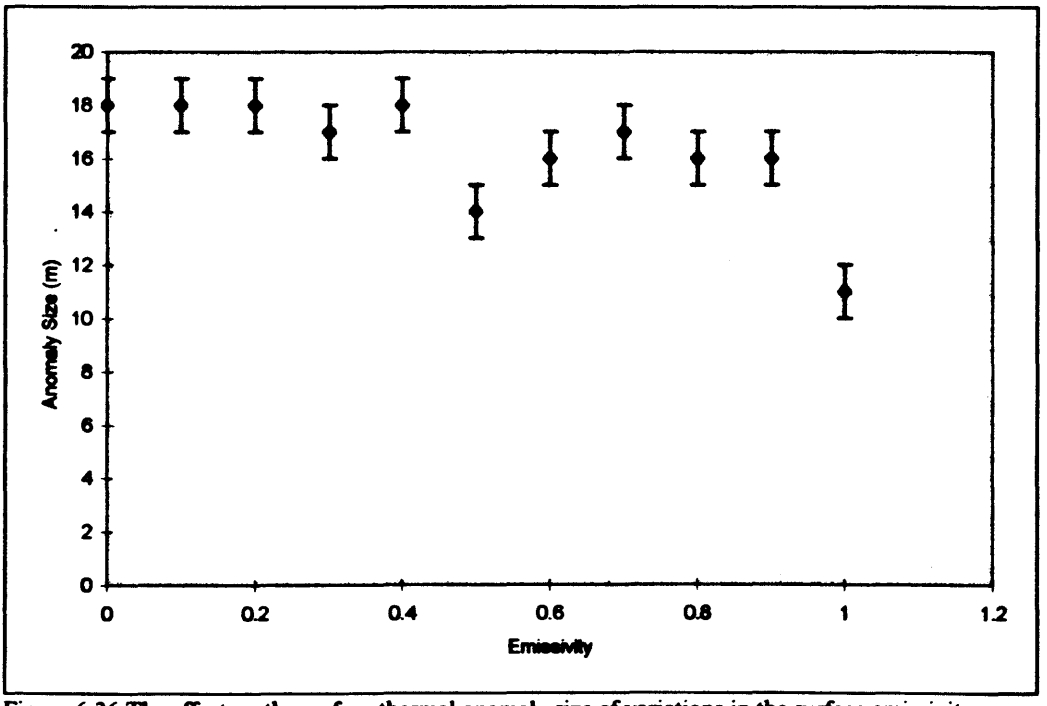


Figure 6.36 The effect on the surface thermal anomaly size of variations in the surface emissivity.

Figure 6.35 shows that the net thermal anomaly decays slightly as a function of emissivity, as would be expected. The range is however, quite small, as the

emissivity also increases radiative transfer from the 'cold' regions of the model, and thus cools the model uniformly.

The thermal anomaly size also seems to decay with increasing emissivity (see Figure 6.36), however it is a very weak trend.

Considering that the emissivity range of real geologic surfaces lies in the 0.9-1 range, it is unlikely that surface emissivity has a significant influence on the size and shape of thermal anomalies.

SERIES 6.4.3 INCIDENT RADIATION VARIATIONS

Series 6.4.3 sets out to identify the effect on the surface thermal anomaly of variations in the average incident radiation flux. To do this, the temperature of the space node, which is radiatively coupled with the surface, was varied (see *Chapter 5: An Introduction to Thermal Modelling using Ansys* for more information on the theory behind this procedure). The space node temperature was varied from 240-330K, corresponding with an incident radiation variation of 190-700Wm^{-2}. These are reasonable real-world values. Other parameters were held at values shown in Table 6.14.

Parameter	Value	Unit
Thickness	10	M
Thot	1000	K
Bulk Temperature	273	K
Convection Film Coefficient	10	$Wm^{-2}K^{-1}$
Space Node Temperature	240-330	K
Initial Temperature	283	K
Rock Thermal Conductivity	2	$Wm^{-1}K^{-1}$
Rock Density	2700	kgm^{-3}
Rock Specific Heat Capacity	800	$Jkg^{-3}K^{-1}$
Emissivity	1	

Table 6.14 Model series 6.4.3 Parameter values.

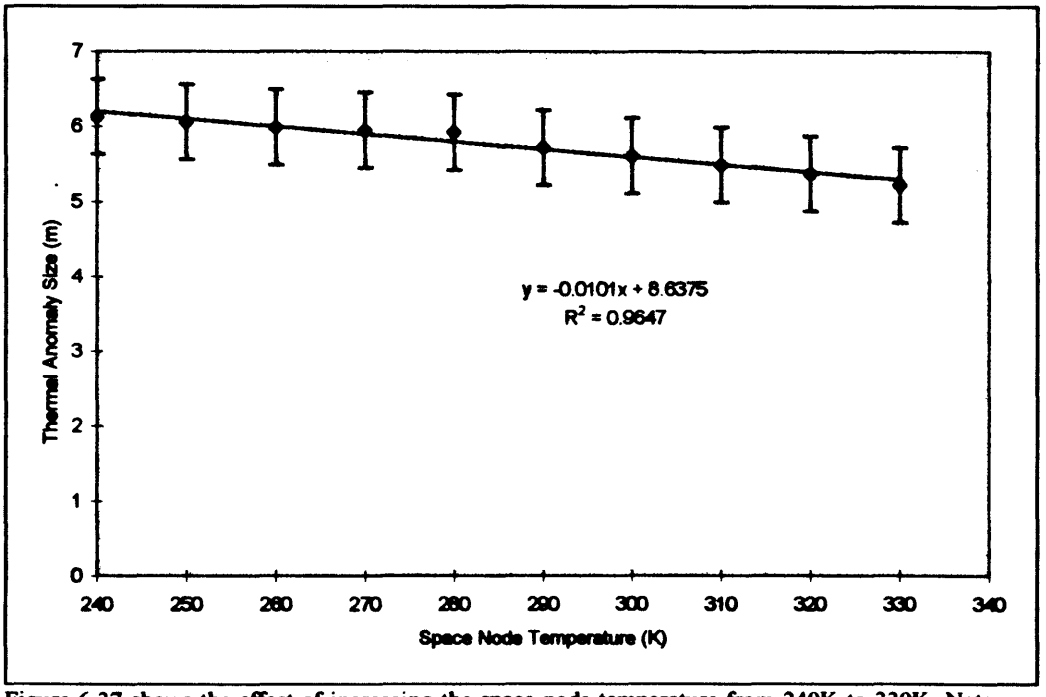


Figure 6.37 shows the effect of increasing the space node temperature from 240K to 330K. Note the steady decay of the thermal anomaly amplitude.

As can be seen from the results plotted in Figure 6.37, increasing the incident radiation flux has only a very slight negative effect on the net thermal anomaly and the thermal anomaly size. This is as would be expected, since increasing the incident radiation flux will tend to increase the temperature uniformly across the model surface. Note that the uncertainty range for the temperature is ±0.5K, thus the total trend of 1K lies well within the error bars. Variations were also noted in the thermal anomaly size, but they were only very slight, decreasing from 18m to 16m across the range of space node temperatures.

Thus variations in the space node temperature are not very significant to the thermal anomaly signature.

SERIES 6.4.4 CONVECTION FILM COEFFICIENT VARIATIONS

Series 6.4.4 sets out to quantify the effect of variations in the convection film coefficient on the thermal anomaly size and magnitude. For all model runs, the standard values were used as shown in Table 6.15. Results are shown in Figures 6.38 ad 6.39.

Parameter	Value	Unit
Thickness	10	m
Thot	1000	K
Bulk Temperature	273	K
Convection Film Coefficient	Varies	$Wm^{-2}K^{-1}$
Space Node Temperature	250	K
Initial Temperature	283	K
Rock Thermal Conductivity	2	$Wm^{-1}K^{-1}$
Rock Density	2700	kgm^{-3}
Rock Specific Heat Capacity	800	$Jkg^{-3}K^{-1}$
Emissivity	1	

Table 6.15 Parameter values for model series 6.4.4

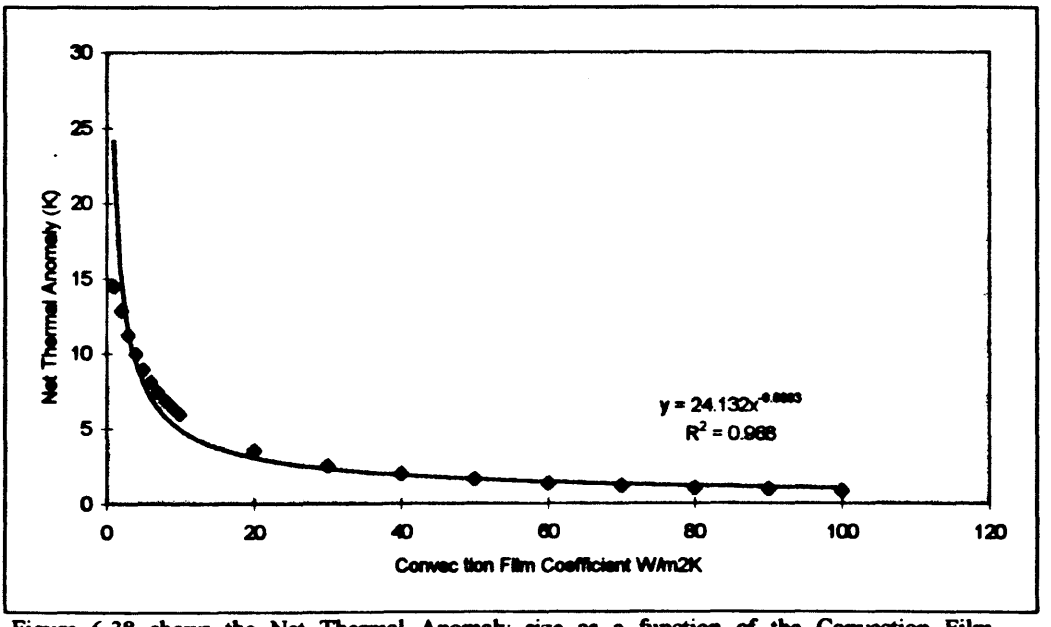


Figure 6.38 shows the Net Thermal Anomaly size as a function of the Convection Film Coefficient. Note how the thermal anomaly size decays toward zero.

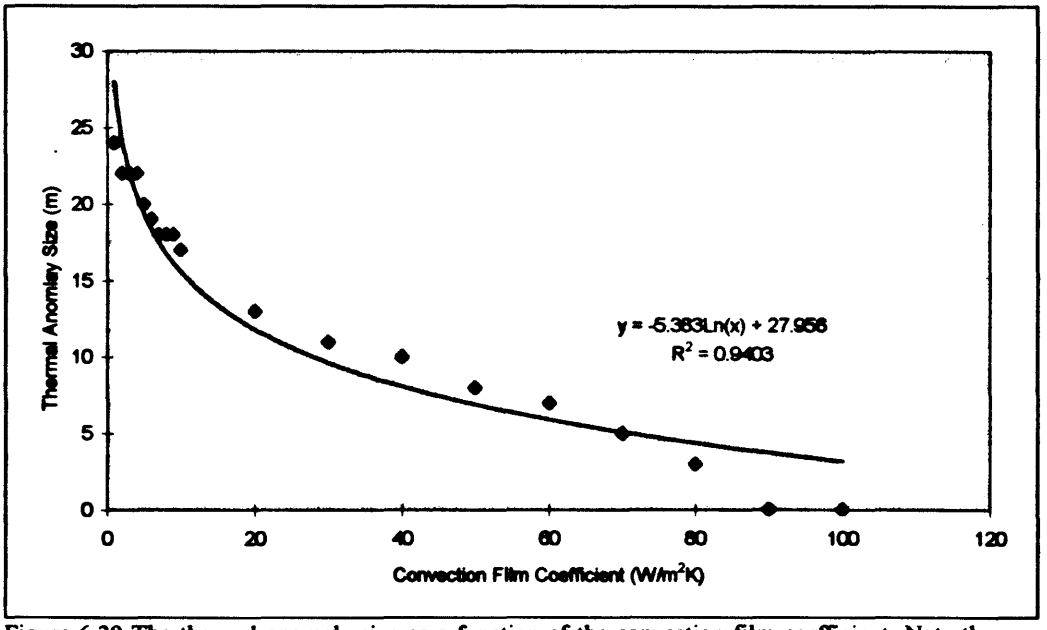


Figure 6.39 The thermal anomaly size as a function of the convection film coefficient. Note the steady reduction in the thermal anomaly size as the convection film coefficient increases.

The thermal anomaly size and net thermal anomaly show approximately inverse logarithmic or power law decay relationships respectively, with increasing convection film coefficient as can be seen in Figure 6.38 and 6.39. The magnitude of the temperature change is also quite extreme, showing that variations in the film coefficient due to wind etc. have the power to effectively disperse thermal signatures of geothermal anomalies. The trend in the thermal anomaly size (Figure 6.39) is less marked than for Net thermal anomaly (Figure 6.38), but clear inverse relationships can be seen. At high values of the convection film coefficient, the thermal anomaly size collapses.

SERIES 6.4.5 BULK TEMPERATURE VARIATIONS

Model Series 6.4.5 set outs to quantify the effect of variations in the bulk temperature (i.e. the mean atmospheric temperature), on the thermal anomaly size and magnitude. For all model runs, the standard values were used as shown in Table 6.16.

Parameter	Value	Unit
Thickness	10	m
Thot	1000	K
Bulk Temperature	Varies	K
Convection Film Coefficient	10	$Wm^{-2}K^{-1}$
Space Node Temperature	250	K
Initial Temperature	283	K
Rock Thermal Conductivity	2	$Wm^{-1}K^{-1}$
Rock Density	2700	kgm^{-3}
Rock Specific Heat Capacity	800	$Jkg^{-3}K^{-1}$
Emissivity	1	

Table 6.16 Model series 6.4.5 parameter values

Variations in the bulk temperature across reasonable terrestrial ranges (267-289K) showed no significant effect on the model. In both the case of the thermal anomaly size and the net thermal anomaly, the variations were less than the uncertainty ranges and showed no clear trend. Variations in the bulk temperature have no significant effect on the size or magnitude of the surface thermal anomaly due to a buried geothermal source.

SERIES 6.4.6 ROCK THERMAL CONDUCTIVITY VARIATIONS

Model series 6.4.6 sets out to quantify the effect of variations in the rock thermal conductivity on the thermal anomaly size and magnitude. For all model runs, the standard values were used as shown in Table 6.17

Parameter	Value	Unit
Thickness	10	m
Thot	1000	K
Bulk Temperature	273	K
Convection Film Coefficient	10	$Wm^{-2}K^{-1}$
Space Node Temperature	250	K
Initial Temperature	283	K
Rock Thermal Conductivity	1-5	$Wm^{-1}K^{-1}$
Rock Density	2700	kgm^{-3}
Rock Specific Heat Capacity	800	$Jkg^{-3}K^{-1}$
Emissivity	1	

Table 6.17 Model series 6.4.6 parameters.

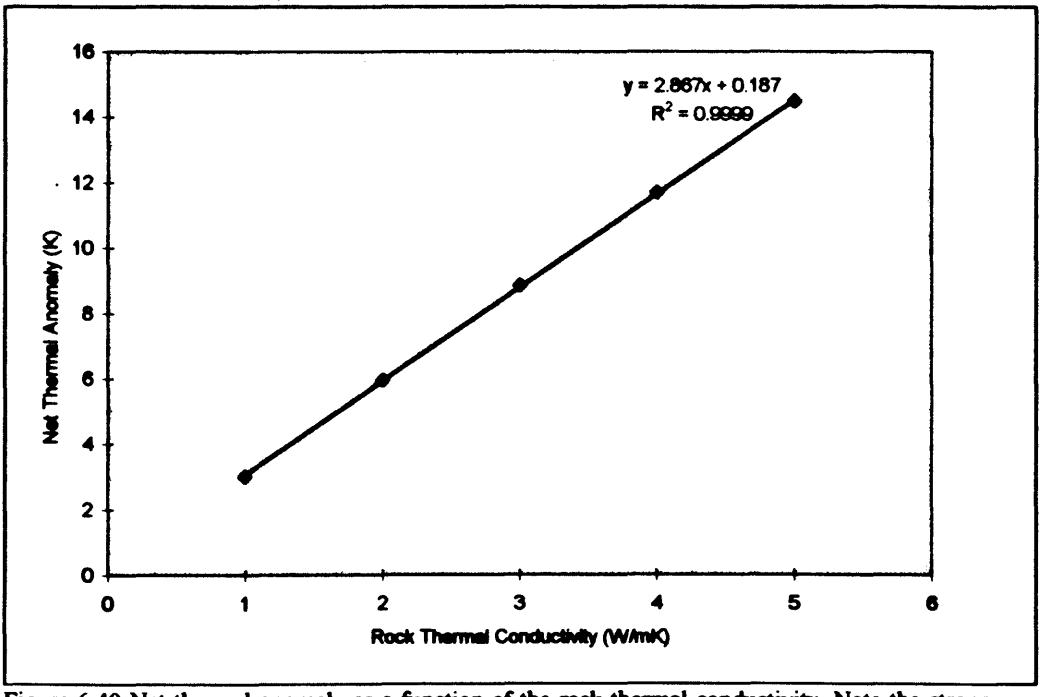


Figure 6.40 Net thermal anomaly as a function of the rock thermal conductivity. Note the strong linear correlation.

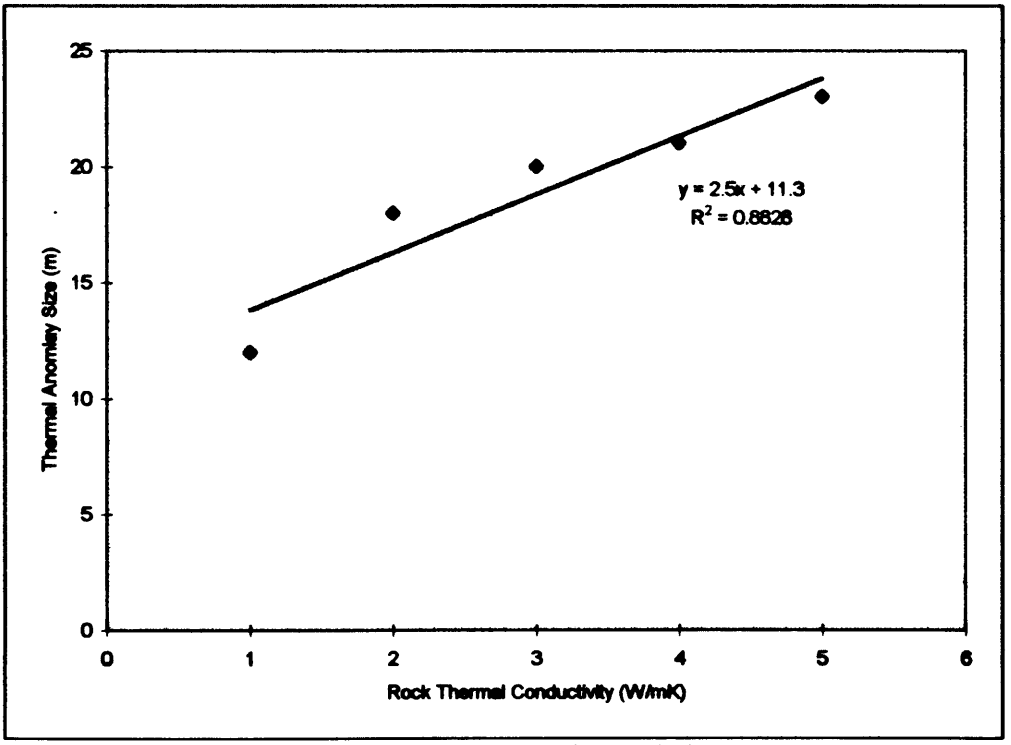


Figure 6.41 The thermal anomaly size as a function of the rock thermal conductivity. Note the strong linear correlation.

Some geological materials have temperature dependent thermal conductivities. For example, Basalt has a temperature dependant thermal conductivity controlled by its vesicularity. To investigate this effect the Bravo model was run using the temperature dependant values for basalt generated using equations 3.2, 3.3 and 3.4 and shown in Figure 3.1. All other parameters are held at the values shown in Table 6.17.

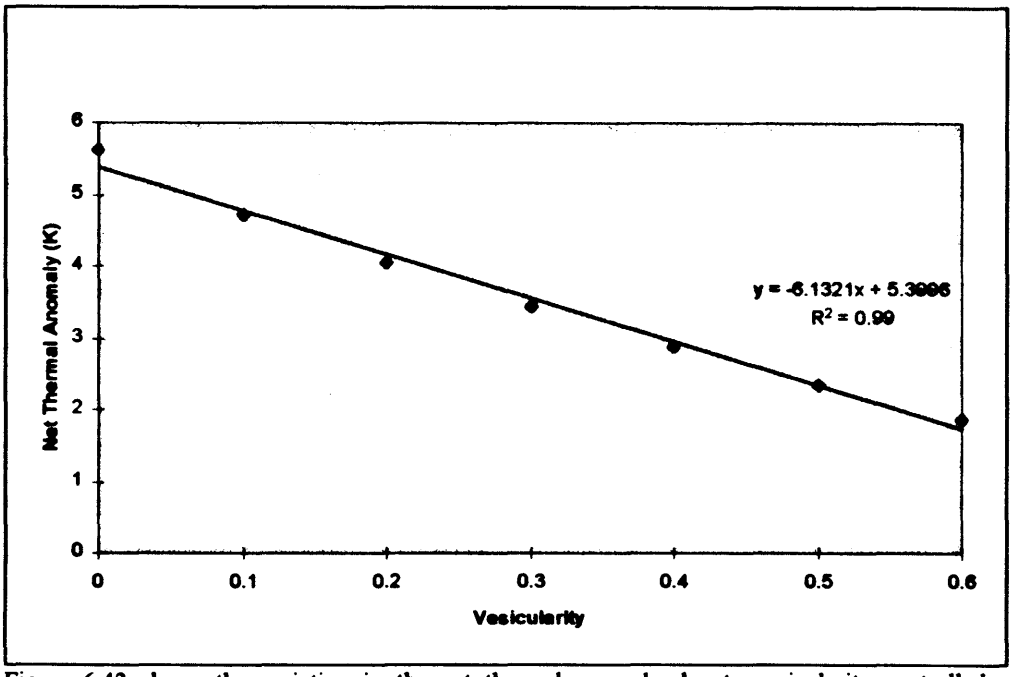


Figure 6.42 shows the variation in the net thermal anomaly due to vesicularity controlled, temperature dependant thermal conductivity. Note the strong decrease in the net thermal anomaly size as a function of increasing basalt vesicularity

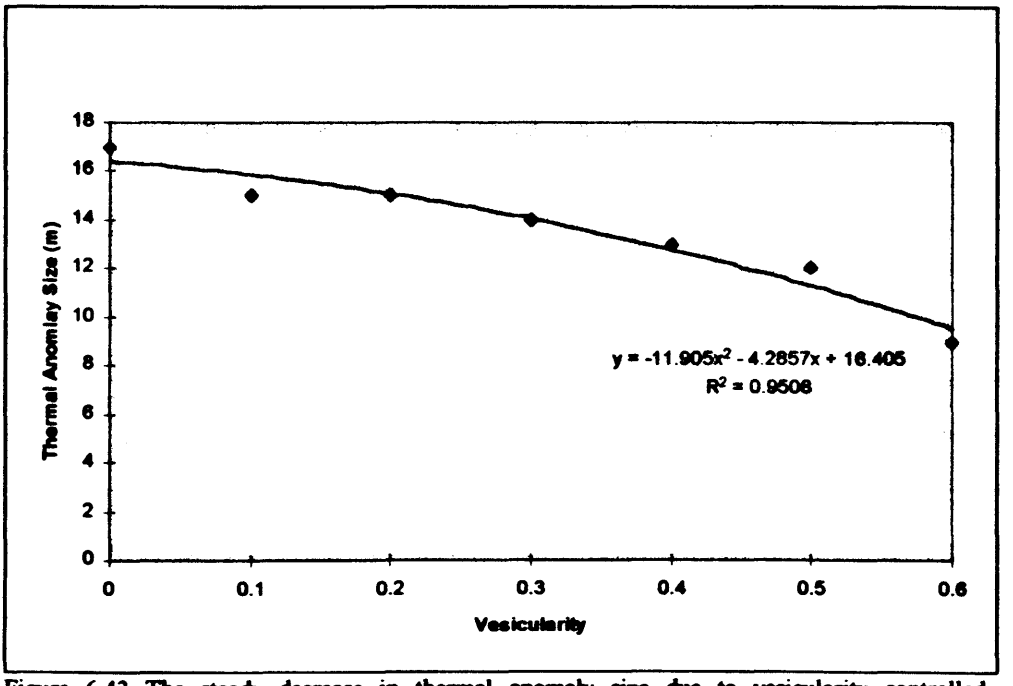


Figure 6.43 The steady decrease in thermal anomaly size due to vesicularity controlled, temperature dependent thermal conductivity.

The data shown in Figures 6.40 and 6.41 show strong positive linear correlations between the thermal anomaly size and magnitude and increasing rock thermal conductivity. It must also be noted that temperature dependent thermal conductivities, controlled by vesicularity in basalt, can play a significant role in the surface temperature distribution. It has not been demonstrated that the temperature dependence is of importance *per se*. A weighted average conductivity across the temperature range of the model may be just as adequate as a dynamic truly temperature dependant value. Considering that using the full temperature dependent values introduces no additional complexities or uncertainties to the model, whereas devising some kind of weighted average most certainly would, it is better to use the complete temperature dependant properties.

SERIES 6.4.7 SOURCE DEPTH VARIATIONS

The purpose of this series of model runs was to quantify the effect of variations in the source depth on the thermal anomaly size and magnitude. For all model runs, the standard values were used as shown in Table 6.18.

As with the equivalent model series in the Alpha model, extra care must be taken during meshing to ensure an accurate result. While the Bravo model has been designed to have an easily adjustable depth, the mesh must still be checked to ensure convergence and stability.

Parameter	Value	Unit
Thickness	1-100	m
Thot	1300	K
Bulk Temperature	273	K
Convection Film Coefficient	10	$Wm^{-2}K^{-1}$
Space Node Temperature	250	K
Initial Temperature	283	K
Rock Thermal Conductivity	2	$Wm^{-1}K^{-1}$
Rock Density	2700	kgm^{-3}
Rock Specific Heat Capacity	800	$Jkg^{-3}K^{-1}$
Emissivity	1	

Table 6.18 Model series 6.4.7 parameter values.

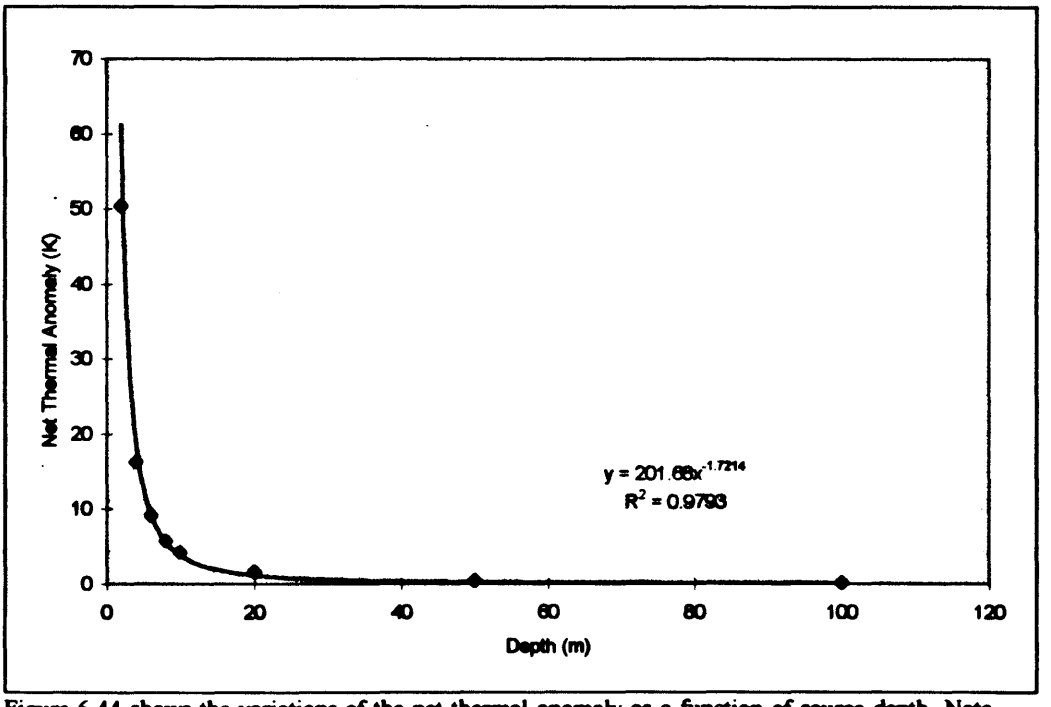


Figure 6.44 shows the variations of the net thermal anomaly as a function of source depth. Note the inverse power relationship between the two variables.

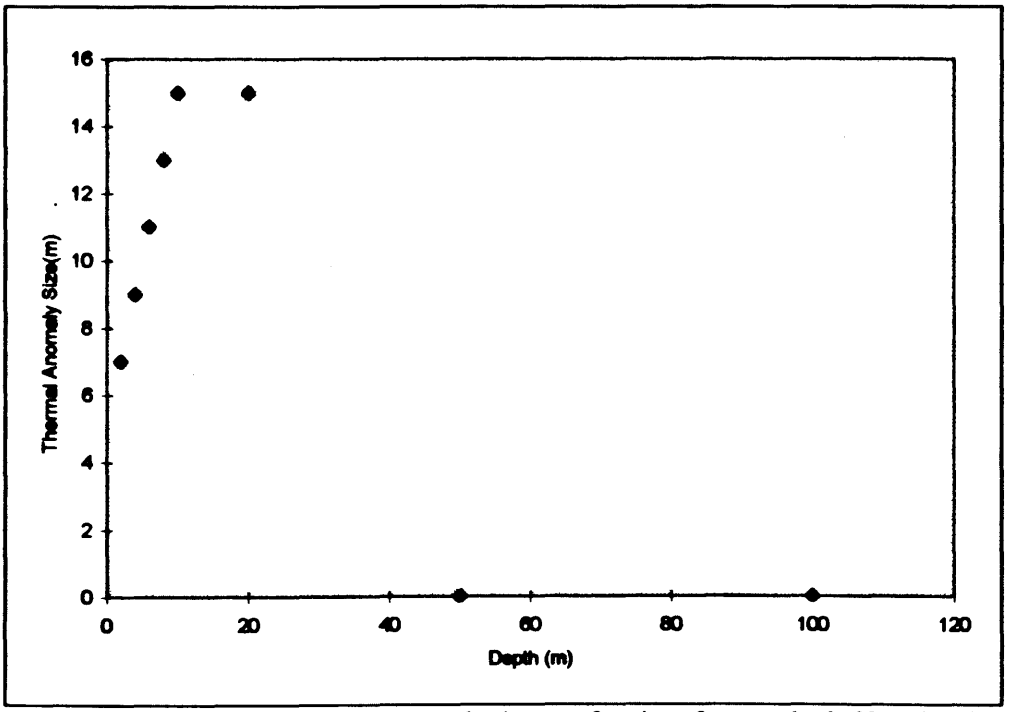


Figure 6.45 Variations of the thermal anomaly size as a function of source depth. Note that the anomaly size increases linearly as a function of depth, and then tops out and collapses as the peak temperature decays to background levels. The same effect is seen in Series 6.2.8, in Figure 6.20

The net thermal anomaly decays rapidly as the source depth increases as shown in Figure 6.44. The thermal anomaly size increases steadily until the net thermal anomaly drops below 1, at which point it disappears, as shown in Figure 6.45. Note the strong similarities with the results in the analogous Alpha model series 6.2.8. This indicates that under the conditions investigated heat sources at depth of greater than approximately 20m will be very difficult to detect at the surface by means of a thermal infrared image.

SERIES 6.4.8 SOURCE TEMPERATURE VARIATIONS

Model series 6.4.8 sets out to quantify the effect of variations in the source temperature on the thermal anomaly size and magnitude. For all model runs, the standard values were used as shown in Table 6.19:

Parameter	Value	Unit
Thickness	10	m
Thot	100-1300	K
Bulk Temperature	273	K
Convection Film Coefficient	10	$Wm^{-2}K^{-1}$
Space Node Temperature	250	K
Initial Temperature	283	K
Rock Thermal Conductivity	2	$Wm^{-1}K^{-1}$
Rock Density	2700	kgm^{-3}
Rock Specific Heat Capacity	800	$Jkg^{-3}K^{-1}$
Emissivity	1	

Table 6.19 shows model series 6.4.8 parameters.

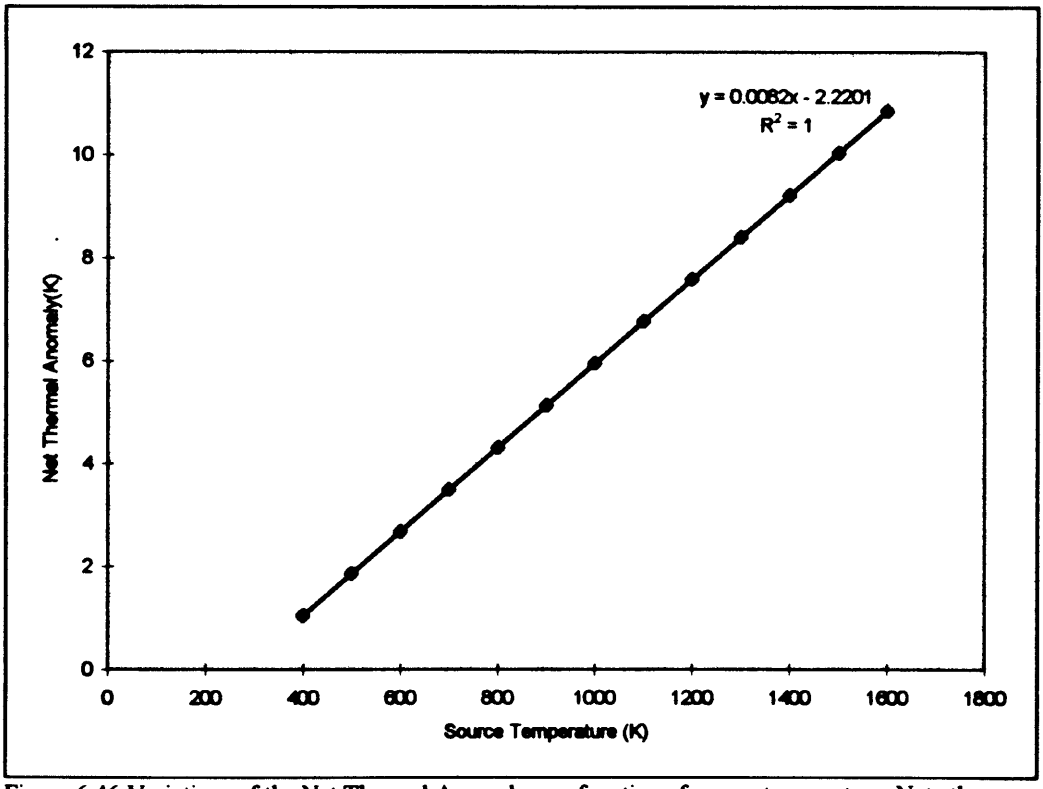


Figure 6.46 Variations of the Net Thermal Anomaly as a function of source temperature. Note the positive linear correlation.

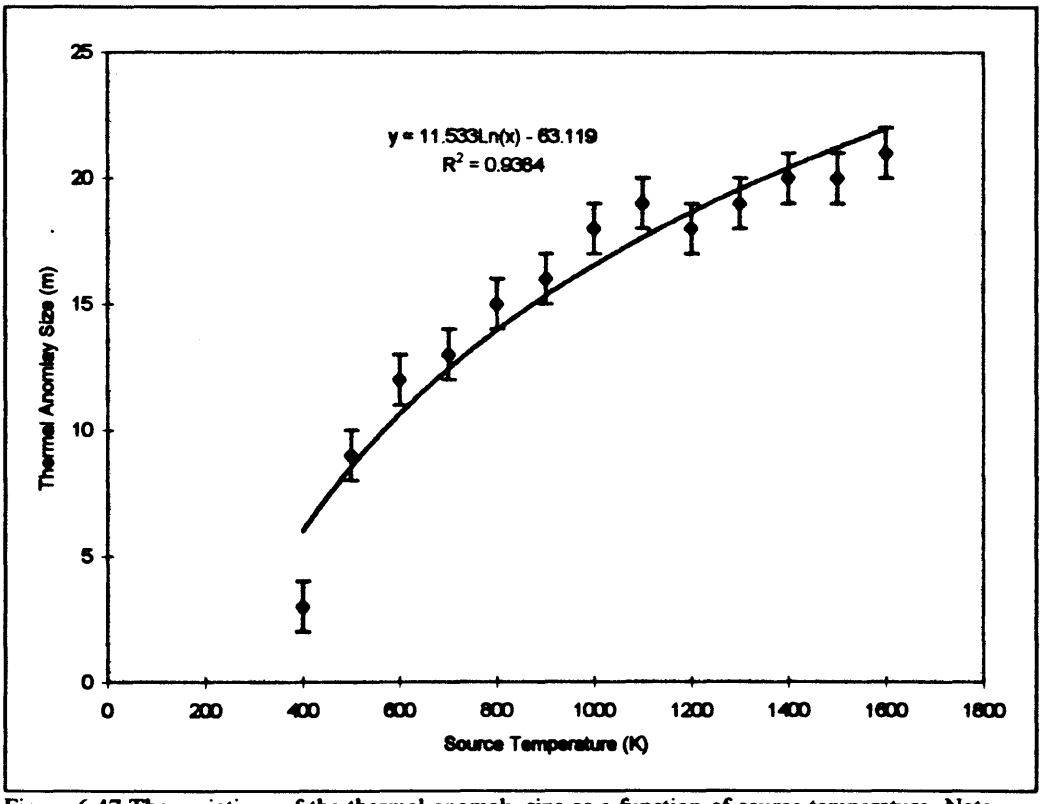


Figure 6.47 The variations of the thermal anomaly size as a function of source temperature. Note the moderate logarithmic correlation.

The net thermal anomaly is strongly linearly correlated with the source temperature. A weaker, logarithmic correlation exists between the thermal anomaly size and the source temperature.

SERIES 6.4.9 CONVECTIVE HEAT TRANSFER

The purpose of this study was to quantify the effect of convective heat transfer in the pore spaces of the material on the size and magnitude of the surface thermal anomaly. The Ansys finite element modelling system is not capable of modelling convective heat transfer in porous media directly. However, since convective heat transfer should occur predominantly in the vertical direction, convection can be modelling by applying a larger thermal conductivity in the vertical direction, i.e.

$$K_{vertical} = CK_{iso} \qquad 6.8$$

Where:

$K_{vertical}$ Effective thermal conductivity in the vertical direction ($Wm^{-1}K^{-1}$)

C Multiplier

K_{iso} Thermal conductivity in the horizontal direction ($Wm^{-1}K^{-1}$)

The constant of proportionality (C) is varied from 1 to 5 depending on the degree of convective heat transfer in the system. For a given system, the actual value can be approximated using the equations in Section 3.1.10 All other parameter are held at the standard model values (see 6.20)

Parameter	Value	Unit
Thickness	10	m
Thot	1300	K
Bulk Temperature	273	K
Convection Film Coefficient	10	$Wm^{-2}K^{-1}$
Space Node Temperature	270	K
Initial Temperature	283	K
Rock Thermal Conductivity	2	$Wm^{-1}K^{-1}$
Emissivity	1	

Table 6.20 Model Parameter values for series 6.4.9

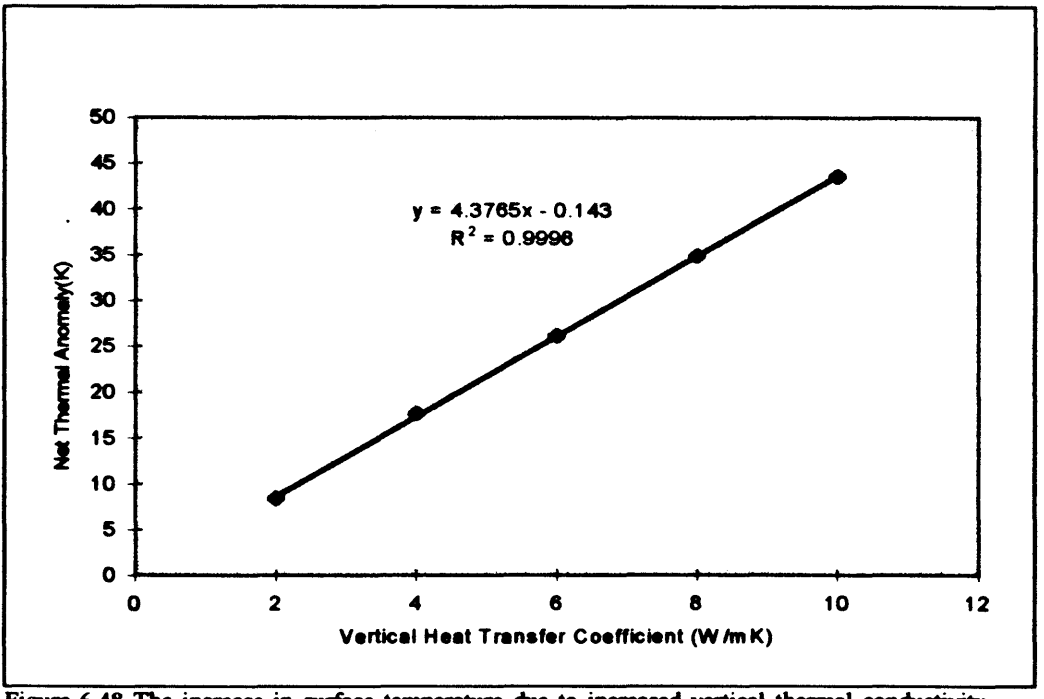


Figure 6.48 The increase in surface temperature due to increased vertical thermal conductivity. Note that the thermal anomaly size increases linearly with increasing vertical thermal conductivity, as would be expected.

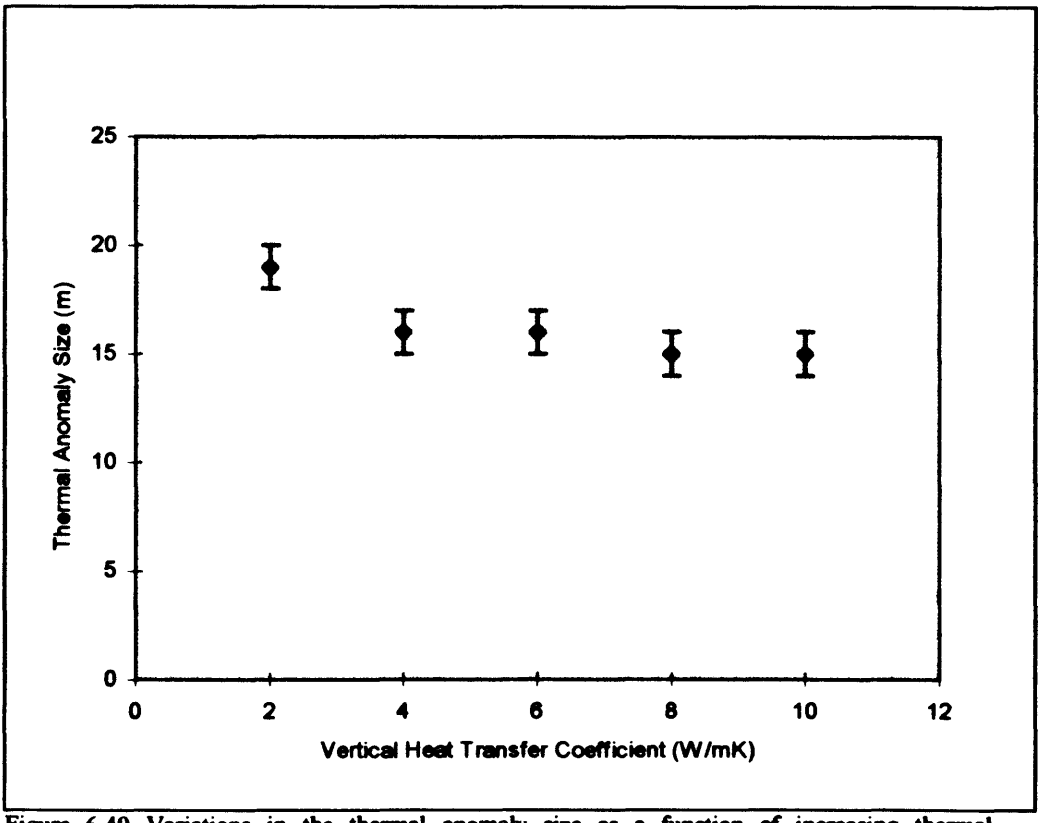


Figure 6.49 Variations in the thermal anomaly size as a function of increasing thermal conductivity.

The net thermal anomaly can be seen to increase steadily with increasing vertical thermal conductivity in the results plotted in Figure 6.48, as would be expected. The thermal anomaly size decreases slightly (see Figure 6.49) as the vertical thermal conductivity increases. This is probably due to the fact that with more efficient vertical heat transfer in the central zone, less heat is available to warm the flanks of the anomaly. The overall effect of increased vertical thermal conductivity due to convective processes is to 'sharpen and tighten' the thermal anomaly signature.

SERIES 6.4.9 TUBE GEOMETRY VARIATIONS

The purpose of series 6.4.9 was to quantify the effect of variations in the lava tube geometry on the size and magnitude of the surface thermal anomaly. All other parameter are held at the standard model values as shown in Table 6.20.

Three model subsets with different geometry's were investigated:

(i) Circle: Using a circular heat source where the dimension varied is the radius of the source.

(ii) Square: Using a square heat source where the dimension varied is the length of side.

(iii) Square: Using a rectilinear heat source 1m high and where the dimension varied is width.

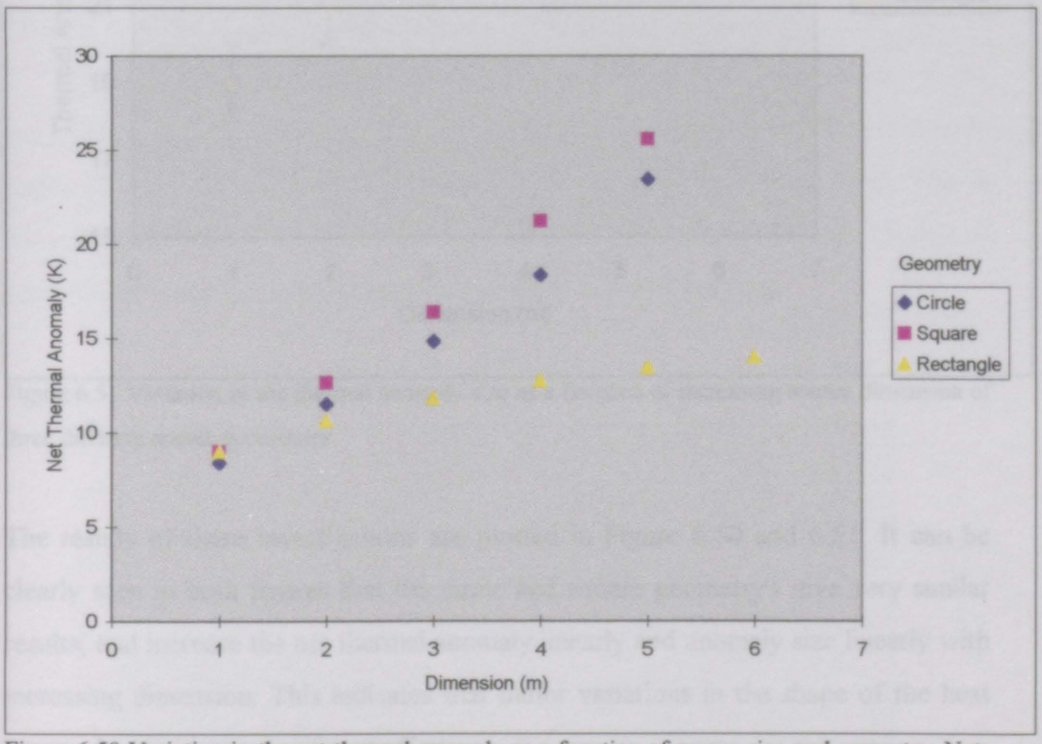


Figure 6.50 Variation in the net thermal anomaly as a function of source size and geometry. Note the increases in the net thermal anomaly size as a function of increasing the principle dimensions of different geometries.

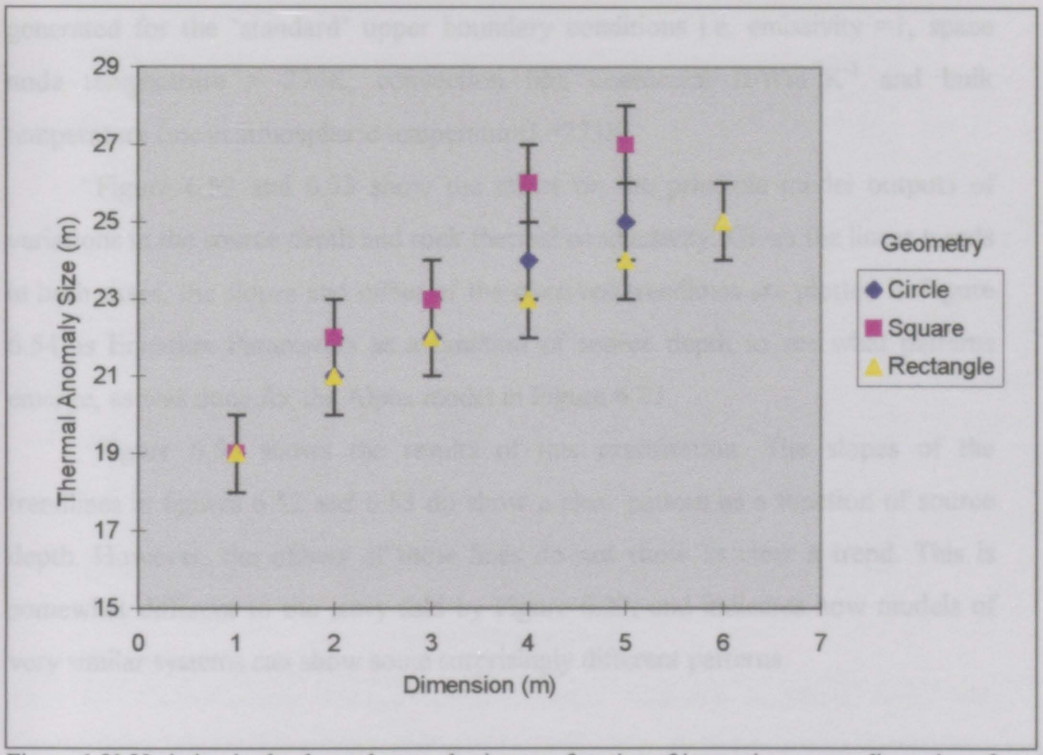


Figure 6.51 Variation in the thermal anomaly size as a function of increasing source dimension of three different source geometries.

The results of these investigations are plotted in Figure 6.50 and 6.51. It can be clearly seen in both figures that the circle and square geometry's give very similar results, and increase the net thermal anomaly linearly and anomaly size linearly with increasing dimension. This indicates that minor variations in the shape of the heat source do not have a significant effect.

The rectangular geometry increases the peak temperature asymptotically as the rectangle enlarges. This is not surprising, as for a sufficiently large rectangle one would expect to see a uniform temperature over most of the source and a tapering 'edge effect' at the sides. The rectangular series increases the anomaly size linearly i.e. a 1m increase in the rectangle width produces a 1m increase in the anomaly size, as might be expected.

SERIES 6.4.10 VARIATION OF MULTIPLE PARAMETERS

As with the Alpha model, variations in the geological thermal properties can be plotted and empirical relationships for a given series of surface boundary conditions can be generated. Figures 6.52 to 6.59, which demonstrate this and are all

generated for the 'standard' upper boundary conditions i.e. emissivity =1, space node temperature = 270K, convection film coefficient=10$Wm^{-2}K^{-1}$ and bulk temperature (mean atmospheric temperature) =273K.

Figure 6.52 and 6.53 show the effect on the principle model outputs of variations in the source depth and rock thermal conductivity. Given the linear trends in both cases, the slopes and offset of the observed trendlines are plotted in Figure 6.54 as Equation Parameters as a function of source depth to see what patterns emerge, as was done for the Alpha model in Figure 6.23.

Figure 6.54 shows the results of this examination. The slopes of the trendlines in figures 6.52 and 6.53 do show a clear pattern as a function of source depth. However, the offsets of these lines do not show as clear a trend. This is somewhat different to the story told by Figure 6.23, and indicates how models of very similar systems can show some surprisingly different patterns.

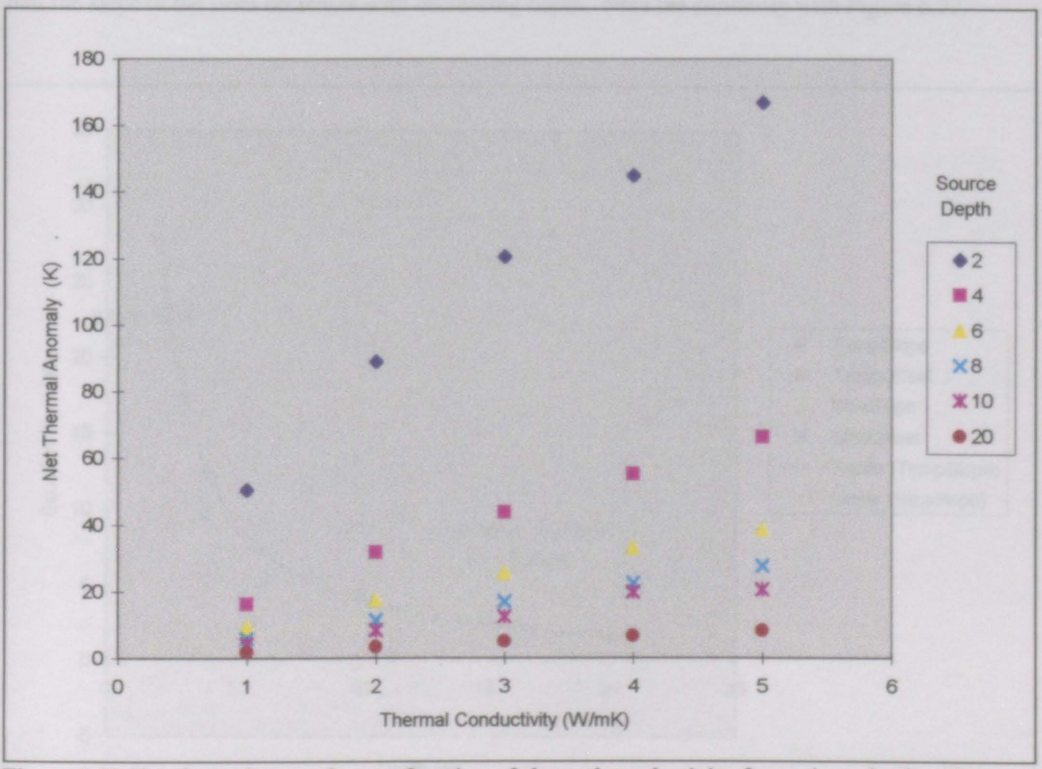


Figure 6.52 Net thermal anomaly as a function of thermal conductivity for various depths. Note that the slope of the lines increases for decreasing depth. Note the similarity with Figure 6.21.

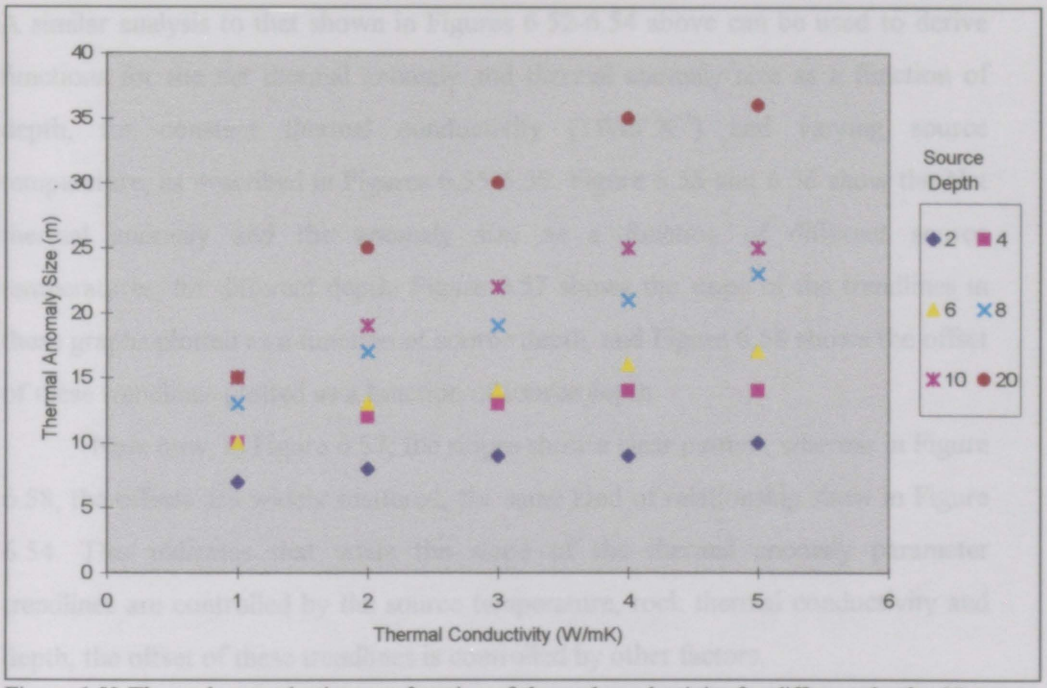


Figure 6.53 Thermal anomaly size as a function of thermal conductivity for different depths. Note that the slope of the lines decreases with decreasing depth. Note the similarity with Figure 6.22.

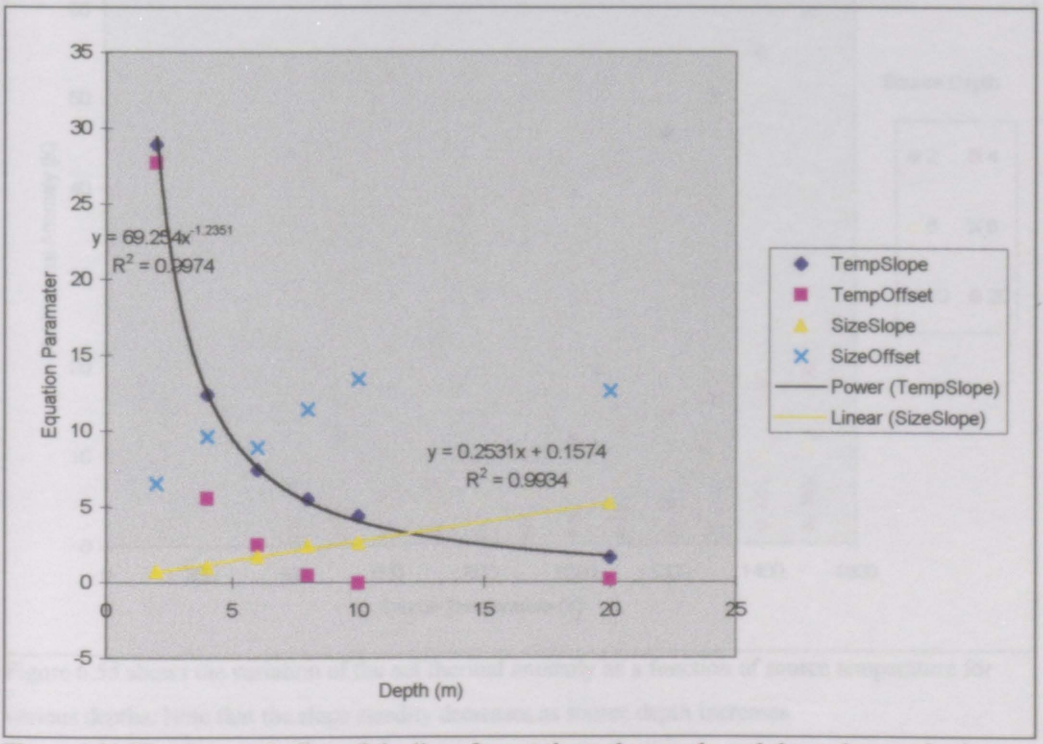


Figure 6.54 The slope and offset of the lines for net thermal anomaly and thermal anomaly size plotted as a function of thermal conductivity. Offsets do not show as clear a pattern as the slopes, and no approximating functions are included for them. Note the similarities between Figure 6.48 and its equivalents for the Alpha model (Figure 6.23).

A similar analysis to that shown in Figures 6.52-6.54 above can be used to derive functions for the net thermal anomaly and thermal anomaly size as a function of depth, for constant thermal conductivity ($1Wm^{-1}K^{-1}$) and varying source temperature, as described in Figures 6.55-6.58. Figure 6.55 and 6.56 show the Net thermal anomaly and the anomaly size as a function of different source temperatures, for different depth. Figure 6.57 shows the slope of the trendlines in these graphs plotted as a function of source depth, and Figure 6.58 shows the offset of these trendlines plotted as a function of source depth.

Note how, in Figure 6.57, the slopes show a clear pattern, whereas in Figure 6.58, the offsets are widely scattered, the same kind of relationship show in Figure 6.54. This indicates that while the slope of the thermal anomaly parameter trendlines are controlled by the source temperature, rock thermal conductivity and depth, the offset of these trendlines is controlled by other factors.

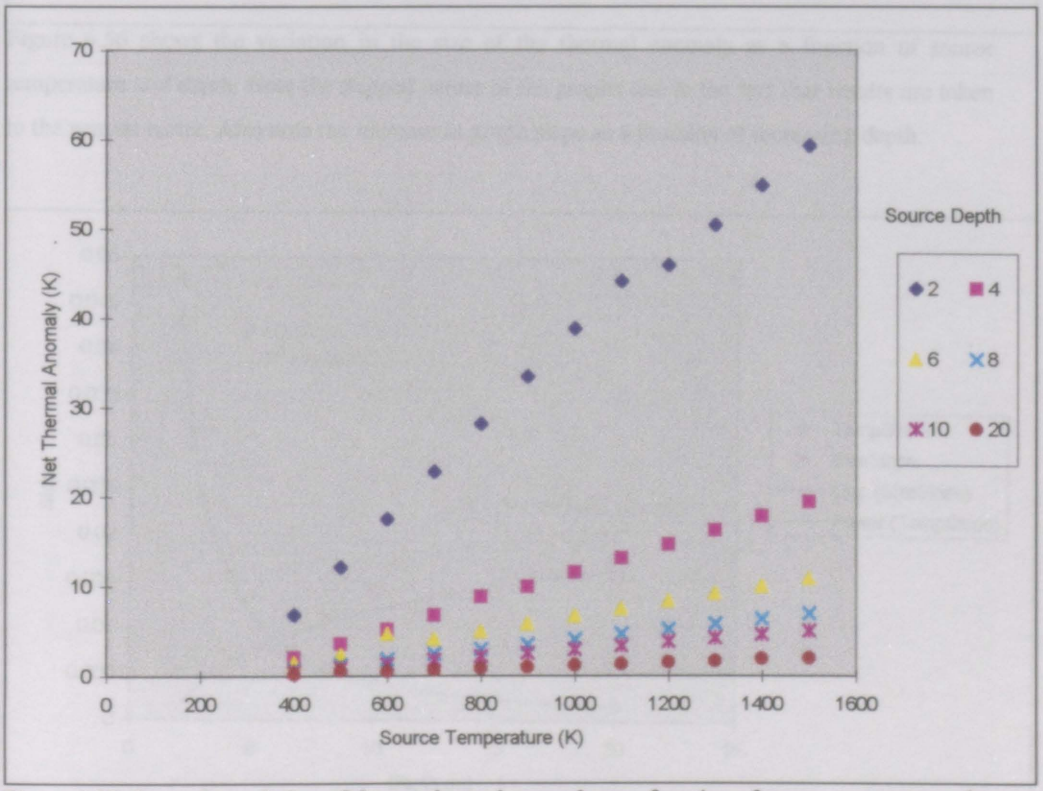


Figure 6.55 shows the variation of the net thermal anomaly as a function of source temperature for various depths. Note that the slope steadily decreases as source depth increases.

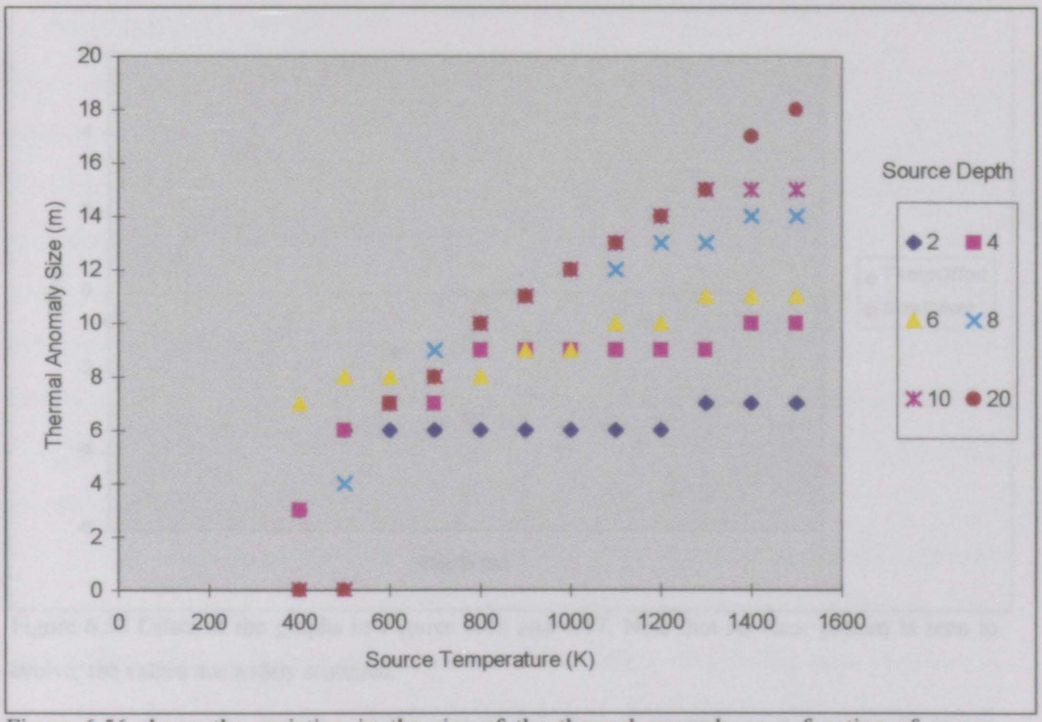


Figure 6.56 shows the variation in the size of the thermal anomaly as a function of source temperature and depth. Note the stepped nature of the graphs due to the fact that results are taken to the nearest metre. Also note the increase in graph slope as a function of increasing depth.

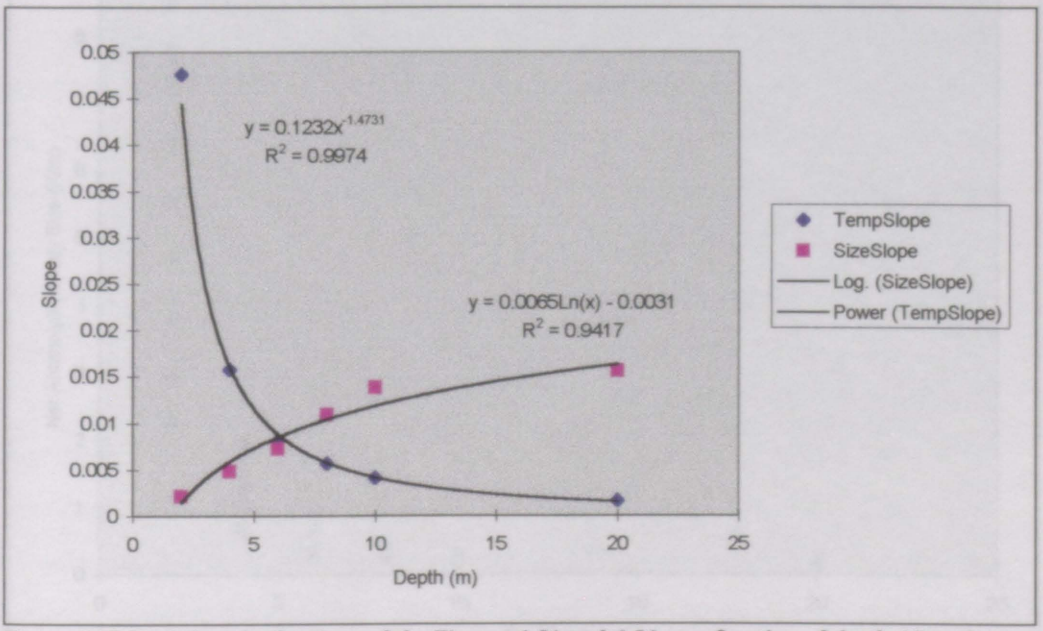


Figure 6.57 Variations in the slope of the Figures 6.54 and 6.56 as a function of depth. Note the inverse power and logarithmic approximating functions.

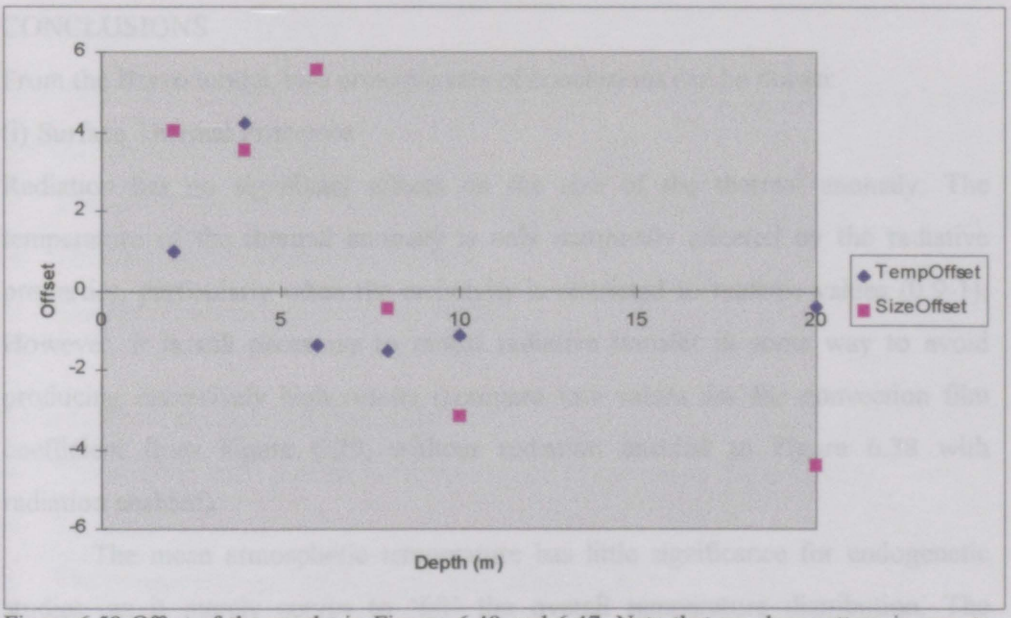


Figure 6.58 Offset of the graphs in Figures 6.48 and 6.47. Note that no clear pattern is seen to evolve, the values are widely scattered.

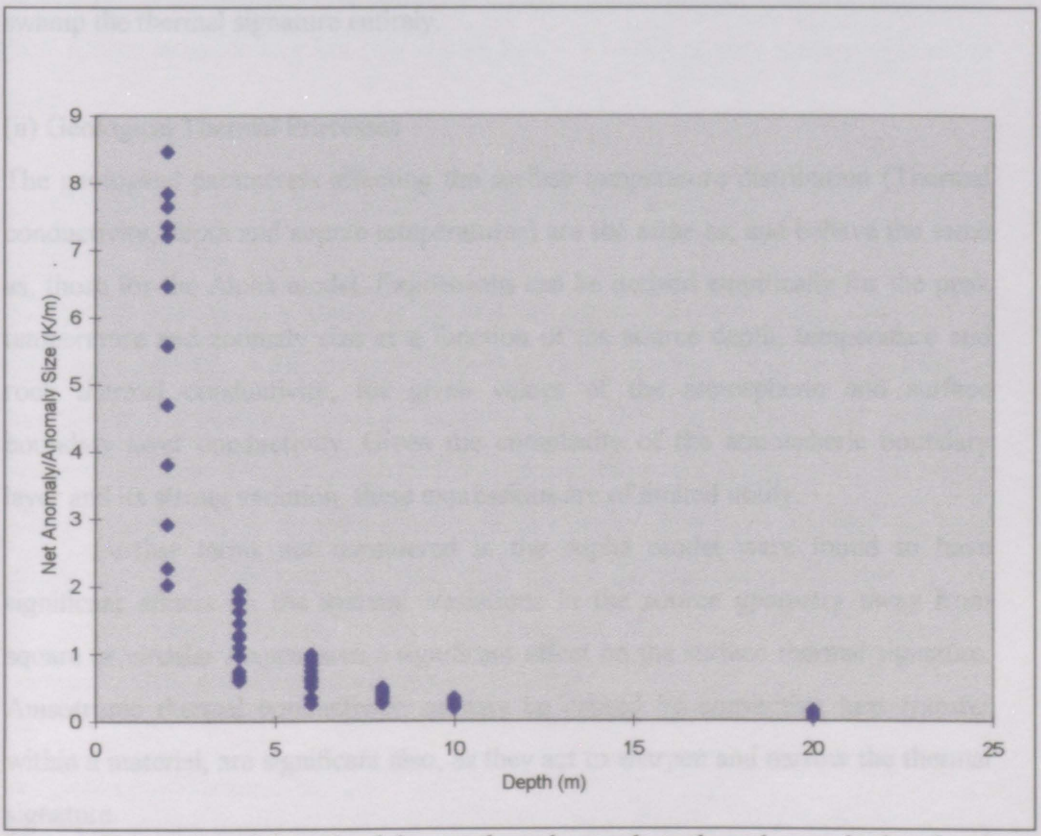


Figure 6.59 Variation of the ratio of the net thermal anomaly to thermal anomaly size plotted against the depth.

CONCLUSIONS

From the Bravo model, two principle sets of conclusions can be drawn:

(i) Surface Thermal Processes

Radiation has no significant effects on the size of the thermal anomaly. The temperature of the thermal anomaly is only marginally affected by the radiative properties, particularly when the emissivity is restricted to realistic values (0.9-1). However, it is still necessary to model radiative transfer in some way to avoid producing excessively high results (compare low values for the convection film coefficient from Figure 6.29, without radiation enabled to Figure 6.38 with radiation enabled).

The mean atmospheric temperature has little significance for endogenetic studies, as it merely serves to 'lift' the overall temperature distribution. The convection film coefficient, which describes the effect of sensible heat transfer, is however a dominant factor in the magnitude of the thermal anomaly, and can act to swamp the thermal signature entirely.

(ii) Geological Thermal Processes

The geological parameters affecting the surface temperature distribution (Thermal conductivity, depth and source temperatures) are the same as, and behave the same as, those for the Alpha model. Expressions can be derived empirically for the peak temperature and anomaly size as a function of the source depth, temperature and rock thermal conductivity, for given values of the atmospheric and surface boundary layer conductivity. Given the complexity of the atmospheric boundary layer and its strong variation, these expressions are of limited utility.

Further terms not considered in the Alpha model were found to have significant affects on the system. Variations in the source geometry away from square or circular shapes have a significant effect on the surface thermal signature. Anisotropic thermal conductivity, as may be caused by convective heat transfer within a material, are significant also, as they act to sharpen and narrow the thermal signature.

6.5 CONCLUSIONS

The important variables in determining the surface thermal signature of a buried geothermal heat source are:

- The nature of the heat source, its depth, shape and temperature.
- The thermal conductivity of the rock
- The sensible heat transfer at the surface

Other parameters have negligible effects:

- The incident solar radiation (expresses as a Space Node Temperature)
- The emissivity
- The density and specific heat capacity of the rock

The results of the finite element models in this chapter boil down to one conclusion, to display an unambiguous temperature change at the surface, a buried geothermal heat source must be very hot (e.g. active lava ~ 1300K) or very shallow (<20m) or both.

COMPARISON BETWEEN ALPHA AND BRAVO MODELS

(i) Surface Thermal Factors

Surface thermal factors affecting the models are not directly comparable due to differing modelling methodologies. However, by inspection it can be seen that the models are generating similar curves, offset by the $5.4 Wm^{-1}K^{-1}$ radiation linearisation term which is integrated into the Alpha model Atmospheric Boundary Layer conductivity to simulate radiative heat transfer. The more detailed approach of the Bravo model is more useful, as it allows the significant variables i.e. the convection film coefficient, representing sensible heat transfer, to be identified separately and easily incorporated into the model.

(ii) Geological Thermal Factors

The Alpha and Bravo models do not differ significantly in their handling of geological heat transfer, or in the variables applied. They thus generate results which are in good agreement with each other.

(iii) Practical Considerations

For relatively simple models with small increases in surface temperature, the Alpha model generates adequate results and the additional processing time required by the Bravo model is not justified by the complexity of the problem. For practical application, however, a number of other factors must be considered:

- The simplification of the upper boundary condition and linearisation of radiation in the Alpha model means that care must be taken to ensure that the peak temperature does not rise to a level where the underlying assumptions of the linearisation will break down. The linearisation also means that real surface parameters such as the emissivity and sensible heat transfer coefficient cannot be directly inputted into the Alpha model.
- Improved model scripting and automation in the Bravo model means that, although more computationally intensive, it is on the whole much faster to use for generating large quantities of results. In any event, the computation time for both models, for a given run is less than two minutes on a 133Mhz Windows machine.

The Bravo model, utilising as it does a non-linear analysis for radiation, is more readily adaptable to transient cases. On balance therefore, while the Alpha model is adequate, the Bravo model is superior to it in several important ways.

APPLICATIONS

It is possible to model a simulated surface thermal distribution of a well-defined heat source, by 'stacking' two-dimensional profiles to produce a virtual temperature distribution. Figure 6.60 shows an example of the surface temperature for a well-defined linear heat source (at source temperature 1400K) such as a lava tube. The source begins at 10m depth, and varies along its length as described in Table 6.21.

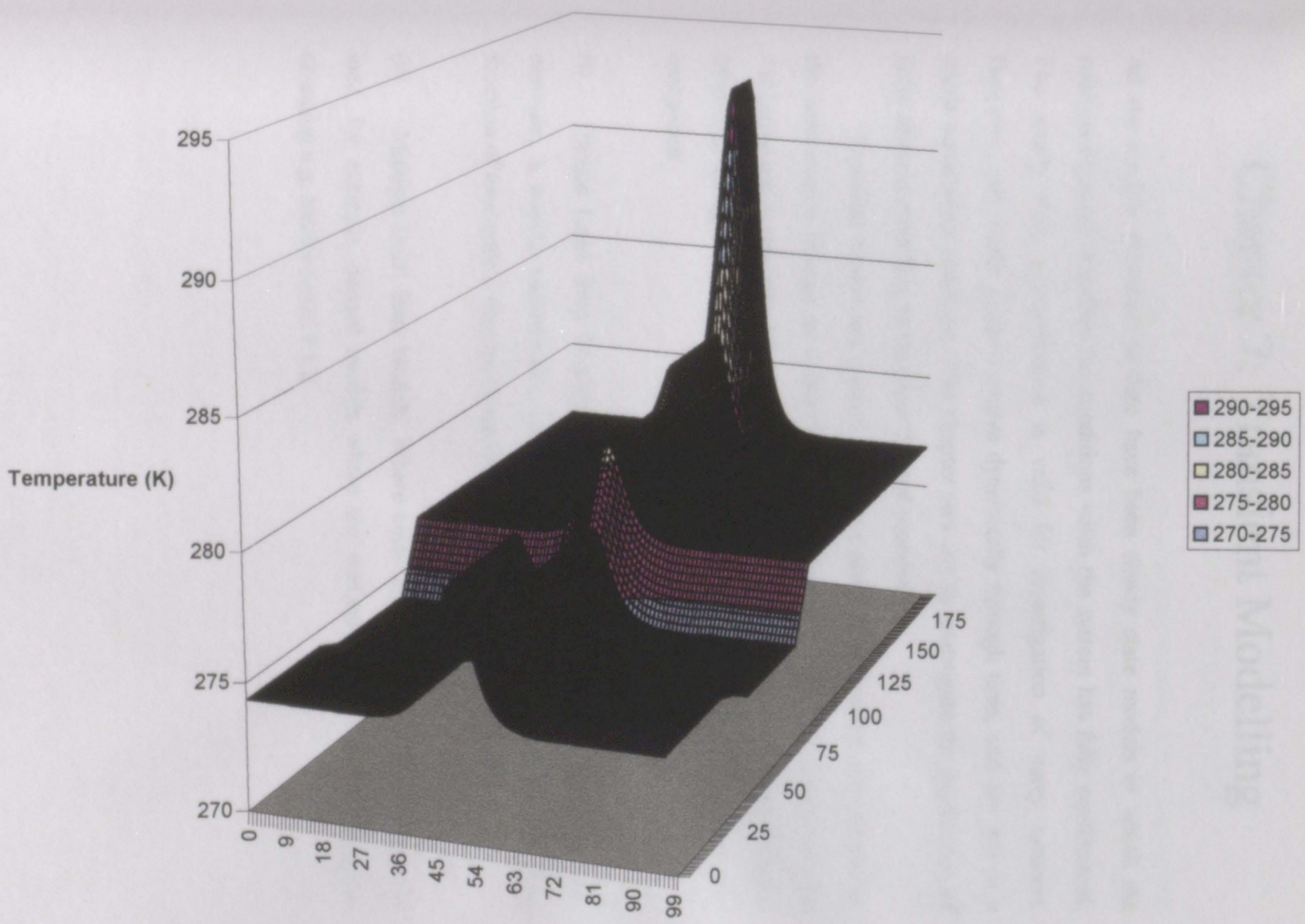
Inspection of Figure 6.60 and its variations illustrates the findings of this chapter. The first four variations all led to fairly minor changes in the thermal anomaly size. Changes in surface properties, while raising or lowering the profile, did not change the net amplitude. By far the largest increase was due to shallowing

of the heat source, which resulted in a large increase in source amplitude. This illustrates how changes in most parameters give results which are ambiguous at best, but changes in the source depth and geometry may have decisive effects. Random variations in the surface properties across the study area may easily mask variation in rock conductivity, but variations in source depth will be far less ambiguous.

Note that the model in Figure 6.60 is for a well-defined linear source of fixed temperature (1400K) and radius (1m) probably a best case example. A diffuse source, of uncertain temperature and spatial extent, such as a coal mine fire, for example would produce a much less well defined temperature distribution which would be very difficult to readily interpret.

	Position (Pixel)	Source Depth (m)	Source Temp. (K)	Rock Thermal Conductivity ($Wm^{-1}K^{-1}$)	Space Node Temp (K)	Emissivity	Convection Film Coefficient ($Wm^{-2}K^{-1}$)
Basic Source	43	10	1400	2	280	1	20
Surface Cover Changes	89	10	1400	2	280	0.9	30
Aspect Change	134	10	1400	2	300	0.9	30
Shallowing	180	8	1400	2	300	0.9	30
Increase in K	200	8	1400	6	300	0.9	30

Table 6.21 Parameter variations in the simulated kinetic temperature map (Figure 6.60)


Temperature (K)
295
290
285
280
275
270
0
9
18
27
36
45
54
63
72
81
90
99
0
25
50
75
100
125
150
175
290-295
285-290
280-285
275-280
270-275

Chapter 7: Transient Modelling

All the models described to date have been steady state models in which the solution obtained describes the conditions when the system has fully equilibrated. The steady state approximation is valid for investigation of many systems. However, real world systems evolve dynamically through time, and are not in a stable equilibrium condition. This chapter sets out to investigate the application of finite element modelling to transient thermal processes.

Transient models are created by using a series of time steps and calculating the temperature change as a function of time for each step. The procedure for validating and conducting transient models is outlined in *Chapter 5: Finite Element Modeling using Ansys*. The models investigated in this chapter fall into two categories:

(i) Single Load Step Models: Where a single thermal load is applied, for example, a source temperature, and the resulting temperature examined as a function of time until it reaches an equilibrium state, e.g. Model series 7.1.1

(ii) Multiple Load Step Models: Where each time step has a different thermal load, for example, diurnal models where the surface temperature is constantly changing e.g. Model series 7.1.2.

7.1 MODELS

SERIES 7.1.1 INVESTIGATION OF A REACTIVATED LAVA TUBE

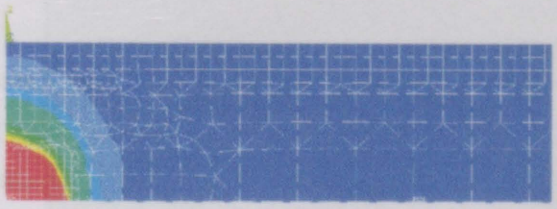
This series describes the temporal thermal signatures surrounding a lava tube which has been refilled with active (i.e. molten) lava. The model uses the same geometry and mesh as the Bravo Model (See *Chapter 6: Steady State Models*), modified for transient analyses according to the procedure outlined *in Chapter 5: An Introduction the Thermal Modelling using Ansys*. As the model mesh has already been tested for use in steady state models, further testing and validation is not required once appropriate timestep intervals are used.

The objective of model series 7.1.1 is to develop techniques in transient thermal modelling and assess the time dependence of the thermal effects of a refilled lava tube. The series sets out to answer the question of how long will it take for a refilled lava tube to produce a temperature change at the surface? The model is investigated for two extreme 'end member' cases. First, a 'fast' example using a 1m radius lava tube buried at 3m depth in solid, permeable basalt *(Appendix C: Basalt 3)*, the most thermally conductive material under consideration. Secondly, a 'slow' case was investigated, for a lava tube of the same radius, embedded in 10m depth of porous, impermeable basalt (*Appendix C: Basalt 4*) the least thermally conductive material.

Parameter	Value	Unit
Thickness	Varies	m
Thot	1400	K
Bulk Temperature	273	K
Convection Film Coefficient	10	$Wm^{-2}K^{-1}$
Space Node Temperature	273	K
Initial Temperature	273	K
Rock Thermal Conductivity	Range 0.66-6.7	$Wm^{-1}K^{-1}$
Rock Density	Range 1020-2700	kgm^{-3}
Rock Specific Heat Capacity	Range 321-1131	$Jkg^{-3}K^{-1}$
Emissivity	1	

Table 7.1 Series 7.1.1 model parameters.

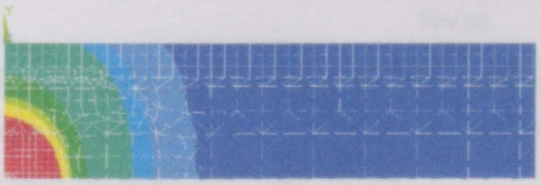
Time=53333 seconds (14.8 hours)



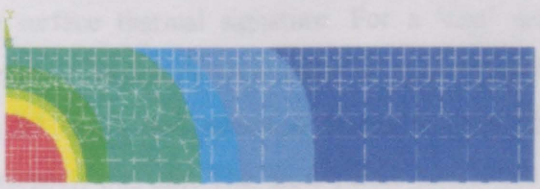
Time=213333 seconds (2.46 days)



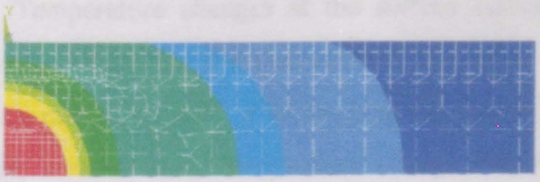
Time=480000 seconds (5.55 days)



Time=0.192x10^{7}seconds (22.22 days)



Time=0.432x10^7 seconds (50 days)



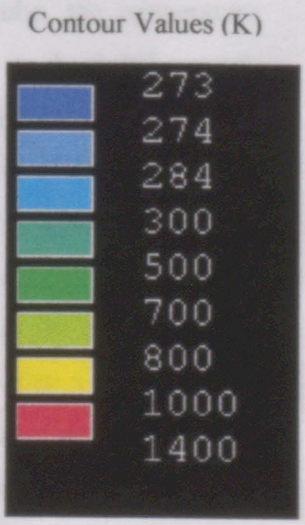


Figure 7.1 shows the evolution of the temperature distribution for a lava tube of 2m diameter at a depth of 3m in Basalt3.

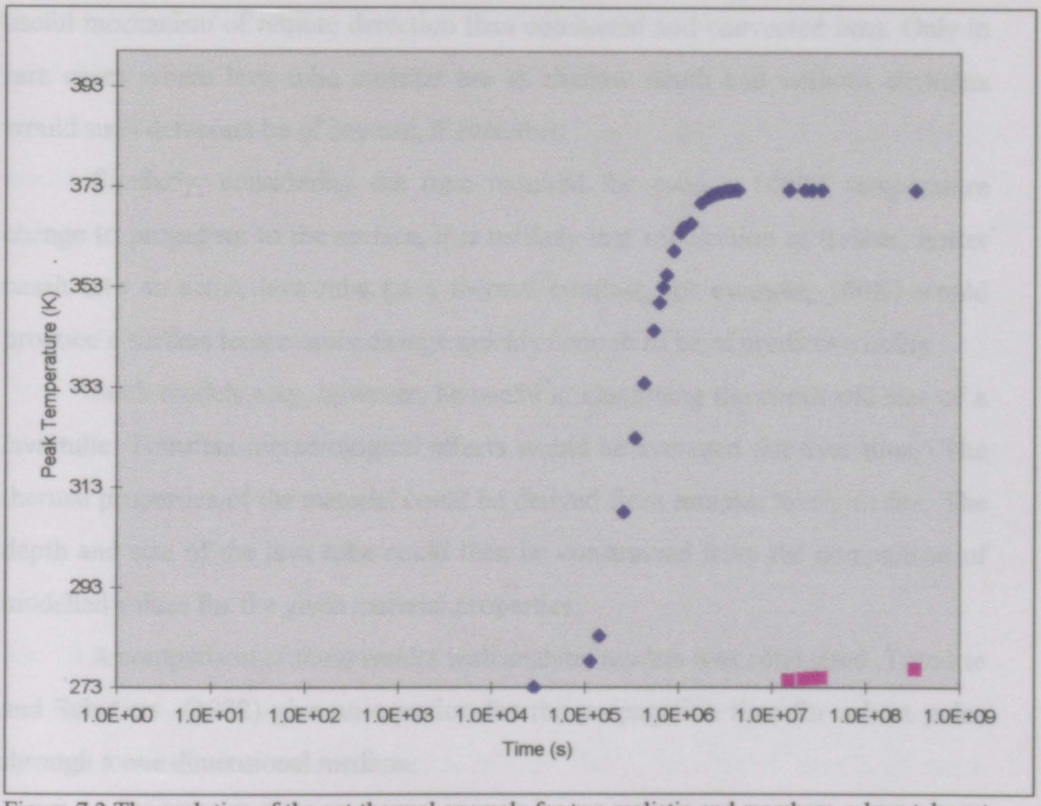


Figure 7.2 The evolution of the net thermal anomaly for two realistic end members, a lava tube set in 3m depth of high conductivity basalt (Basalt Type 3- in blue), and a lava tube set in 10m depth of low conductivity basalt (Basalt Type 4-in red)

Figure 7.2 demonstrates the considerable variation in the temporal evolution of the surface thermal signature. For a 'fast' case lava tube, the temperature converges to its steady state value of approximately 373 K in about 10^6 seconds (about 27 days), and shows a detectable temperature change at the surface in approximately one day. The 'slow', least conductive case scenario takes almost 500 days to reach its equilibrium temperature of 276.2 K, and takes almost six months to produce a detectable (1 K) temperature change in the surface.

Temperature changes at the surface cannot therefore be used to detect reactivation of any but the shallowest of lava tubes. Consider that a lava tube may refill at a rate of 1-2 ms^{-1}, a 10 km long tube will begin to effuse lava within 5,000 seconds, whereas as no temperature change will occur at the surface for 10,000 seconds. For lava tubes in highly conductive basalt at shallow depth thermal detection of lava tube refilling may be of use as a hazard warning. It is likely that in such shallow cases, direct thermal radiation via skylights would be a much more

useful mechanism of remote detection than conducted and convected heat. Only in rare cases where lava tube systems are at shallow depth and without skylights would such detection be of any use, if even then.

Similarly, considering the time required for even a 1000K temperature change to propagate to the surface, it is unlikely that re-injection of fresher, hotter basalt into an active lava tube (at a thermal contrast, for example, 100K) would produce a surface temperature change quickly enough to be of predictive utility.

Such models may, however, be useful in identifying the depth and size of a lava tube. Transient meteorological effects would be averaged out over time, The thermal properties of the material could be derived from samples taken on site. The depth and size of the lava tube could then be constrained from the comparison of modelled values for the given material properties.

A comparison of these results with analytic models was conducted. Turcotte and Schubert (1982) give an equation for the propagation time for a heat pulse through a one dimensional medium:

$$D=\sqrt{(\kappa_d t)} \qquad 7.1$$

Where:

D Distance to which a temperature change propagates (m)

κ_d Thermal diffusivity of the material (m^2s^{-1})

t Time (s)

This describes the distance which a temperature change will propagate over a given time. The equation is not a precise representation as it was a designed for a one dimensional problem in a solid, however it can give a general approximation.

For the examples given above, the equation predicts a temperature change will propagate to the surface for the fastest case (Basalt 3, $\kappa_d=3.23\times10^{-6}m^{-2}s^{-1}$) in about 3×10^6 seconds (34 days) , and for the slowest case (Basalt 4, $\kappa_d=1.9\times10^{-6}m^{-2}s^{-1}$) a time of about 5.3×10^7 seconds (613 days). In both cases the times predicted by the analytical expression correlate closely with those of model series 7.1.1.

SERIES 7.1.2 THE DIURNAL CYCLE: THERMAL INERTIA COMPARISONS

Model series 7.1.2 sets out to model the surface temperature as a function of time subject solely to diurnal thermal fluctuations. The model uses a simple 'brick' geometry, composed of Plane 55 elements with a layer of Surf 19 element on the upper surface, radiatively coupled with a 'space node' (*See Chapter 5: Introduction to Thermal Modelling Using Ansys*). After applying an initial equilibrium loadstep, 24 one-hour load steps are applied, with radiative and convective loads derived from meteorological data. The model uses two layers of varying thickness, to facilitate modelling of thermal inertia variations due to buried materials of different thermal inertia.

Model Mesh

The model mesh is an evolution of the steady state mesh used for early validation studies in *Chapter 5: Introduction to Thermal Modelling Using Ansys*. It has been adapted for radiative and transient modelling. The model uses a very high mesh density near the surface (see Figure 7.3). This mesh design is highly conservative, but is designed with a view to future adaptation for lunar thermal modelling, where the highly temperature dependent behaviour of lunar regolith may prove challenging to a less robust mesh.

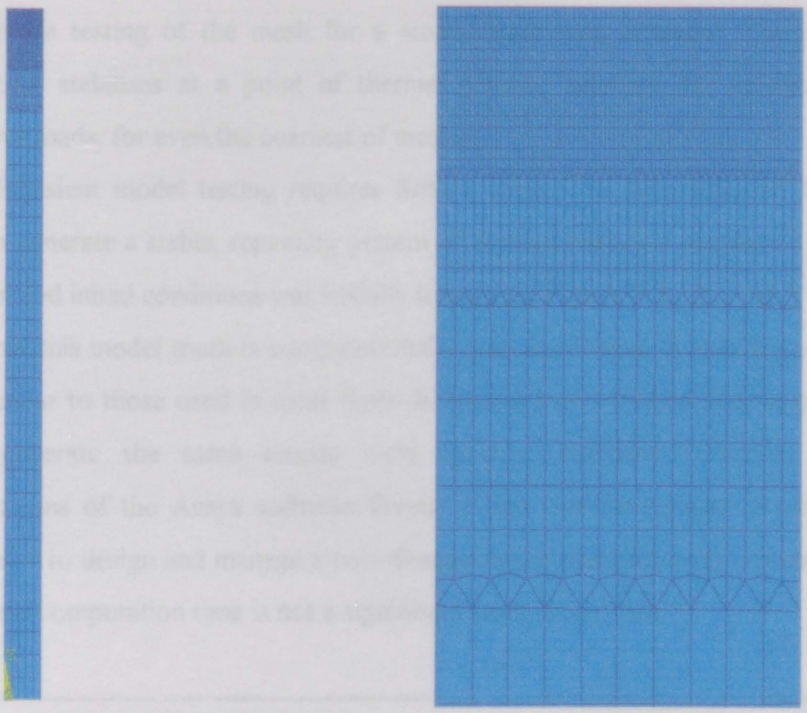


Figure 7.3 The mesh of the brick model. On the left is the complete mesh (dimensions 1m wide by 15m deep). On the right is an enlargement of the upper 2m of the model, showing selective mesh refinement

Mesh Validation and Testing

Convergence testing of the mesh for a steady state case is trivial. The surface temperature stabilises at a point of thermal balance between the radiative and convective loads, for even the coarsest of meshes.

Transient model testing requires further steps. The time required for the model to generate a stable, repeating pattern of thermal variation unaffected by the approximated initial conditions was initially tested (see Figure 7.4). It is worth noting that this model mesh is computationally quite inefficient. A one-dimensional mesh, similar to those used in most finite difference based thermal inertia models, should generate the same results more quickly. However, practical usage considerations of the Ansys software favour a thin two-dimensional mesh. It is much easier to design and manage a two-dimensional model than a one-dimensional model, and computation time is not a significant issue in any case.

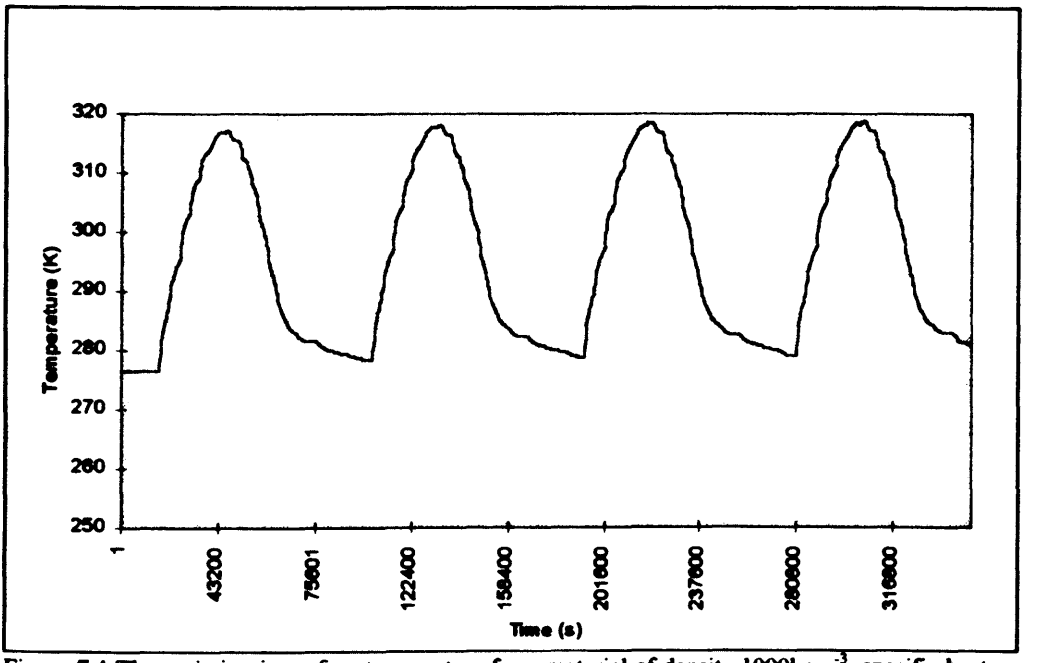


Figure 7.4 The variation in surface temperature for a material of density $1000kgm^{-3}$, specific heat capacity $1000Jkg^{-1}K^{-1}$ and thermal conductivity $1Wm^{-1}K^{-1}$, subjected to varying diurnal loads. It can be seen from inspection that the initially chosen initial temperature of 278K was too low, and that as the result the temperatures for the first day cycle are too low, however, after day two the temperature distribution is stable, rising by only a fraction of a degree between cycles.

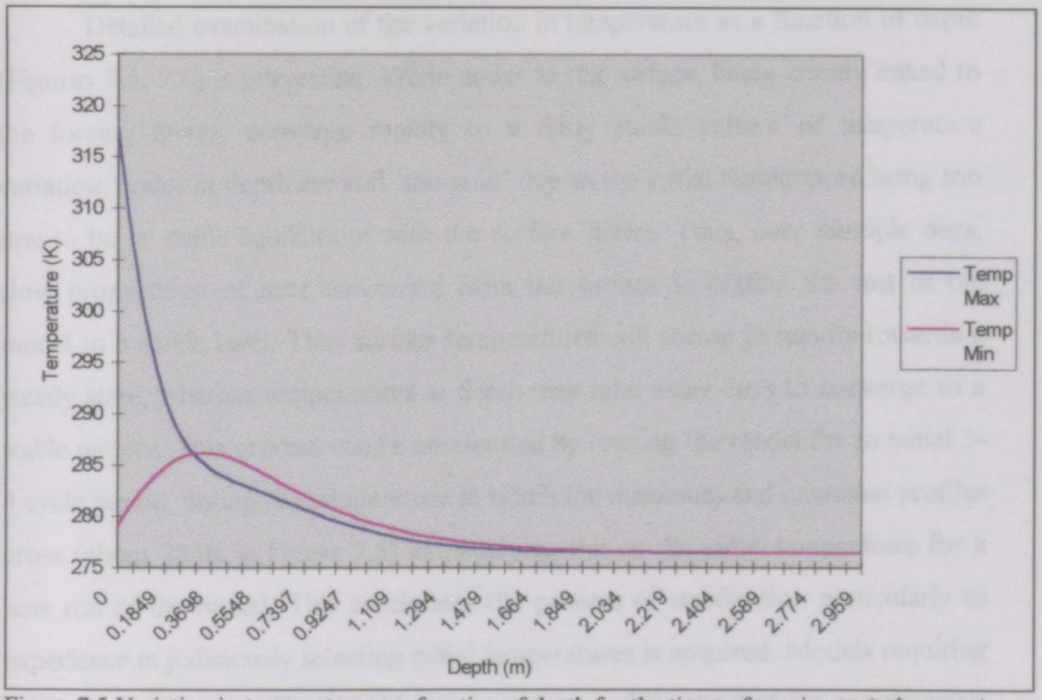


Figure 7.5 Variation in temperature as a function of depth for the times of maximum (solar noon) and minimum (pre-dawn) temperatures during the diurnal cycles.

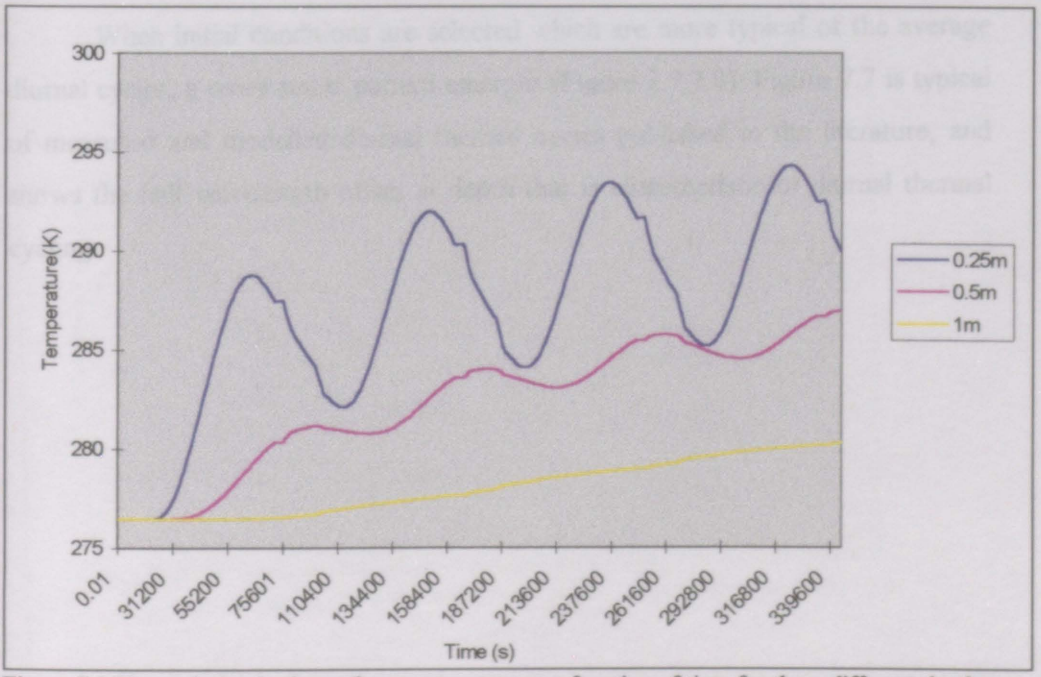


Figure 7.6 The variation in the surface temperature as a function of time for three different depths of the brick model. For all depths, the temperature rises significantly over time. At shallow depths, the rise is cyclical modulated by diurnal forcing, but at greater depth, where diurnal fluxes do not propagate, the temperature rises steadily. Note also that in the evening of each cycle there is a 'glitch' approximately a third of the way down from the peak.

Detailed examination of the variation in temperature as a function of depth (Figures 7.5, 7.6) is interesting. While nodes at the surface, being closely linked to the forcing fluxes, converge rapidly to a fairly stable pattern of temperature variation, nodes at depth are still 'too cold' due to the initial temperature being too low to be in stable equilibrium with the surface fluxes. Thus, over multiple days, slow propagation of heat downward from the surface is heating the rest of the model to a stable level. Thus surface temperatures will converge rapidly towards a steady state, whereas temperatures at depth may take many days to converge to a stable pattern. This process can be accelerated by running the model for an initial 3-4 cycle period, noting the temperature at which the maximum and minimum profiles cross (about 285K in Figure 7.5) and applying this as the initial temperature for a new run of the model. This accelerates the process of stabilisation particularly as experience in judiciously selecting initial temperatures is acquired. Models requiring depth/temperature profiles should, however, be carefully checked for convergence, and great care should be exercised in the selection of the initial variables.

When initial conditions are selected which are more typical of the average diurnal cycles, a more stable pattern emerges (Figure 7.7,7.8). Figure 7.7 is typical of measured and modelled diurnal thermal cycles published in the literature, and shows the half wavelength offset at depth that is characteristic of diurnal thermal cycling.

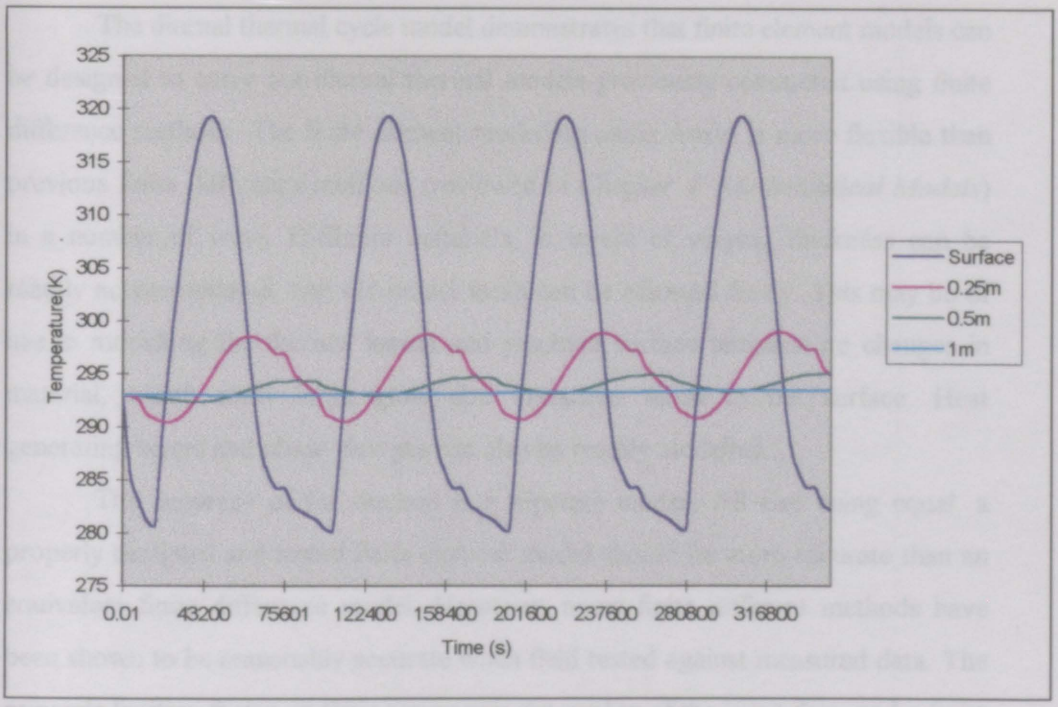


Figure 7.7 Variation in temperature across four diurnal cycles for different depths.

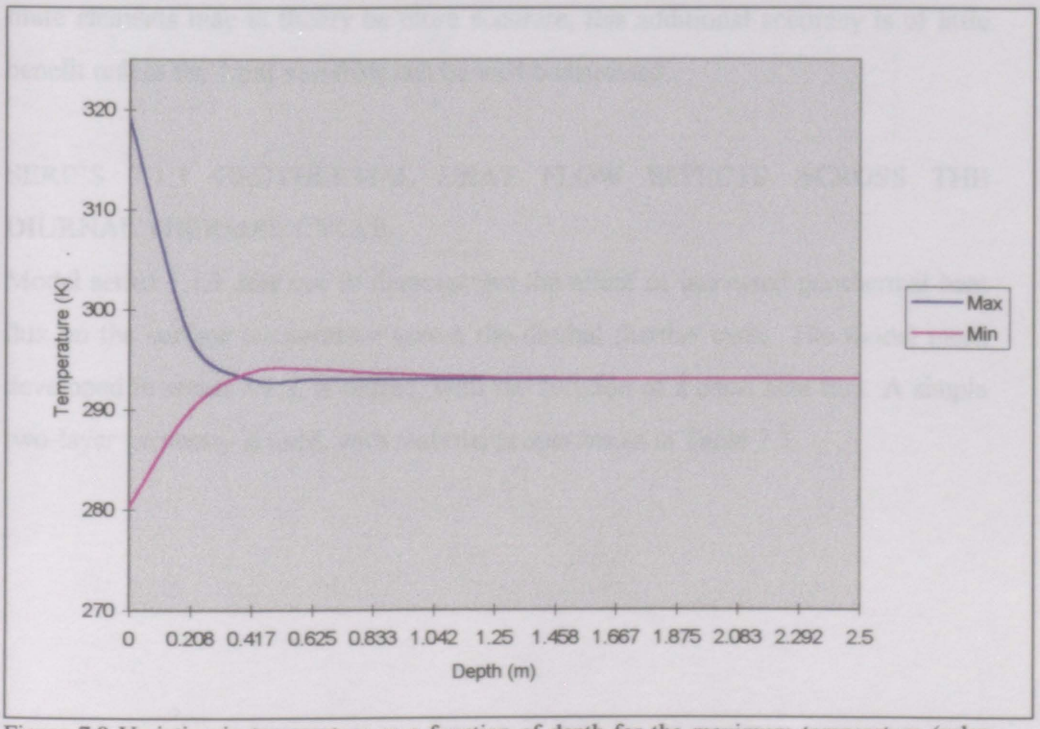


Figure 7.8 Variation in temperature as a function of depth for the maximum temperature (solar noon) and minimum temperature (just before dawn) curves.

The diurnal thermal cycle model demonstrates that finite element models can be designed to carry out diurnal thermal models previously conducted using finite difference methods. The finite element modelling using Ansys is more flexible than previous finite difference methods (reviewed in *Chapter 4: Mathematical Models*) in a number of ways. Different materials, in layers of varying thickness can be readily accommodated, and the model mesh can be adjusted freely. This may be of use in modelling the thermal inertia and resultant surface temperature changes in material, which show large grain size variations close to the surface. Heat generating layers and phase changes can also be readily modelled.

The accuracy of the method is a separate matter. All else being equal, a properly designed and tested finite element model should be more accurate than an equivalent finite difference model. However, many finite different methods have been shown to be reasonably accurate when field tested against measured data. The principle limiting factor on their accuracy is the quality of the input data, and a finite element model will be just as sensitive to this as a finite difference model. While finite elements may in theory be more accurate, this additional accuracy is of little benefit unless the input variables can be well constrained.

SERIES 7.1.3 GEOTHERMAL HEAT FLOW EFFECTS ACROSS THE DIURNAL THERMAL CYCLE.

Model series 7.1.3 sets out to demonstrate the effect of increased geothermal heat flux on the surface temperature across the diurnal thermal cycle. The model mesh developed in series 7.1.2, is reused, with the addition of a basal heat flux. A simple two-layer geometry is used, with material properties as in Table 7.3.

Parameter	Value	Unit
LOADS		
Bulk Temperature	Varies Diurnally 270-290K	K
Convection Film Coefficient	10	$Wm^{-2}K^{-1}$
Space Node Temperature	Varies Diurnally 249-365K	K
Initial Temperature	273	K
Surface Emmisivity	1	
LAYER 1		
Layer 1Thermal Conductivity	2	$Wm^{-1}K^{-1}$
Layer 1 Density	1000	kgm^{-3}
Layer 1 Specific Heat Capacity	1000	$Jkg^{-3}K^{-1}$
Layer 1 Thickness	10	m
LAYER 2		
Layer 1Thermal Conductivity	1	$Wm^{-1}K^{-1}$
Layer 1 Density	2700	kgm^{-3}
Layer 1 Specific Heat Capacity	800	$Jkg^{-3}K^{-1}$
Layer 1 Thickness	10	m

Table 7.3 series 7.1.3 Model Parameters

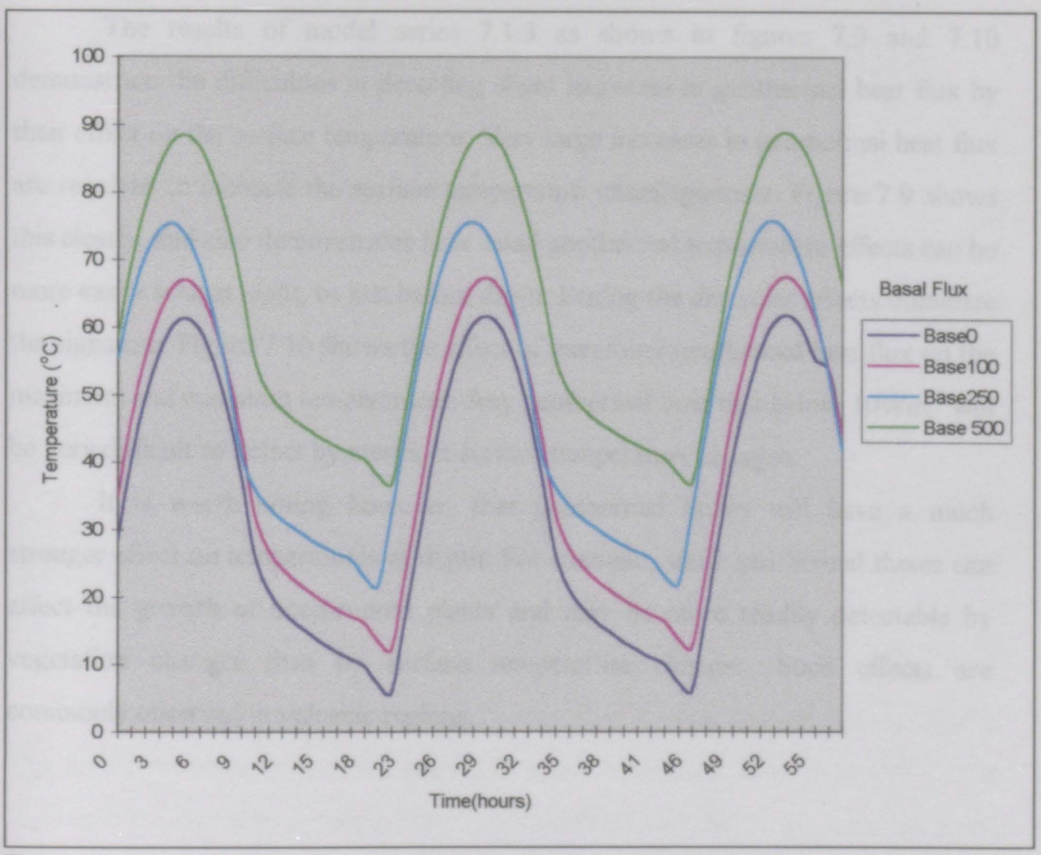


Figure 7.9 Variation in the surface temperature for identical surface loads and varying basal fluxes (0 to 500 Wm^{-2})

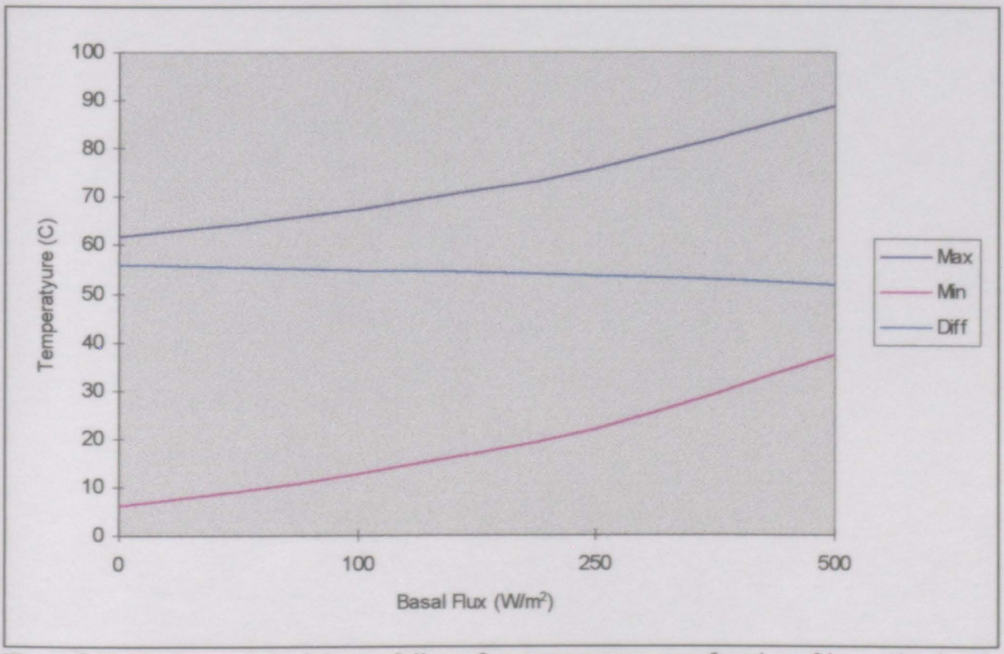


Figure 7.10 Maximum and minimum daily surface temperatures as a function of increasing basal flux.

The results of model series 7.1.3 as shown in figures 7.9 and 7.10 demonstrate the difficulties in detecting slight increases in geothermal heat flux by their effect on the surface temperature. Very large increases in geothermal heat flux are required to increase the surface temperature unambiguously. Figure 7.9 shows this clearly, and also demonstrates how small geothermal temperature effects can be more easily seen at night, or just before dawn, During the day solar effects dominate the signature. Figure 7.10 shows the effect of increasing geothermal heat flux on the maximum and minimum temperatures. Any geothermal heat flux below $10Wm^{-2}$ will be very difficult to detect by means of surface temperature changes.

It is worth noting however, that geothermal fluxes will have a much stronger effect on temperatures at depth. For example, small geothermal fluxes can affect the growth of deep-rooted plants and may be more readily detectable by vegetation changes than by surface temperature changes. Such effects are commonly observed in volcanic regions.

Chapter 8: Phase Change Modelling

The purpose of this chapter is to investigate the feasibility of modelling processes involving phase change of geological materials using the finite element method. A number of geological processes involve thermally controlled phase changes, and modelling the effect of such changes on the surface temperature distribution may suggest whether or not thermal infrared images would be of use in monitoring such processes.

The Ansys software has a capacity for modelling phase changes. These processes are modelled by assigning the temperature dependent thermal properties to the materials in the model.

The investigations of phase changes has been divided into two types. First, the effect of material phase changes on steady state analyses, where the position of the boundary between the two phases is stable over time, is investigated by the example of a steady heat source buried in cryolithosphere. Secondly, transient phase changes are investigated, where the position of the boundary between the two phases may change over time.

8.1 STEADY STATE PHASE CHANGE MODELS

Steady state phase change models are conducted by assigning a temperature dependent thermal conductivity to the materials in the model. From *Chapter 6:Steady State Models*, we note that in steady state analysis, the specific heat capacity and density of a material have no effect on the result. The same is true for a steady state phase change model. The specific heat capacity of a material and thus the enthalpy of the material, in the sense used by Ansys as a term of energy storage should have no effect on the final result. In tests this was found to be the case.

SERIES 8.1.1 HEATED CRYOLITHOSPHERE

Model series 8.1.1 sets out to investigate the importance of water/ice phase changes. The case examined is that of a relatively cool heat source at shallow depth in cryolithosphere. The model uses the Bravo model mesh, with a temperature dependent thermal conductivity calculated for a Sandstone Water/Ice mix with a porosity of 0.5. The temperature dependent thermal conductivity rises from 1.61 $Wm^{-1}K^{-1}$ to 2.61 $Wm^{-1}K^{-1}$ across the water-ice phase change. An equivalent series of non-phase change models is also run for the same material with an averaged, fixed thermal conductivity of 2.11 $Wm^{-1}K^{-1}$. Other model parameters are as outlined in Table 8.1. The model is a steady state model, and thus the boundary between the rock-ice and rock-water phases does not move over time.

Parameter	Value	Unit
Thot	200	K
Source Depth	10	M
Bulk Temperature	200	K
Convection Film Coefficient	10	$Wm^{-2}K^{-1}$
Space Node Temperature	200	K
Rock Thermal Conductivity	1.61-2.61	$Wm^{-1}K^{-1}$
Emmissivity	1	

Table 8.1 model series parameters. Thermal conductivity is varied as for *Sandstone-Ice Mixes, Appendix C.*

Figures 8.1 and 8.2 show how a phase change enabled model (red trend) produces a marginally smaller, cooler anomaly than a phase change disabled model for the same materials and conditions (yellow trend).

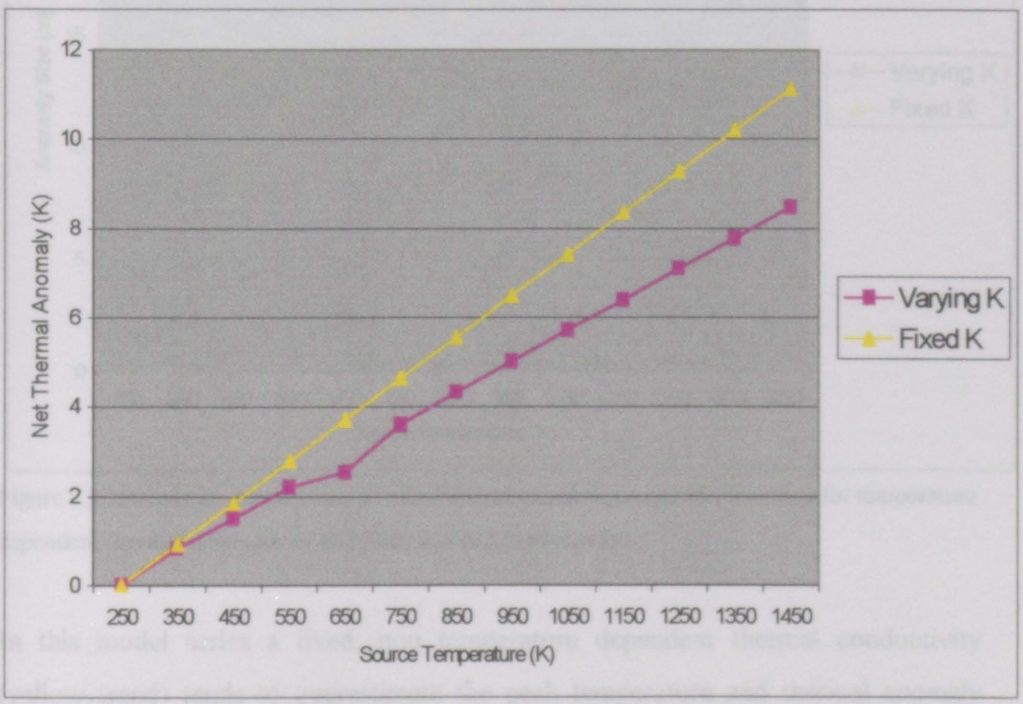


Figure 8.1 The variation in the net thermal anomaly (difference between peak temperature and background temperature) for increasing source temperature. The red trend is the phase change enabled, the yellow trend is phase change disabled.

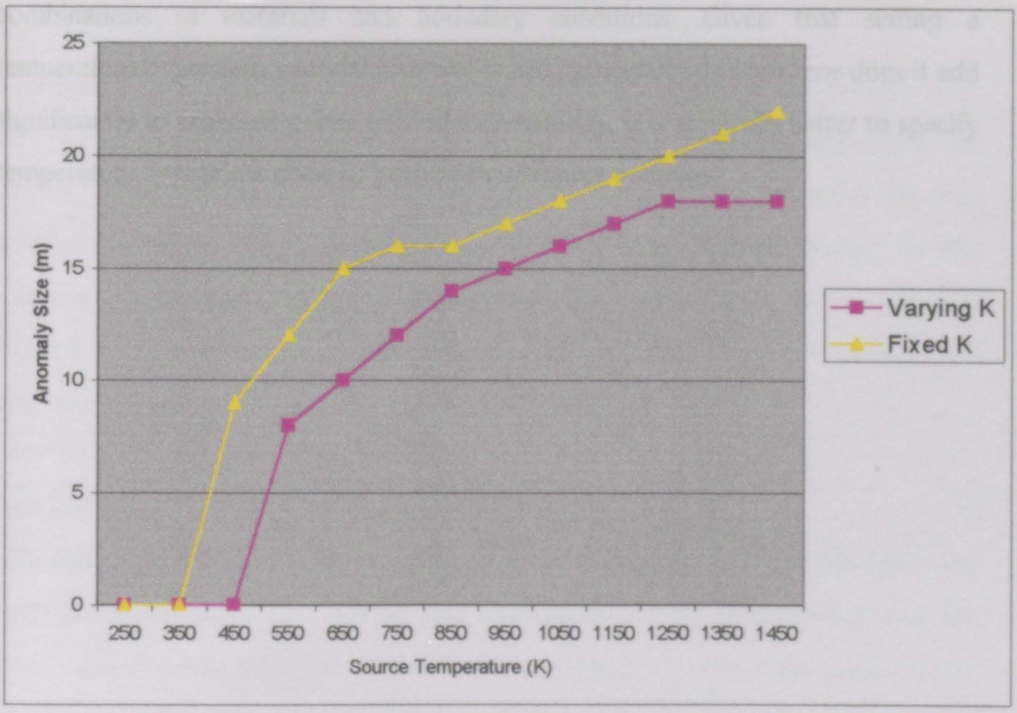


Figure 8.2 Increase in anomaly size as a function of increasing source temperature for temperature dependent thermal conductivity and fixed thermal conductivity.

In this model series a fixed, non temperature dependent thermal conductivity (yellow trend) tends to overestimate the peak temperature and thermal anomaly size. Figure 8.1 shows a clear, straight line trend as would be expected. For non-temperature dependent thermal conductivity, the results also produce a straight line trend but with a slightly smaller gradient. Figure 8.2, the thermal anomaly size follows a curve of similar shape for both cases, but with slightly smaller size for the phase change enabled case (i.e. temperature dependent thermal conductivity). In both cases the differences are very slight, only marginally above the uncertainty ranges of the Bravo model.

The similarity of the results for the phase change enabled and disabled solutions suggests that the effect of the phase change is small, affecting the surface by no more than a 1-2 degrees K. By using a value for a fixed thermal conductivity that is slightly lower than a simple average of the temperature dependent conductivity, it would be possible to model the system with acceptable accuracy, without temperature dependent (i.e. phase change controlled) properties. There is no guarantee however, that what is true for this case is true for all possible

combinations of materials and boundary conditions. Given that setting a temperature dependent material property is not particularly difficult, nor does it add significantly to processing time or model uncertainty, it is generally better to specify temperature dependent material properties wherever possible.

8.2 TRANSIENT PHASE CHANGE MODELS

Transient phase change models are somewhat more complex to investigate than steady state phase change models. As noted in *Chapter 7: Transient Models*, the values of the specific heat capacity and density are required to model the heat storage over time. These, together with the latent heat of phase change for the material, can be combined to give an enthalpy value (see *Chapter 3: The Physical Model*) which is temperature dependent. It is this enthalpy value which Ansys uses as a measure of heat storage in a transient phase change model.

SERIES 8.2.1 COOLING LAVA TUBE

The aim of model series 8.2.1 is to examine the importance of phase change in the surface temperature over evolving lava tube systems. This model series uses the Bravo model mesh, modified for transient behaviour. From the initial conditions of an evacuated lava tube, the 'tube' region of the model is loaded to a temperature of 1400K to represent refilling by active basalt, and allowed to reach thermal equilibrium.

Assuming that after equilibrium is reached, new inflows of active lava cease, and thus the 1400K temperature load is removed. The model is allowed to cool back towards equilibrium.

Effects of cool air moving through the lava tube after it has drained of lava are also not considered, and it is assumed that the lava tube is 'sealed'. Air cooling in the lava tube would lead to significantly faster cooling overall, as thermal energy would no longer have to 'wait' for slow, conductive processes, but could be convected away quickly across surfaces with a high temperature contrast. This effect, however, would not be affected by phase change processes in the basalt.

Solid, impermeable basalt (*Basalt 2, Appendix C*) is used as the material in this example. Model parameters are summarised in Table 8.2

Parameter	Value	Unit
Thot	1400K	K
Source Depth	10	m
Bulk Temperature	273	K
Convection Film Coefficient	10	$Wm^{-2}K^{-1}$
Space Node Temperature	273	K
Rock Thermal Conductivity	2.08-0.974	$Wm^{-1}K^{-1}$
Density	2700	kgm^{-3}
Specific Heat Capacity	800-1131	$Jkg^{-1}K^{-1}$
Emissivity	1	

Table 8.2 Model series 8.2.1 parameters for the investigation of a cooling lava tube.

Figure 8.3 shows the results of this model series. On inspection, results are largely as one would expect. The phase change enabled model heats and cools more slowly than the 'solid' model, as one would expect given the additional heat storage within the system. However, the equilibrium temperature for the phase change model is approximately 0.5K lower than that for the solid model, where one would expect similar results.

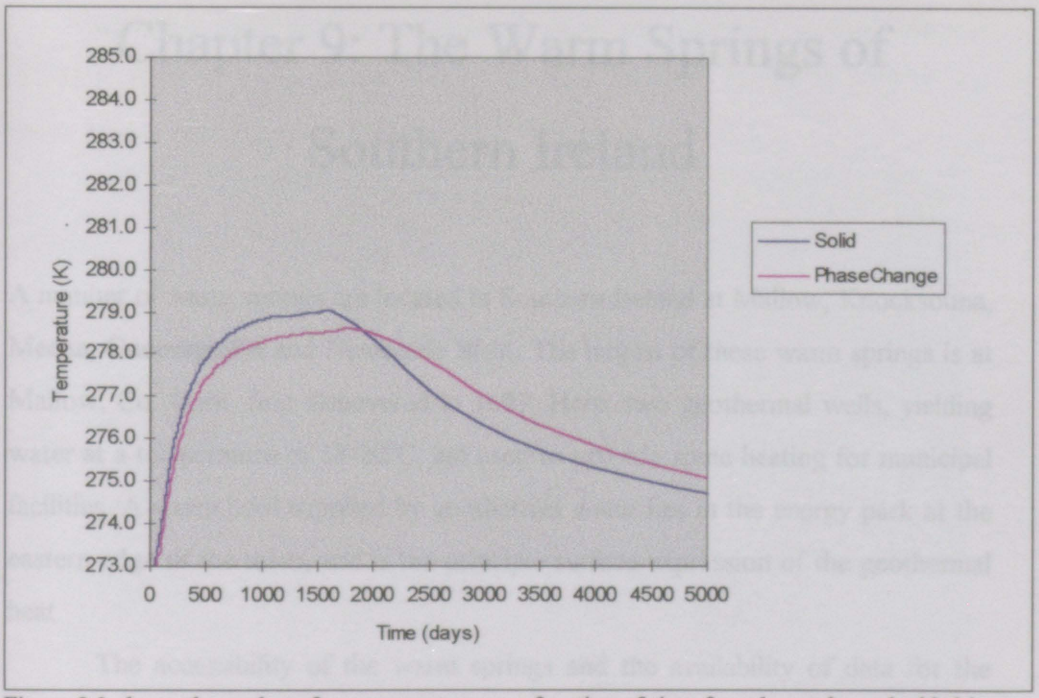


Figure 8.3 shows the peak surface temperature as a function of time for a lava tube embedded in Basalt 2 for phase change enabled (blue) and phase change disabled (red) models.

The size of the variations between the phase change enabled and phase change disabled cases is less than the approximate error range of the Bravo model mesh (± 1K). The scale of the variations is small enough to be of little use in interpreting surface temperature changes as a result of phase change processes at depth.

A number of factors are, however, not considered by the model. Physical erosion of the tube bottom by flowing lava is not considered in this model. This complex process could be addressed by Computational Fluid Dynamics (CFD) models of lava flow in the tube, or by applying a time varying lava tube geometry based on 'known' downcutting rates. Downcutting of lava tubes is difficult to measure in the field, and may not be geometrically significant.

Chapter 9: The Warm Springs of Southern Ireland

A number of warm springs are located in Southern Ireland at Mallow, Knocksouna, Meelin, Gneeveguillia and Newcastle West. The largest of these warm springs is at Mallow, Co. Cork, first discovered in 1687. Here, two geothermal wells, yielding water at a temperature of 18-20°C, are used to provide some heating for municipal facilities. A warm pool supplied by geothermal water lies in the energy park at the eastern edge of the town, and is the principle surface expression of the geothermal heat.

The accessibility of the warm springs and the availability of data for the region suggested these warm springs as an initial case study. This chapter sets out to examine the feasibility of detecting the warm springs using thermal infrared remote sensing and computer modelling of the heat transfer in the springs system to predict and explain any observed temperature distribution.

The warm springs lie close to the Killarney-Mallow fault zone. This is a zone of thrust faulting marking the northern edge of the main Variscan deformation in the south of Ireland. It has been suggested that these southern dipping faults may provide a channel for relatively rapid upward migration of geothermal waters from depth, at a rate faster than would allow them to reach thermal equilibrium with the surrounding rock (Brück et al 1986).

Two Landsat Thematic Mapper (TM) quarter scenes have been examined. The Landsat TM instrument is described in *Appendix D*. The scene was acquired on June 4 1989 by the mid-morning Landsat pass, and covers most of Cork and Kerry.

The climate of the region is mild and humid, with average temperatures for the period 1951-1980 ranging from 4.9°C (February) to 14.8°C (July). Sunshine is generally about 30% of the maximum possible. Rainfall is high, with mean monthly values for the same period ranging from 148mm (January) to 64mm (June). The mean annual windspeed is $5.4ms^{-1}$.

Meteorological data are available from weather stations at Cork Airport (51°51'N 8°29'W 154m above MSL), Shannon Airport (51°41'N 8°55'W 3m above MSL), and Kilkenny (52°40'N 7°16'W 63m above MSL).



Figure 9.1 Location of Mallow Warm Springs. Map after UC Texas on line map library

9.1 REMOTE SENSING ANALYSIS

The TIR signature is dominated by the vegetation types with areas of freshly cut grass appearing much warmer (lighter) than heavier crops of grass. On the Mallow visible band image (Figure 9.2) a railway line is visible as a lineament to the south of the town. At this resolution major features such as the River Blackwater are barely visible, and features such as the warm spring to the east of the town are not visible on inspection. The Thermal infrared image (Landsat TM band 6) appears as a uniform, featureless, greyscale image unless it is stretched or processed in some way.

FILTERING

The conventional approach to detection of pattern not immediately evident on inspection is to apply filtering and contrast enhancement. It would be expected that generalised heating of the ground surface would produce elevated surface temperatures and hence elevated DN in a roughly east-west orientation parallel to the structural trend in the region. Various filtering and image processing techniques were applied to Band 6 (Thermal Infrared) data. The discussion below refers specifically to the Mallow image, as it contained the warmest springs and the most variation in surface temperature.

Three filtering techniques examined for assess their usefulness in enhancing such features, Low Pass Filtering, High Pass Filtering and Directional Filtering.



Figure 9.2 The Mallow Town region in a false colour, visible image, (Band colour assignments: RGB432). The River Blackwater is clearly visible running east-west across the centre of the image. The Dublin-Cork rail line runs north south through the centre of the image. Mallow town lies to the east of the railway line in the centre of the image. Fields which have been recently harvested for silage appear blue in the image. The image is approximately 6km across. Image was taken at approximately 10.30 A.M. local time, June 4th 1989.

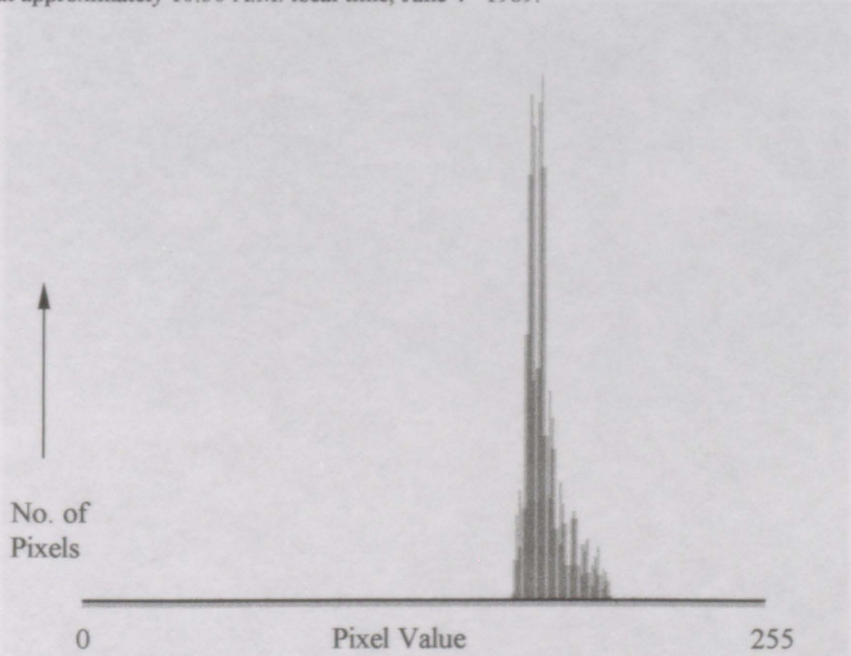


Figure 9.3 A pixel value histogram (unstretched) for the thermal infrared band at Mallow. It can be seen that there is little variation in the pixel values. Surface radiances vary across less than 15% of the dynamic range of the sensor.

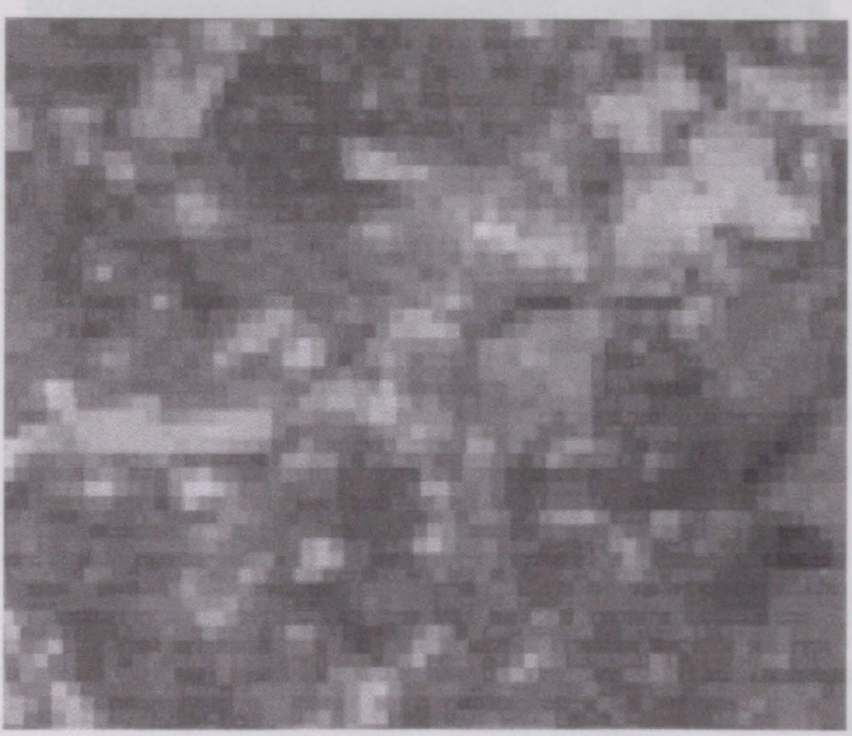


Figure 9.4 The effect of applying a contrast stretch to the thermal infrared band image, essentially flattening and widening the histogram shown in Fig 9.3.

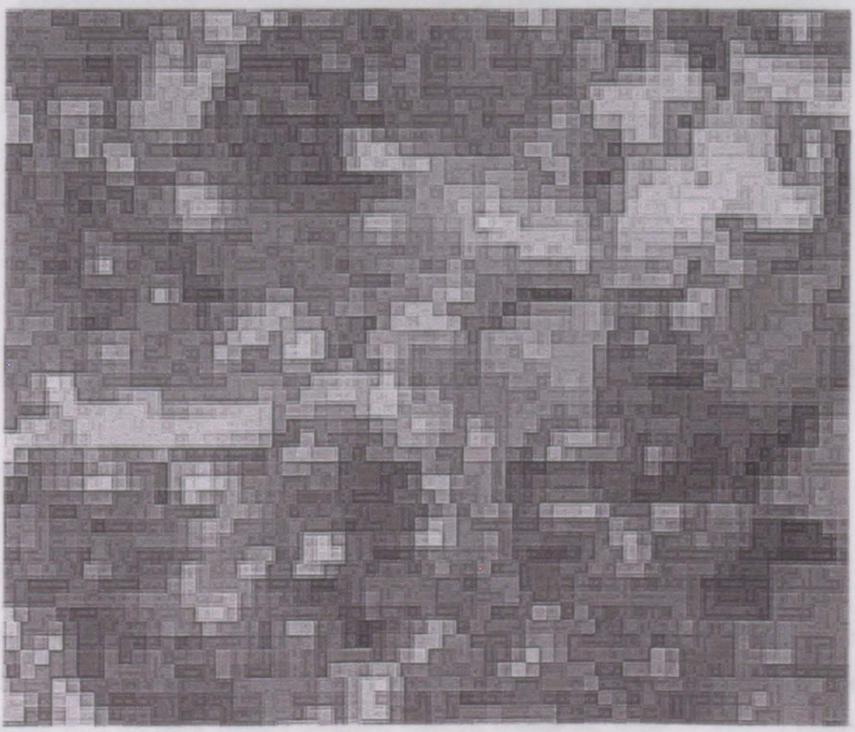


Figure 9.5 The effect of applying a 3x3 high pass filter to the thermal image.

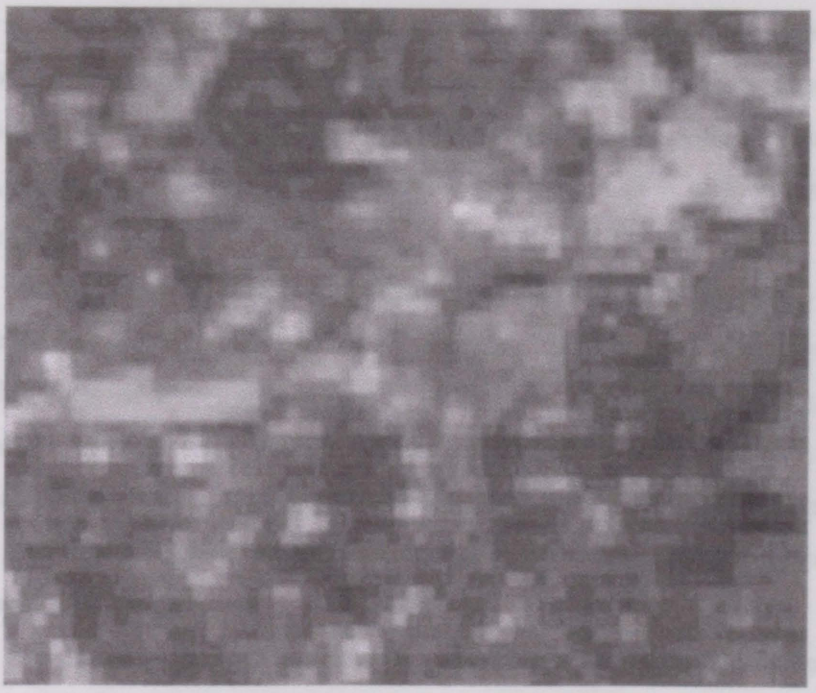


Figure 9.6 A low pass filtered thermal image of Mallow town, subsequent to contrast stretching. This technique essentially 'blurs' the image to reduce the resolution, thus removing small, high amplitude features and emphasising more regional features.

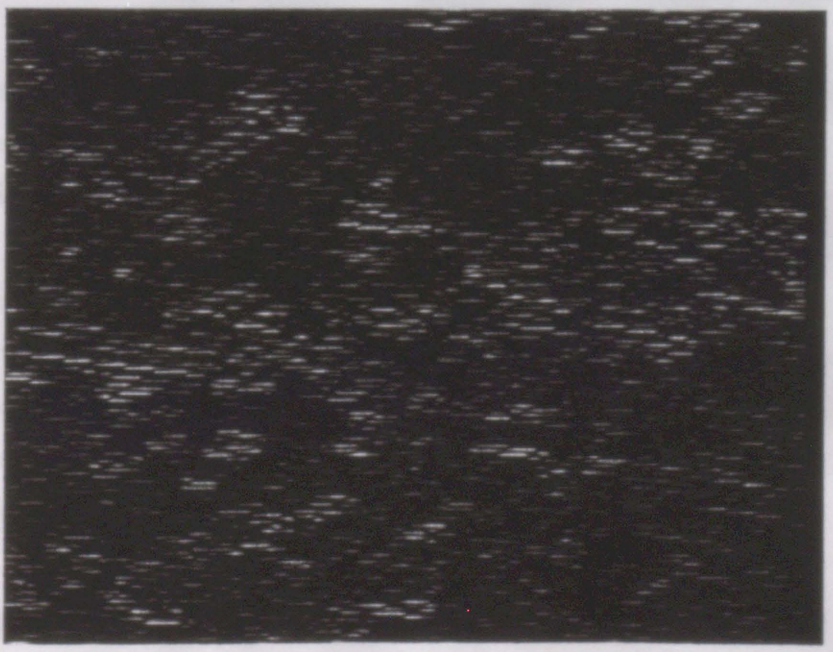


Figure 9.7 shows the effect of Directional Filtering: This technique utilises a directional filter to emphasis linearity's which run in a particular orientation. In this case it can been seen, on comparison with the other images, to highly contrast around the edges of warmer parts of the image.

Contrast stretching of the original thermal image provides an image (Figure 9.4) with a good, relatively clear overview of the principle thermal features of the region. These features strongly correlate with surface features evident in the visible bands, suggesting that they may be controlled by variations in surface cover type and emissivity.

Application of the high pass filter technique to the Mallow image (Figure 9.5) failed to produce significant results, serving only to highlight small, relatively high frequency features, such as small fields. The low pass filter (Figure 9.6) suggests a general east-west trend of elevated temperature. However, the directional filter (Figure 9.7) failed to detect the Blackwater River, which, as a fairly major cold feature would be expected to be more visible than any geothermal sources in the region.

Visual inspections of the images produced by applying these techniques show little evidence of geothermal sources. While all images show a relatively marked east-west band of elevated DN, this can be correlated directly with the band of fields from which grass had been freshly cut. The short aftercrop of grass has a much lower thermal inertia than the more vegetated surrounding fields and thus appears warmer in the mid-morning sun. All the features in the thermal infrared images and processed image products can be correlated with variations in surface material seen in the visual band images.

A variety of other image processing and filtering techniques were applied, ranging from haze reduction and crisping filters and Fourier transform processing. However, none of these techniques highlighted any thermal features which could not be correlated with visible variations in the surface material, and thus temperature variations due to meteorological effects and surface emissivity variations.

RESOLUTION

The principle technical limitation of the Landsat TM thermal infrared channel is the low spatial resolution (120m per pixel). A significant heat source is required to elevate the temperature of an entire pixel of surface area 14,400m^2 by a detectable amount. To demonstrate the difficulty of this, consider a square geothermal pool of

side 10m, surface area $100m^2$ (0.007 of pixel area). Assuming the average surface temperature to be 0°C, and all materials in the pixel are blackbodies, the mean temperature in the pixel is given by an area weighted average, using the formula:

$$T=(P)T_{hot}+(1-P)T_{back} \qquad 9.1$$

Where:

T Temperature (K)

P Proportion of Pixel

T_{hot} Temperature of hot portion (K)

T_{back} Background temperature of pixel (K)

See *Chapter 2:Thermal Infrared Remote Sensing* for further details on subpixel sources.

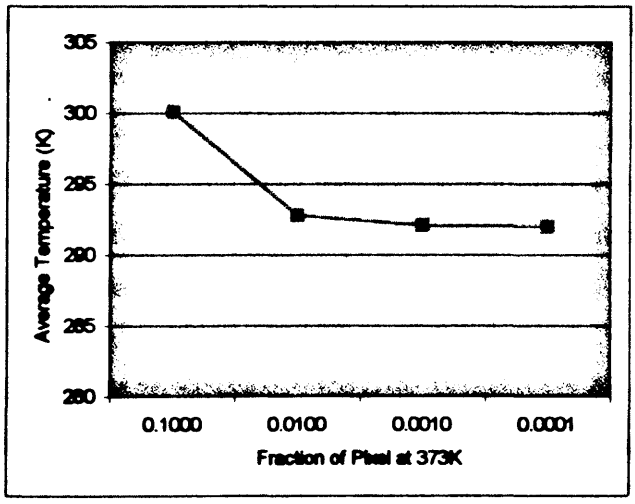


Figure 9.8 Average temperature for a pixel with a fraction occupied by a 373K hotspot, against a 292K background temperature.

To elevate the average temperature of a pixel by 1K the warm spring described above would have to be at a temperature of over 433K. If 50% of the pixel surface area were elevated by 2K, this would have the same effect (or if the background pixel temperature formed a normal distribution centred on 1K). Essentially, the smaller the portion of the pixel occupied by the hot component, the hotter it must be to elevate the temperature of the entire pixel, as can be seen in

Figure 9.8. Thus, it can be clearly demonstrated that the heat source at the Mallow warm springs is not large enough, or hot enough, to be detectable in the thermal infrared image.

POWER OUTPUT AND TEMPERATURE

At temperature ranges typical of the earth's surface, a surface whose temperature is elevated will lose 10-20 Wm^{-2} through atmospheric and radiative processes for every degree of increase above the surface equilibrium temperature (see *Chapter 3: The Physical Model*). For a warm springs system to sustain an entire Landsat TM band 6 pixel at a temperature one degree in excess of background, would require an additional geothermal power input of 144kW.

The warmest of the Munster Warm Springs, the Ladys' Well spring, in Mallow, produces approximately 100 litres/min of water at a temperature of about 19°C (Bruck et al 1983). Compared with a non-thermal spring (at background groundwater temperature of 11 °C) this should provide an additional 56kW/pixel, insufficient to support a detectable elevated pixel temperature.

Even in an ideal case, of a pixel sized pool of water at best spring outflow temperature of 20 °C, a significant signature in the thermal infrared could not be generated, as the temperature lies well within the range of surface temperatures at the time of image acquisition.

SURFACE THERMAL NOISE

Chapter 3: The Physical Model describes in detail the factors contributing to the surface temperature and the uncertainty in their measurement. Of the available data, the data from Kilkenny was chosen as the most appropriate for comparison with the Mallow site, as both Cork and Shannon weather stations are situated close to the sea (Shannon) and on a hilltop (Cork) and are thus less likely to be representative of an inland site.

At the time of image acquisition, windspeeds at Kilkenny were 4-5 knots (2-2.5ms^{-1}). Detailed air and surface temperature data are not available, however, mean air temperatures for the day were 13.3°C, mean soil (10cm) temperatures were 12.5°C, giving a total temperature gradient of approximately 1°C, although that value is likely to be higher in the mid-morning.

Sufficient data are not available to allow use of the most precise method of sensible heat transfer calculation, eddy correlation. Exact surface-air temperature profiles are also not available, so the only remaining method, the profile method, is also not usable. However, assuming that surface-air temperature gradients are less than 5°C m^{-1} we can, using equation 3.26, estimate that the sensible heat fluxes are between 200 and 300Wm^{-2}. Note that the scale of the uncertainty is far higher than the energy output from the warm spring, when averaged across a pixel.

The same problems recur in the calculation of latent heat fluxes. Even the meteorological data from the weather stations do not include sufficient soil and air humidity information to even begin to estimate sensible heat fluxes using any of the methods of calculation outlined in *Chapter 3: The Physical Model*. Based on the moist climate one can only assume that they are of a similar order of magnitude to that of the sensible heat fluxes.

Thus, uncertainties in measurement and calculation of the surface thermal fluxes are several orders of magnitude greater that the net geothermal flux. In some cases where a uniform surface exists, these errors can be eliminated as the surface properties can be assumed to be relatively homogenous. In the Mallow region, however, critical surface properties such as albedo, surface roughness and surface cover insulation and thermal inertia can vary greatly from pixel to pixel, and will contribute variations in the order of 100Wm^{-2} (1000's kW/Pixel). To produce a detectable surface temperature change, a geothermal heat source would have to produce a power output greater than this surface thermal noise level. In this respect, the Mallow warm springs power output is at least an order of magnitude below that required to produce a detectable temperature change in the model.

NON-THERMAL DETECTION

It is worth noting the possibility of detection of warm springs at wavelengths other than the thermal infrared. In more arid regions, spring lines may be really detectable by increased surface vegetation. In southern Ireland, while certain vegetation assemblages are characteristic of damp ground, it is difficult to identify these and correlate them with spring systems due to the restricted spatial and spectral resolution of the Landsat images. Essentially, these assemblages are not large or spectrally distinct enough to be visible, and the correlation of damp ground with

spring system is tenuous. Intensive surface agriculture will also tend to obscure 'natural' vegetation variations. It may be worth looking for such regions using techniques more sensitive to soil moisture, such as thermal inertia and Synthetic Aperture Radar (SAR). Such searches would be made more difficult by the generally high soil moisture in southern Ireland.

In areas of strong geothermal activity, elevated subsurface temperatures can have a significant effect on vegetation type due to heating of the deeper roots (Derion et al 1995). However, it is unlikely that this would be a significant factor in the Mallow area due to the low thermal contrast between the warm springs and the background soil temperatures.

9.2 NUMERICAL MODELLING

Numerical modelling of the regional heat flow may still be possible without reference to the remote sensing images. Borehole temperature data and regional geothermal heat flow data may be useful in validating such models. However, the modelling software used in this study, Ansys, is not appropriate for such work, as it does not incorporate much functionality for fluid flow modelling in porous media. It is possible in a limited way to 'bootstrap' such flow onto the conductive heat flow in relatively well understood, simple systems for which a Nussult number can be calculated. This approach is, however, not appropriate for the warm springs of Munster. The Munster spring system are complex, and incorporate many different variables, such as variable recharge rates, relative buoyancy of geofluids and a complex underlying geology. The thermal component of the groundwater problem - a temperature contrast of about 10°C between thermal groundwater and background non-thermal groundwater, is a only one, relatively minor, component to the geothermal system. Thus purely thermal modelling would be inappropriate to describe the system.

Modelling of such systems could be more effectively carried out using specialist hydrogeologic software. Such a model could utilise the extensive available data on from boreholes and pump tests as constrains, and would be of interest and utility in facilitating the economic extraction of thermal energy from the springs system. This would be a large project in itself, and, having no direct ramifications on the surface temperature, such a work lies beyond the scope of this study.

9.3 CONCLUSIONS

REMOTE SENSING

Detection of the warm springs in South Munster using the available thermal infrared data is not possible for a number of reasons, chiefly, the low spatial resolution of the data, and the poor signal-noise ratio of the source being sought. The extent and variability of soil moisture and local microclimates, the thickness of overburden and the extent of human activity make it highly unlikely that thermal infrared remote sensing using Landsat data, would be of any utility in detecting such springs.

Thermal infrared data cannot be entirely ruled out. Short of using 1.1km resolution AVHRR data, Landsat band 6 data is perhaps the single least suitable thermal infrared dataset for this analysis, in terms of spatial, spectral and temporal analysis. As outlined above, the spatial resolution of Landsat TM band 6 is far too low (120m) for this application. A higher resolution dataset would make the problem somewhat more tractable. Small, relatively low temperature sources, such as multi metre scale regions of warmed earth close to warm spring lines, might then be potentially detectable.

The temporal resolution of Landsat is also a problem. The Landsat images being studied were taken in mid morning of high summer, almost the worst possible time to look for subtle geothermal sources, as the thermal signature is dominated by meteorological heat fluxes. An image acquired just before dawn on a cold winters' day would be much more likely to indicate geological thermal sources.

The spectral resolution of Landsat also presents difficulties. If multiple thermal infrared bands were available this would facilitate detection of subpixel thermal anomalies (see *Chapter 2: Thermal Infrared Remote Sensing*) and would be helpful in constraining the exact temperature distribution of a geothermal source.

In simple terms, a metre sized 'warm patch' at 20°C will be much more readily detected at night, against background temperature of 10°C at a 1m resolution, that during the day, with background temperatures of 20°C and 120m resolution. Successive 'stacking' of co-registered, multiple, predawn, datasets would make the task easier still.

The ASTER instrument, launched on the EOS AM-1 platform in early 2000, will reduce some of these problems. The spatial resolution (90m) is slightly higher,

and the spectral resolution is greatly improved (5 bands instead of 1). The orbital parameters of the instrument are similar, but as the instrument is non-commercial it would be economically feasible to acquire a multi-temporal dataset during the winter months, when cooler surface temperatures and late sunrises would make geothermal sources more detectable. The Landsat Enhanced Thematic Mapper operates at a 60m thermal infrared resolution and offers a considerable improvement, but it a commercial instrument, and thus extensive data collection would be costly.

COMPUTER MODELLING

The complexity of the Mallow hydrothermal system means that purely conductive thermal modelling of the system using Ansys is of littleuse. The complex fluid flow regime means that Ansys is simply not the tool for the job. Some progress could be made using specialist hydrogeology software capable of dealing with the complex fault controlled groundwater flow. If warm springs could be detected in thermal infrared images, their positions and extent could be used as constraints to such a model.

In summary, using currently available datasets, and the computer modelling software available, it is not possible to combine techniques of thermal infrared remote sensing and computer modelling to learn more about the warm springs of Southern Ireland. However, it would be worth re-examining the detectability of the warm springs in the event of more suitable thermal infrared data becoming available in the future. It would also be worthwhile to study the problem of groundwater circulation in the springs system using specialist hydrogeological modelling software.

Chapter 10: The Kilauea Lava Flow

An active lava tube system represents an ideal test case for a study using thermal infrared remote sensing combined with numerical thermal modelling. Fortunately, a detailed dataset exists for a recent eruption of the East Rift Zone of Kilauea, at Pu'U'Oo, in September 1995. The quality of the dataset provides a unique opportunity to attempt to model the depth and temperature of the lava tubes, and study the evolution of the tubes through time.

For this case study, a small segment of the image was selected for examination, containing a 500m section of lava tube with relatively few skylights, which is clearly delineated in the images (see Figures 10.3, 10.10). Surface kinetic temperatures were extracted from the thermal images. The measured across-tube temperature profiles were then compared with modelled profiles to constrain the depth, temperature and thermal properties of the subsurface lava tube.

No previous work has been conducted and published using this dataset. Prior work was carried out using TIMS data of the 1988 tube fed Kupaianaha lava flow at Kilauea (Realmuto et al 1992). Realmuto identified thermal anomalies of 10°C or more over active lava tubes, and anomalies of 2-5 °C associated with lava emplaced up to 10 months prior to image acquisition. See *Chapter 2: Thermal Infrared Remote Sensing* for a more detailed review of this paper and the *Appendix D* for a TIMS instrument description.

The lava flows imaged in the TIMS dataset from the Pu'U'Oo Episode 53 lava. The Pu'U'Oo eruption sequence prior to 1992 is divided into 55 eruptive episodes of varying duration and extent. Episode 55 consisted of a relatively stable tube fed pahoehoe flow which began when lava from the refilled Pu'u'Oo lava lake flowed out of the crater and began to flow into the sea at Kamaoamoa in November 1992. The episode continued for approximately four years, during which an area of 14.6km^2 was covered by the flow, and a total volume of 535x10^{6}m^3 of rock was extruded.

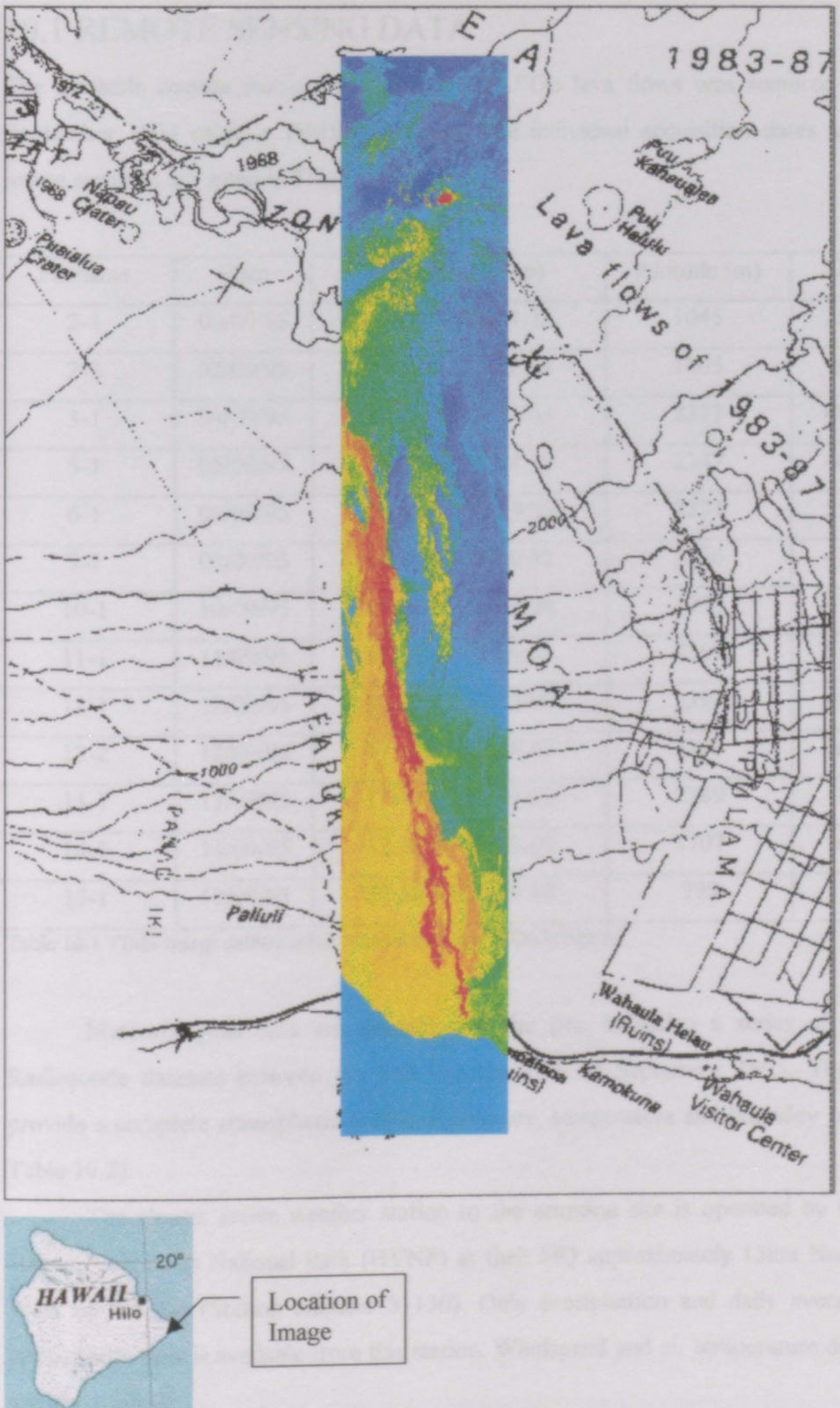


Figure 10.1 False colour enhanced TIMS image map of part of the east rift zone area of Kilauea, Hawaii, overlain on USGS topographic.. Image is approximately 12km long.

10.1 REMOTE SENSING DATA

The available remote sensing data for the Pu'U'Oo lava flows was acquired in September 1994 using a TIMS instrument. The individual acquisition dates and image numbers are listed in Table 10.1

Filename	Date	Time (start/stop)	Altitude (m)	Lines
2-1	02/09/95	23:32:42/23:34:32	1045	2568
2-2	02/09/95	23:50:02/23:52:38	1005	n/a
3-1	03/09/95	19:17:42/19:21/03	2377	4800
5-1	05/09/95	18:21:46/18:24:36	2347	4062
6-1	06/09/95	18:10:06/18:13:55	2374	5532
9-1	09/09/95	18:38:07/18:40:32	2356	4782
10-1	10/09/95	19:05:50/19:09:08	2036	4758
11-1	11/09/95	18:51:46/18:55:35	2365	5556
12-1	12/09/95	16:59:12/17:02:09	2399	4230
12-2	12/09/95	17:05:38/17:08:47	2399	n/a
13-1	13/09/95	17:42:17/17:45:07	2389	4296
14-1	14/09/95	17:58:46/18:02:04	1707	n/a
17-1	17/09/95	20:56:53/20:59:18	799	3361

Table 10.1 TIMS image dataset information for the Pu'U'Oo image set.

Meteorological data are available for the site, including a series of 10 Radiosonde datasets between the 2nd and the 14th of September 1995. These provide a complete atmospheric profile of pressure, temperature and humidity (see Table 10.2).

The closest active weather station to the eruption site is operated by the Hawaii Volcanoes National Park (HVNP) at their HQ approximately 15km North West of Pu'u'Oo (Station Number 51130). Only precipitation and daily average temperature data is available from this station. Windspeed and air temperature data are not available.

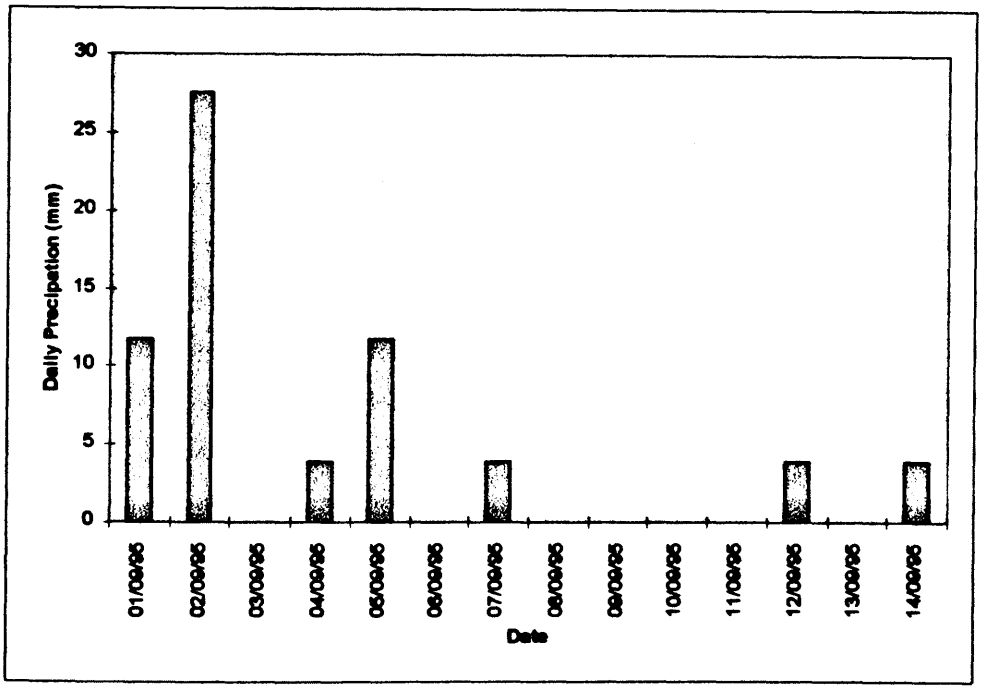


Figure 10.2 Precipitation in mm at the HVNP HQ weather station.

Date	Launch Site	Temperature °C	Relative Humidity	Pressure (mbar)
02/09/95	Chain of Craters	29	61	1009.5
03/09/95	Kalapana	27.05	64.8	1015
05/09/95	Pu'u'Oo	24.22	73.5	932.9
06/09/95	Pu'u'Oo	23.52	94.4	932.7
09/09/95	Kalapana	23.84	70.2	1016.6
10/09/95	Kalapana	26.73	60.3	1011.0
12/09/95	Kalapana	18	83.5	1009.0
13/09/95	Kalapana	18	83.5	1009.1
14/09/95	Kalapana	21.24	90.6	1010.8
14/09/95	Kalapana	27.88	70.4	985.3

Table 10.2 Radiosonde near surface data for the Pu'U'Oo area. Data provided by Elsa Abbott, J.P.L.

For the purposes of direct comparison with surface temperatures predicted by the finite element method, some processing of the data is required to produce a reliable kinetic temperature map. The procedure for carrying out this transformation for TIMS data is described here. The image processing was carried out using a

procedural data processing language called IDL (Student Edition). This resulted in some limitations. The maximum allowable array size of 65536 elements limited the size of the area which could be examined. Image processing scripts written for this process in IDL are included in Appendix G. The area of interest is shown in Figure 10.1, and is approximately 90m wide by 500m long. It lies immediately to the north of the tube mouth, which is at an elevation of approximately 680m.

The initial dataset, when received, had already been preprocessed at the Jet Propulsion Laboratory (JPL) using the TIMSCAL software, which converted the 8 bit digital number into 16 bit radiance values. A subset of the radiance image containing the area of interest was then extracted for processing. The main processing procedure consisted of five steps:

1. Generation of Radiant Temperature Maps.
2. Geometric Correction.
3. Atmospheric Correction considerations.
4. Identification of subpixel thermal anomalies.
5. Generation of Kinetic Temperature Maps.

RADIANT TEMPERATURE MAPS

Radiant temperature maps were generated from the calibrated TIMS radiance data using a lookup table (provided by Ron Alley, Jet Propulsion Laboratory) as described in *Chapter 2: Thermal Infrared Remote Sensing*. A radiant temperature map based on image 6-1 is shown in Figure 10.3. Spectral profiles of the radiant temperature in the 6 TIMS bands for 3 points in the image are also shown in figure 10.3.

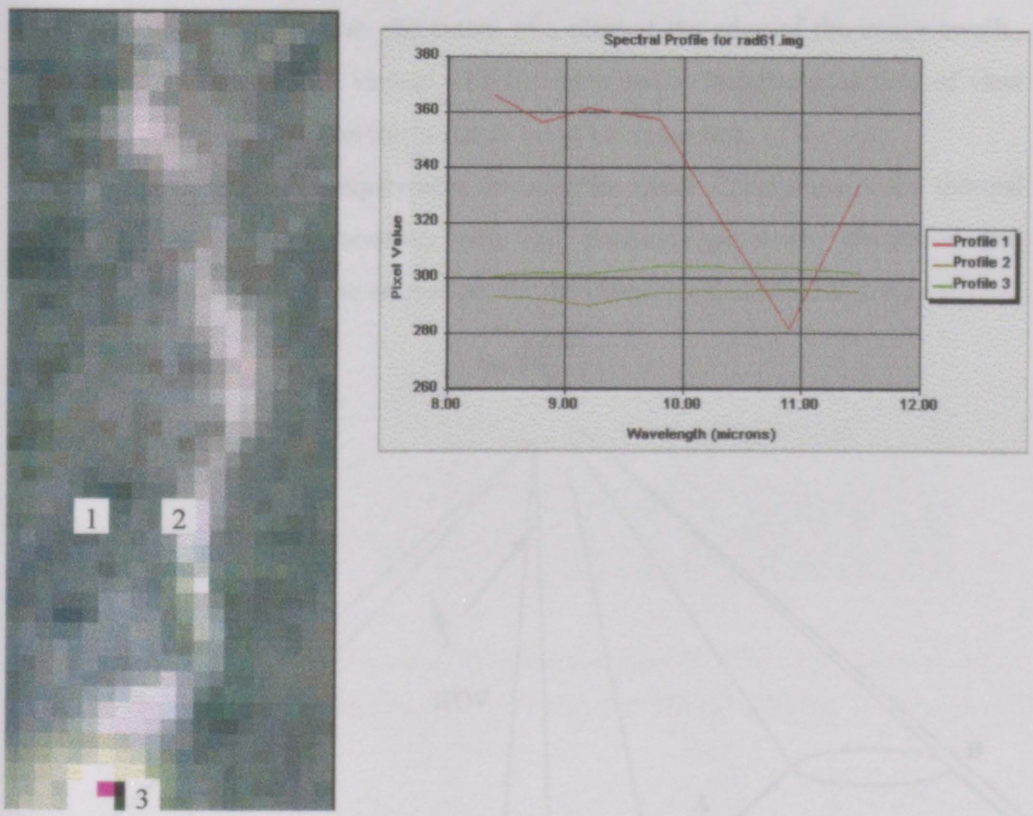


Figure 10.3 Radiant temperature image of the lava tube region, Colour assignments are RGB234, (From Image 06/09/95) Spectral profiles for 3 points in the image are shown. Note that profiles 2 and 3 are fairly uniform, representing regions with 'well behaved' surface temperatures, all six bands being in broad agreement as to the radiant temperature, and variations being due solely to surface emissivity. Profile 3, at a skylight, is 'contaminated' by elevated emission at shorter wavelengths due to a major subpixel hotspot, and possibly also due to effects of fumarole emissions and sensor response.

GEOMETRIC CORRECTION

Satellite based remote sensing systems generally do not require extensive geometric correction as the imaging system is at such great elevation that there is little difference in the pixel sizes between the points directly below the sensor and points at the edge of the swath. However, this is not the case for airborne imaging systems (See Figure 10.4). On the right hand side of the figure describes the origin of topographic distortion. *A* indicates a slope facing the sensor which will appear elongated, where *B* will appear heavily foreshortened. An example of this can be

seen in Figure 10.5. *D* shows the across track extent of a single pixel directly below the sensor (nadir), C shows the extent of a pixel at the edge of the image swath., Note that both pixels are viewed with the same sensor instantaneous field of view (IFOV) and thus appear on the image as being the same size.

Considering the requirement for accurate spatial dimensions of the thermal anomaly, such as the anomaly size and position, geometric correction and rectification will have to be carried out for the image segments under study.

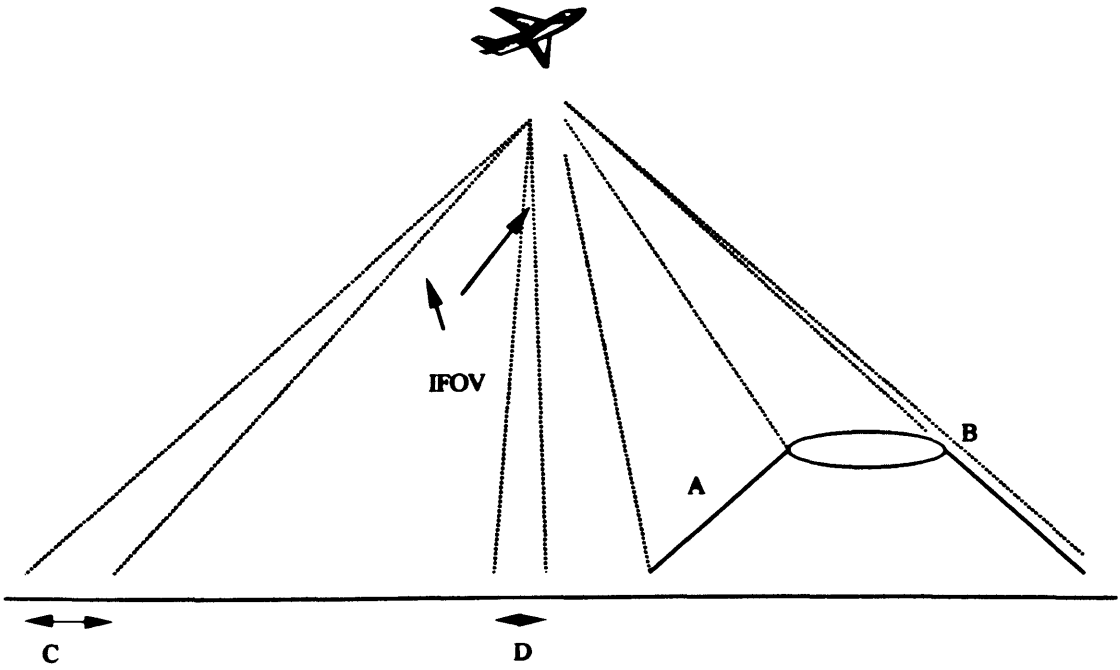


Figure 10.4 The different kind of geometric distortion present in the image. Sensor flight line is perpendicular to the page.

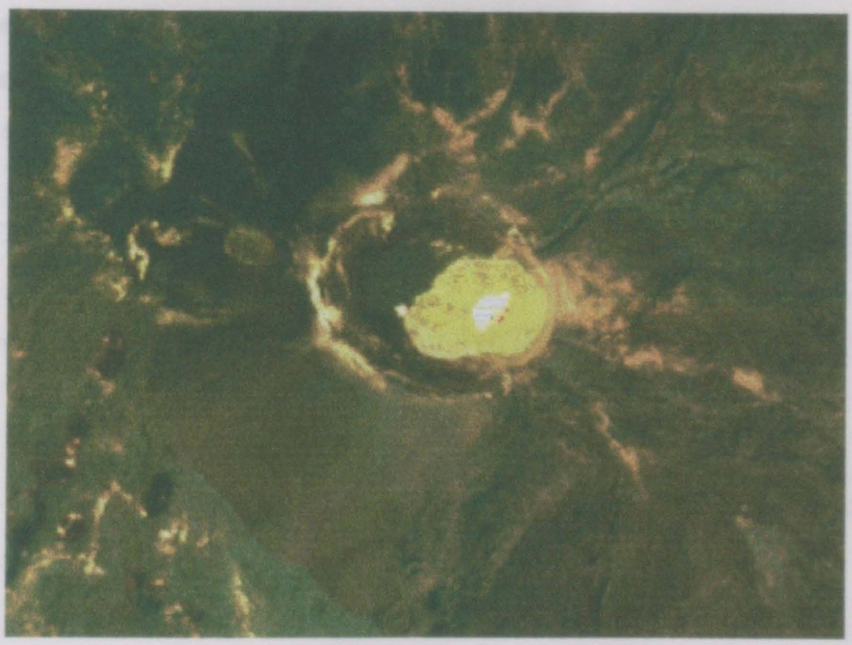


Figure 10.5 An example of geometric distortion due to topographic effects of the type indicated on the right and side of Figure 10.4 (Pu'u'Oo Cinder cone, East Rift zone, Kilauea, TIMS image 6-1, RGB351)

Along Track Resolution

The along track resolution R_{et} of the image segment was calculated by the formula:

$$R_{et}=S_{air}/L_I \qquad 10.1$$

Where:

R_{et} Along Track Resolution (m)

S_{air} Airspeed (600kts/ 304ms^{-1})

L_I Instrument Scan Rate (variable 7.3,8.7,12 or 25 Lines/second)

The along track pixel position can be calculated by multiplying the along track resolution by the line number. All the TIMS images in the dataset were acquired at a scan rate of 25 lines per second, and an airspeed of 206ms^{-1} giving an along track resolution of 8.24m

Across Track Resolution

The across track pixel position can be calculated based on the distance of the pixel from the flight line centre P_a.

$$P_a = hTan(n*2.094x10^{-3}) \qquad 10.2$$

Where:

P_a Distance of pixel from the flight line centre (m)

h Instrument height above the surface (m)

n Number of columns to the flight line centre pixel column (image column number).

The across track resolution R_{at} can be calculated from:

$$R_{at} = P_a(n) - P_a(n-1) \qquad 10.3$$

Where:

R_{at} Across track resolution (m)

After calculation of the correct centre pixel position, the radiant temperature values for each pixel are mapped into a new raster array of 1m resolution pixels, to facilitate direct quantitative comparison of processed data from each image.

ATMOSPHERIC CORRECTION

Atmospheric correction for terrestrial sources is described briefly in *Chapter 2: Thermal Infrared Remote Sensing*. This correction is problematic, and better avoided if possible. Since this study is more concerned with relative temperature contrast than absolute surface temperatures, it is possible to greatly simplify atmospheric correction without interfering with the results.

The degree of atmospheric absorption is proportional to the path length through which the radiation must pass. In the case of TIMS images, the path length variation between the nadir and the edge of the image swath is 22%. To assess the

importance of differential atmospheric absorption on this image, it was assumed that the sea surface temperature was constant (as in Warner and Levandowski 1992).

When the across-track variation in radiant temperature distribution (Figure 10.6) was examined it was found that for all bands of TIMS, the difference in the observed radiant temperature between the centre and edge of their image swath was normally less than 2K. The area of interest is less than 10% of the half swath width. Thus, the variation in observed radiant temperatures across the region is likely to be less than 0.2K, well within an acceptable error range.

Figure 10.6 shows that while within each band there is approximately 1K of limb darkening, there is also significant variation between bands 2,3,4,5 and bands 1 and 6. This may be due to variations in the emissivity of the sea surface from a uniform value, or selective atmospheric absorption at longer wavelengths. In either case, the effect can be removed by careful selection of an emissivity curve which will generate the same kinetic temperature from all six radiant temperatures, as described in the section below

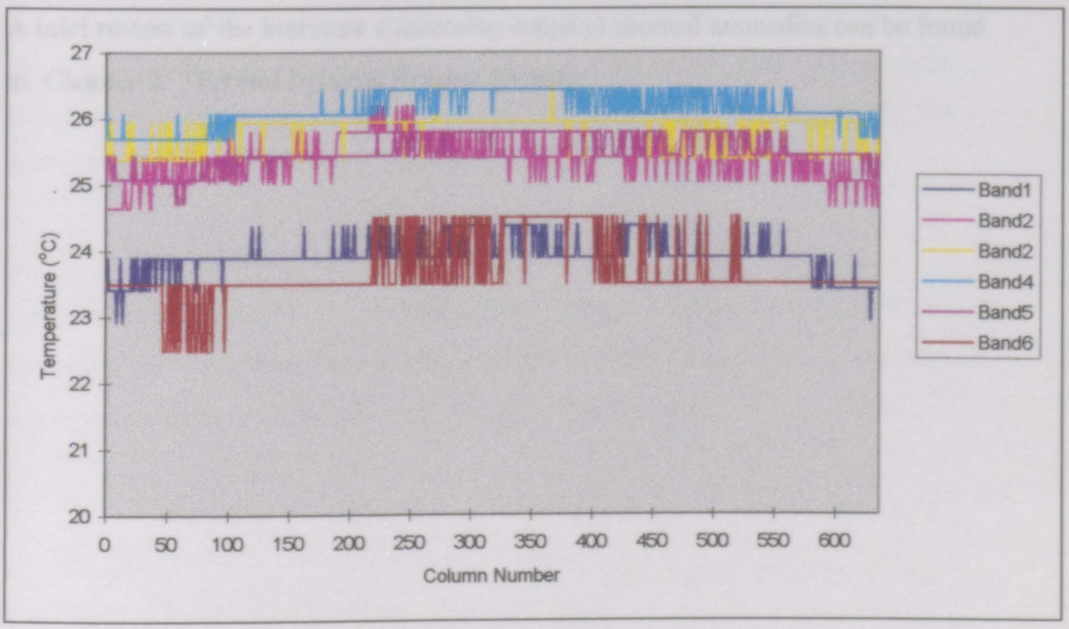


Figure 10.6 The effect of atmospheric absorption due to longer path lengths towards the edge of the TIMS image swath. Data is extracted from a segment of image 5-1 over the sea, which is assumed to have a uniform surface temperature and emissivity (0.98). Note the 'limb darkening' effect reducing the observed radiant temperature at the edges of the images.

SUBPIXEL THERMAL ANOMALIES

Subpixel fractures and vents have the effect of increasing the measured pixel temperature. Before selecting surface temperature profiles to compare with analytic model, it is necessary to identify regions containing subpixel thermal anomalies so that they can be avoided. There would be little benefit in modelling the thermal distribution over a lava tube if that distribution was in fact due to increased surface fracturing and not heat transfer within the basalt.

For multiband data, hot subpixel anomalies will have the effect of disproportionately increasing the observed radiant temperature at shorter wavelengths, as shown in Figure 10.7.

Assuming spatially uniform emissivity, regions with subpixel thermal anomalies can be crudely identified as areas with unusually high differences between the Band 1 and Band 6 radiant temperatures. Variation due to subpixel thermal anomalies can thus be avoided by excluding sections that have such characteristics. A brief review of the literature concerning subpixel thermal anomalies can be found in. *Chapter 2: Thermal Infrared Remote Sensing.*

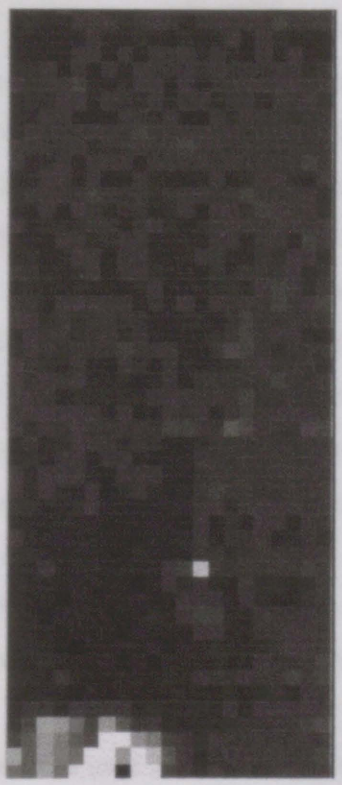


Figure 10.7 Diifference image between the Band 1 and Band 6 radiant temperatures. For most of the region the differences are constant in the order of 1-2 °C (black areas), due to emissivity variations between the two bands. At skylights, the differences are much higher, due to anomalously high shorter wave emissions due to the hot subpixel regions.

KINETIC TEMPERATURE MAPS

For direct comparison of results from thermal modelling with observed temperatures, the radiant temperatures must be converted to kinetic temperatures. Radiant and kinetic temperatures are related by the formula:

$$T_r^4 = \varepsilon T_k^4 \qquad 10.4$$

(Cracknell and Xue 1997)

Where:

T_r Radiant Temperature (K)

T_k Kinetic Temperature (K)

ε Emissivity

While approximate emissivity curves for basalt flows are available (e.g. Realmuto et al 1992) the emissivity is spatially and spectrally variable, particularly in the regions with geothermal heat sources. Fresh basalt flow surfaces can vary in emissivity from 0.98-0.90 across the range of sensitivity of the TIMS instrument (Realmuto et al 1992) as shown in Figure 10.8. Variation of the emissivity between these end values produces a variation in the average kinetic temperature of 6.5°C. Published curves of basalts of various ages are included in Figure 10.8 for comparison (Realmuto 1989). Note the disagreements in the region of TIMS bands 3 and 4 (central wavelengths 9.2 and 9.8μm). These may be due to relatively strong absorption due to stretching vibrations of sheet silicates (the 'B' feature in Crisp, Kahle and Abbott 1990) and weaker absorption due to chain silicates (the 'C' feature in Crisp, Kahle and Abbott 1990). The disagreements may also be due to differential atmospheric absorption in the different bands, which has not been previously corrected for.

The emissivity curve to be used in calculating the kinetic temperature could come either from published sources or could be calculated directly from the image using pixels without subpixel thermal sources and estimating a kinetic temperature from that pixel. In both cases there are possibilities for further error. Published curves may not be appropriate to the specific study area (and in any case, may use estimated kinetic temperatures in their derivation), and the pixel selected for calculation of the emissivity may be incorrect or have an incorrect estimate of surface kinetic temperature.

In this study, the emissivity curve was derived by assigning the band 6 an emissivity of 0.95 consistent with known emissivities of silicates at that band (reference channel method, see Kealy and Hook 1993) and calculating the emissivities from this reference value. This produces kinetic temperatures derived from each band which are in agreement to within 1°C. These are then averaged to produce an overall kinetic temperature map, an example of which is shown in Figure 10.9.

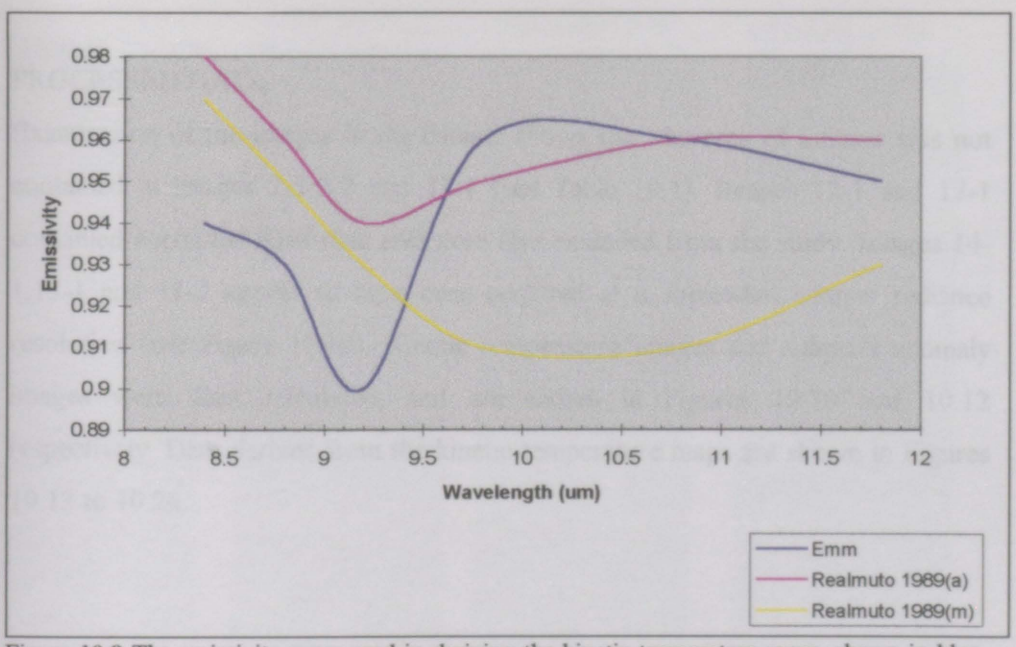


Figure 10.8 The emissivity curve used in deriving the kinetic temperature maps, shown in blue, compared with the maximum and minimum ranges measured by Realmuto (1989).

Thus a kinetic temperature map can be generated from the measured TIMS radiance. From this, surface temperature profiles for comparison with modelled values, are extracted.

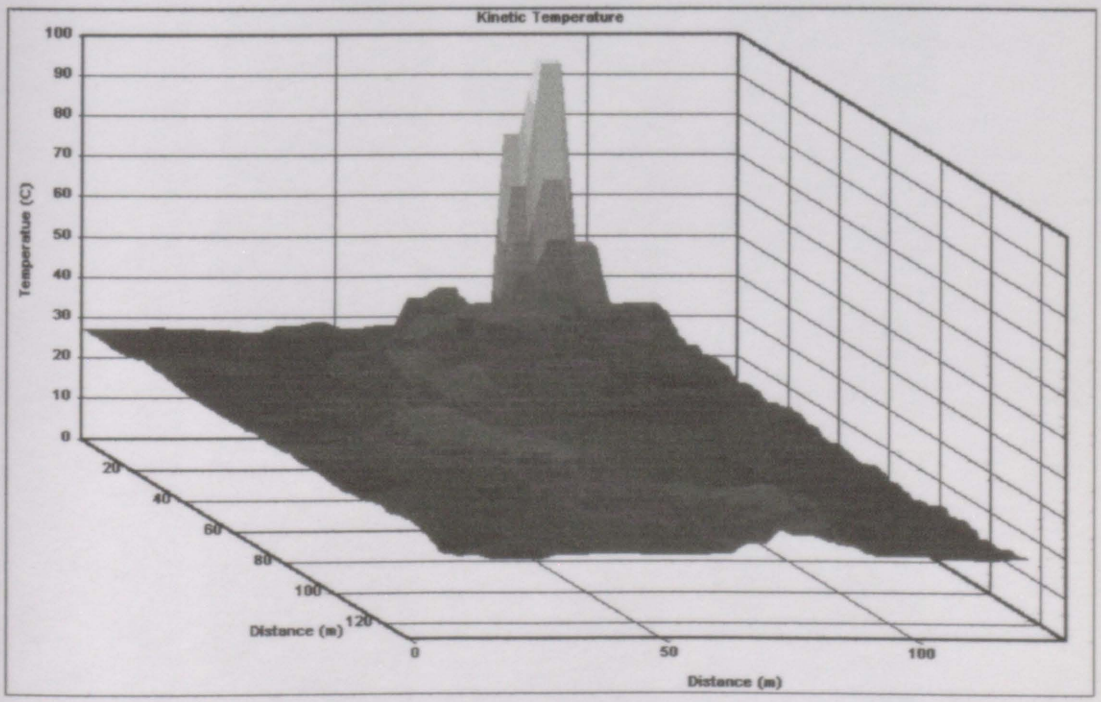


Figure 10.9 A 3-D plot of the derived surface kinetic temperature (From image 6-1). Kinetic Temperature axis is in degree centigrade.

PROCESSED DATA

Examination of the images in the dataset shows that the area of interest was not contained in images 2-1,2-2 and 17-1 (see Table 10.1). Images 12-1 and 17-1 contained corrupted band data and were also excluded from the study. Images 14-1,13-1 and 11-1 appear to have been acquired at a somewhat coarser radiance resolution (see Figure 10.10). Kinetic temperature images and subpixel anomaly images were then calculated, and are shown in Figures 10.10 and 10.12 respectively. Data derived from the kinetic temperature maps are shown in Figures 10.13 to 10.24.

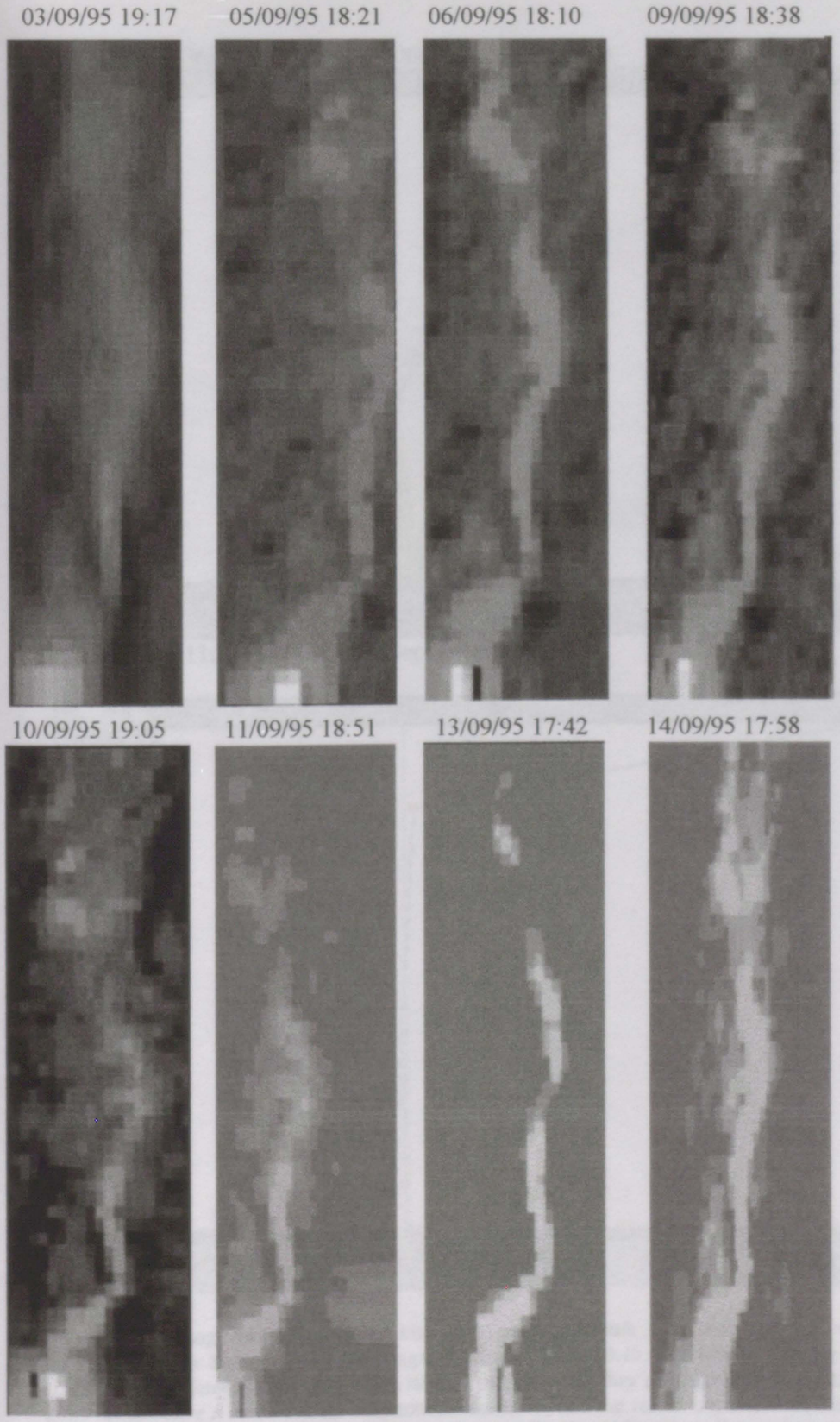
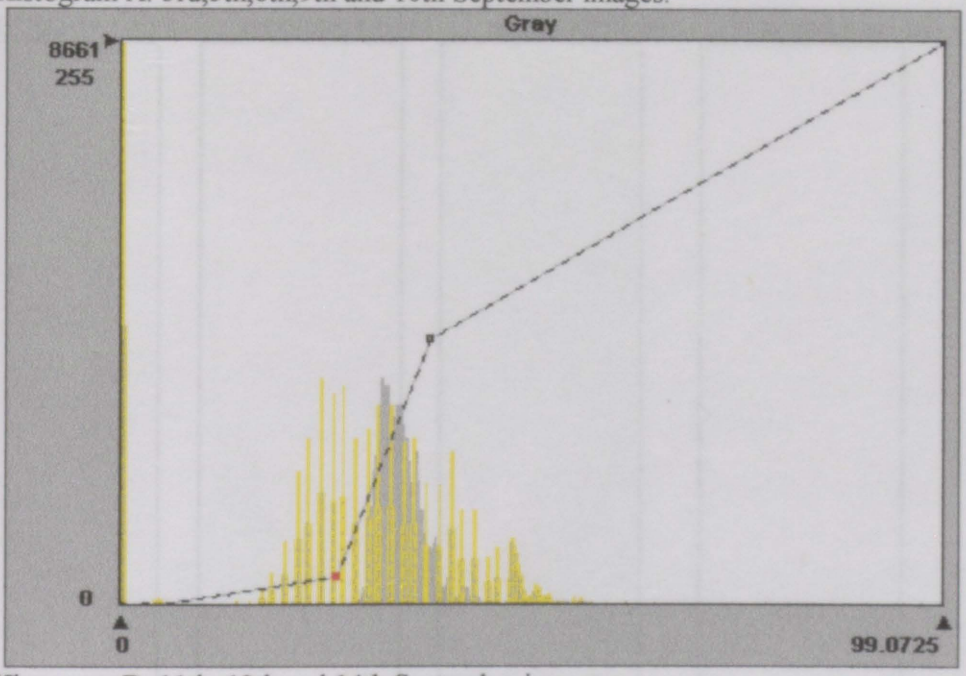


Figure 10.10 The kinetic temperature images, processed and geometrically corrected as described in text, for the region under study. Images represent areas 120m across by 500m long. Image greyscales vary, but all image temperatures are in span a 10-15Krange.

Histogram A: 3rd,5th,6th,9th and 10th September images.



Histogram B: 11th, 13th and 14th September images

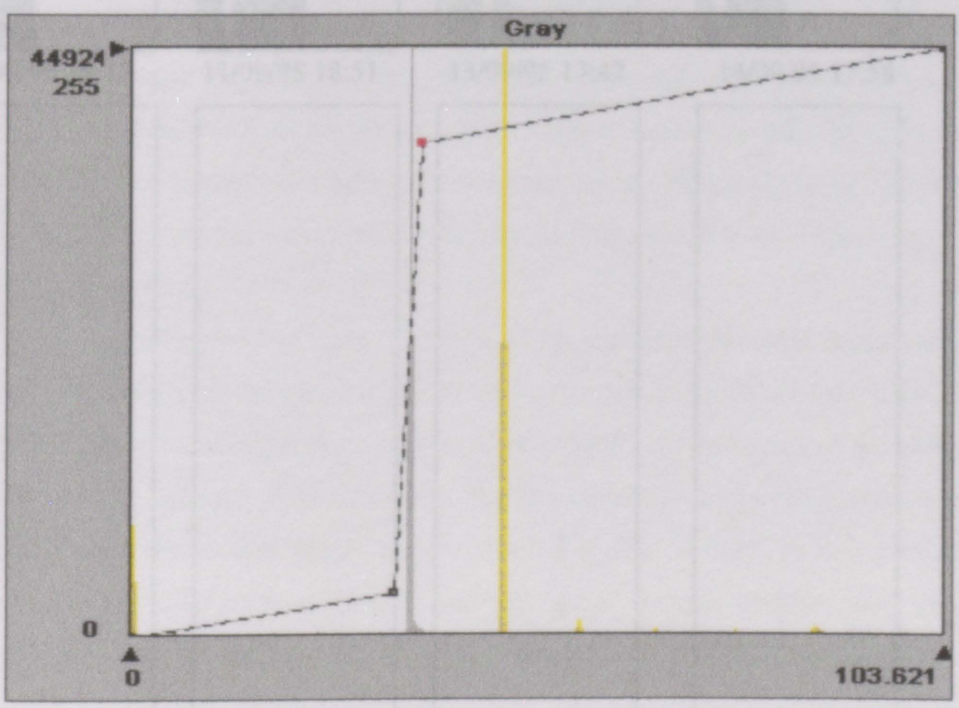


Figure 10.11 Image histograms (gray histogram) applied stretch (line) and resultant image histogram (yellow histogram) for the images shown in Figure 10.10. The first five images were acquired at a different sensor gain to the later three, and while they give similar results, the last three images have a much coarser temperature resolution, and the results are effectively 'sliced' into broader temperature bins at acquisition. This results in tonally much flatter images, with reduced information content.

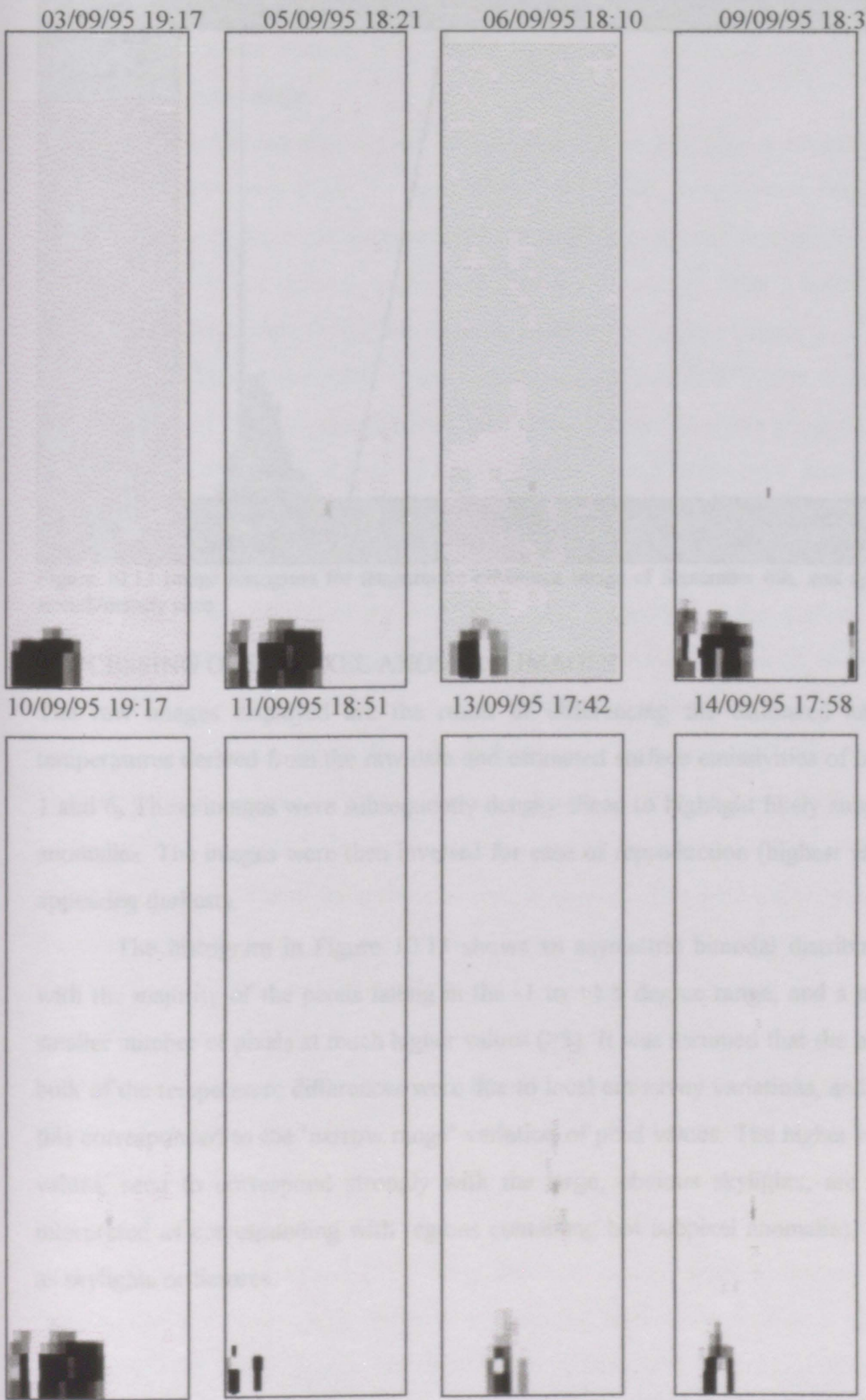


Figure 10.12 Band 1 minus band 6 radiant temperatures images, an approximate indicator of subpixel thermal sources. Images represent areas 120m across by 500m long.

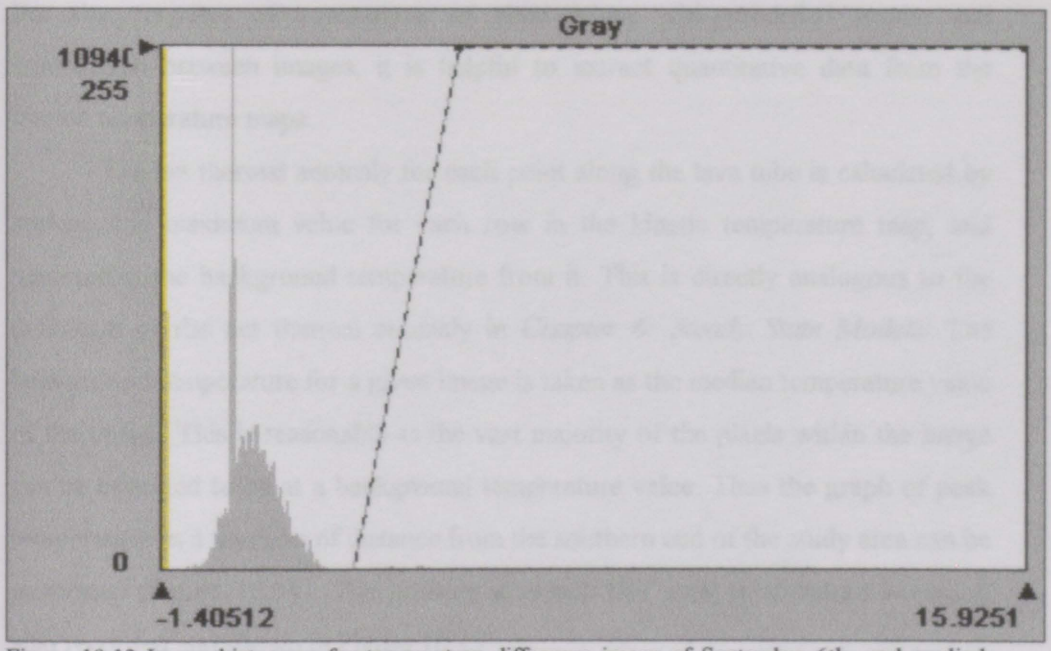


Figure 10.13 Image histogram for temperature difference image of September 6th, and applied stretch/density slice.

PROCESSING OF SUBPIXEL ANOMALY IMAGES

The raw images displayed are the result of differencing the estimated kinetic temperatures derived from the raw data and estimated surface emissivities of bands 1 and 6. These images were subsequently density sliced to highlight likely subpixel anomalies. The images were then inverted for ease of reproduction (highest values appearing darkest).

The histogram in Figure 10.13 shows an asymettric bimodal distribution, with the majority of the pixels falling in the -1 to +1.5 degree range, and a much smaller number of pixels at much higher values (>5). It was assumed that the broad bulk of the temperature differences were due to local emissivity variations, and that this corresponded to the 'narrow range' variation of pixel values. The higher range values, seen to correspond strongly with the large, obvious skylights, are thus interpreted as corresponding with regions containing hot subpixel anomalies, such as skylights or fissures.

UNIVERSITY COLLEGE CORK Library

QUANTITATIVE RESULTS

For the purposes of comparison of observations with modelled results and comparison between images, it is helpful to extract quantitative data from the kinetic temperature maps.

The net thermal anomaly for each point along the lava tube is calculated by seeking the maximum value for each row in the kinetic temperature map, and subtracting the background temperature from it. This is directly analogous to the definition of the net thermal anomaly in *Chapter 6: Steady State Models*. The background temperature for a given image is taken as the median temperature value of the image. This is reasonable as the vast majority of the pixels within the image can be expected to be at a background temperature value. Thus the graph of peak temperature as a function of distance from the southern end of the study area can be generated (Figure 10.14). The position at which this peak temperature occurs is also recorded and shown in Figure 10.15.

The geometric size of the lava tube is also considered in the analyses. The edge of the tube generated thermal anomaly is chosen as the point at which the temperature drops to less than one degree above the background. This is chosen, both as a convenient threshold and to facilitate comparison with the thermal anomaly size figure from the finite element models. The value is derived by starting at the column containing the maximum value for each row and moving left (or right) along the row until the threshold value is reached. The distance between the maximum value position and the threshold value position is then plotted for each side of the lava tube (see Figures 10.17,10.18) to gain a measure of the anomaly size which can be used for comparison with numerical models. Figure 10.19 shows the difference between the values for each side. Note how large and variable the difference is. For an ideal heat source in a homogenous medium, the thermal anomalies should be symmetric, and all the values in Figure 10.19 should be zero. The complexity of Figure 10.19 indicates just how far the real environment differs from an idealised case. Figure 10.20 shows the total anomaly width for the first five images, and a average value. Note how while the total width follows a clearer pattern than the width of each side, there is still, at best, 20m of variation from day to day. In Chapter 6 we noted that thermal anomaly size was very sensitive to

meteorological factors, and at Pu'U'Oo we see a concrete example of this sensitivity.

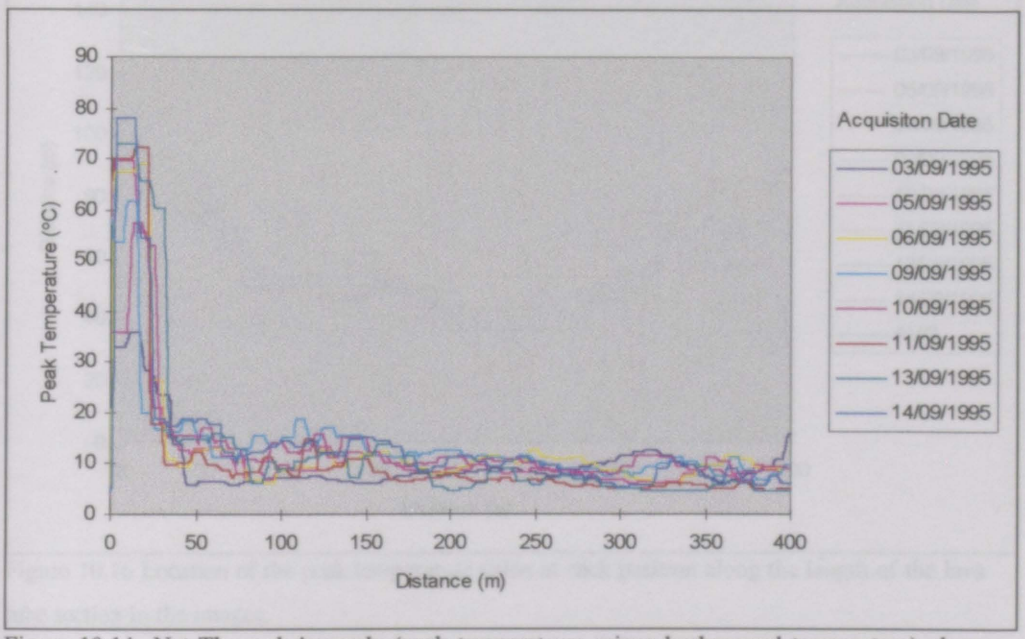


Figure 10.14 Net Thermal Anomaly (peak temperatures minus background temperature) along the length of the lava tube section in the images.

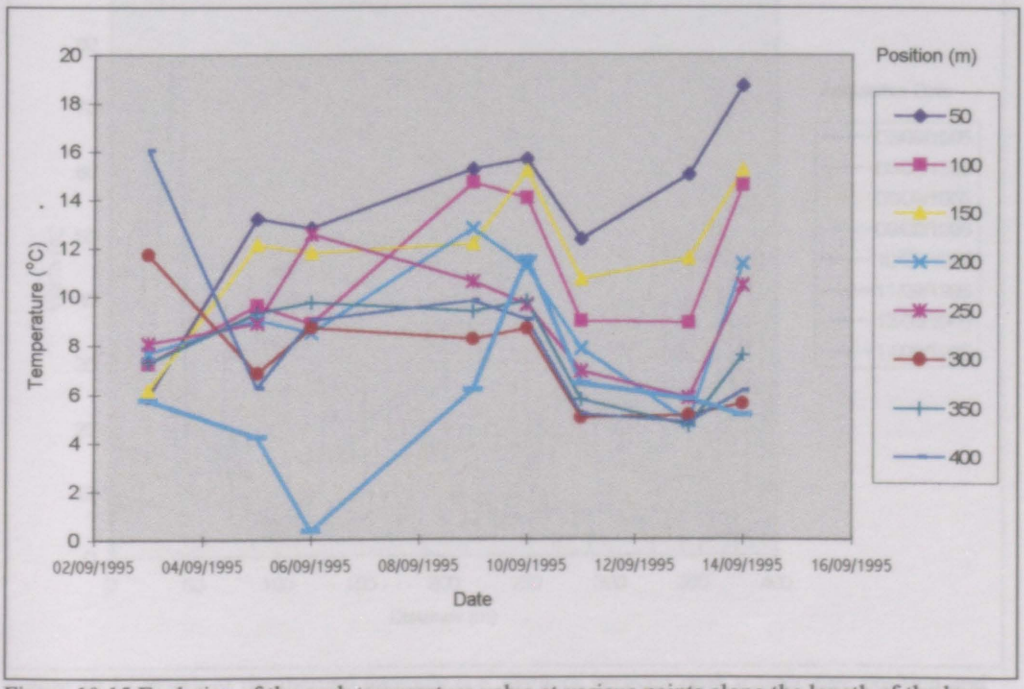


Figure 10.15 Evolution of the peak temperature value at various points along the length of the lava tube section in the images. The median temperature value (less 25°C to allow same scale comparison) for each scene is also shown for comparison (thick blue line).

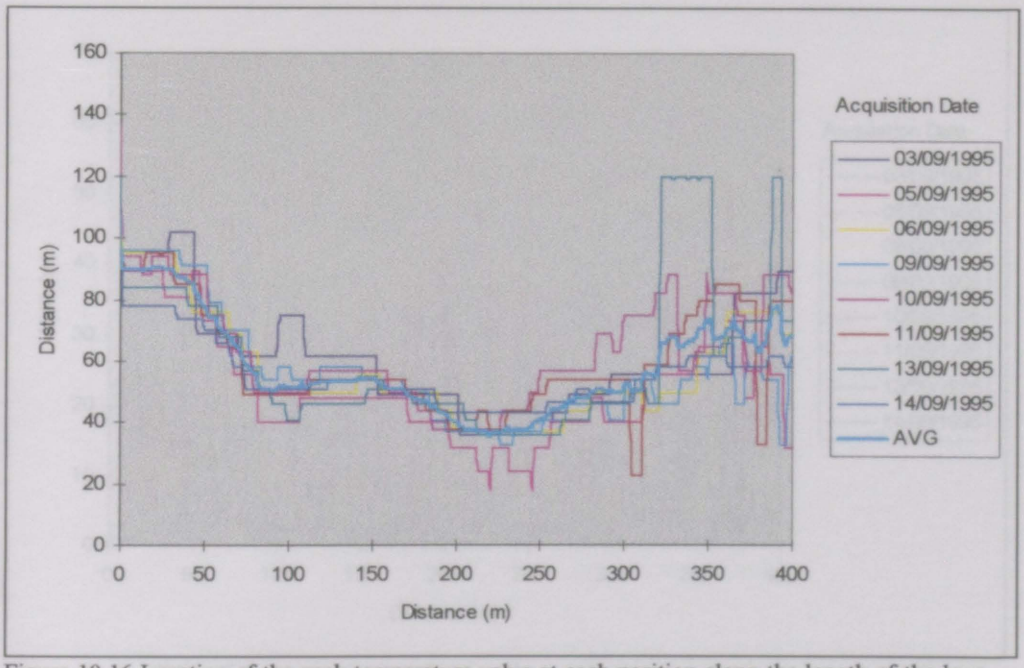


Figure 10.16 Location of the peak temperature value at each position along the length of the lava tube section in the images.

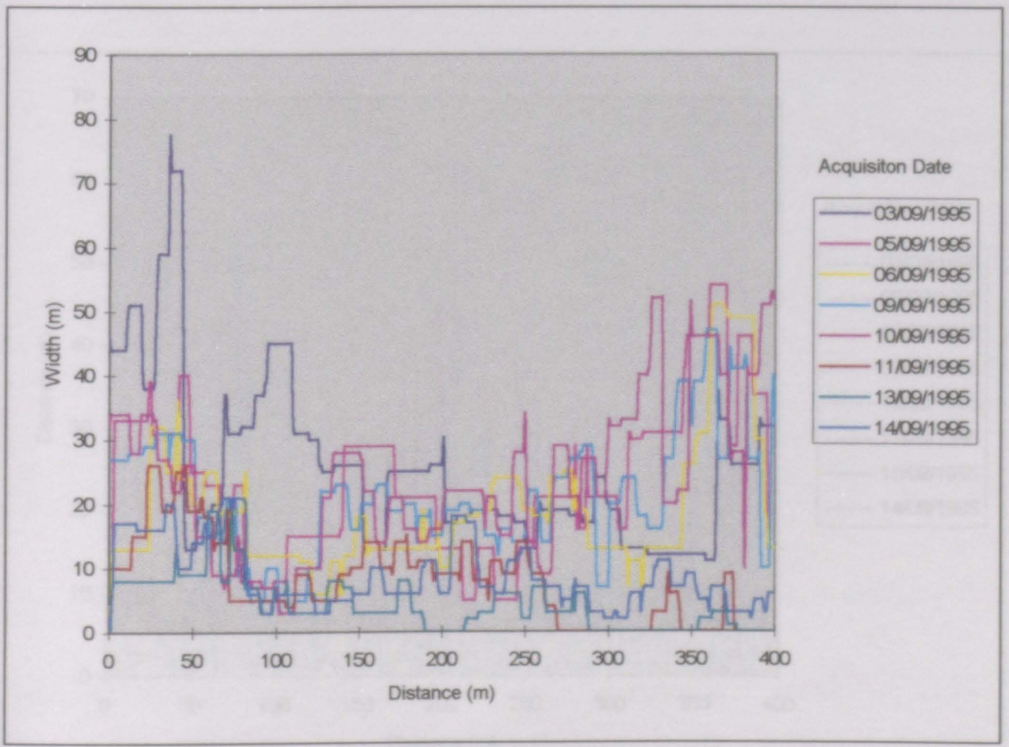


Figure 10.17 Width of the thermal anomaly (i.e. distance between peak temperature position and the point where the temperature drops to less than 1 degree above the background temperature) to the west of the tube at each position along the length of the lava tube section in the images.

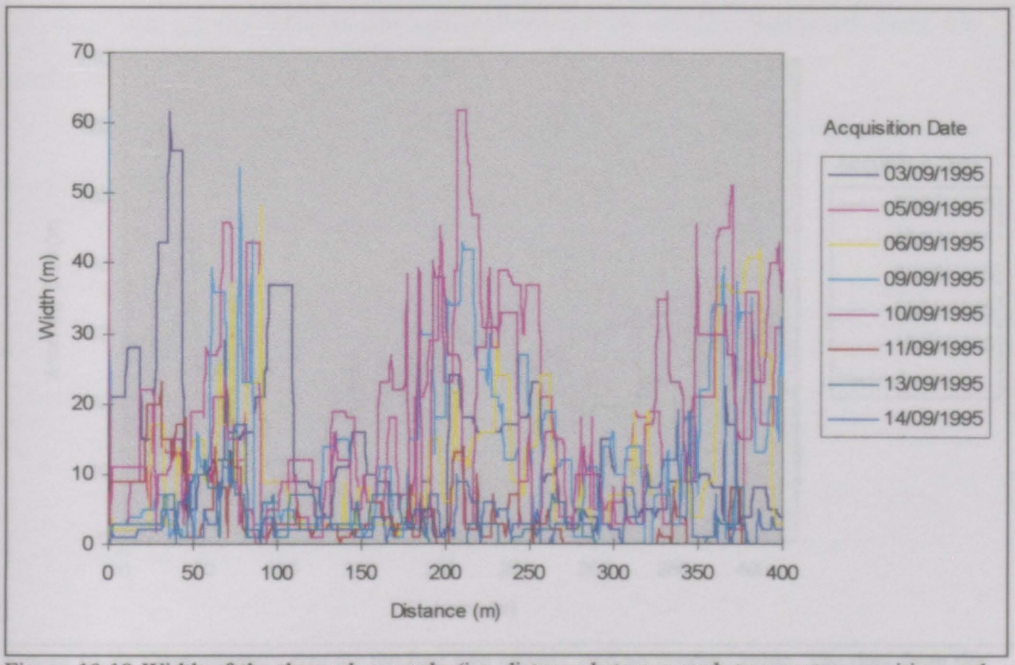


Figure 10.18 Width of the thermal anomaly (i.e. distance between peak temperature position and the point where the temperature drops to less than 1 degree above the background temperature) to the east of the tube at each position along the length of the lava tube section in the images.

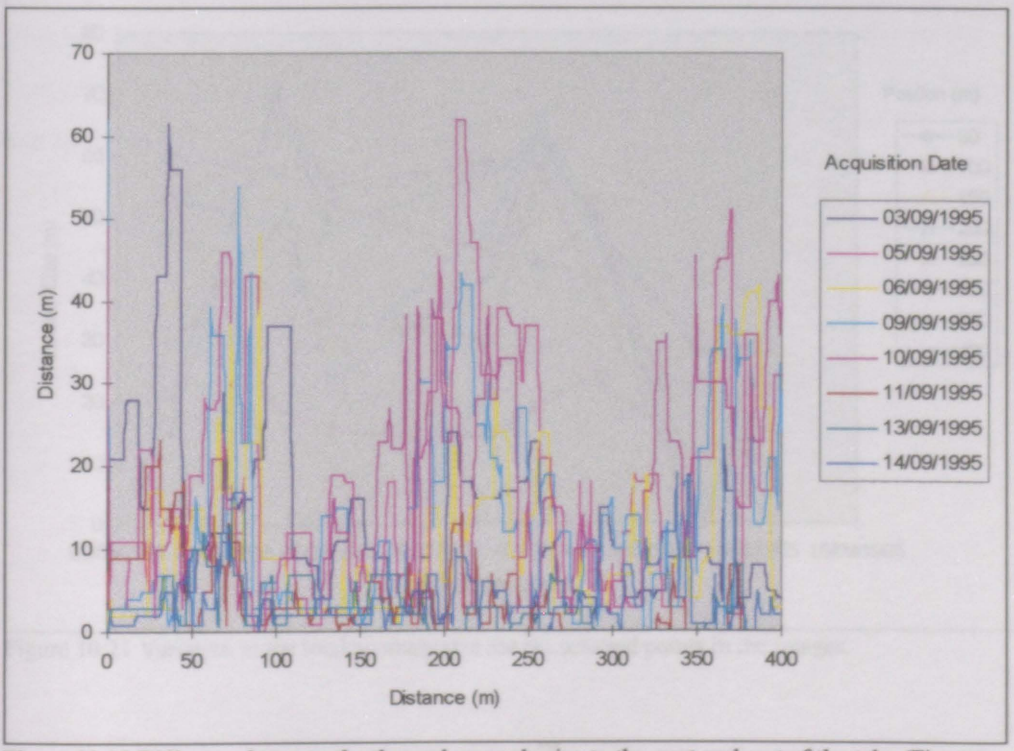


Figure 10.19 Difference between the thermal anomaly size to the west and east of the tube (Figures 10.15 and 10.16) for each position along the length of the lava tube section in the images.

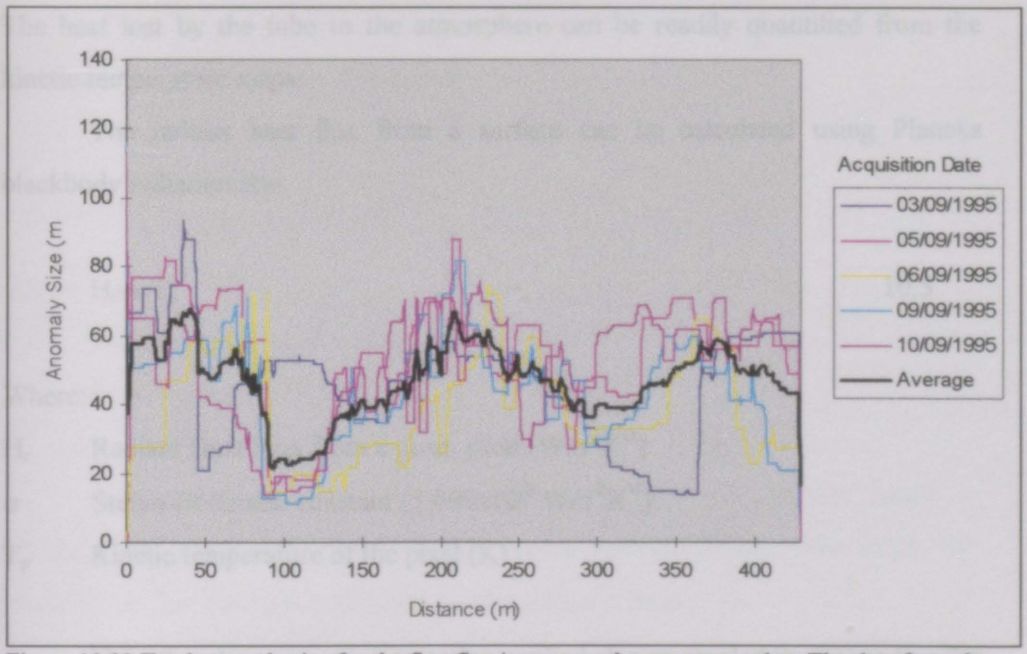


Figure 10.20 Total anomaly size for the first five images, and an average value. The data from the last three images is not included as anomaly size values are poor. The average values are shown with a heavy black line.

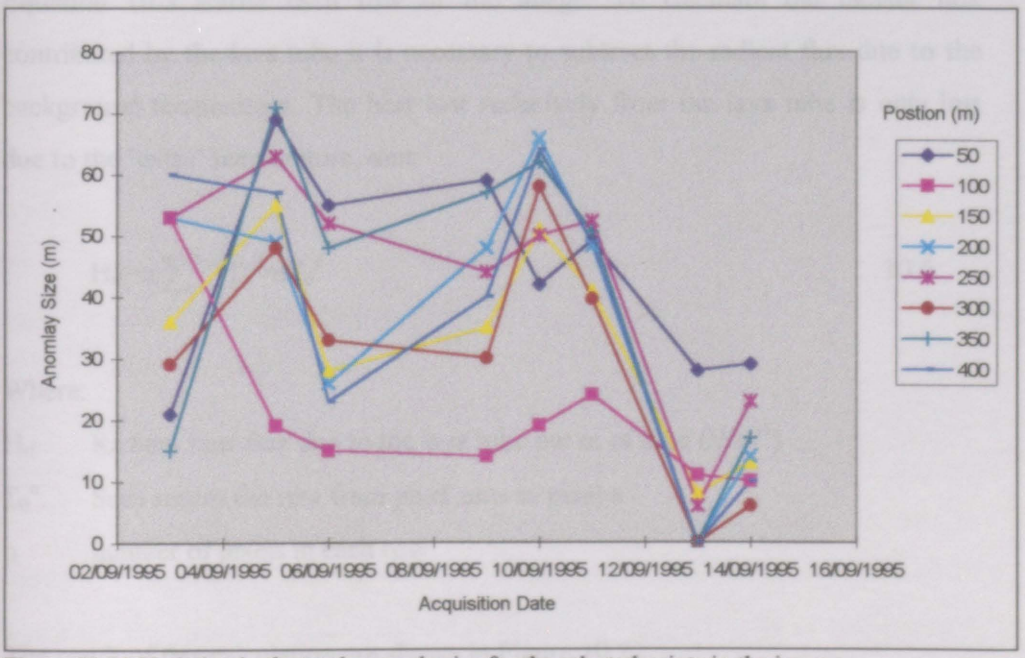


Figure 10.21 Variation in the total anomaly size for the selected points in the images.

HEAT FLUXES

The heat lost by the tube to the atmosphere can be readily quantified from the kinetic temperature maps.

The radiant heat flux from a surface can be calculated using Plancks blackbody radiation law:

$$H_r=\sigma T_p^4 \qquad 10.5$$

Where:

H_r Radiant Heat Flux from a given pixel ($Wm^{-2}K^{-1}$)

σ Stefan-Boltzman constant ($5.669x10^{-8}$ $Wm^{-2}K^{-4}$)

T_p Kinetic temperature of the pixel (K)

Note that the geometric correction applied also resampled the image to a 1m square pixel size, thus area conversions are not required for the calculation.

The radiant flux per metre length of the lava tube is calculated by integrating Equation 10.5 across each row of the image. To calculate the radiant flux contributed by the lava tube it is necessary to subtract the radiant flux due to the background temperature. The heat lost radiatively from the lava tube is only lost due to the 'extra' temperature, thus:

$$H_{rl}=\sigma \sum_o^n T_p^4-nT_b^4 \qquad 10.6$$

Where:

H_{rl} Radiant heat flux due to the lava tube per m of tube (Wm^{-1})

Σ_0^n... Sum across the row from pixel zero to pixel n

n number of pixels in each row

The result of this calculation are shown in Figure 10.22

A similar process is used to calculate the heat loss due to sensible heat transfer. From Newton's Law of cooling, the sensible heat flux from a given pixel can be shown as an equation of the form:

$$H_s=h(T_p-T_a) \qquad 10.7$$

Where:

h Sensible Heat flux transfer coefficient ($Wm^{-2}K^{-1}$)

T_a Air Temperature (K)

As with radiant heat fluxes, the value per metre of the tube length is calculated by integrating equation 10.7 across each row, and subtracting the sensible heat flux due to the background temperature, thus:

$$H_{rs}=h(\Sigma_0^n T_p-\Sigma_0^n T_a)- h(\Sigma_0^n T_b-\Sigma_0^n T_a) \qquad 10.8$$

The terms containing the air temperature cancel, leaving:

$$H_{rs}=h(\Sigma_0^n T_{pa}- \Sigma_0^n T_b) \qquad 10.9$$

Where:

H_{rs} Sensible heat flux from a given pixel row (W)

T_{pa} Anomalous temperature (K)

T_b Background temperature (K)

T_a Air temperature (K)

The value of h is not known, and there is insufficient meteorological data to derive it. It is assumed to be at unity to calculate the results shown in Figure 10.20 which are thus per unit heat transfer coefficient h. The intricacies of calculating h are discussed in *Chapter 3: The Physical Model.*

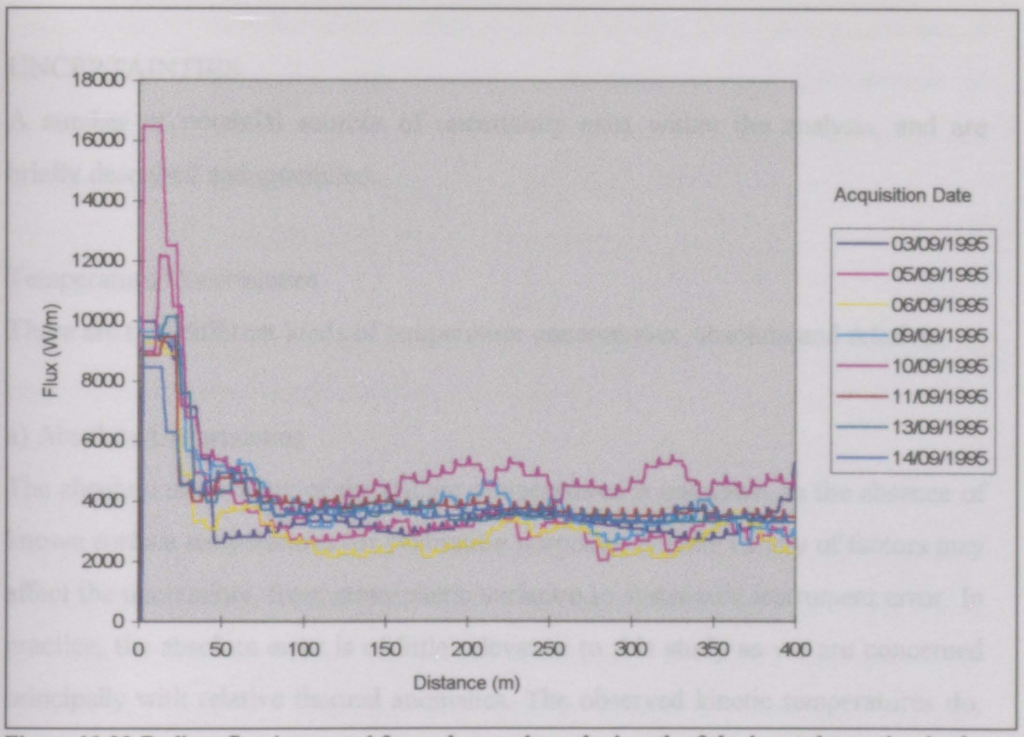


Figure 10.22 Radiant flux integrated for each row along the length of the lava tube section in the images.

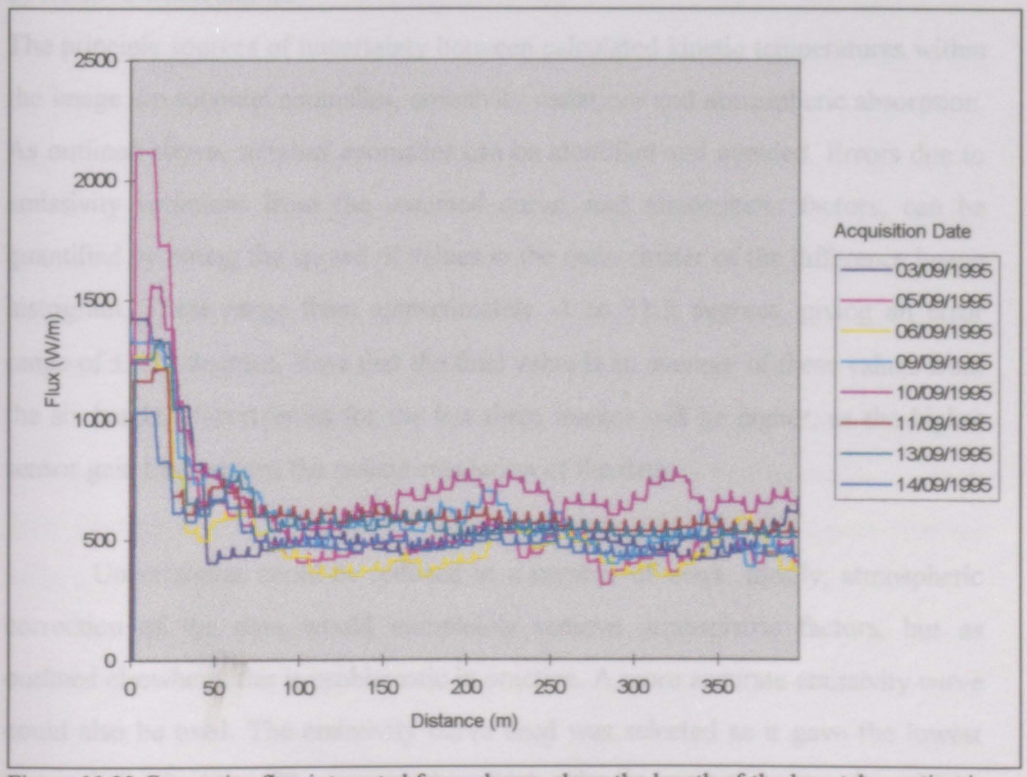


Figure 10.23 Convective flux integrated for each row along the length of the lava tube section in the images, for a convective heat transfer coefficient (h) of $1 Wm^{-2}K^{-1}$.

UNCERTAINTIES

A number of potential sources of uncertainty exist within the analysis, and are briefly described and quantified.

Temperature Uncertainties

There are two different kinds of temperature uncertainties, absolute and relative.

a) Absolute Uncertainties

The absolute uncertainty of the radiant temperatures is unknown, in the absence of known surface temperatures for calibration purposes. A wide variety of factors may affect the uncertainty, from atmospheric variation to systematic instrument error. In practice, the absolute error is of little relevance to this study as we are concerned principally with relative thermal anomalies. The observed kinetic temperatures do, however, seem to give reasonable values for the environment.

b) Relative Uncertainties

The principle sources of uncertainty between calculated kinetic temperatures within the image are subpixel anomalies, emissivity variations and atmospheric absorption. As outlined above, subpixel anomalies can be identified and avoided. Errors due to emissivity variations from the assumed curve, and atmospheric factors, can be quantified by noting the spread of values in the main cluster of the difference image histogram. These range from approximately -1 to +1.5 degrees, giving an error range of ±1.25 degrees. Note that the final value is an average of these values from the six bands. Uncertainties for the last three images will be higher, as the higher sensor gain has reduced the radiant resolution of the data.

Uncertainties could be reduced in a number of ways. Ideally, atmospheric correction of the data would completely remove atmospheric factors, but as outlined elsewhere, this is problematic in practice. A more accurate emissivity curve could also be used. The emissivity curve used was selected as it gave the lowest uncertainties in tests. The process by which this curve was generated could be enhanced to derive a unique emissivity curve for every location in the array.

Detailed on site mapping of the surface emissivity using a field spectrometer would also reduce or eliminate such uncertainty. Contemporaneous measurement of surface kinetic temperatures would provide data points for absolute calibration and would further reduce uncertainties.

Spatial Uncertainties

Spatial uncertainties can be divided into two categories, Geometric correction errors and anomaly size uncertainties.

a) Geometric correction errors

The principle source of spatial uncertainty in the dataset comes from the process of geometric correction of the images. Within the image swath, and particularly within the area of interest, very few readily identifiable landmarks for spatial co-registration exist. To facilitate approximate geometric correction and co-registration of images two assumptions were made.

Firstly, it was assumed that the area of interest started at the brightest pixel of the fumarole. The fumarole is, however, not a fixed landmark, but may evolve and change position and shape dynamically with time. This will result in along track variations in image co-registration of a maximum of 2 or 3 pixels (up to 25m). Slight variations of this nature can be identified on close inspection of the images, but in general, the wavelength of surface features is longer than the spatial uncertainty, and thus is not significant. The brightest fumarole position was also chosen as a fixed point for across track co-registration, resulting in similar variations in the across track co-registration (See Figure 10.16)

Secondly, it was assumed that the flight lines were parallel. This is apparent by inspection of the full flight line images. Figure 10.16, however, shows variation in the peak temperature position of up to 15m between images. Some peak position paths appear to cross over, and this is probably due to non-parallel flight lines.

In summary, spatial position uncertainties are approximately 25m (along track) and 15m (across track). There is little scope for improving this in the current dataset. However, given the nature of the data being extracted this spatial uncertainty does not compromise the results, as only relative spatial data (anomaly size) is sought, rather than absolute positions.

b) Anomaly size uncertainties.

A visual inspection of the data in Figures 10.17 and 10.18 shows that they are spatially very 'noisy'. This is due to the fact that selection of the threshold value (one degree greater than the minimum temperature) is subject to considerable absolute uncertainty. While spatial uncertainties in the data can be largely filtered by the process of extracting a difference between two spatial positions rather than an absolute position, the uncertainty in the kinetic temperature leaves great range for error. Given the kinetic temperature error range of ±1.25°C, the threshold temperature may be in error by up to 2.5 °C. This could lead to significant spatial errors of up to 20-30m. The 'binning' of values which has taken place in the last three images increases these kinetic temperature uncertainties still further, degrading the accuracy of the result and as a result, the quantitative utility of anomaly size data is severely impaired. Qualitative trends are, however, evident from the data.

DISCUSSION

The kinetic temperature maps shown in Figure 10.10 give a broad overview of the surface temperature distribution. The change in instrument settings after September 10th make visual interpretations difficult. However, it is possible by inspection to subdivide the lava tube into five different segments. Note that spatial locations along the tube use the main fumarole location as the origin.

Segment A is dominated by the main lava tube fumarole, and occupies the lower 50m of the image. This can be clearly identified in all Figures. The size and shape of this region varies over time. This is due to a number of factors. Different sampling occurs between images as the imaging pixels fall across the skylight region in different ways in each image. The skylight shape itself may be evolving over time as sections roof over and others collapse. Gas emission at the skylight may also be affecting the signature, as thermal emission from hot gases will affect the measured temperature. In the subpixel anomaly map (Figure 10.12) the skylight intensity seems to diminish drastically in the last three images of the set. This is again an artefact of the different image acquisition settings. The reduced gain leads to

temperature values from bands 1 and 6 (which would be in sufficient disagreement to suggest a fumarole) being binned to the same measured value.

Heat flow from this region is dominated by large scale radiative transfer from the skylights, in the range of 10-15kWm^{-1} of tube. Convective transfer is very high, and convective heat transfer coefficients (by which the value plotted in Figure 10.23 must be multiplied to gain a true figure) are very high also, but cannot be estimated from available data.

Segment B shows a relatively narrow, hot thermal signature, and runs from 50m to 150m north of the fumarole. The region shows a relatively narrow thermal signature (<40m) and somewhat variable peak temperatures in the 10 degree range. The subpixel anomaly map suggests a small skylight approximately 120m north of the main fumarole. This feature is evident in the images from the September 5th onwards, and is strongly enhanced in the images on the September 13th and September 14th, when small satellite skylights appear. The tendency of the data in the last three images to mask skylights suggest that major fissuring or 'unzipping' of the lava tube roof may be taking place. Heat fluxes in the segment are slightly low, in the 4000Wm^{-1} range for the radiant fluxes and 500Wm^{-1} per unit h for the convective fluxes. Based on comparison with theoretical models investigated in *Chapter 6: Steady State Models*, this suggests a narrow, shallow tube.

Segment C shows a broader, cooler thermal signature, and runs for the remainder of the study area. The thermal anomaly size is wider (>40m) and the peak thermal anomaly temperature is fairly steady, averaging around 8 degrees. Heat fluxes in the segment lie in the 4000Wm^{-1} range for the radiant fluxes and 600Wm^{-1} per unit h for the convective fluxes. No skylights are evident in the region. This suggests a deeper lava tube.

In some of the images an apparent gap or offset occurs in the lava tube at approximately 320-350m. This is most evident in the image and derived data from 13/09/95 (see Figure 10.10). The feature is unclear, and does not appear in all images. It may represent a short, sudden dip in the lava tube or a band of low conductivity material.

Time dependent variations are shown in Figure 10.15 and Figure 10.21. In general, the temperature variations tend to 'shadow' the variations in the minimum temperature. The net thermal anomaly is derived by subtracting the image minimum

temperature from the maximum value for each row. Thus, the variations in the minimum temperature should be filtered out of the data. A similar process exists for calculation of the anomaly sizes, where the threshold value is set at 1°C plus the minimum temperature. However, both figures broadly follow the trend of the minimum temperature variation, shown on Figure 10.14. This suggests two things, one relevant to the data extraction and one to the physical system itself. First, the background temperature can not be filtered from the peak temperatures by simple subtraction, nor does the selection of the threshold temperature as background+1 °C filter the background temperature from the anomaly size data. Secondly, the observed temporal variations in the net thermal anomaly and thermal anomaly size, since they broadly follow the trend of the background temperature, appear to be controlled by meteorological processes external to the lava tube. This is directly contradictory to the relationship suggested by the models *in Chapter 6: Steady State Models*.

Thus, when variations in meteorology, instrument settings and uncertainties in the derived data are considered, there is little significant variation in the thermal signature of the lava tube over the time period covered in the data.

Thermal Budget

Keszthelyi (1995) discusses the heat flow of a similar lava tube system, and estimates conductive heat losses from the tube to be about 10 kWm^{-1} and convective losses from the lava tube to approximately $10kWm^{-1}$, with an additional $5kWm^{-1}$ plus due to rainfall effects, depending on the weather.

Rainfall data from the HVNP HQ weather station (summaries in Figure 10.2) shows rainfall only occurred on two of the days when images used in this study were acquired, the 5th and 14th of September. On September 5th approximately 4mm of rain fell between the hours of 17.00 and 18.00 (image acquired at 18.21) However, the temperature values in this image are not reduced, so it is unlikely that the rainfall, which took place prior to image acquisition, has had an effect. On September 14th the same amount of rainfall fell, between the hours of 08.00 and 09.00, and is unlikely to have affected the image acquired at 17.58. Thus rainfall related effects can be effectively eliminated from the instantaneous thermal budget of the lava tubes at the time of image acquisition.

Thus, using Keszthelyi's estimates, approximately 20kWm^{-1} of heat loss from the lava tube need to be accounted for. Some of this will be conducted into the ground, but the derived instantaneous surface thermal budget of the lava tube segment under study could readily accommodate such heat loss, with approximately 4kWm^{-1} due to radiative cooling, and 16kWm^{-1} due to convective cooling. This assumes a value of the sensible heat transfer coefficient of approximately 25 Wm^{-1} K^{-1}, a reasonable value for heat transfer to the atmosphere under Hawaiian conditions.

10.3 FINITE ELEMENT MODELLING OF LAVA TUBES

This section compares the observed thermal signature of the lava tubes with modelled thermal signatures, and hence attempts to constrain the physical properties and parameters of the lava tube system. The parameters of the physical system are described with consideration of their likely ranges in the case of the Pu'U'Oo lava tube. These parameters are used in finite element models of the lava tube. The Bravo Model, described in *Chapter 6: Steady State Models* is used for this analysis. By varying the parameters of the finite element model within acceptable ranges to attempt and match the observed thermal signatures, the parameters of the real system may be constrained.

THE PHYSICAL SYSTEM

Lava tubes are essentially long 'pipelines' of molten lava within a solidified lava flow. They occur in low viscosity lava flows and allow flows of great length to be emplaced slowly by relatively low effusion rate eruptions.

Lava tubes can be very extensive, principally due to the fact that relatively little heat is lost through the tube wall. Thus, the lava may travel a great distance without cooling significantly. Typical cooling rates are of the order of 0.5-1°C per kilometre (Helz et al 1991) but in the Kilauea system the rates are somewhat higher, at 5-10°C per kilometre, due to slower flow rates (Hon et al 1994). When volcanic activity ceases, lava tubes often 'drain' of their lava leaving a long linear cave, (e.g. Ape Cave, Mt. St. Helens). On the moon, rilles have been interpreted as being collapsed lava caves, and catenae, linear systems of crater chain/collapse structures, may represent partially collapsed lava tubes. Many active terrestrial lava tubes occur on the kilometre length scale and in non-terrestrial environments lava caves left by active lava tubes may be many tens or hundreds of kilometres in length.

Lava tubes form in low viscosity lava flows by one of two mechanisms, channel roofing or flow localisation. In channel roofing, a channeled lava flow becomes sealed over, by a combination of growth of overhanging banks of solidified lava, and foundering of floating 'rafts' of solid material. Eventually this seals the roof of the channeled flow leaving an enclosed 'lava tube'. Lava tubes can also form

by localisation of lava movement within an active flow lobe. As a flow lobe cools and solidified, the liquid melt become successively restricted to a smaller and smaller area. Eventually, if a steady supply of fresh lava continues to feed the flow lobe, this region becomes thermally stable and forms a lava tube.

Heat transfer from lava tubes and the heat budget of lava tubes have been reviewed extensively by Keszthelyi (1994, 1995). Keszthelyi found that in the thermal budget of steady state lava tubes, the principle factors governing the heat were conduction through the walls, evaporative cooling due to rainfall, radiation via skylights and convection through fissures in the surrounding lava.

Radiative heat transfer can be calculated from the fissure area and lava temperature, but is only relevant where skylights and fissures occur. In the theoretical examples (*Chapter 6: Steady State Models*) and in this case study sections of tube containing skylights are not investigated, hence, this term need not be considered.

Cooling due to rainfall is an important process in the period of percolation immediately after precipitation, and affects the overall heat balance. However, it has only a transient effect on the temperature distribution. Modelling the actual transient effect of rainfall on the temperature distribution at any serious level rapidly becomes an extremely complex problem, involving two phase fluid flow, convective and conductive heat transfer. This is beyond the scope of this thesis. Precipitation is quite low in the case studies considered in this chapter. Thus cooling due to rainfall need not be considered here.

This leaves two principle processes, conduction in the lava tube and convection in fissures in the lava.

Conductive Heat Transfer from a Lava Tube

Incropera and De Witt (1990) give a useful expression for the conductive heat loss from a hot wire in a semi-infinite half space:

$$Q_{cond}=2\pi\Delta Tk/Cosh^{-1}(2h_o/D+1) \qquad 10.11$$

Where:

Q_{cond} Conductive heat loss from wire (Wm^{-1})

ΔT Temperature difference between the wire and the surface. (K)

k Thermal conductivity of the material ($Wm^{-1}K^{-1}$)

h_o Roof thickness (m)

D Diameter of wire (m)

This expression is readily adaptable to lava tubes and results of this equation for lava tubes of various sizes and depths are graphed in Figure 10.24.

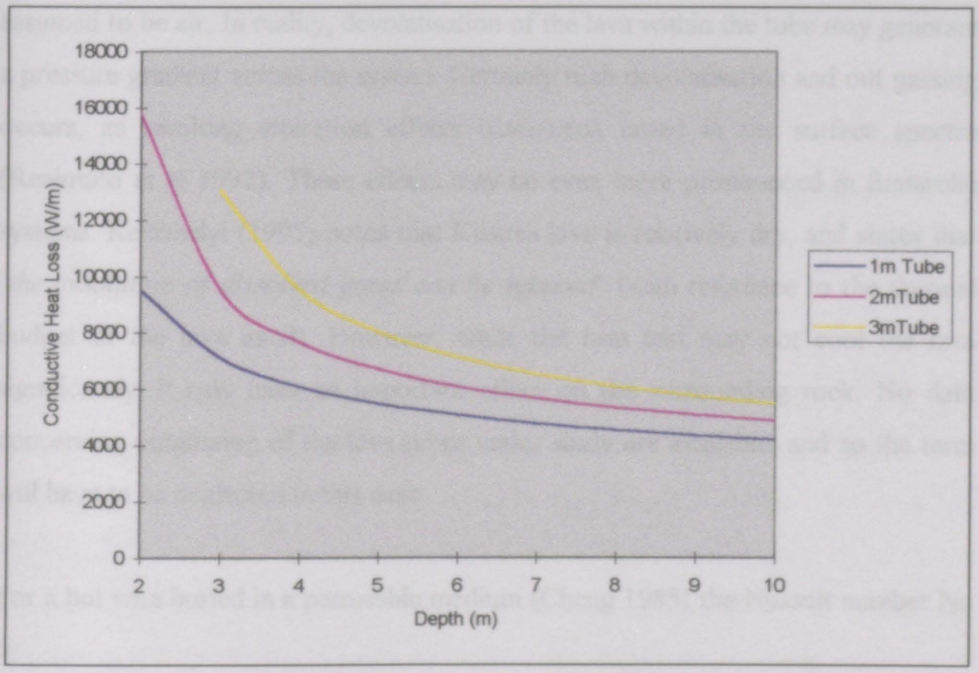


Figure 10.24 Conductive heat transfer from a lava tube of given diameter, calculation using an analytic expression (Equation 10.11). Note that the curve for each tube terminates when its centre comes within a diameter of the surface. A distince break of slope occurs when the tube centre approaches Diameter+1 m of the surface.

Convective Heat Transfer from a Lava Tube.

Convective heat transfer is more complex, but is also solvable. Since convective heat transfer can be assumed to occur largely in the vertical direction (warm air rising), the convective heat transfer can be approximated by applying an anisotropic thermal conductivity. The additional term in the vertical direction can be calculated from the Rayleigh number of the system using equation 3.28 and preceding equations. The resultant Nussult number is however, subject to a number of variables, chiefly the permeability of the basalt, which is widely variable.

This approach also assumes free convection in the pore media, which is assumed to be air. In reality, devolatisation of the lava within the tube may generate a pressure gradient across the system. Certainly such devolatisation and out gassing occurs, as resulting alteration effects have been noted in the surface spectra (Realmuto et al 1992). These effects may be even more pronounced in fumarolic systems. Keszthelyi (1995) notes that Kilauea lava is relatively dry, and states that *'the exsolution of dissolved gases can be ignored'* (with reference to the thermal budget of the lava itself). However, while the heat lost may not cool the lava significantly, it may have an important effect on the surrounding rock. No data concerning outgassing of the lava tubes under study are available, and so the term will have to be neglected in this case.

For a hot wire buried in a permeable medium (Cheng 1985) the Nussult number Nu is:

$$Nu = 0.565Ra^{1/2} \qquad 10.12$$

The Rayleigh number, Ra, is:

$$Ra = \rho_f \beta g K \Delta T D/(\eta_f k_d) \qquad 10.13$$

Where:

ρ_f Density of the pore fluid (air) (kgm^{-3})

β Coefficient of thermal expansion of the pore fluid (K^{-1})

g Acceleration due to gravity ($9.81 ms^{-2}$)

K Permeability of the rocks

ΔT Temperature difference between the tube and the surface (K)

D Diameter of the wire (m)

η_f Kinematic Viscosity of the pore fluid (air) (m^2s^{-1})

k_d Thermal Diffusivity of the saturated rock (m^2s^{-1})

The total heat transfer from a unit length of a hot wire due to convective processes is:

$$Q_{conv} = \pi Nuk\Delta T \qquad \text{for } 1<Ra<100 \qquad 10.14$$

(Cheng 1985)

Where:

k Thermal conductivity of the dry rock ($Wm^{-1}K^{-1}$)

This equation is readily applicable to convective heat transfer from a lava tube. Using this equation, Kesthelyi estimates heat loss from a 2m diameter lava tube due to convection in wall rocks to be in the range 0.2-8kWm^{-1}, but probably closest to 2kWm^{-1} for Hawaiian pahoehoe tubes of this radius. Figure 10.25 shows the convective heat flux that would result from using this equation, for a lava tube in a medium of unit thermal conductivity, for a 1000K thermal gradient.

To be incorporated into finite element models a heat transfer coefficient analogous to the thermal conductivity must be derived from this term. This can be approximated by dividing both sides of the Equation by a characteristic dimension for the system, in this case πD. This characteristic dimension is an approximation and is required to convert convective heat flow, theoretically an integral across an infinite surface, into a useful value. The bulk of the convective heat transfer will occur in a region of diameter πD across. The average heat transfer from a hot wire (or lava tube) to the surface can thus be approximated as:

$$Q_{avg} = Nu\Delta T\, k_{rock} / D \qquad 10.15$$

Where:

k_{rock} Thermal conductivity of the saturated rock($Wm^{-1}K^{-1}$)

Thus, the total vertical heat transfer coefficient will be:

$$k_{total} = (Nu/D)k_{rock} + k_{rock} \qquad 10.16$$

Note that when no convection occurs, the Nussult number will be zero and heat will be transferred by thermal conduction alone.

This approximation is necessary to facilitate 'bolting on' of convective processes to an essentially conductive model architecture. Ideally, the fluid motion and heat transfer through the porous media should itself be the subject of a concurrent numerical model. Construction of such a 'double' model would be a thesis in itself.

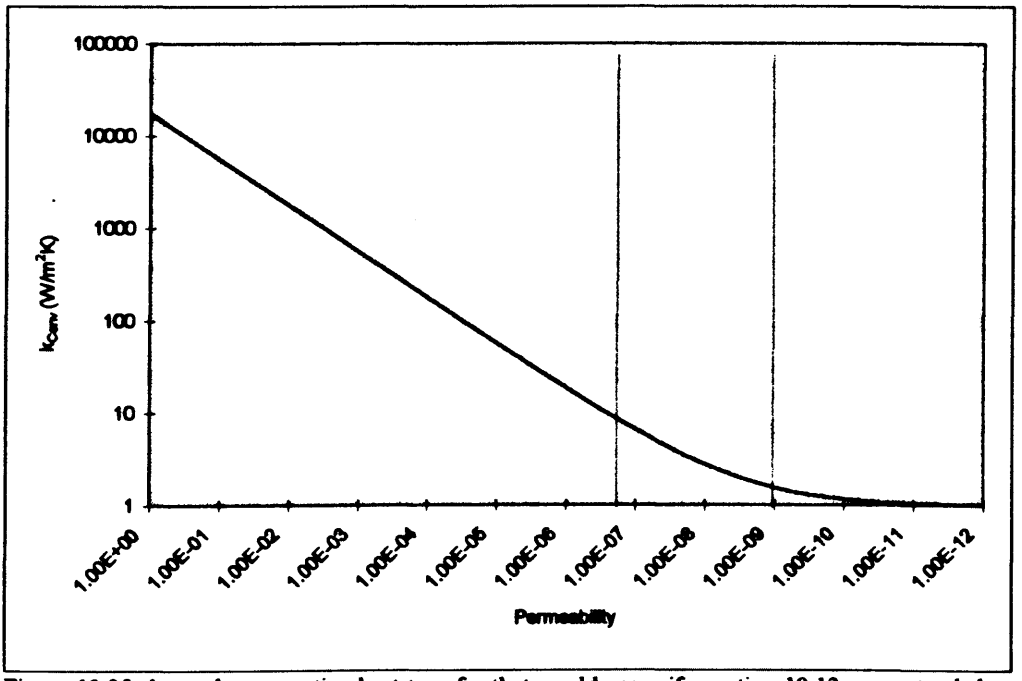


Figure 10.25 shows the convective heat transfer that would occur if equation 10.13 was extended across the full range of permeability, for a lava tube in a medium of unit thermal conductivity and 1000 Kelvin thermal gradient. The dashed lines indicate the formal limits of applicability of the equation.

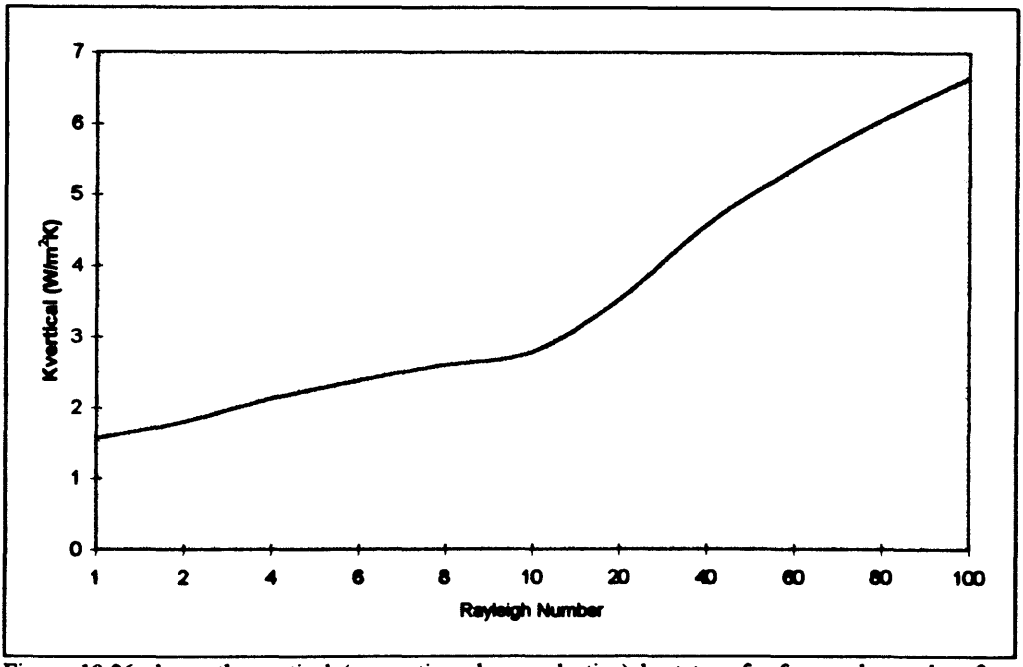


Figure 10.26 shows the vertical (convective plus conductive) heat transfer from a lava tube of diameter 2m, with air as the saturating pore fluid, in a rock with unit thermal conductivity. Note that the kink in the graph occurs due to a change of scale on the X-axis. Note that for Rayleigh numbers below the lower limit of validity of Equation 10.14 (Ra<1), the convective heat flow will be negligible, and above the limit of validity (Ra>100) cooling will be essentially convective.

ADAPTATION OF FINITE ELEMENT MODELS

Extensive work has been carried out in *Chapter 6: Steady State Models* concerning theoretical finite element models of cooling from lava tube like source. This work can be quickly adapted for use in this case study. The Bravo model, being the more realistic and efficient of the two models, was used as a basis for the model of the Kilauea lava tubes.

The only alterations required to the Bravo Model are a substitution of temperature dependant material properties for the thermal conductivity and specific heat capacity, and addition of anisotropic thermal conductivity to simulate convective heat transfer, (as *outlined in Chapter 3: The Physical Model*). Procedures for including these components are outlined in the *Chapter 5: Introduction to Thermal Modelling Using Ansys*.

PHYSICAL PARAMETERS

Surface Temperature

This is well known for the tube system from the thermal-infrared image, as described above. The ranges of peak temperature are the primary parameters to match with the finite element model results. The thermal anomaly size is not clear enough in the extracted data to be used for matching (see Figure 10.20), however, the radiant heat flux (Figure 10.22) is much better constrained and will be used to refine the search

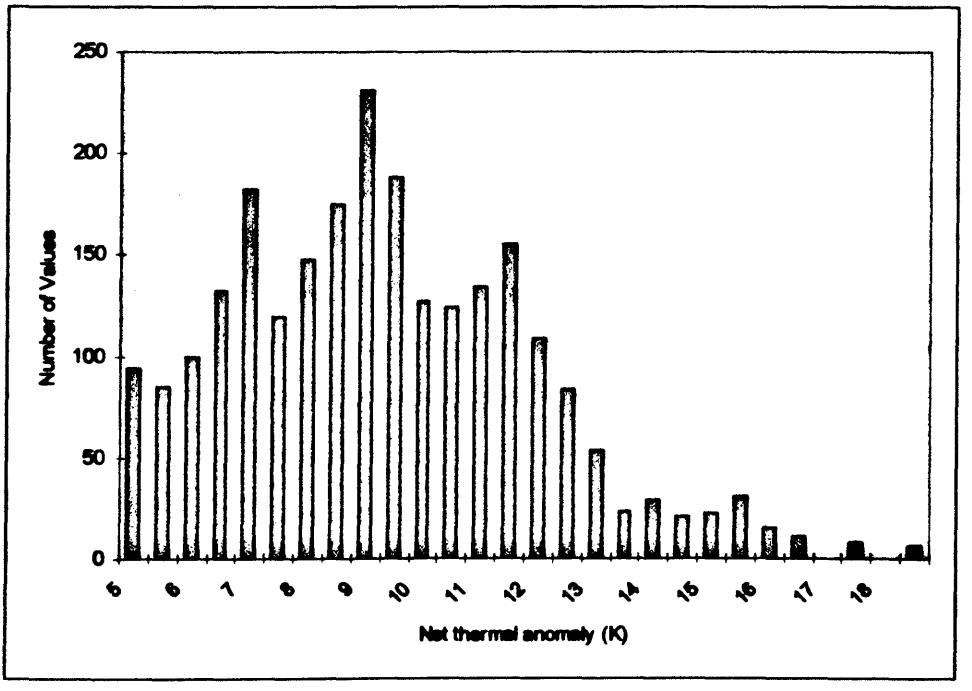


Figure 10.27 A binned frequency distribution of measured net thermal anomaly values. The Full Width Half Maximum lies in the range 6-12K

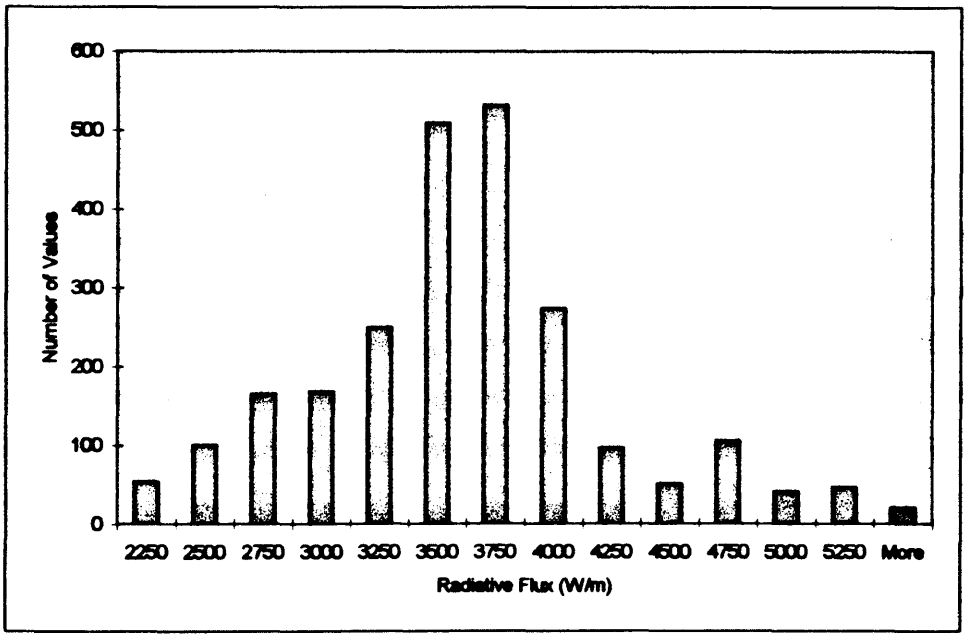


Figure 10.28 shows a binned frequency distribution of measured radiative flux values.

Surface Emissivity

The surface emissivity is known fairly well for the system from the procedure for extracting the kinetic temperature, and averaged 0.94 for the tube in question. While the true figure may vary from this, investigations of emissivity variations in *Chapter 6: Steady State Models* suggests that the effect of surface emissivity variations within the likely range is minimal.

Incident Radiation

In the Bravo model incident radiation is controlled by the space node temperature. The space node temperature was found to influence the peak temperature and the background temperature in approximately equal measure. This is demonstrated in *Chapter 6: Steady State Models*. where it was found to be of negligible importance, and is for convenience set at 303K.

Mean Atmospheric Temperature

The mean atmospheric temperature has negligible effects on the net thermal anomaly thus is of little importance in this study. This is demonstrated in model

series 6.4.1. Radiosonde data suggest surface air temperatures of approximately 298K±5, and this figure will be used for the bulk atmospheric temperature.

Sensible Heat Transfer

The value for the convective heat transfer coefficient is unknown. No contemporaneous data are available for near surface windspeeds or temperature gradients, or for surface roughness, aerodynamic drag coefficients or any of the wide variety of variables required by the equations reviewed in *Chapter 3: The Physical Model* to calculate sensible heat flow. It is therefore not possible to accurately calculate this term from available data. It can, however, be constrained to within reasonable limits.

Assuming that the windspeed lies in a reasonable range of $<5ms^{-1}$, (Kesthelyi measured windspeeds of $3\text{-}4ms^{-1}$, and assuming $<30°C$ contrast between the surface and the atmosphere, the Richardson number equation suggests that the sensible heat transfer operates in a damped forced convection mode. Qualitatively, this is supported by observations of wind driven gas plumes in some images. Based on the discussion in *Chapter 3: The Physical Model* and realistic estimates of the surface parameters across likely ranges the sensible heat transfer coefficient will be assumed to lie in the range $0\text{-}100Wm^{-2}K^{-1}$. Kesthelyi measured a value of between 50 and $100Wm^{-2}K^{-1}$ in a field experiment at a similar lava tube system.

The sensible heat transfer coefficient will also be assumed to be uniform for all surface temperatures. Given the relatively low range of surface temperatures (measured anomaly sizes being about 10 degrees) this is a reasonable assumption.

Source Temperature

As the material under study is an active basaltic lava the source temperature is therefore constrained to the range 1430±50K. Given the relatively continual movement of lava along the tube ($1\text{-}2ms^{-1}$), and very low measured thermal gradients within lava tubes ($1\text{-}2°Ckm^{-1}$, Keszthelyi, 1995) the source temperature will be constrained to be the same for all models of contemporaneous sections across the tube, in the range 1430±50K.

Depth

The depth to the lava tube is unknown. Keszthelyi (1995) estimates possible values for the Waha'ula lava tubes, a similar lava tube system further along the east rift zone, of between 0.5 and 4m and this range will be taken for this system.

Tube geometry

The size and shape of the lava tube system is unknown.

Effective Thermal Conductivity

The thermal conductivity of basalt is highly variable. Based on the values and discussion in *Chapter 3: The Physical Model*, the ranges of acceptable values for the effective vertical and horizontal thermal conductivity are shown in Figure 10.29. Note that the most extreme anisotropy (highest $k_{vertical}$ and lowest $k_{horizontal}$) is associated with high basalt porosities and permeabilities. The vesicularity of the Kilauea lava flow is not well known, however the Kupianaha lava flow was measured as having a vesicularity of 60% (Keszthelyi 1994) but it is likely that the vesicularity and thus the thermal conductivity may be highly variable across the flow. For convenience, values for the thermal conductivity of 'standard basalts' have been generated from the expressions for thermal conductivity of basalt and convective heat transfer coefficients. The detailed values are listed in *Appendix C*.

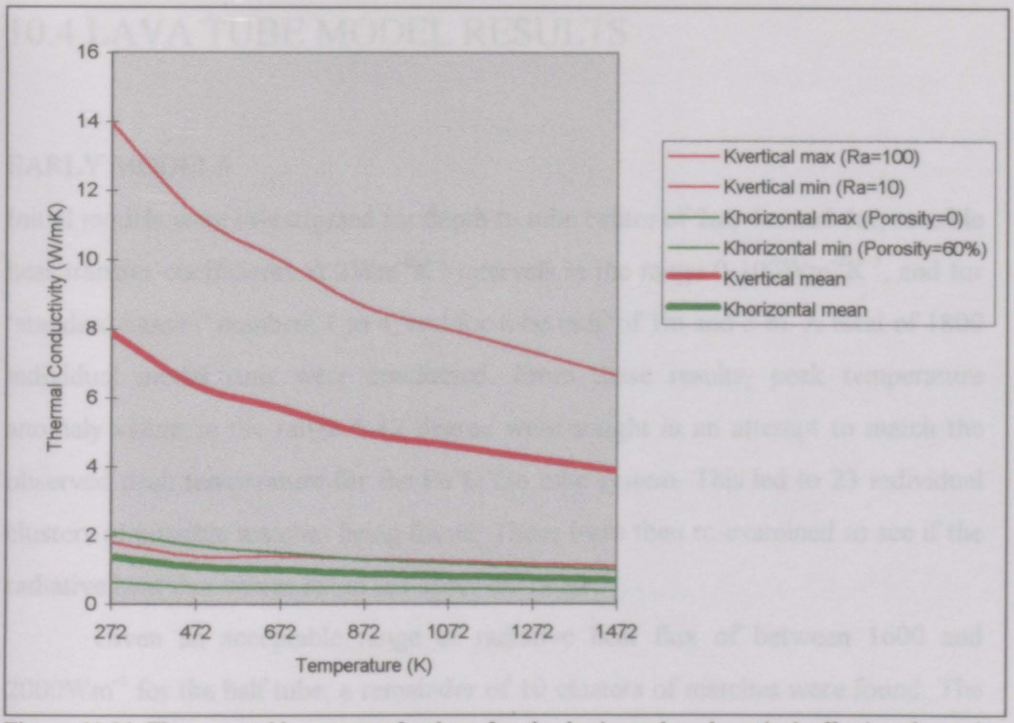


Figure 10.29 The acceptable ranges of values for the horizontal and vertical effective thermal conductivity. Mean values are shown in the heavier lines.

Density

The density of basalt is approximately 2650kgm^{-3} (Tiab and Sigurdsson 1994) however it may be affected by the vesicularity of the material. A basalt of 40% vesicularity will obviously be much less dense than a basalt of the same composition without vesicles. As the vesicularity of the lava flow is not known, the density of the basalt can only be constrained to between 2200 and 2800kgm^{-3}. In any event, the density has an effect on transient thermal models and processes only, and for a fairly stable lava tube system the uncertainty in the density is of little concern, however, consistent values for each 'standard basalt' are used (see *Appendix C Properties of Selected Materials)*.

Specific Heat Capacity

Equation 3.1 (from Touloukian 1989) is used to generate a temperature dependent specific heat capacity for the material. The specific heat capacity only has an effect on transient thermal models and processes, however, consistent values for each 'standard basalt' are used. (see *Appendix C Properties of Selected Materials*).

10.4 LAVA TUBE MODEL RESULTS

EARLY MODELS

Initial models were investigated for depth to tube centre of 2m, 4m and 6m, sensible heat transfer coefficients at $2Wm^{-2}K^{-1}$ intervals in the range $0\text{-}100Wm^{-2}K^{-1}$, and for 'standard basalts' numbers 1 to 4, and for tube radii of 1m and 3 m. A total of 1800 individual model runs were conducted. From these results, peak temperature anomaly values in the range 6-12 degree were sought in an attempt to match the observed peak temperature for the Pu'U'Oo tube system. This led to 23 individual clusters of possible matches being found. These were then re-examined to see if the radiative heat flux values fell in the observed range.

Given an acceptable range of radiative heat flux of between 1600 and $2000Wm^{-1}$ for the half tube, a remainder of 10 clusters of matches were found. The resulting matches for tube parameters are listed in Table 10.3.

No.	Basalt Type	Depth (m)	Radius (m)	Sensible Heat Coefficient ($Wm^{-2}K^{-1}$) Min-Max
1	Basalt4	4	1	18-38
2	Basalt2	6	1	14-36
3	Basalt1	8	1	56-66
4	Basalt3	8	1	90-98
5	Basalt4	4	3	30-98
6	Basalt2	6	3	28-62
7	Basalt1	8	3	60-98
8	Basalt3	8	3	62-98
9	Basalt1	10	3	40-98
10	Basalt3	10	3	44-90

Table 10.3 Parameters generating possible flux matches.

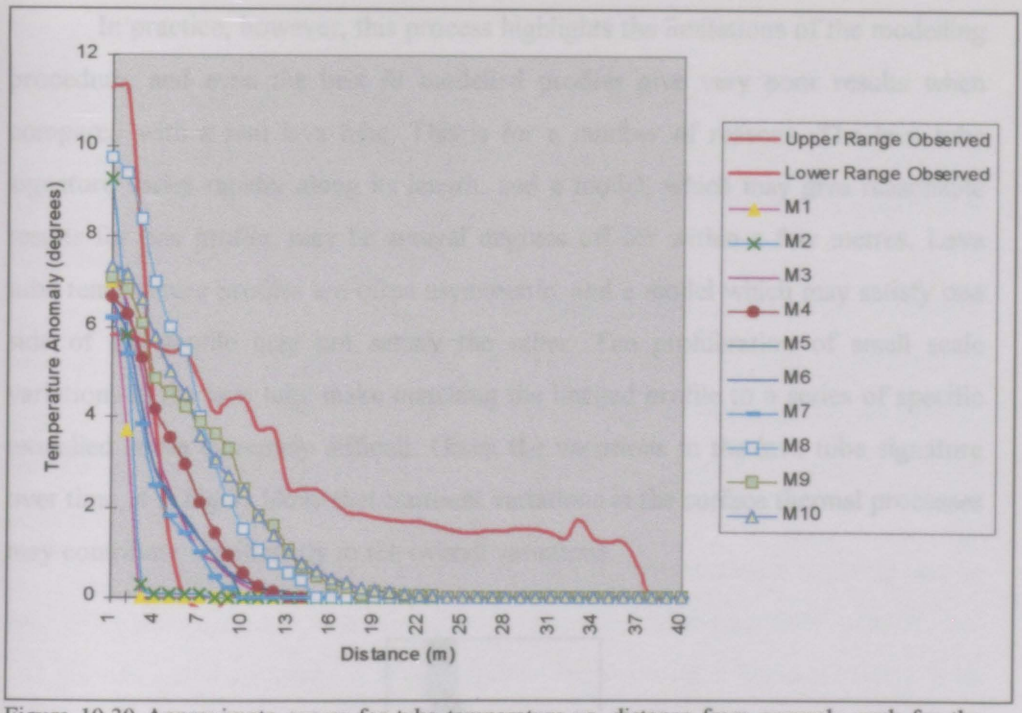


Figure 10.30 Approximate curves for tube temperature vs. distance from anomaly peak for the maximum and minimum tube profiles. Note that a continuum of profiles exists between these two extremes. Plotted temperature curves from the various matching models are also shown. Curves generated using mid range values for sensible heat flux.

Detailed examination of these 'matches' in Table 10.3 introduced some problems. While all produce peak temperatures in acceptable ranges, most of the observed lava tube cross-sections are closer to 40m across than the 10m across shown in Figure 10.30. Thus all of the modelled profiles are simply too narrow to adequately explain the observed temperature distribution. Based on the observed behaviour of the surface temperature profiles examined in *Chapter 6: Steady State Models* the observed profiles may be generated by either a much larger lava tube at greater depth, or a rectangular or irregular lava tube cross section.

VIRTUAL THERMAL IMAGES

Once an acceptable matching profile or cluster of profiles has been acquired, these can be assembled into a 'virtual thermal image', to facilitate direct comparison with remotely sensed data. The one dimensional lava tube profiles can be assembled linearly to form a two dimensional image which can be directly compared with the kinetic temperature maps extracted from the thermal infrared image.

In practice, however, this process highlights the limitations of the modelling procedure, and even the best fit modelled profiles give very poor results when compared with a real lava tube. This is for a number of reasons. The lava tube signature varies rapidly along its length, and a model, which may give reasonable results for one profile, may be several degrees off for within a few metres. Lava tube temperature profiles are often asymmetric, and a model which may satisfy one side of the profile may not satisfy the other. The proliferation of small scale variations in the lava tube make matching the imaged profile to a series of specific modelled curve extremely difficult. Given the variations in the lava tube signature over time, it is highly likely that transient variations in the surface thermal processes may contribute significantly to the overall variations.

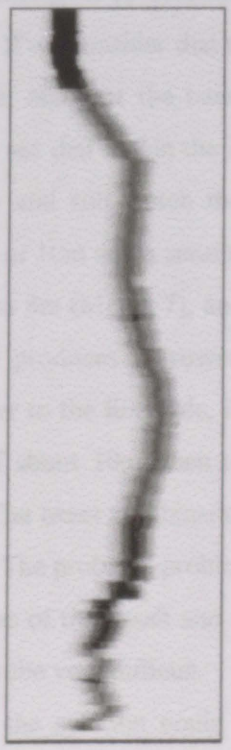


Figure 10.31 A virtual thermal images of a lava tube derived from stacked two dimensional finite element model results shown in Figure 6.30. Note that darker areas are warmer.

10.5 CONCLUSIONS

Two principle conclusions can be drawn from this case study.

Firstly the use of finite element models in conjunction with remote sensing data can be of help in broadly constraining the type and nature of a geothermal source such as a lava tube.

Secondly, the case study also demonstrates the limitations of the technique, used in this study. The parameters of the system need to be well constrained to produce a unique solution, Even for a relatively, well constrained, simple system, remote sensing data alone are not sufficient to extract a unique source configuration.

The models arrived at to explain the lava tube temperature anomaly can be seen to be non-unique, but an intelligent consideration of the potential matches can still provide useful information. If we consider that the surface fluxes are likely to be the same across a given image, and that the basalt type is relatively uniform (a dangerous assumption), we can see that within the image, it is plausible for the tube to change depth and geometry and still match the observed signature. The tube could be set in basalt 1 at depth of 10m and a sensible heat flux of about $60Wm^{-1}K^{-1}$ radius 3m (Match 9), then rise to 8m (Match 7), and then narrow to 1m (Match 3). We know that shallower tube produces narrower hotter profiles, closer to the maximum profile observed closer to the fumarole, it is not unreasonable to suggest that the tube starts at depth of about 10m, then rises to 8m and narrows before opening out onto the surface. The exact combination of depths and tube diameters is dependent on the basalt type. The probable proliferation of small scale variation in the presumed constant properties of the basalt and the surface make precise, metre by metre, modelling of the lava tube very difficult.

The non-uniqueness of the solution could be greatly reduced, and in all probability eliminated, if adequate data concerning the surface fluxes and the basalt properties were available. The 4 'standard basalts' considered represent end members of a large series of porosity and permeabities, which could be easily constrained by field measurements. This alone would probably be sufficient to reduce the solution to a single viable scenario, and would allow production of an accurate depth map of the lava tube based on the TIMS images and Finite Element

Modelling techniques. Constraining the sensible heat flux would also be of benefit, but since the range of fluxes for which given solutions may 'fit' the observed curves is very broad, it is less critical.

Ideally, a field exercise should be conducted in conjunction with TIMS overflight. The exercise would involve sampling of the basalt at regular intervals and measurement of its thermal properties, surface based temperature measurements to assist in calibrating the TIMS images, measurement of the sensible heat flux, and assessment of tube outgassing to constrain the levels of convective heat flux in the system. Alternative geophysical methods, such as electromagnetic surveying, could be used to constrain the size and depth of the tube system. Applying this kind of detailed analysis, is of course an expensive exercise, particularly if the lava flow is in a remote location. Consideration of the complexity of the field exercise that would be required to generate such data illustrates the usefulness of even approximate data from a remote sensing system.

In conclusion, finite element modelling can be used to extract more useful information about lava tube geometry from TIMS images, but some ground truth data, and measurements of the thermal properties of the basalt, are required for the technique to produce a unique, predictive solution. Once this has been done, the above techniques could be used to monitor the underground state of an active lava flow.

Chapter 11: Lunar Thermal Modelling

In many ways the Moon presents an ideal environment for the study of thermal anomalies. The anhydrous surface, devoid of biomass and atmospheric clutter, eliminates virtually all sources of extraneous noise in the surface thermal boundary condition. However studies of the shape and internal structure of the Moon (Zuber et al 1994) note that:

"Volcanism and tectonism indicative of substantial heat loss from the lunar interior essentially ceased by 2.5-3.0 billion years ago"

This would suggest that while studies of lunar data may be ideal in terms of absence of thermal noise, the fact that the Moon is tectonically dead would seem to rule out significant geothermal anomalies.

This chapter sets out to assess the utility of combining thermal infrared remote sensing data and Finite Element modeling techniques, for the study of lunar geology. The chapter will first outline the relevant previous work on lunar geology and thermal processes. A number of situations are investigated to explore applications of finite element modeling to lunar thermal processes.

11.1 THE THERMAL GEOLOGY OF THE MOON

This section briefly reviews relevant background material and previous work concerning the Moon, its thermal characteristics and near surface geological structure which may be of thermal significance. It is in no way intended as a comprehensive review of lunar geology. Detailed reviews of known lunar geology can be found in *Lunar Sourcebook*, edited by Heiken, Vaniman and French (1991), the *Science* Clementine special issue (December 16th 1994) and the *Science* Lunar Prospector special issue (September 4th 1998)

Briefly, the Moon can be divided into two broad geologic types, the older lunar highlands, composed of diverse rock types, but principally anorthosite, and the lunar maria, composed of massive basaltic lava flows. Both terrain types are heavily cratered and as a result are thickly covered with a layer of regolith.

The surface thermal balance of the Moon is much simpler than that of the earth. Only four terms contribute to the surface energy balance, incident solar radiation, and radiant emission from the surface, near surface thermal storage and geothermal heat flux. The complex meteorology required to quantify the thermal fluxes due to sensible and latent heat transfer are completely eliminated, as the Moon has no significant atmosphere (Heiken, Vaniman and French 1994).

Potential thermal anomalies on the Moon can be divided into two broad types, endogenetic anomalies, due to internal heat, and exogenetic thermal anomalies, due to external thermal forcing, such as thermal inertia and aspect controlled anomalies.

ENDOGENETIC GEOTHERMAL ANOMALIES

The lunar geothermal gradient is constrained from the Apollo missions to 29 mWm^{-1}, slightly less than half the average terrestrial continental value (Langsieth and Keihm 1977). No active or recent volcanism of any kind has ever been observed, either directly, or indirectly, on the Moon. Thus the presence of endogenetic thermal anomalies due to volcanic activity is unlikely. Similarly, coal mine fires, hydrothermal fluid circulation and evaporite layers, while known to increase local heat flow on Earth and create local thermal anomalies, are highly

improbable in the lunar environment, and no alternative systems to locally increase heat fluxes are known.

In theory, there should be considerable heat generated by impact cratering. The controversial Lunar Transient Phenomena (LTP) may have some thermal component. Neither of these two highly transient events have been observed in the thermal infrared, nor are they likely to be observed in the near future, given that no further lunar explorations are presently being planned.

EXOGENETIC GEOTHERMAL ANOMALIES

The principle sources of variation in thermal infrared images of the lunar surface are aspect controlled solar heating (dayside images) and surface thermal inertia variation (nightside images). The extremely long lunar day, and the absence of any atmospheric damping effects create a situation where lunar surface temperatures vary from a pre dawn low of about 100K to a post noon maximum of 390K (Heiken, Vaniman and French 1991). Variation in aspect strongly affects the absorption of solar radiation, and thus dayside thermal infrared images are largely aspect controlled (Jakosky et al 1997).

Studies of the thermal inertia variations in the Apollo 17 ISM images have indicated that they are principally controlled by material size variations, with large boulders and solid outcrop having a much higher thermal inertia than lunar regolith (Mendell 1976).

THERMAL PROPERTIES OF LUNAR MATERIALS

Basalt

The thermal properties of solid rocks are not affected by their environment (with the exception of pressure and temperature dependencies already noted). Thus for lunar rocks, terrestrial values described in *Chapter 3: The Physical Model* can safely be used. Figure 11.1 shows a comparison of the calculated values of specific heat capacity for terrestrial basalt, and the measured values for specific heat capacity of lunar basalt. These can be seen to be in reasonable agreement. Care should be taken when using Maxwell's formula (Equation 3.2) for thermal conductivity in porous rocks, as the 'material' in the pore spaces will be vacuum. In

addition, basalt in planetary environments can also be expected to have a higher vesicularity than terrestrial analogues due to the lower atmospheric pressures at extrusion. It should be noted that Kesthelyi's formula for the temperature dependence of basalts (Equation 3.6) is an empirical fit to experimental data and unlikely to be valid at low temperatures.

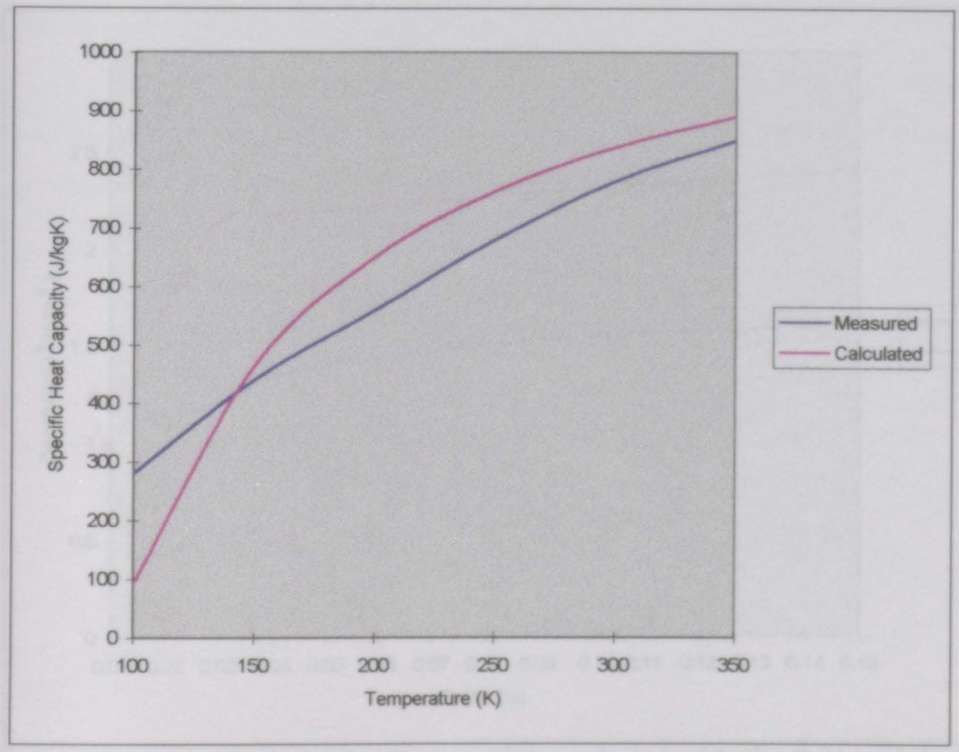


Figure 11.1 Variation in the specific heat capacity as a function of temperature for lunar basalt sample 15555, from the Hadley-Apennine landing site (Black line, Hemingway, Robie and Wilson 1973) compared with a calculated value for terrestrial basalt using equation 3.1 (red line, Touloukian 1989). Except at very low temperatures the values are in reasonable agreement.

Regolith

Lunar regolith completely blankets the lunar surface, with the possible exception of steep sided crater walls and lava channels. Regolith layer thicknesses are estimated at 4-5m in the Lunar Maria and up to 10-15m in older highland regions (Heiken, Vaniman and French 1991). Regolith is composed of small, highly angular fragments of lunar material, very loosely packed. Thermally, one could more

precisely describe regolith as a vacuum with rock chips in it, rather than as a solid material.

(i) Density

The density of lunar regolith generally increases with depth due to compaction, and is well constrained from measurement of lunar cores (see Figure 11.2).

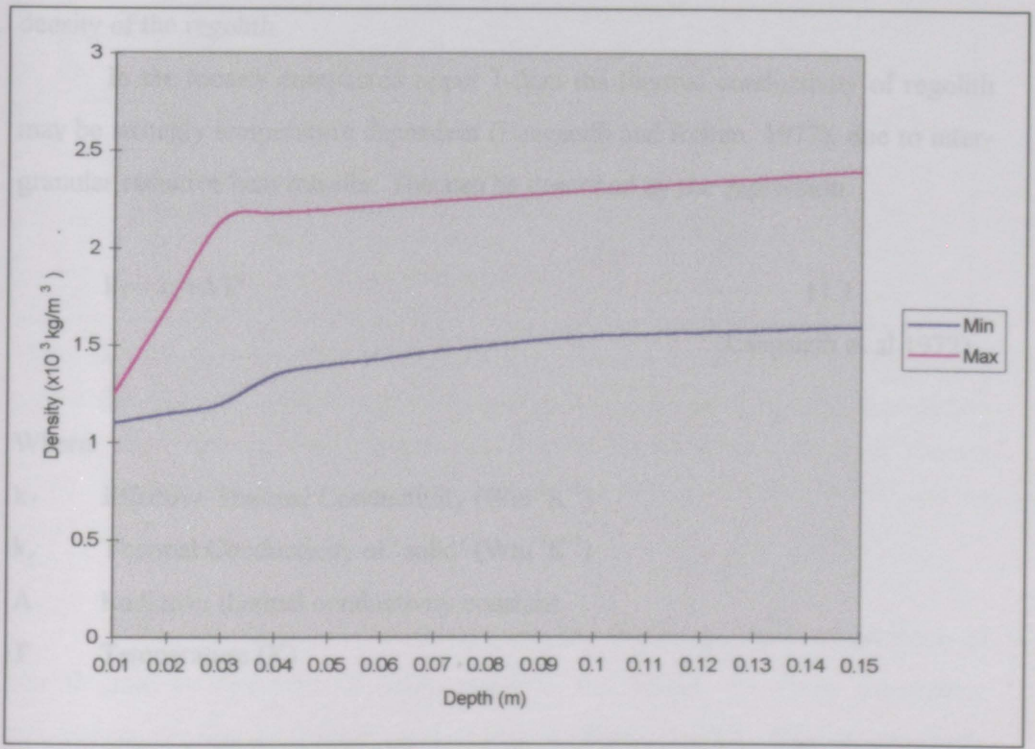


Figure 11.2 The variation in density of lunar regolith as a function of depth (after Langsieth and Keihm 1977)

(ii) Thermal Conductivity

Thermal conductivity in lunar regolith is more complex than in most materials. For a particulate medium, the thermal conductivity is governed by three terms, the solid thermal conductivity i.e. heat transfer across grain boundaries, conduction in the pore fluid in the intergranular spaces, and radiative heat transfer across pore spaces. In the terrestrial environment the mean free path is generally less than the pore size, so heat transfer in pore spaces is not constant. Pore fluid conduction is not significant in the lunar environment, as there is no pore fluid. In contrast, radiative heat transfer across grain boundaries is not generally significant in terrestrial

environments, as the materials' temperatures occupy such a narrow range. In the lunar environment, where near surface temperature can vary by 150K, temperature dependent radiative effects can be dominant.

In situ measurements (Langsieth and Keihm, 1977) of the thermal conductivity of lunar regolith give very low values of approximately 2.2×10^{-3} $Wm^{-1}K^{-1}$ (at Apollo 17 landing site, Langsieth, et al 1973). These values vary significantly with depth, increasing with the degree of compaction and hence the density of the regolith.

In the loosely compacted upper 1-2cm the thermal conductivity of regolith may be strongly temperature dependent (Langseith and Keihm, 1977), due to inter-granular radiative heat transfer. This can be described by the expression:

$$k_T = k_c + AT^3 \qquad 11.1$$

(Langsieth et al 1972)

Where:

k_T Effective Thermal Conductivity ($Wm^{-1}K^{-1}$)

k_c Thermal Conductivity of 'solid' ($Wm^{-1}K^{-1}$)

A Radiative thermal conductivity constant

T Temperature (K)

The ratio between the first term (k_T) and second (k_c) term is approximately 2±0.5, for typical conditions (Langsieth et al 1972). The mean effective thermal conductivity is approximately 1.5×10^{-3} $Wm^{-1}K^{-1}$.

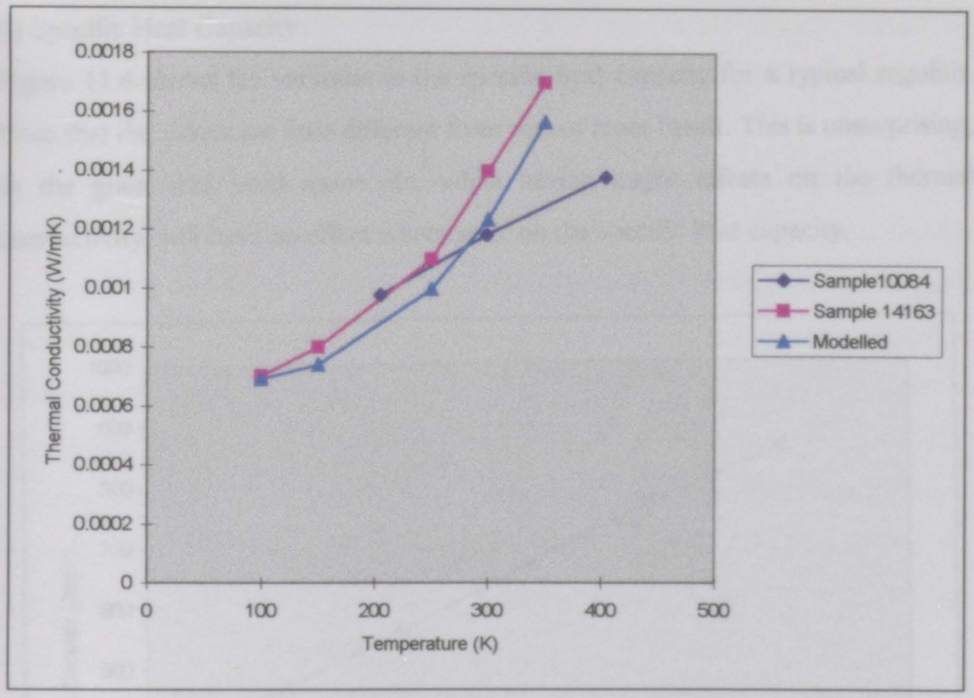


Figure 11.3 Thermal conductivity of lunar regolith as a function of temperature. Sample 10084 is surface fines from the Apollo 11 site measured by Lunar sample Preliminary Examination Cremers (1970). Sample 14163 is surface fines from the Apollo 14 site measured by Cremers (1972). The modelled curve is derived from equation 11.1 with $k_c = 0.67 \times 10^{-3} Wm^{-1}K^{-1}$ and $A = 3 \times 10^{-11} Wm^{-1}K^{-1}$.

While equation 11.1 adequately describes the temperature dependence of the thermal conductivity of lunar regolith, the values for these parameters themselves vary in proportion to the density of the regolith. The density/depth profile is itself highly variable. For the purposes of modelling it is necessary to simplify this somewhat. Two distinct thermal conductivities will be required, one for the near surface fines (depth < 3cm) and one for deeper, denser regolith (depth > 3cm). Equation 11.1 was used to derive a theoretical curve to approximate measured values, as shown in Figure 11.3, using values for k_c and A to generate a best fit with observed data. The modelled values will be used for the shallow regolith, and a constant value of $0.008 Wm^{-1}K^{-1}$ will be used for deeper regolith thermal conductivities, consistent with Langsieth and Keihm 1977.

(i) Specific Heat Capacity

Figure 11.4 shows the variation in the specific heat capacity for a typical regolith. Note that the values are little different from that of lunar basalt. This is unsurprising, as the grain size, void space etc, while having major effects on the thermal conductivity, will have no effect whatsoever on the specific heat capacity.

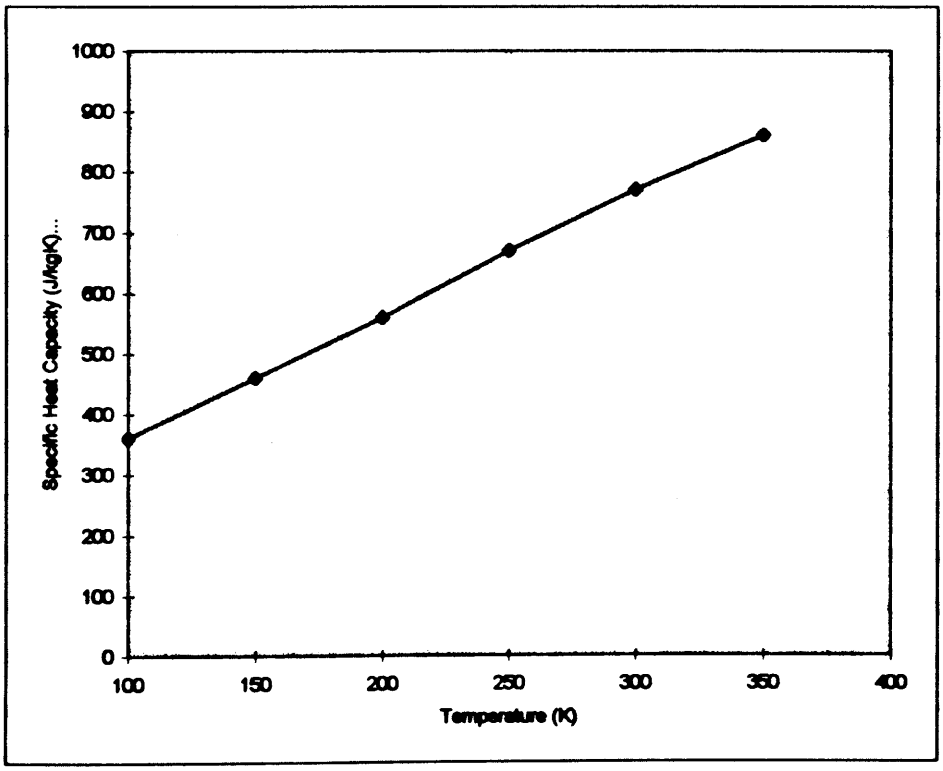


Figure 11.4 Variation of specific heat capacity with temperature of near surface fines (sample 60601, Apollo 16 (Hemingway et a.1973)

LUNAR REMOTE SENSING THERMAL DATA

Thermal Imagery of the Moon exists in three forms, terrestrial thermography, Apollo 17 orbital images and the Clementine Long Wave Infra-Red (LWIR) camera dataset.

The earliest thermal infrared remote sensing ever conducted was of the Moon, when Lord Rosse made the first measurement of radiated heat from the Moon from Birr Castle in 1868 (Rosse 1869). Later work using ground based thermography was more detailed, and identified almost 1000 thermal anomalies in scans of the eclipsed Moon (Shorthill, 1972). Almost all of these anomalies were

correlated by Shorthill with surface features and radar bright regions, suggesting that they were in fact due to thermal inertia variations, themselves due to variations in the distribution of surface blocks.

The earliest closer range images were acquired from the Apollo 17 spacecraft at a surface resolution of 2.2km per pixel, and identified complex thermal structures on the lunar nightside. Thermal inertia related hotspots were again identified, mostly in the center and walls of younger craters, and probably caused by increased concentration of high thermal inertia blocks. (Mendell 1976). Studies of the region in and around the crater Aristarchus (Schultz and Mendell 1978) suggested that 11-16% of the crater interior is bare outcrop. These images are of relatively high resolution and were acquired over the region during lunar night, the optimum time for imaging geothermal sources. Unfortunately, this dataset is not presently available in a usable format.

In 1994 the Clementine Spacecraft spent $2^1/_2$ months in lunar orbit. Thermal infrared imagery was acquired by the LWIR instrument aboard Clementine from the 8-9.5 μm spectral region (Nozette et al 1994). The imagery is available from a number of on line sources. Image resolution is variable dependent on the orbital geometry and can be as high as 55m per pixel. Image quality is also highly variable due to instrument noise and limited instrument dynamic range, Figure 11.5 shows one of the better quality images . Detailed analysis of this dataset has not yet been conducted.



Figure 11.5 Clementine LWIR image of a lunar Rille (Rima Bradley). Pixel resolution is 55m/per pixel. Note that this picture is one of the better quality thermal images, and has been filtered to remove the 'Salt and Pepper" effect of bad pixels.

11.2 THERMAL MODELS OF THE LUNAR SURFACE

SERIES 11.2.1 DIURNAL THERMAL CYCLE

The lunar period of rotation is approximately 28 days. Given this slow rotation and the lack of atmosphere, it would be expected that surface temperature variations would be extreme, and this is known to be the case. This preliminary investigation sets out to predict the surface temperature and depth temperature profiles. Since these parameters are well constrained from measurements taken on the Apollo 15 and 17 missions (Langseith and Keihm 1977), and earlier work, this modelling will serve chiefly as a validation exercise.

This investigation uses an improved version of the linear model used for the terrestrial diurnal cycle in series 7.1.2. In this case the finite element model was optimised by the addition of a third, 5cm thick layer at the surface to represent fines (near surface regolith). The finite element mesh was redesigned for improved computation time. The new mesh was convergence tested in the usual way, and test results using the same materials and boundary conditions were in reasonable agreement with those of the less efficient meshes used in series 7.1.2.

For the purposes of simulation of the lunar environment, convective loads were set at zero, to represent the absence of atmospheric effects. Radiative loads were calculated based on the latitude of the Apollo 15 site (26°N) assuming a solar declination of zero and a background 'sky' temperature of 10K. The upper 5cm layer of the model was set as Regolith Type 1, Near Surface Fines and the remainder as Regolith Type 2, Subsurface Regolith. The standard regolith materials properties are tabulated in full in *Appendix C: Properties of Selected Materials* Surface emissivity was set at 1.0.

Results of this model series are plotted in Figures 11.6, 11.7 and can be compared with measured data of the temperature-depth profile as a function of time measured by the Apollo 15 heat flow experiment (Figure 11.8)(Langsieth and Keihm 1977).

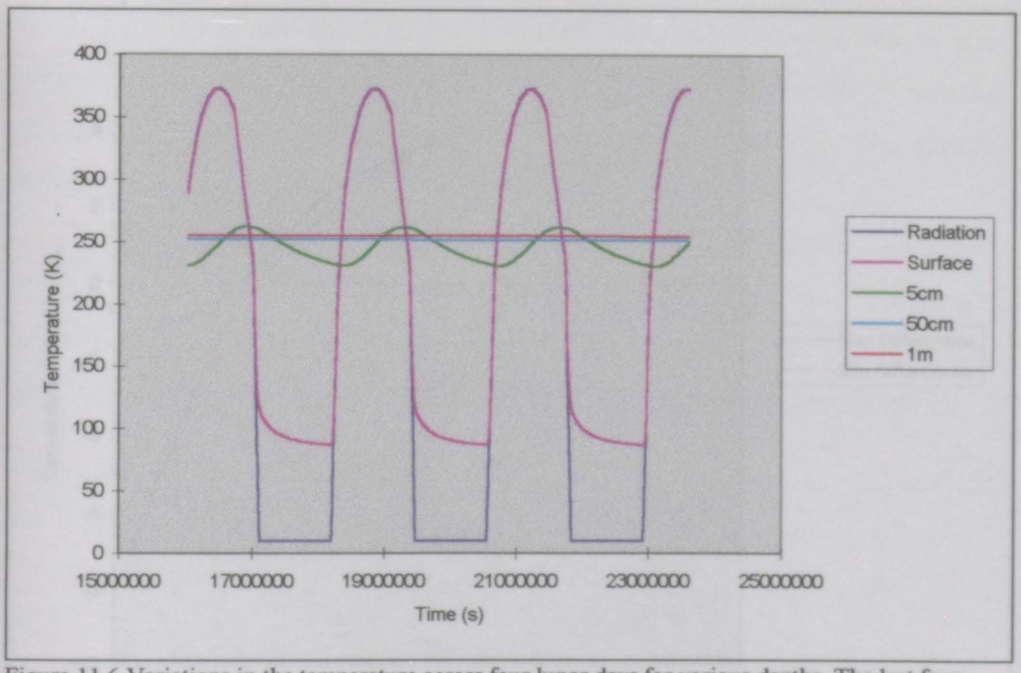


Figure 11.6 Variations in the temperature across four lunar days for various depths. The last four cycles of a ten cycle run are shown, as the model takes 3-4 cycles to converge. The radiation curve indicates the space node temperature at 26°N.

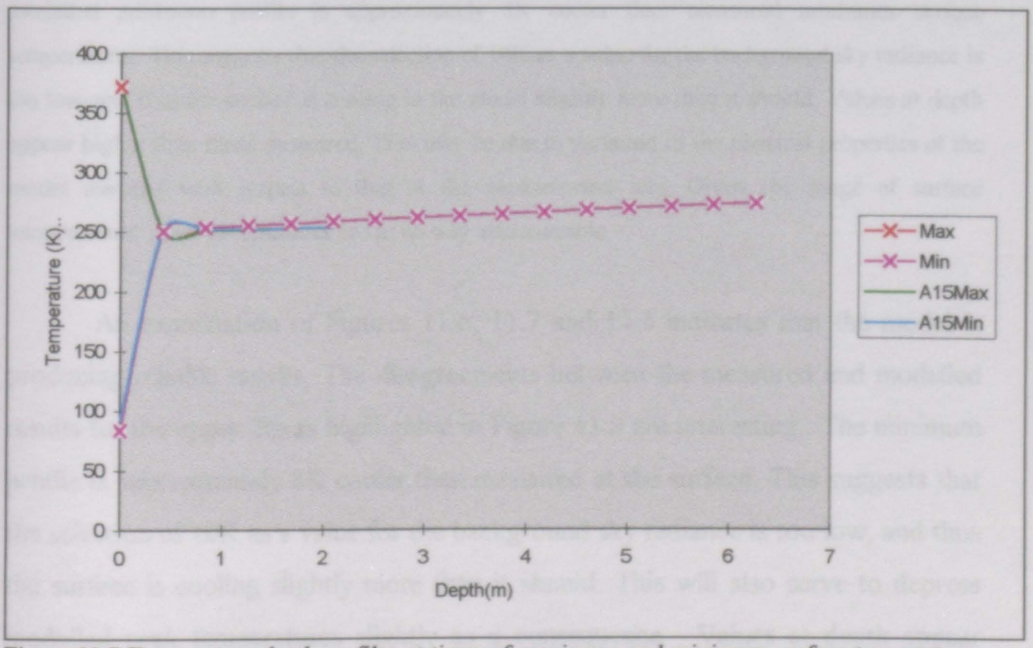


Figure 11.7 Temperature-depth profiles at times of maximum and minimum surface temperature, and the measured profiles from the Apollo 15 heat flow instrument, Probe1 (after Langseth and Keihm 1977). The calculated curves and the measured Apollo curves are reassuringly difficult to distinguish.

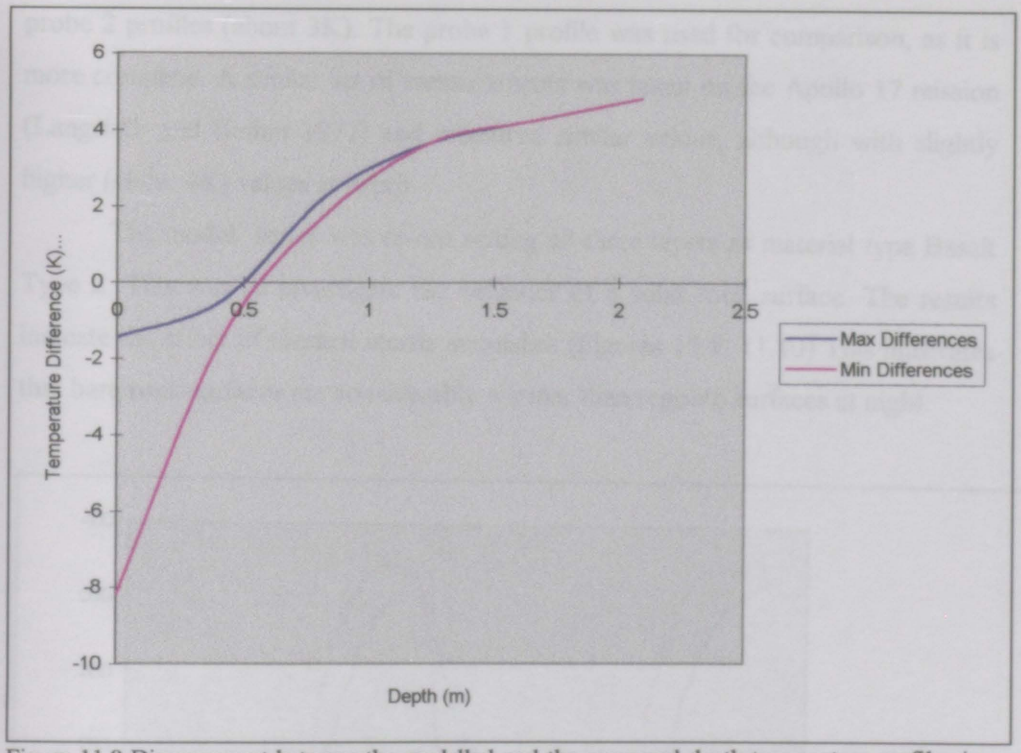


Figure 11.8 Disagreement between the modelled and the measured depth-temperature profiles in the upper 2m, for the times of minimum and maximum temperatures across the lunar day. The modelled minimum profile is approximately 8K cooler than measured minimum surface temperatures. This suggests that the selection of 10K as a value for the background sky radiance is too low, and thus the surface is cooling in the model slightly more than it should. Values at depth appear higher than those measured. This may be due to variation in the physical properties of the model material with respect to that at the measurement site. Given the range of surface temperatures, these uncertainties are in no way unreasonable.

An examination of Figures 11.6, 11.7 and 11.8 indicates that the model is producing reliable results. The disagreements between the measured and modelled results for the upper 2m as highlighted in Figure 11.8 are interesting.. The minimum profile is approximately 8K cooler than measured at the surface. This suggests that the selection of 10K as a value for the background sky radiance is too low, and thus the surface is cooling slightly more than it should. This will also serve to depress modelled peak temperatures slightly as a consequence. Values at depth appear higher than those measured. This could be due to fine variation in the material properties of the regolith which is not represented in the model.

The total disagreement at the surface is less than 3% of the temperature range, and at depth is similar to the differences between the Apollo 15 probe 1 and

probe 2 profiles (about 3K). The probe 1 profile was used for comparison, as it is more complete. A similar set of measurements was taken on the Apollo 17 mission (Langsieth and Keihm 1977) and measured similar values, although with slightly higher (circa. 4K) values at depth.

The model series was re-run setting all three layers as material type Basalt Type 2. This was to investigate the behavior of a solid rock surface. The results indicate the effect of thermal inertia anomalies (Figures 11.9, 11.10) This illustrates that bare rock surfaces are considerably warmer than regolith surfaces at night.

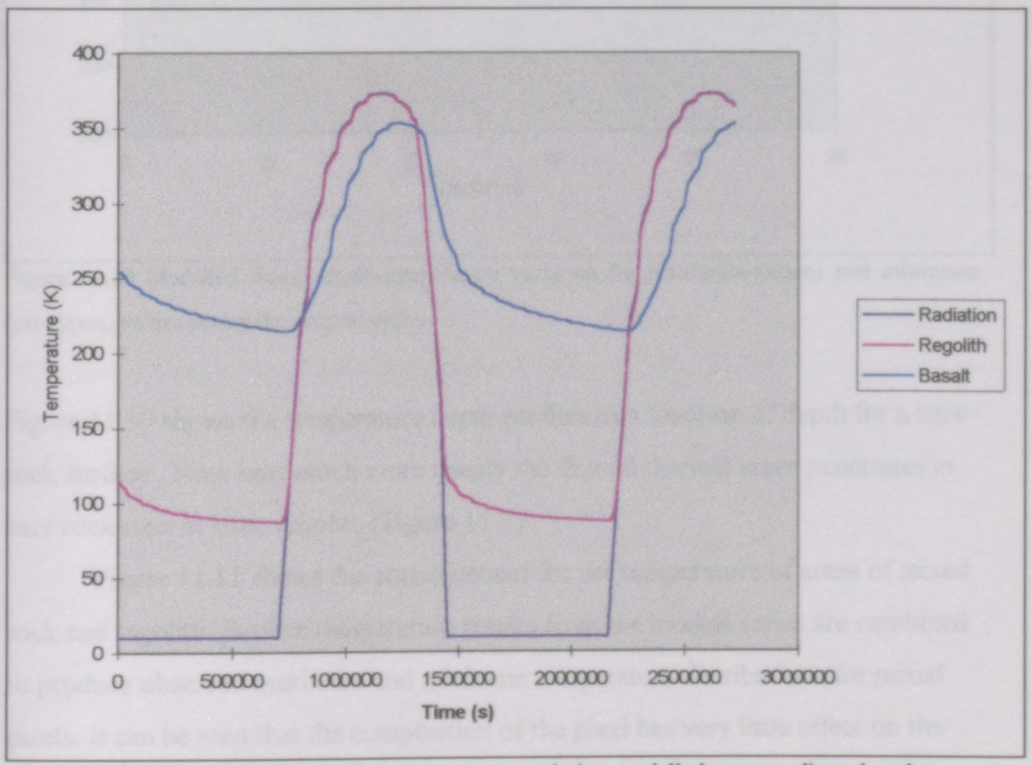


Figure 11.9 Basalt and regolith surface temperature variation modelled across a diurnal cycle.

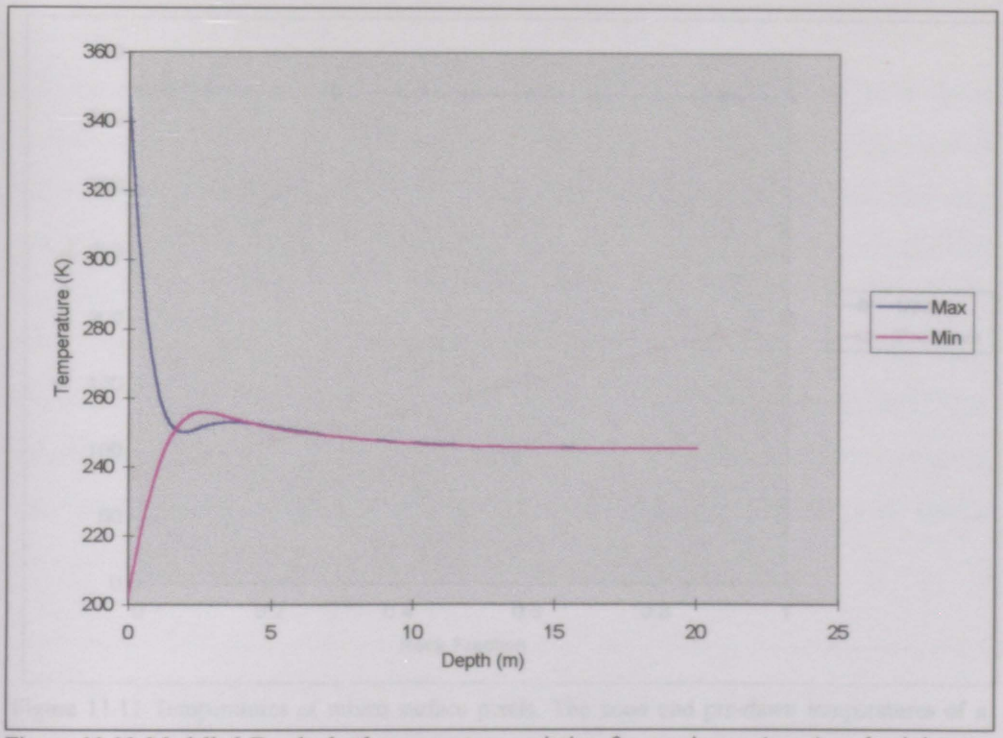


Figure 11.10 Modelled Basalt depth-temperature variation for maximum (noon) and minimum (pre-dawn) values across the diurnal cycle.

Figure 11.10 shows the temperature depth profiles as a function of depth for a bare rock surface . Note how much more deeply the diurnal thermal wave penetrates in bare rock than in lunar regolith (Figure 11.7).

Figure 11.11 shows the consequences for the temperature of areas of mixed rock and regolith. Surface temperature results from the models series are combined to produce observed maximum and minimum temperature distributions for mixed pixels. It can be seen that the composition of the pixel has very little effect on the peak (noon) temperature, which is controlled by solar insolation, but has a much more dominant effect on the minimum (pre-dawn) temperature.

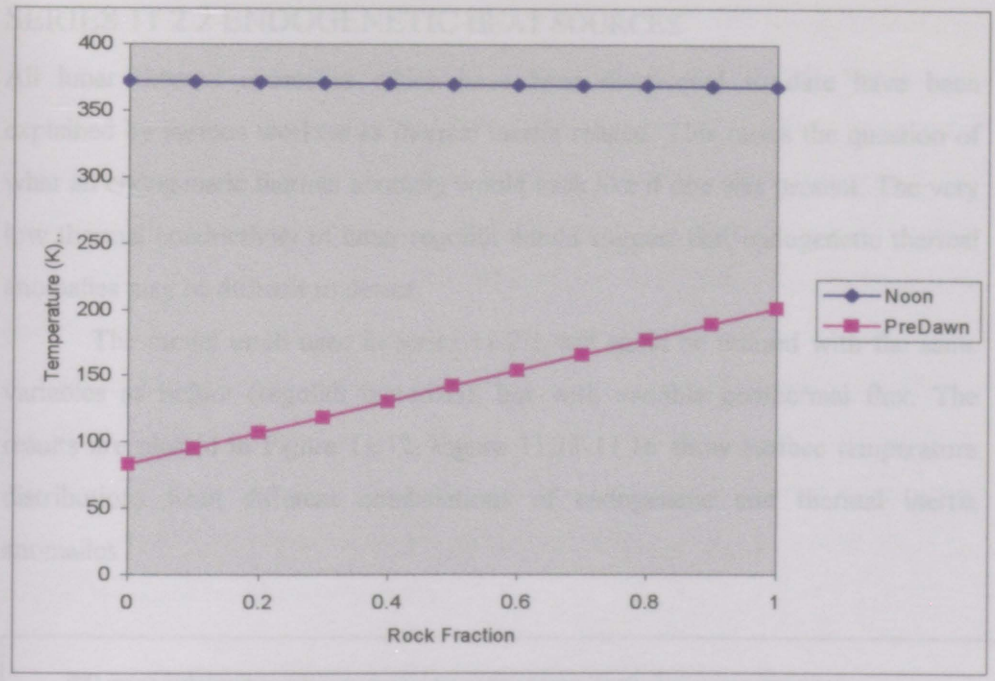


Figure 11.11 Temperatures of mixed surface pixels. The noon and pre-dawn temperatures of a mixed pixel are plotted against the Rock/Regolith surface area ratio. Results from the above models of rock and regolith diurnal cycles are used to generate maximum and minimum temperatures. Note how pre-dawn temperatures are largely controlled by rock compositional variations. Thus pre-dawn temperatures give strong indication of the abundance of rock on the surface.

SERIES 11.2.2 ENDOGENETIC HEAT SOURCES

All lunar thermal anomalies which have been discovered to date have been explained by various workers as thermal inertia related. This raises the question of what an endogenetic thermal anomaly would look like if one was present. The very low thermal conductivity of lunar regolith would suggest that endogenetic thermal anomalies may be difficult to detect.

The model mesh used in series 11.2.1 will again be utilised with the same variables as before (regolith materials), but with variable geothermal flux. The results are plotted in Figure 11.12. Figure 11.13-11.16 show surface temperature distributions from different combinations of endogenetic and thermal inertia anomalies.

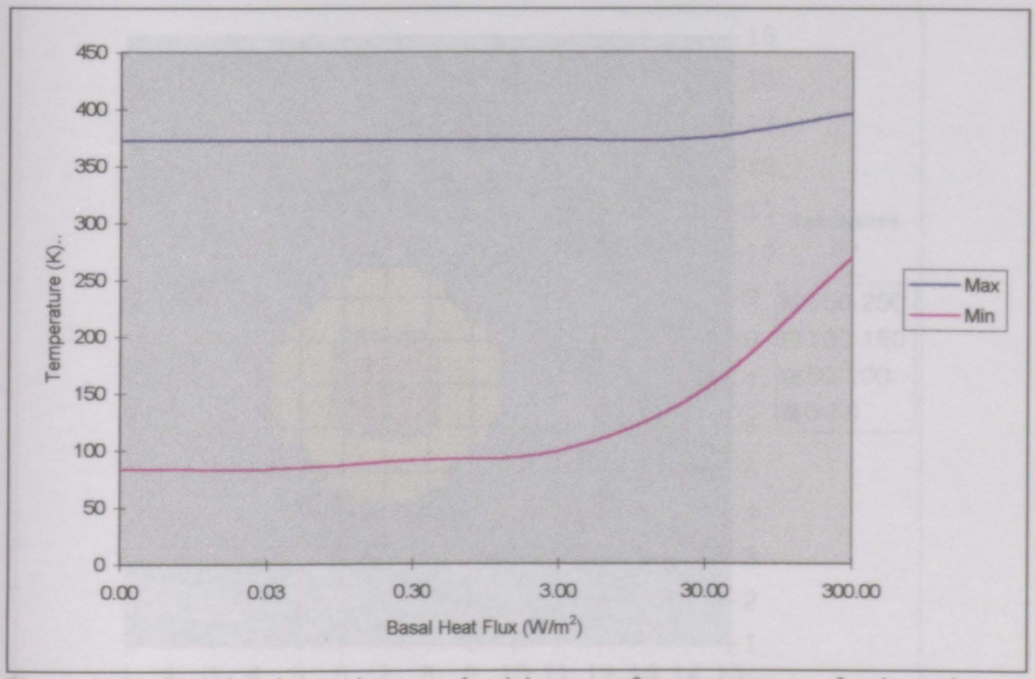


Figure 11.12 Variation in maximum and minimum surface temperatures for increasing geothermal flux. Geothermal heat fluxes at the base of the model in excess of two orders of magnitude larger than the lunar average of $30mWm^{-2}$ are required to show a clear increases in the minimum surface temperature.

It can be observed from a comparison of the results in Figure 11.12 and Figure 11.11 that an endogenetic thermal anomaly cannot be unambiguously distinguished from a thermal inertia anomaly in the lunar context unless the basal

heat fluxes are very large. Previous work in the thermal infrared has thus tended to assume that any thermal anomalies are due to thermal inertia variations. The thermal infrared image alone is insufficient to support this. A region of rock outcrop and a region of elevated heat flow will both produce elevated pre dawn temperatures, and show small to ambiguous variation in the daytime temperature compared to their surroundings. Figures 11.13 to 11.15 compare the virtual thermal images for a 60% coverage rock outcrop with a 30 Wm^{-2} heat flow anomaly from a buried heat source in regolith, at noon and pre-dawn. The virtual thermal images are derived from the results of the model series 11.2.1 and 11.2.2 above. The images are derived by assembling one dimensional surface temperature calculations into a two dimensional image array, and calculating apparent radiant temperatures due to mixed pixels by an area weighted temperature average.

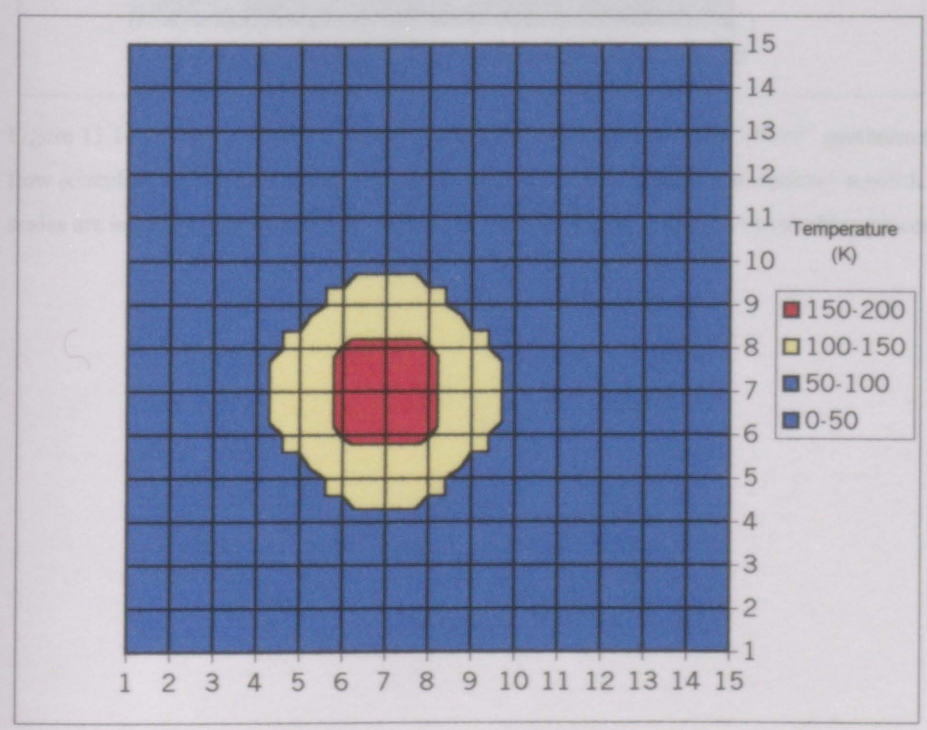


Figure 11.13 Pre-dawn Virtual Thermal Image of a region of 60% rock outcrop (circular, 4.24 pixels across) set in a region of ordinary regolith. Axis scales in pixels, temperatures are in Kelvin. Image has been smoothed by graphing process.

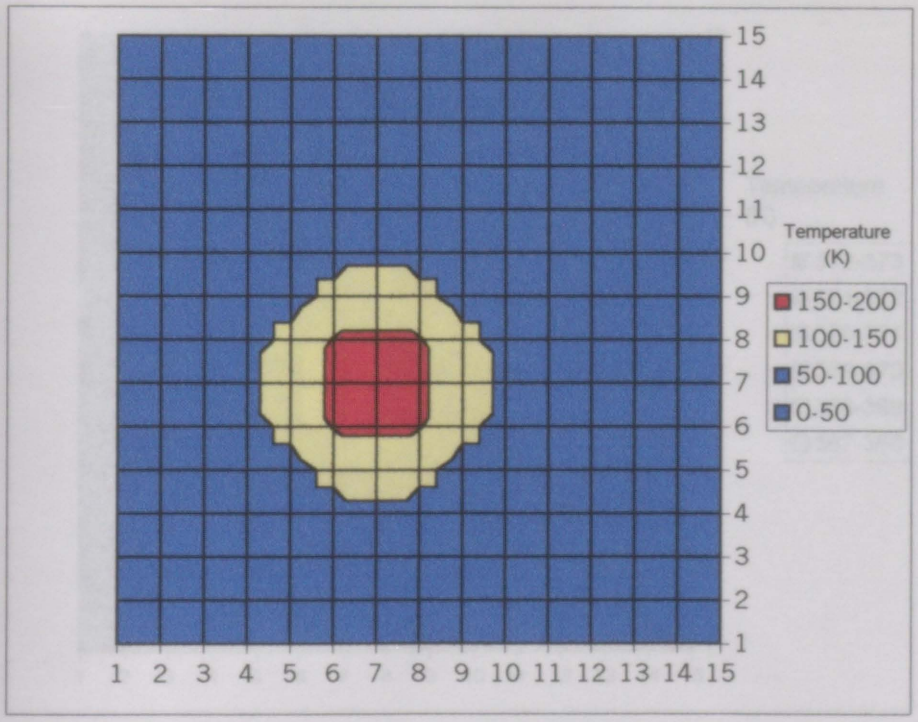


Figure 11.14 Pre-dawn Virtual Thermal Image of a region of anomalous 30Wm^{-2} geothermal heat flow (circular, 4.24 pixels across, centred on pixel 7,7) set in a region of ordinary regolith. Axis scales are in pixels, temperatures are in Kelvin. Image has been smoothed by graphing process.

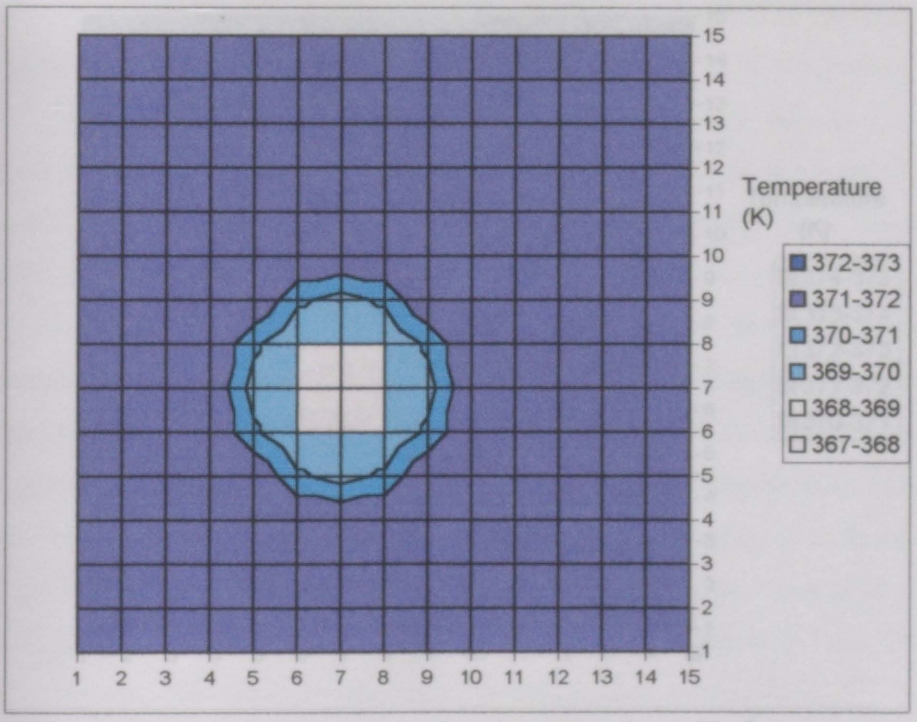


Figure 11.15 Noon Virtual Thermal Image of a region of 60% rock outcrop (circular, 4.24 pixels across) set in a region of ordinary regolith. Note that the region appears as a cold spot, due to efficient conduction of incident radiant energy to depth. Axis scales are in pixels, temperatures are in Kelvin. Image has been smoothed by graphing process.

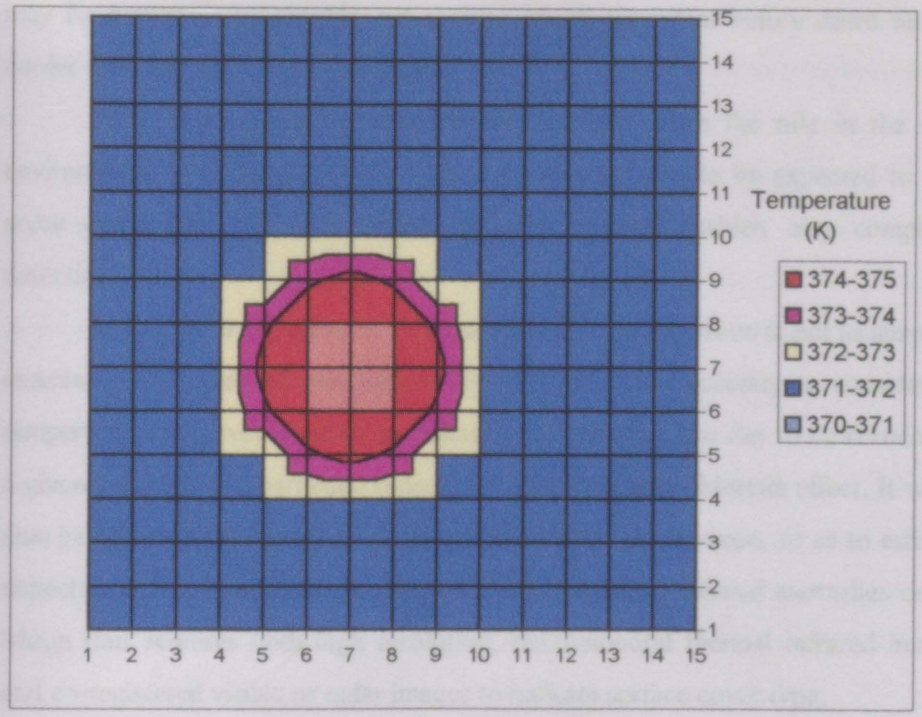


Figure 11.16 Noon Virtual Thermal Image of a region of anomalous $30Wm^{-2}$ geothermal heat flow (circular, 4.24 pixels across) set in a region of ordinary regolith, at local noon. Axis scales are in pixels, temperatures are in Kelvin. Image has been smoothed by graphing process.

Figures 11.13 and 11.14 are identical showing warm regions of equal size and shape set against a background of regolith. The outcrop and heat source creating the warm regions in these figures are indistinguishable in the thermal infrared. Figures 11.15 and 11.16 are distinguishable by the fact that an outcrop in Figure 11.15 will appear cooler than its surrounding regolith at night, whereas the heat source will appear warmer.

Thus endogenetic thermal anomalies cannot be easily distinguished on the basis of a single thermal infrared image, unless they are very large (> circa. $100Wm^{-2}$). A calculation based on Fouriers laws of heat conduction tells us that for a regolith cover (Thermal conductivity~$10^{-3}Wm^{-1}K$), a heat source would have to be at temperature more commonly associated with nuclear physics than geology. Thus looking for warm areas in regolith is unlikely to meet with much success.

However, for solid basalt, with much higher thermal conductivities, active lava near to the surface would certainly elevate the pre-dawn temperature of a rock outcrop above that explicable by thermal inertia effects alone. Smaller heat fluxes

may be detectable by seeking out regions which are warm before dawn but not cooler than their surroundings at noon.

Bare basalt surfaces are the exception rather than the rule in the lunar environment. Even the rockiest of regions could reasonable by expected to have some patches of thin, and highly insulating regolith, which may complicate detection.

Searches for endogenetic thermal anomalies on the Moon is not as simple as examining a thermal infrared image for hot spots. It is necessary to consider the temperature of a given anomaly at different times of the lunar day to be certain that a given hot spot, at a particular time, is not due to a thermal inertia effect. It would also be beneficial to characterise the surface material in advance, so as to estimate expected surface temperatures. Mapping of endogenetic thermal anomalies on the Moon thus requires both high resolution, multitemporal thermal infrared images, and co-registered visible or radar images to indicate surface cover type.

STABILITY OF REGOLITH ICES.

Recent radar investigations (Nozette et al 1996, Feldman et al 1998) have confirmed the existence of volatile ices, probably water, in the lunar regolith at high latitudes. It is thought that these ices originated with cometery impacts on the lunar surface and collected in very cold regions of permanent shadow such as the Aitken Basin. The interiors of evacuated lava tubes are also regions of permanent shadow, and this suggests that they may also serve as potential reservoirs for volatile ices at relatively low lunar latitudes. Such ices may be stable in a lava tube if the temperature of the tube interior rarely rises above the sublimation point temperature for water ice, 133K in vacuum.

Solution of the problem of temperature at depth in regions of permanent shadow is trivial, and use of the finite element method to solve it would be excessive. If we assume that there are no transient effects, and thus the situation is in stable equilibrium, the Fourier heat conduction equation can be used to solve the problem. By substitution into the Fourier heat conduction equation of the values for thermal conductivity of coarse regolith ($8x10^{-3}$ $Wm^{-1}K^{-1}$) the surface temperature (40K) and the geothermal heat flux ($30mWm^{-2}$) we can calculate a thermal gradient of $3.75K\ m^{-1}$. In solid basalt, with a conductivity of $2Wm^{-1}K^{-1}$ there is a much lower

gradient of 0.004K m^{-1}. This implies that in regions of permanent shadow, water ice will be stable in the coarse lunar regolith from the surface down to a depth of about 62m. Feldman et al (1998) state in their discussion of the results from the Lunar Prospector probe, that water ice in the upper 40cm of the regolith will be removed by other, non-thermal processes such as photodissociation and particle sputtering.

In areas that are not in permanent shadow, the problem is more complex due to transient solar heating, and thus requires more complex modelling. Examination of the results in model series 11.2.1 shown in Figures 11.7 and 11.10 shows that at no depth is the temperature below the sublimation point across the diurnal cycle. Thus ices will not be stable across the diurnal cycles at any depth for regolith or solid outcrop at low latitudes. This is consistent with the fact that core samples taken by the Apollo 15,16 and 17 missions, indicated no water or hydrous minerals of any kind to a maximum depth of 3m (Heiken, Vaniman and French 1991), and with low epithermal neutron counts at low latitudes measured by the Lunar Prospector probe (Feldman et al 1998).

This suggests that ice will not be stable in the lunar regolith except in regions of permanent shadow, or regions of near permanent shadow at very high latitudes. Ices will not be stable at low latitudes at any depth, so it is unlikely that shallow subsurface cavities such as lava tubes contain ice deposits at low latitudes.

CONSEQUENCES OF THERMAL MODELS FOR DETECTION OF LUNAR LAVA TUBES.

Extensive lava tubes are believed to occur in the Lunar Maria, and some rilles and catenae (crater chains) are thought to represent collapsed lava tubes. The lower gravity environment of the Moon has a significant effect on the possible morphologies of lunar lava tubes. They may occur at great depth within the lunar maria, as deep as 3000m, without risk of collapse, and may support spans of over 100m across (Heiken et al). The lunar environment also contributes to their potential length, active lunar lava tubes may be thermally stable for up to 1000km (Kesthelyi, 1995). The observed scale of lunar lava flows, rilles and catenae support these figures.

Ideally, cavities should generate a thermal inertia anomaly if they are at a shallow enough depth, as a vacuum has no capacity to store heat, and thus will have a thermal inertia of zero. However, measurements from Apollo 15 (Heiken,el at) suggest that diurnal thermal waves do not penetrate more than 60cm into the regolith, and this is supported by the finding of model series 7.2.1. Thus thermal inertia based lava tube detection is unlikely, except for very shallow cavities in solid outcrop (See model series 11.2.1).

Where skylights are present, however, another possibility for detection exists. For a sufficiently small skylight, the empty lava tube should emit radiation through the skylight as a pure blackbody at the lava tube wall temperature (blackbody radiation and cavity radiation being the same thing). Thus such a skylight should give a steady thermal signature night and day, compared with the varying background. This however, presumes that the lava tube is 'infinite' compared with the skylight size, and thus that the radiation emitted through the skylight does not significantly affect the heat balance within the tube. This can be demonstrated analytically, assuming that conduction through the lava tube roof is negligible. This is a reasonable assumption considering the very low thermal conductivity of lunar regolith. The radiation up through the skylight ($T^4_{skylight}$ in equation 11.2) is the sum of the geothermal heat flux into the floor of the tube divided by the skylight diameter (term 1, right hand side) plus the radiation down the skylight (second term on the right hand side).

$$\sigma T^4_{skylight} = D_{tube} Q_{geot} / D_{skylight} + \sigma T^4_{space} \qquad 11.2$$

Where:

σ Stefan Boltzmann Constant (5.669×10^{-8} $Wm^{-2}K^{-4}$)

$T_{skylight}$ Apparent temperature of the skylight (K)

D_{tube} Diameter of lava tube (m)

Q_{geot} Geothermal Heat Flow (Wm^{-2})

$D_{skylight}$ Diameter of skylight (m)

The results of this equation are graphed in Figure 11.17. Essentially, the closer to unity the skylight size/tube size ratios become, the more the skylight acts like a permanently shadowed pit and less like a cavity with a small opening. However, only when the ratio of the skylight area/lava tube floor area approaches 1/100000 will the radiant temperature begin to decrease as a result of this effect. For lava tubes many kilometres long, this ratio may not be an issue, if skylights are not abundant. The radiant temperature will stabilise at the temperature determined by the geothermal gradient. For less favourable ratios, the skylight will appear colder. Eventually, when the ratio reaches unity, it will act simply as a permanently shadowed pit.

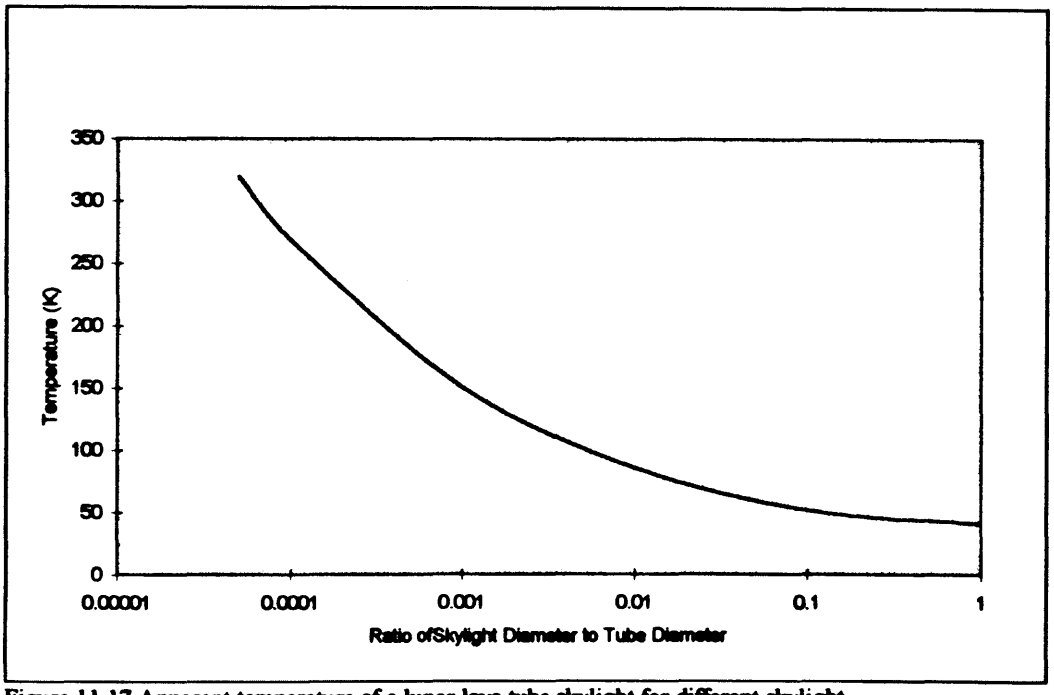


Figure 11.17 Apparent temperature of a lunar lava tube skylight for different skylight diameter/lava tube diameter ratios.

Proximate to the lava tube opening a second factor must be considered, however. Areas at the lava tube floor, exposed to large proportion of cold sky, may perhaps cool anomalously. The local radiative heat balance is described in Figure 11.18 and by Equation 11.3

$$P\sigma(T_{skylight}^4 - T_{tube}^4) + (1-P)\sigma(T_{skylight}^4 - T_{space}^4) = 0 \qquad 11.3$$

Where:

P Fraction of lava tube roof occupied by skylight ($0<P<1$)

σ Stefan Boltzmann Constant. (5.669×10^{-8} $Wm^{-2}K^{-4}$)

$T_{skylight}$ Radiant Temperature of skylight (K)

T_{tube} Radiant Temperature of Lava Tube walls (K)

T_{space} Radiant Temperature of space seen up through skylight (Approximately 40K).

This equation assumes a steady state, i.e. the floor of the lava tube as seen through the skylight is in radiative equilibrium with its surroundings, and that

geothermal heat flow is a negligible contributor to the heat balance of that pixel. At $30mWm^2$ this is a reasonable assumption.

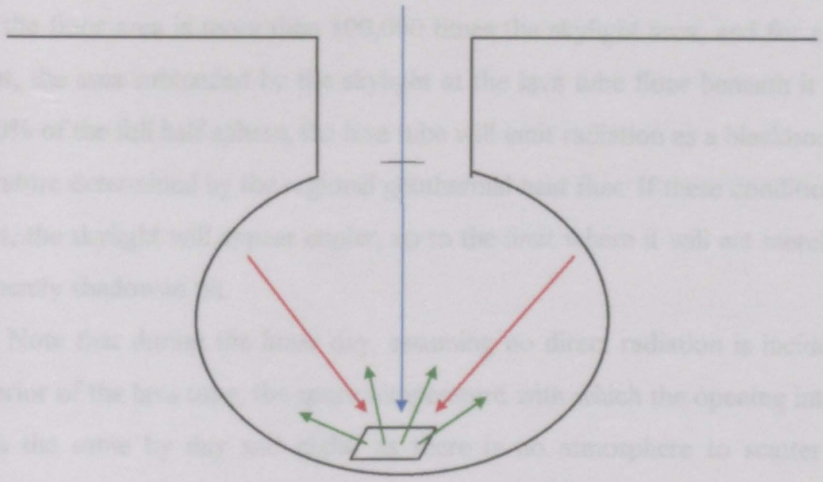


Figure 11.18 Radiative equilibrium model described mathematically in equation 11.3. For a steady state to occur, the temperature of the lava tube floor seen through the skylight (box at bottom of tube) must be such that the heat acquired by radiation from the tube walls and roof (Red arrows) plus the heat gained from the sky (Blue arrow) must be balanced by the heat lost by the floor of the lava tube (green arrows)

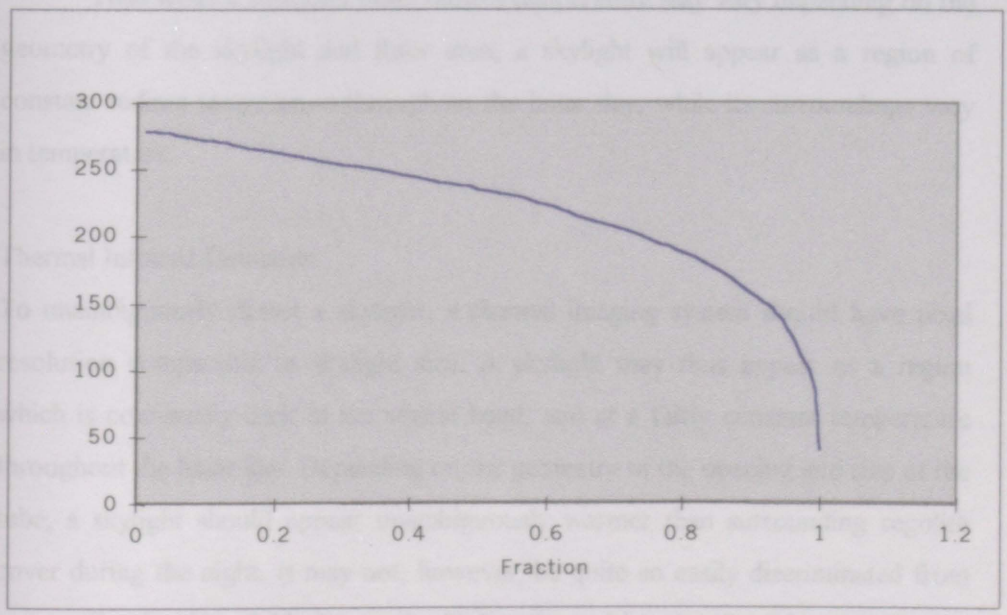


Figure 11.19 shows the apparent radiant temperature of a lava tube skylight for a lava tube with a wall temperature of 280K and a space temperature of 40K for increasing skylight size as a fraction of the tube diameter.

From Figure 11.19, skylight size is not a concern unless more than 10% of the lava tube floors field of view is occupied by the skylight. Thus, given a lava tube where the floor area is more than 100,000 times the skylight area, and for a given skylight, the area subtended by the skylight at the lava tube floor beneath it is less than 10% of the full half sphere, the lava tube will emit radiation as a blackbody at a temperature determined by the regional geothermal heat flux. If these conditions are not met, the skylight will appear cooler, up to the limit where it will act merely as a permanently shadowed pit.

Note that during the lunar day, assuming no direct radiation is incident on the interior of the lava tube, the space temperature with which the opening interacts remains the same by day and night, as there is no atmosphere to scatter solar radiation. The only diurnal effects which may reach the interior of a permanently shadowed pit or tube are secondary radiations from surfaces in direct sunlight, which are visible from the shadowed region (the side of a pit, for example). While this effect may be significant for a permanently shadowed pit with a wide opening, it is unlikely to be significant for a skylight with a relatively narrow opening.

Thus while a skylights exact radiant temperature may vary depending on the geometry of the skylight and floor area, a skylight will appear as a region of constant radiant temperature throughout the lunar day, while its surroundings vary in temperature.

Thermal Infrared Detection

To unambiguously detect a skylight, a thermal imaging system should have pixel resolution comparable to skylight size. A skylight may thus appear as a region which is continually dark in the visible band, and at a fairly constant temperature throughout the lunar day. Depending on the geometry of the opening and size of the tube, a skylight should appear unambiguously warmer than surrounding regolith cover during the night. It may not, however, be quite so easily discriminated from surrounding boulder field, due to the higher thermal inertia of solid rocks. During the day, a skylight should appear unambiguously cooler than its surrounding rock or regolith surface. Daytime detection is, however, complicated by the issue of shadow. Is a particular region cooler because it is a skylight, partial pit, or

temporarily shadowed region? Co-registered, high-resolution day-night image pairs of very high spatial resolution are thus required to detect lava tube skylights.

The maximum available thermal infrared resolution is 55m, (Clementine) and this is clearly insufficient for skylight detection. To emit as a blackbody at the wall temperature a lava tube with a 55m diameter skylight this would be of improbable size, even by lunar standards. A skylight of such size would more probably act as a permanently shadowed pit, appearing consistently cool and dark.

11.4 CONCLUSIONS

The Finite Element method is more than adequate for the accurate modeling of lunar surface thermal processes. In many cases, simple analytic models are entirely sufficient to predict surface temperatures, and to giver considerable insight into lunar processes.

The very low thermal conductivity of lunar regolith, and its ubiquity, make the detection of endothermic lunar thermal anomalies very difficult. Pre-dawn Thermal Infrared images of the lunar surface can, if of sufficiently high resolution, be used to identify endogenetic thermal anomalies if these anomalies lie under bare basalt. Endogenetic thermal anomalies overlain by lunar regolith will be very difficult to discriminate at any time unless regolith layers are very thin (<30cm) or the anomaly is extraordinarily hot.

The resolution required for the detection of an endothermic anomaly is obviously dependent on the size of the anomaly. In contrast to with terrestrial studies, images taken just at noon are the most useful for detecting such anomalies, because solar heating will mask thermal inertia effects. Supplementary data concerning surface material type, boulder distribution etc. is also beneficial to aid in discriminating high thermal inertia rock outcrop from genuine endogenetic thermal anomalies.

For detection of lava tube skylights, high resolution, co-registered day night image pairs are required. Presently available data is of insufficient quality and resolution to locate lava tube skylights by this method. Multitemporal images of near metre scale resolution would be required to unambigiously distinguish skylights, pits and shadows.

Figure 11.20 is illustrative of the different thermal profiles of differing surface types across the lunar day. It is worth noting that one could expect to observe a continuum of surface cover types between the basalt curve (red) and the regolith curve (pink). High resolution visible or radar images could serve to reduce the quantity of 'mixed pixels'. Similarly, differing pit and skylight geometry's would create a continuum of sources with fixed temperature values. When aspect variations and resulting transient shadows are considered, the position becomes more complex again. High resolution (near metre scale) multitemporal image

coverage's with supplementary visible band or radar data at similar or higher resolution would be required to interpret intermixed thermal signatures. Overall, pre-dawn images give the widest spread between the observed ideal temperature profiles of surface types. Noontime images are however, also required to adequately discriminate skylights and areas of deep shadow. Before dawn, shadows could be confused with regolith, and skylights, depending on their geometry, could be confused with mixed surfaces.

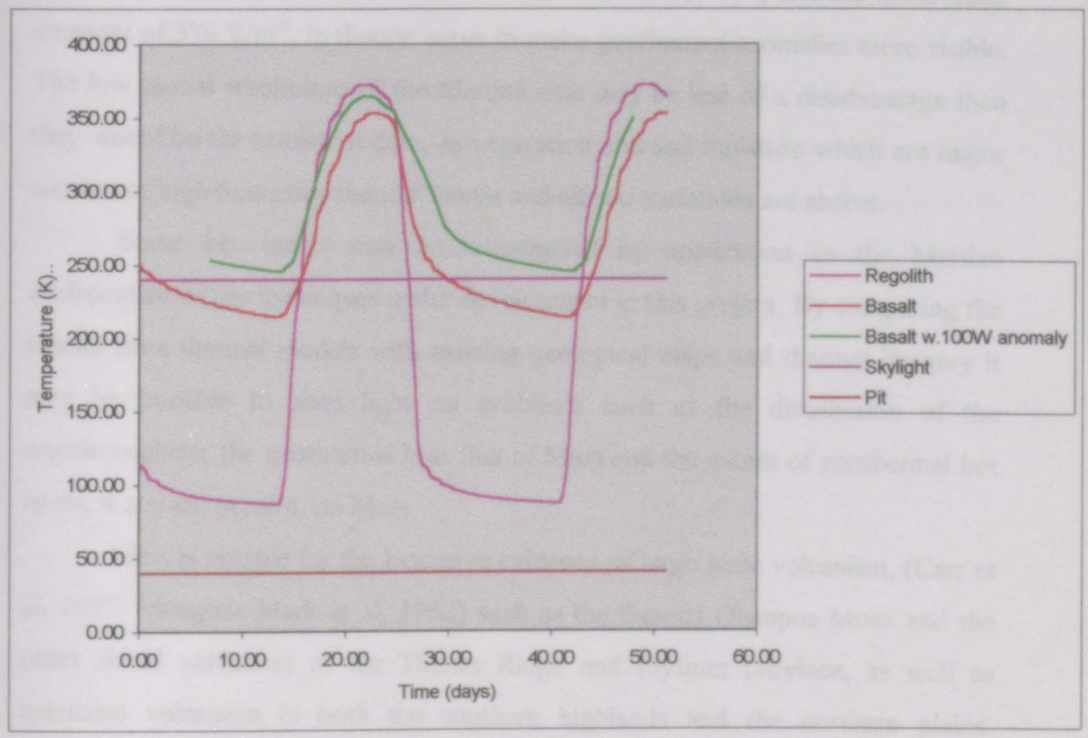


Figure 11.20 Summary of the diurnal temperature variation in basalt (red), regolith (pink), basalt with 100Wm^{-2} basal heat flux (green), a lava tube skylight (brown) and a permanently shadowed pit (black). This shows how different kinds of lunar surfaces do give distinctive thermal signatures over time.

Chapter 12: Mars

The cold, arid environment of Mars is highly suited to geothermal studies and thermal inertia modelling. Some of the difficulties inherent with the use of terrestrial thermal data such as the importance and complexity of surface boundary layer processes are absent or greatly reduced in the Martian environment, while other processes, such as the thermal effect of atmospheric dust, are greatly compounded. Colder surface temperatures of 130-270K (Keiffer et al, 1977) and the lower solar constant of 576 Wm^{-2}, in theory, serve to make geothermal anomalies more visible. The low spatial resolutions of the Martian data may be less of a disadvantage than they would be for terrestrial data, as vegetation and soil moisture which are major sources of high frequency thermal inertia and albedo variations are absent.

Some key issues may be investigated by application to the Martian environment of the techniques under development in this project. By comparing the results from thermal models with existing geological maps and thermal imagery it may be possible to shed light on problems such as the distribution of the cryolithosphere, the geothermal heat flux of Mars and the extent of geothermal hot spots, if any are present, on Mars.

Mars is notable for the extensive evidence of large scale volcanism, (Carr et al, 1977, Mouginis-Mark et al, 1982) such as the famous Olympus Mons and the other shield volcanoes of the Tharsis Ridge and Elysium province, as well as extensive volcanism in both the southern highlands and the northern plains. Extrusive volcanic rock is thought to cover at least half the surface of Mars (Tanaka et al, 1988). Very recent activity may have occurred at Hecates Tholus (Scott, 1982) and on the floor of the Valles Marineris (Lucchita, 1987a,b), but the limitations of crater age dating make it difficult to quantify exactly how recent. Certain radar observations of the region west of Pavonis Mons (Muhleman et al, 1991) have been interpreted as an ash band several metres thick, presumably recent in origin, as aeolian activity has not yet dispersed it. To date no certain contemporary volcanic activity has been identified. Thermal modelling may help to identify the effect on surface temperature of subsurface magma chambers, both directly through increased geothermal heat flow, and indirectly by the extent to

which a hot magma chamber will melt a large volume of surrounding cryolithosphere and hence affect the local thermal inertia. This would be of assistance in identifying regions of active volcanism.

Studies have shown that throughout its history Mars may have outgassed sufficient water from its crust to cover the surface with a layer of water between 50m and 1000m thick (Baker et al, 1988). Extensive morphological features such as rampart craters and debris flows suggest that a great deal of this water may remain as cryolithosphere (Squyres et al, 1992). Both the distribution of morphological features and theoretical modelling of ground ice stability under Martian conditions suggest a layer of cryolithosphere at a depth to the base of 1-3 km at the equator and 2-8 km at the poles (Squyres et al, 1992). This cryolithosphere volume is equivalent to a global liquid water inventory 70-700m deep (Clifford 1984, 1987b). Any excess water may exist in liquid form underneath this ice layer (Squyres et al, 1992). Most figures concerning the cryolithosphere have error ranges of an order of magnitude.

12.1 THE THERMAL GEOLOGY OF MARS

Previously published work on thermal processes on Mars can be most conveniently classified according to the dataset from which it was derived. With the exception of some preliminary work using Mariner data, the bulk of the Martian thermal studies have been conducted using Viking data. A limited amount of work has been carried out using the TERMOSKAN dataset, and the more recent Pathfinder and Global Surveyor datasets.

VIKING Infrared Thermal Mapper

The Viking Infrared Thermal Mapper (IRTM) was flown aboard both Viking spacecraft in the 1970's, and provided thermal infrared imagery in 6 infrared bands. It is described in further detail in *Appendix D: Description of Instruments* . The Viking IRTM dataset is presently available on CD-ROM.

The principle resource on the geology and geomorphology of Mars are Panchromatic photomosaics based on visible band images also from the Viking missions. Very little work could be carried out without the availability of these photomosaics for reference. They are, fortunately, available widely online.

Investigations using Viking IRTM data (Keiffer et al, 1977) found a stronger than anticipated atmospheric contribution to the observed radiance due to atmospheric dust, especially at larger view angles. Atmospheric optical depths were found to vary from 0.08 at 20μm to 0.14 at 9μm (Keiffer et al, 1977). This peak in the thermal infrared is thought to be due to silicates in suspended atmospheric dust particles (Hanel et al, 1972a). Simple one dimensional finite difference modelling of expected predawn surface temperatures were carried out by Kieffer et al (1977), using uniform values of albedo, emissivity and thermal inertia. After comparison with measured predawn temperatures it was found that:

"The magnitude of the Predawn temperature variations was unexpected.... most are not well understood, and some are simply baffling."

Keiffer et al, 1977

Many of the variations in the pre-dawn temperature were later correlated with topography or thermal inertia variations. Anomalous predawn warming was widely observed and some areas were warmed by up to 6K above predicted values. This may have been due to formation of water ice ground fogs (Flaser and Goody, 1976). The most extreme warm variations were found on the floor of the Valles Marineris. Many smaller features had variation of between 2K and 8K.

Mapping of thermal inertia shows a strong correlation between thermal inertia and surficial geological units (Spudis and Greeley, 1976). In general thermal inertia values were quite low. This is thought to be due to very fine-grained aeolian deposits and highly porous volcanic material. A strong correlation was found between thermal inertia and elevation, probably due to the effect of varying atmospheric pressure on pore space conductivity. Anomalies were found, such as a low inertia region in the usually high inertia cratered terrain of Arabia, whose midday temperatures are anomalously high. Volcanic regions have also been noted to have inertia which increases as a function of apparent age (Keiffer et al, 1977) This may be due to infilling of pore spaces by collapse or secondary crystal growth. The resolution of the thermal inertia survey was very low, readings were collated into 2 degree square bins. In general, due to the low resolution (60-200km per pixel) of the IRTM data, it was unlikely that any volcanic activity, unless very extensive, would be detected. However, no detailed study of the data accounting for albedo variations was carried out.

TERMOSKAN

The TERMOSKAN instrument was flown aboard the ill fated Phobos probes in 1989. The Phobos 1 craft was lost in transit to Mars and only four instrument pans were acquired (see Table 12.1) before loss of contact with the Phobos 2 spacecraft.

The TERMOSKAN dataset has not been as extensively 'worked over' as has the Viking IRTM data but it is of limited quality and aerial extent.



Figure 12.3 Thermal infrared image of the region shown in Figure 12.1. No obvious 'hot' pixels are evident, with the exception of regions showing elevated solar heating due to aspect, such as the canyon wall on the top-left, and the two crater rims. It is probable that any endogenetic heat may be is of small aerial extent insufficient to greatly elevate the pixel temperature.

MARS GLOBAL SURVEYOR

The Mars Global Surveyor (MGS) Thermal Emission Spectrometer (TES) Imaging system uses a 3x2 detector array, and has three principle detectors, a wideband visible, TIR sensor, and a Michelson interferometer, providing high resolution spectra in the range 6-50μm. The instrument is primarily designed to map mineral abundances by means of their thermal infrared spectra. System resolution in the nominal mapping orbit is 3km.

A limited quantity of data is becoming available from the MSG-TES since the system began acquiring data in the spring of 1998. Difficulties with the aerobraking manoeuvre designed to circularise the crafts orbit delayed commencement of systematic mapping. Unfortunately the primary data are not in an image format, which makes them more difficult to use. In addition, the system

Selivanov interpreted the plumes as volcanic. They could also be interpreted as cloud or windblown dust. Detailed examination of high resolution visual images (Viking and MOC) and other thermal datasets (IRTM and TES) would be advisable before coming to any conclusions.

Extensive work was carried out on the TERMOSKAN dataset by Betts (1994). Betts identified thermally distinct ejecta blankets and studied thermal inertia of channels in the Valles Marineris. Betts also studied the thermal effects of the shadow of Phobos, captured in pans 3 and 4, and carried out finite difference modelling of these effects.

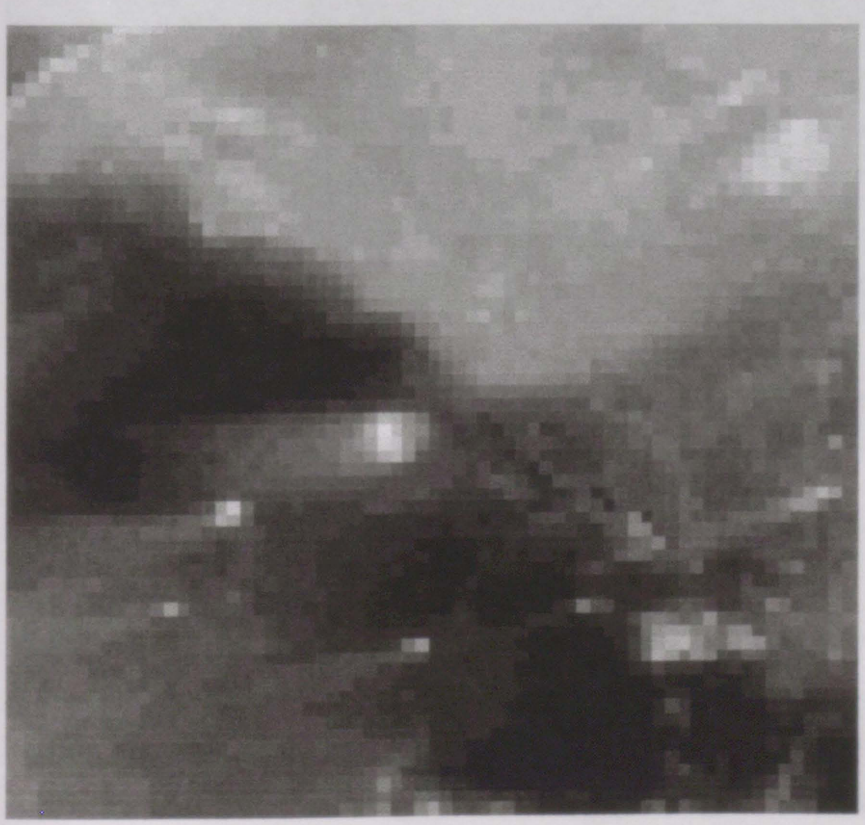


Figure 12.2 Visible band TERMOSKAN image of the candidate volcanic activity noted by Selivanov (Selivanov et al, 1992) Note the long plume orientated in the prevailing wind direction.

resolution of 3km (lower than that of the TERMOSKAN system) reduces the utility of the data. It is thus likely that this dataset will be more useful for following up candidate sites rather than for conducting detailed anomaly searches.

The Mars Orbital Camera instrument (MOC) is also operational aboard MGS. This instrument is a visible band sensor with an optimum spatial resolution of 3m. This data, when they become available, will be very useful for following up potential anomalies in the visible part of the spectrum.

12.2. PHYSICAL PROPETIES OF MARTIAN GEOLOGIC MATERIALS

BEDROCK

The exact nature of the Martian bedrock is not well known, but is likely to be more diverse than that of the moon. At the Ares Vallis site of the Mars Pathfinder landing, a wide variety of volcanic and probable sedimentary rock types were observed (Rover Team, 1997). Few measurements exist for the thermal properties of Martian rocks. Densities and thermal inertias are approximately 260kgm^{-3} and 1670 Jm^{-2}s$^{-1/2}$K^{-1} respectively (Christensen and Moore (1992), Moore and Jakosky (1989)). Assuming typical values of specific heat capacity (800Jkg^{-1}K^{-1}) this gives thermal conductivites of 1.3Wm^{-1}K^{-1}. These values are somewhat low by terrestrial standards, but may be explained by a general reduction in thermal conductivity from solid values due to porosity. In addition, the specific heat capacity estimate may be too high, as it would be if the specific heat capacity followed the same temperature dependent relationship as for lunar basalt.

Based on the known physical parameters of Martian rocks, and assuming them to be similar in nature and behaviour to well quantified rock types, it seems reasonable to use the same values for low porosity lunar basalt to describe Martian rocks. This assumption is also reasonable for this thesis given that most of the models being investigated in this chapter (lava tubes, endogenetic heat sources) would occur in extrusive volcanic regions.

REGOLITH

Martian soil types are likely to be much more varied than those of the moon. Observations from the Mars Pathfinder lander and Sojourner rover (Rover Team, 1997) show a wide variety of soil types, thought to range from aeolian deposits to well consolidated pans. A selection of estimated physical parameters from published sources are listed in Table 12.2.

Material	Density kgm^{-3}	Thermal Inertia $Jm^{-2}s^{-1/2}K^{-1}$	Source
VL1 Block	1150	100	(Christensen and Moore (1992), Moore and Jakosky (1989)
VL1 Drift	1600	387	(Christensen and Moore (1992), Moore and Jakosky (1989)
VL2 Clump	1400	262	(Christensen and Moore (1992), Moore and Jakosky (1989)
MP Overall	1520	450	Rover Team (1997),(Edgett 1996)

Table 12.2 Thermophysical Parameters of Martian Soils.

Assuming that the specific heat capacity obeys the same temperature dependence noted for other similar materials at low temperatures (such as lunar basalts and regolith material), the thermal conductivity can be estimated. Note that, since the thermal inertia is derived from day night temperature differences, the derived thermal conductivity will be an average value for the temperature range of the material. Temperature dependant variations in the thermal conductivity are not described. Such variations are likely to be complex, since they will be affected by the porosity, and the pore fluid pressure. Derived physical parameters of the four soil types listed above are specified in *Appendix C.2.4 MARTIAN SOILS*.

12.3 THERMAL MODELS OF THE MARTIAN SURFACE

SERIES 12.3.1 DIURNAL THERMAL MODELLING

The diurnal thermal modelling carried out aims toward modelling the surface temperature of Mars as a function of the underlying geology and surface boundary layer processes. This will serve largely as a validation exercise for comparison with existing thermal models to ensure that the diurnal component of the fully transient endothermic models is realistic. Unlike the lunar examples, no detailed 'ground truth' exists for comparison of temperature-depth profiles. Detailed meteorological data exist for the Mars Pathfinder landing site.

The investigations will use the linear mesh used previously in *Chapter 11: Lunar Thermal Modelling* (model series 11.3.1) but adapted for the Martian environment. This adaptation involves using different materials, changing the timebase to reflect the shorter Martian Diurnal cycle, and modifying the physical parameters to reflect Martian conditions.

Physical Parameters of the Model series

The physical parameters of a model can be classified into three types, the material properties, the upper boundary conditions, and the lower boundary conditions.

(i) Material Properties

Basalt Type 2 (see *Appendix C*) is used for the lower two layers of the model. A temperature dependent specific heat capacity is applied, but the thermal conductivity is held static at $2Wm^{-1}K^{-1}$. A range of Martian soils are used in the models for the upper 5cm layer.

(ii) Lower Boundary Conditions

The basal geothermal flux for Mars, required to define the lower boundary condition of the model, is unknown. Estimates based on chondrite models vary, from $30mWm^{-2}$ (Fanale, 1976), to $35mWm^{-2}$ (Toksoz and Hsui, 1978), to as high as $40mWm^{-2}$ (Davies and Arvidson, 1981). In any event, based on experience of prior investigations in other environments, these fluxes are so low as to have little

effect on the surface temperature, so this term is set to zero. Later models will explore the effect of variations in this parameter.

(iii) Upper Boundary Conditions

The upper boundary conditions can be constrained using the Mars Pathfinder Atmospheric Structure Instrument/Meteorology (ASI/MET) data (Schofield et al, 1997).

Schofield et al (1997) noted that atmospheric temperature variations were very consistent from day to day, and a detailed meteorological dataset exists. However, the atmospheric temperature is likely to have little or no effect on the surface temperature due to its low density (see below).

The temperature of the space node, (the node with which the surface of the model interacts radiatively) was calculated in the usual way. First the expected incident radiance from solar and atmospheric emission was calculated. Then by inverting the Planck radiation formula a space node temperature was calculated which would simulate the emission.

Incident solar radiation was calculated assuming a latitude of 19.17°, (Mars Pathfinder latitude), a median solar constant of 586Wm^{-2} and an atmospheric transmissivity of about 0.6 (Smith et al, 1997)

Calculation of atmospheric emission is more complex. Early published work (Kieffer et al, 1977, Clifford et al, 1987) used a technique called the 2% assumption, setting a constant downward atmospheric flux of 2% of the maximum solar incident radiation. Subsequent work by Haberle and Jakosky (1991) found this figure to be too low. Using a multilayered atmosphere model and calculating emission for CO_2 and atmospheric dust they derived a numerical model describing the atmospheric flux as a function of dust opacity. The Haberle and Jakosky atmospheric emission values (ranging from 25-40Wm^{-2} over the day) are used in this investigation as they represent expected emission for typical dust opacity of the Pathfinder site (0.5, Smith et al, 1997). Note that the Haberle and Jakosky values were calculated for the VL-1 site (latitude 23°N) and would not be expected to differ significantly from the conditions at the Pathfinder site (latitude 19.17°S). However atmospheric pressure at the Pathfinder site was about 1mbar lower (Schofield, 1997).

The convective heat transfer coefficient is more difficult to quantify, and may not be thermally significent. Kieffer et al, (1977), showed the conductive fluxes in the absence of wind to be negligible. Jakosky (1979) calculated that, even in the most extreme cases, sensible heat transfer could amount to no more than 3% of maximum insolation.

The ASI/MET instrument aboard Mars Pathfinder measured windspeeds in the range 5-8ms. Turbulent convection was also observed in the atmospheric boundary layer from 0730 to 1645 Local Time as heat built up on the Martian surface. At other times the atmosphere was thermally neutral atmosphere and heat transfer was by conduction only. While the actual meteorology of the surface boundary layer may be complex, the amount of heat transferred from the surface is negligible, even when convection is active, and this term can be safely omitted.

It is worth noting that at Martian surface atmospheric pressures, CO_2 frosts begin to form at 149K, a matter which may greatly complicate the surface boundary condition if such temperatures are reached overnight. Frost formation will introduce a latent heat of phase change term to the surface boundary condition, as heat is used up and released during frost condensation and sublimation, Frost introduces a non linearity in the surface emissivity, as the emissivity of surface CO_2 frost is about 0.65, much lower than that of bare soil, which is normally in the 0.9-1.0 range. Given that these models are being conducted for relatively low latitudes, it is not however, anticipated that the frost point threshold will be crossed.

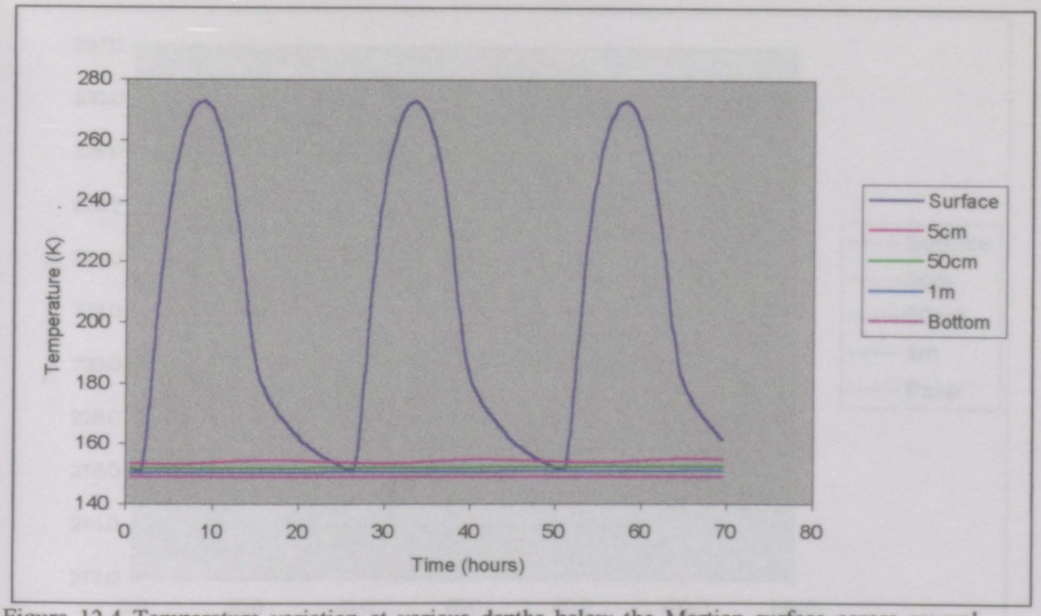


Figure 12.4 Temperature variation at various depths below the Martian surface across several diurnal cycles

Figure 12.4 shows a sample of the results set, commencing three days into a model run, using a VL1 Blocky soil types. It can be seen from the graph that the surface temperature has converged to a stable solution while temperatures at any depth are hardly affected by the surface temperature variations at all. This is due to the very low thermal conductivity of the soil type. To see if the model converges correctly for results at depth, a more conductive material must be used.

Figure 12.5 shows the results calculated for a more conductive material, Basalt Type 2. It can be seen that the solution converges almost immediately.

Figure 12.6 shows the modelled surface temperature variations for different surface materials. Note the differences between the behaviour of Martian soils in this figure to the behaviour of lunar regolith in Figure 11.9.

Figure 12.7 summarised the temperature variation range for different materials. Note how materials with lower thermal inertia exhibit higher temperature variations, as would be expected.

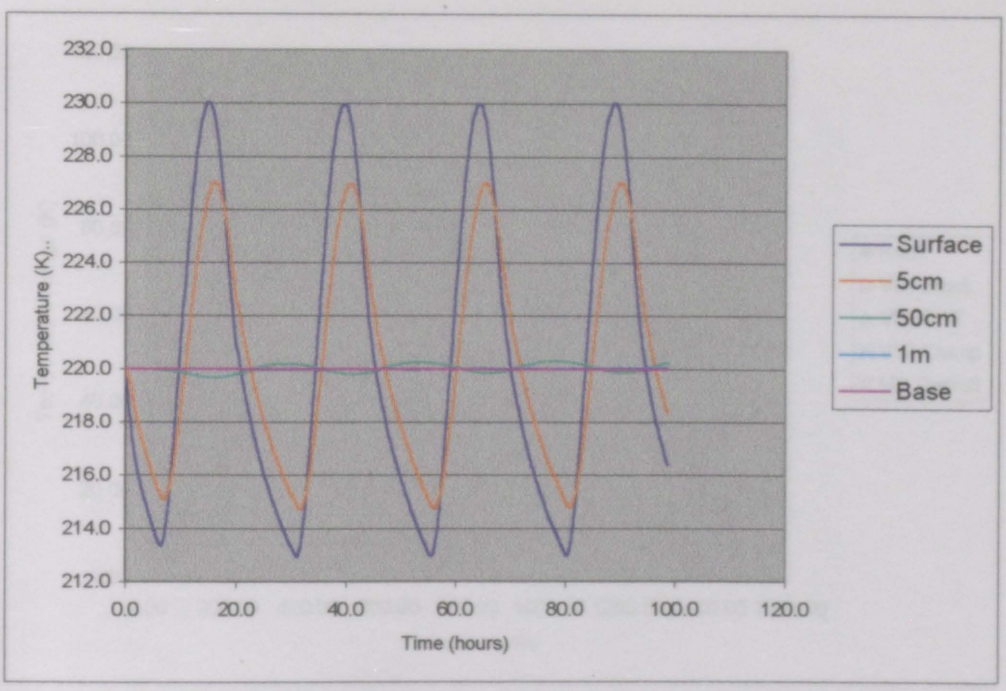


Figure 12.5 Diurnal temperature variations at various depths for solid basalt 2, for an initial temperature of 225K, the solution converges almost immediately.

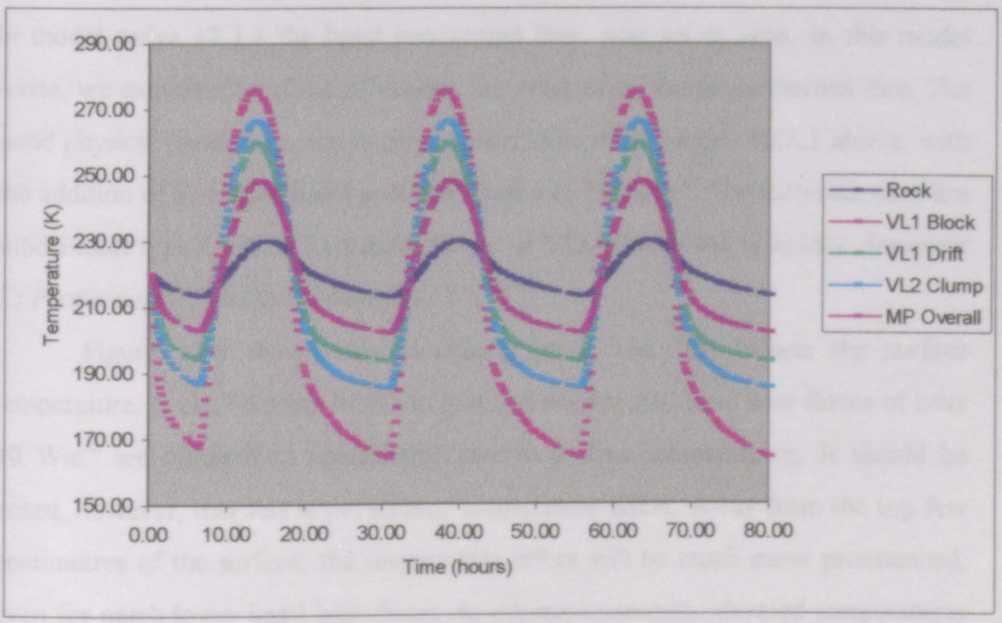


Figure 12.6 Martian surface temperature variations for different surface materials.

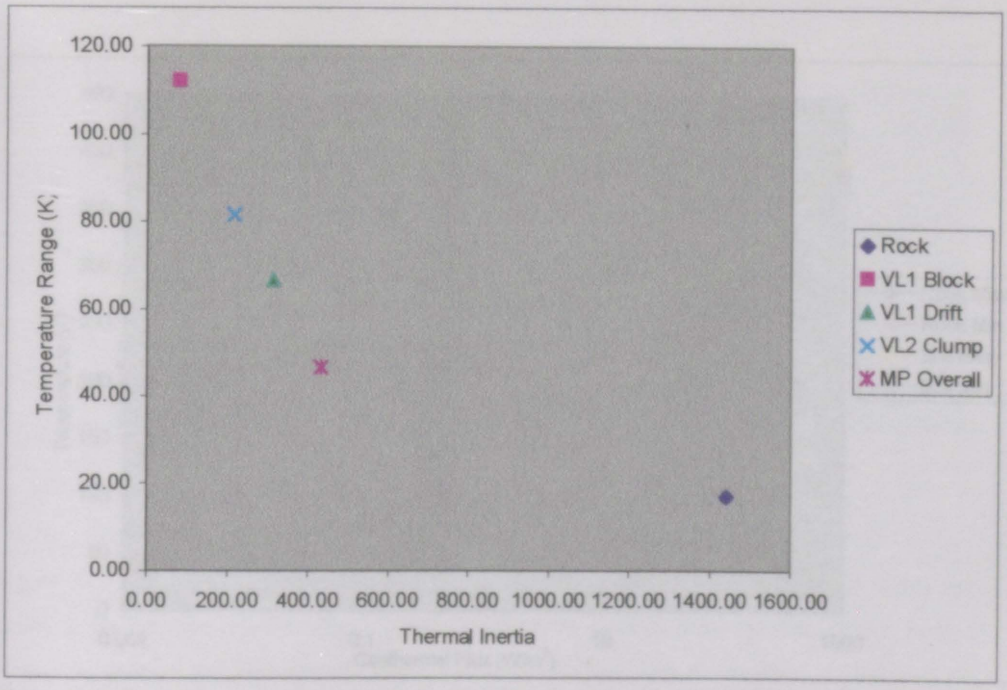


Figure 12.7 Temperature range versus thermal inertia for the materials in Figure 12.6. Note the classic inverse relationship, as would be expected.

SERIES 12.3.2 ENDOGENETIC HEAT SOURCES

In model series 12.3.1 the basal geothermal flux was set at zero. In this model series, we examine the effect of varying the value of the basal geothermal flux. The same physical parameters and mesh are used as in model series 12.3.1 above, with the addition of a variable basal heat flux from 0 to 100Wm^{-2}. The materials used are solid Basalt type 2 with a 5cm surface layer of VL1 Blocky soil type (*See Appendix C: Properties of Selected Materials*).

Figure 12.8 shows how increasing basal heat flux affects the surface temperature. It can be seem from the graphed results that basal heat fluxes of over 10 Wm^{-2} are required to significantly elevate surface temperatures. It should be noted, however, that this is the surface temperature effect. Away from the top few centimetres of the surface, the temperature effect will be much more pronounced, even for much lower basal heat fluxes. In dry environments, elevated temperatures at depth would have no significance for the detection of the heat source by remote sensing methods. However, in regions with cryolithosphere, increases in temperature at depth would cause ice melting, subsidence and outgassing of H_2O at the surface, without having any direct effect on the surface temperature.

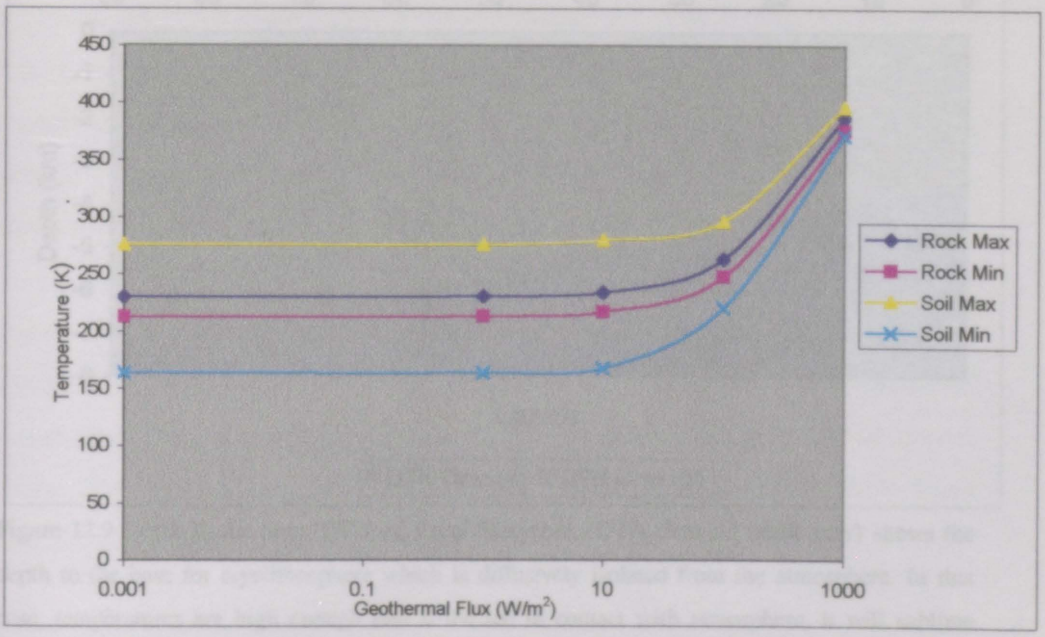


Figure 12.8 Surface temperature variation for increasing basal geothermal flux (Rock type is Basalt 2, Soil type VL1 Blocky Soil). 'Min' refers to coldest night-time temperature, 'Max' to hottest daytime temperature.

SERIES 12.3.3 GROUND ICE STABILITY AND GEOTHERMAL HEAT

The effects of ground ice are very evident across the Martian landscape, the resulting landforms have been considered at length in the published literature (Squyres et al, 1992). The depth at which ground ice will be stable can be easily calculated using Fouriers law of heat conduction using an average annual surface temperature as a fixed upper boundary condition.

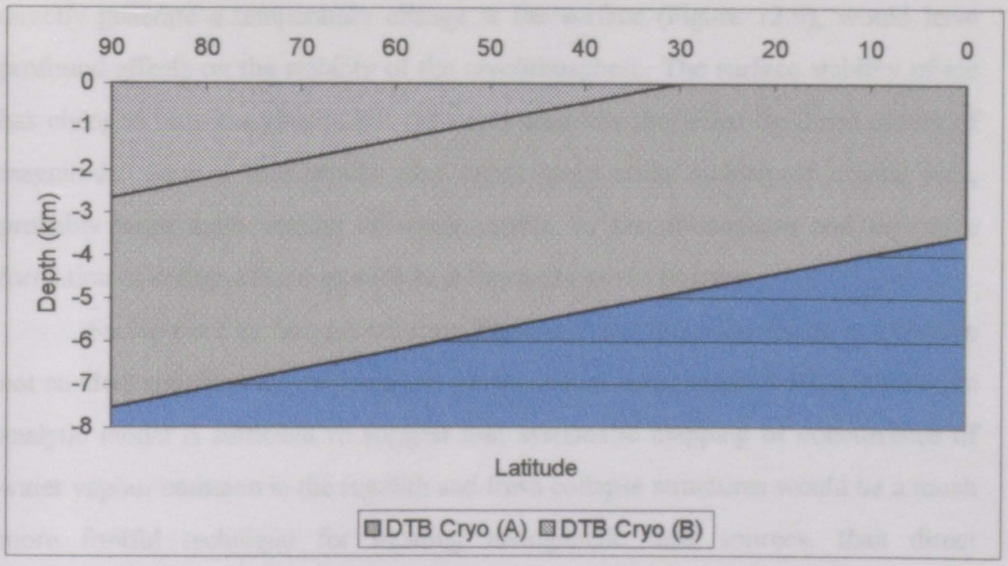


Figure 12.9 Depth to the base (DTB) of Cryolithosphere. 'DTB Cryo A' (dark grey) shows the depth to the base for cryolithosphere which is diffusively isolated from the atmosphere. In this case, temperatures are high enough that if the ice in contact with atmosphere, it will sublime away. In these cases, it is likely that the lithosphere will be dessicated of ice to considerable depth. Case 'DTB Cryo B' (pale grey) shows the regions where the ice is cold enough that it will not sublime, even if in contact with the atmosphere. The blue region shows where liquid water may occur, if diffusively isolated from the atmosphere. The model assumes a basal geothermal flux of $30mWm^{2}$ and thermal conductivity of $2Wm^{-1}K^{-1}$ (*After Squyres et al, 1992).*

Figure 12.9 shows the result of a calculation using Fouriers law of heat conduction. The figure indicates the regions where ice in the pore spaces of rock (cryolithosphere) will be stable. Below the base of the cryolithosphere, liquid water may occur. At the upper boundary, near surface layers are expected to be desiccated of water ice to varying depths. As one might expect, no near surface ground ice will occur at latitudes below 30°. Mapping of surface features affected by ice such as rampart craters, terrain softening, debris flows etc. corroborate this distribution (Squyres et al, 1992).

Localised increases in the geothermal gradient will elevate the base of the cryolithosphere, (see Figure 12.10) potentially to a point where it may approach the surface and cause extensive venting of water vapour into the atmosphere. Such venting events may have been observed at Solis Lacus (25°S, 85°W) and Noachis-Hellespontus (30°S, 310°W) (Huguenin and Clifford, 1982). Note how in Figure 12.11 even a 'small' increase in geothermal flux of $10Wm^{-2}$, which would not

directly generate a temperature change at the surface (Figure 12.9), would have profound effects on the stability of the cryolithosphere. The surface stability of ice has changed only marginally, but the depth axis has shortened by three orders of magnitude. Such a flux would thus cause large scale melting of crustal ices, probably large scale venting of water vapour to the atmosphere and extensive formation of collapse features such as alases and chaotic terrains.

Seeking out surface temperature changes in the thermal infrared is therefore not an ideal approach for mapping out geothermal areas in Mars. A relatively simple analytic model is sufficient to suggest that systematic mapping of concurrence of water vapour emission in the regolith and fresh collapse structures would be a much more fruitful technique for locating endogenetic heat sources, than direct examination of thermal infrared images.

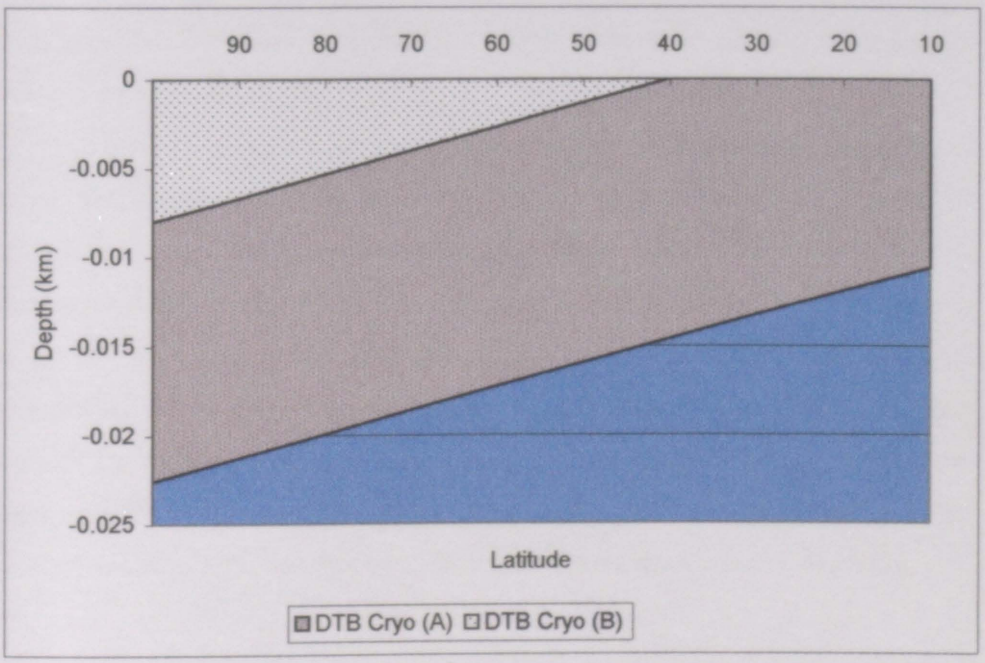


Figure 12.11 Shows the effect of a $10Wm^{-2}$ basal heat flux on the depths to base (DTB) of cryolithosphere. Note that at all latitudes the cryolithosphere will be melted to within a few metres of the surface.

SERIES 12.3.3 LAVA TUBE SKYLIGHT DETECTABILITY

The argument laid out in section 11.3.4 for the detectability of lunar lava tubes are also valid for the case of Martian lava tubes, as are the conclusions. In 11.3.3 we

noted that the contrast due to temperature differences between lava tube interior temperatures (circa 280K) and surface temperatures were not large enough to allow unambiguous discrimination of lava tubes from surrounding clutter. For the Martian environment, this conclusion also holds true. Lava tube interior temperatures, in the range 200-300K (depending on geometry and thermal conductivity), will not represent adequate contrast with surface temperatures which may be only approximately 50-60K cooler at night, depending on the latitude and surface rock composition. As with the moon, very high resolution multi-temporal thermal infrared imaging may yield better results, but mapping of linear features, crater chains and collapse structures in high resolution visible band images would also be of considerable benefit.

12.4 CONCLUSIONS

Thermal infrared images are likely to be of only limited utility in mapping of geothermal anomalies on Mars. Due to the nature of the environment, it is likely that any geothermal anomaly will have a very pronounced effect on the geomorphology and local atmospheric water content of the overlying surface long before it has any direct effect on the surface temperature. Any increase in local geothermal heat fluxes will have profound environmental effects through melting of ground ices, long before generating any surface temperature variation, as can be seen in series 12.2.3. Only in areas where ground ice is entirely absent might thermal infrared images be of use for detecting geothermal anomalies.

For the detection of evacuated lava tubes on Mars, thermal infrared images, as they stand today, are likely to be of limited usefulness. High resolution, co-registered day night thermal infrared image pairs would be required. In practice, as with geothermal sources, examination of high resolution visible band images is likely to be more beneficial.

Thermal images are, of course, still of utility for mapping surface material types. The investigations discussed in this chapter serve to illustrate the point that 'No dataset is an Island'. Consideration of a broad range of data types, ranging from atmospheric water vapour measurements to surface geomorphologic analyses is of far more benefit to the study of any given phenomenon than isolated examination of a single datatype. It is also worth noting that, for regions of Mars without ice, thermal infrared images would be useful in discriminating endogenetic thermal anomalies, were they of sufficient size relative to the imaging system resolution and of sufficient flux (c. $10Wm^{-2}$) to elevate the surface temperature.

Chapter 13: Conclusions

In *Chapter 1: Introduction*, we asked the questions: What can we learn about buried geologic heat sources from examining their effect on surface temperature? The answer to that is a little, but not as much as we might have hoped at the beginning.

The main question was subdivided into three principle scientific questions:

(i) Under what circumstances will a geothermal heat source produce a detectable temperature change at the surface?

In the case studies examined, there is no hard and fast rule. However, it can be said that in all cases the geothermal heat flux required was never less than 2% of the noontime solar insolation.

(ii) From the surface temperature distribution, can the properties of the geothermal heat source be constrained by modelling the expected thermal signature and comparing it with that observed in the thermal infrared image?

Yes, a geothermal source can be constrained, but only if the other variables in the physical system are extremely well known. The smaller the uncertainties, the better constrained the source properties can be.

(iii) Can the heat source be readily discriminated in a thermal infrared image from surrounding surface clutter?

Geothermal flux will produce an unambiguous, detectable change in surface temperatures if its magnitude is larger than any uncertainties in the other factors in the surface heat balance equation. It is possible for a heat source to produce a detectable temperature change (e.g. 1K), which could not be unambiguously discriminated from surrounding clutter.

When using thermal finite element modelling techniques, we also implicitly raised a technical question: Does finite element modelling represent an advance on

techniques which have previously been applied in this field, and is it useful to apply it in conjunction with thermal infrared imaging?

For two or three-dimensional modelling, or for temperature dependent processes, yes, finite element modelling is strongly advantageous. For simple one-dimensional models without temperature dependent factors there is no inherent advantage of finite element models over finite difference models. As the example of *Chapter 11, The Kilauea Lava Tube* illustrates, it is most certainly informative to consider the results of finite element models of geothermal heat sources in light of Thermal infrared images of such sources.

In the course of the thesis, we also examined the effect of various aspects of the physical system on the final surface temperature. In turn, the steady state physical properties, the effect of time varying fluxes, and the effect of material phase changes were considered, and their relative importance quantified.

Across twelve Chapters, several thousand numerical models and three worlds, these questions have been considered in this thesis and the answers summarised above are reviewed in this Chapter.

13.1 EFFECT OF GEOTHERMAL HEAT SOURCES ON SURFACE TEMPERATURE

The increase in geothermal heat fluxes required to produce a detectable temperature change at the surface is highly variable from environment to environment. There is no simple rule to estimate the minimum flux required for a given environment. The breadth of case studies considered in this thesis gives some basis for approximation, however. Similarly, what is 'detectable' is a non trivial question, dependent on everything from the physical environment to the sensing instrument design. In general, a temperature contrast of 1 degree is taken as being detectable for most sensing systems.

In terrestrial examples, (see *Chapter 6: Steady State Models*) an approximate value of $25Wm^{-2}$ is required to produce a 1°C temperature change at the surface. This figure is derived from the results shown in Figure 6.19, and requires a temperature of 100°C at 10m depth to sustain. This is corroborated *by Chapter 9: The Warms Springs of Southern Ireland* and *Chapter 10: The Kilauea Lava Tube*. The geothermal heat flux from the Mallow Warm Spring system is estimated at about $4Wm^{-2}$. As one might expect, the springs do not produce a detectable temperature change at the surface. In contrast, The Kilauea Lava Tubes generate peak fluxes of over $1kWm^{-2}$, and most certainly do produce a temperature change at the surface.

On the Moon (*Chapter 11 Lunar Thermal Models*), an unambiguous temperature increase requires about $3Wm^{-2}$ in regolith (see Figure 11.11). Given the very low thermal conductivities of lunar regolith, the temperatures required to sustain this flux across any thickness of regolith are improbably high, requiring geothermal gradients in the order of $1000Km^{-1}$.

On Mars geothermal fluxes of about $10Wm^{-2}$ would be required to begin to elevate surface temperature above normal values (see Figure 12.9). Considerable environmental uncertainties exist for the Martian surface, given that only 3 'points' of ground truth exist.

The case studies were selected to give a diverse set of examples, with wide variety of physical properties and processes. Obviously, the exact values for the

'thresholds' given above will vary considerably from environment to environment, and ideally should be derived from models for each specific site of interest.

In all cases, however, the geothermal flux required to produce a detectable temperature change at the surface can be qualitatively described as 'large'. In general, it is never less than 2% of the maximum solar insolation. The value must also be larger than any uncertainties in the surface thermal balance that could be due to other factors.

13.2 DERIVING INFORMATION ABOUT GEOTHERMAL HEAT SOURCES FROM THEIR SURFACE THERMAL ANOMALY

Deriving qualitative information about the shape and size of a buried geothermal anomaly from a thermal infrared image is not difficult, if the heat source is sufficient to generate an unambiguous surface thermal anomaly. Simple inspection of the thermal infrared images from the Kilauea lava flow (for example Figure 10.3) can provide good general information about the shape and spatial extent of a geothermal heat source.

Extraction of quantitative information about a geothermal heat source from thermal infrared images is much more problematic. Even given a moderately well constrained system, as was examined in *Chapter 10: The Kilauea Lava Flow*, it is difficult to extract precise quantitative data. For the tubes in the Kilauea lava flow, it was possible to constrain the physical properties of the lava tube to a number of possible solutions, but it was not possible to give an exact solution. The numerical analysis was, however, very useful in providing support to a qualitative analysis of the lava tube section under consideration. In the case of the Pu'U'Oo lava tube, it was possible to extract qualitative information about the depth of the lava tube and its size, and learn about the extent of variations in the material properties of the basalt.

The principle difficulty in extracting quantitative information is the uncertainty in the physical parameters of the system. Unless the system is very well constrained, a variety of possible geologic configurations may produce a surface thermal anomaly consistent with that observed in the thermal infrared image. In essence, this technique shares the fundamental problem of all investigations that seek to 'invert' measured data to extract information about underlying processes: A question has only one answer, but an answer may have many questions.

Finite element modelling of geothermal heat sources is however, still useful. Modelling of the expected surface thermal anomalies from a given source gives a greater understanding of the relative importance of the different physical parameters. An understanding of the relative importance of the different physical

parameters is useful in identifying what situations the modelling techniques are appropriate to, and what level of data is required.

It is also possible to use the results from finite element models to constrain the physical system to one of a number of solutions. Insight gained from numerical modelling of the system can help to refine and guide qualitative descriptions of the geothermal system.

13.3 DISCRIMINATION AND IDENTIFICATION OF GEOTHERMAL HEAT SOURCES

Consider an ideal thermal image that provides perfect surface kinetic temperature measurements at as high a resolution as one may choose. Using such a data source it may still not be possible to detect a geothermal heat source which would, in theory, provide a detectable temperature change at the surface. While an image may allow one to detect a variation, it is another matter to be able to identify with certainty what is causing the variation. A temperature variation may be due to any number of factors other than a purely endogenetic process.

Figures 11.12 and 11.13 in *Chapter 11: Lunar Thermal Modelling*, give an example of what kind of confusion is possible. The two virtual thermal images show the surface kinetic temperatures from an area of rock outcrop and an area of elevated heat flow just before dawn. The resultant virtual thermal images are absolutely identical. The two sources are impossible to distinguish by the thermal images alone. Figures 11.14 and 11.15, however, show the same virtual scene at local noon. Here the two images can be clearly discriminated. Similarly, a high-resolution visible band or radar image would allow the observer to identify areas of high rock outcrop and eliminate them as potential endogenetic heat sources. Looking at a single thermal infrared image is thus not sufficient to identify endothermic thermal anomalies. One must consider a wider context of multi-temporal images, and visible band images, and consider the effect of a thermal anomaly on the environment. Perhaps a thermal anomaly in cryolithosphere will dry the overburden, decrease the thermal inertia and make the surface look colder at night? Perhaps vapour emissions from geothermal heated soils will create cool, near surface fogs? Seeking thermal anomalies in a thermal infrared image alone is not sufficient.

Chapter 10: The Kilauea Lava Tubes, gives an example of a best case scenario for the discrimination of a buried heat source. The surface material is apparently homogeneous. Minor variations exist between basalt flows of different ages, but there is certainly no variation large enough to be confused with an

endogenetic thermal anomaly. The multispectral character of the source data also allows the user to map and identify these small-scale variations in a way that a simple kinetic temperature map does not allow (see Figure 10.1). Availability of a topographic map allows the observer to identify aspect related variations in the image by inspection. The relative simplicity of the surface, combined with a small amount of supporting data, allows endogenetic thermal anomalies to be clearly discriminated.

In sharp contrast, the thermal infrared image of Mallow Town (Figure 9.3) shows no such clarity. A profusion of different terrain types and surface boundary conditions creates a complex image. As it stands, one could easily place the lava tube system at Kilauea anywhere in the Mallow area and it would be unnoticed in the Landsat TM thermal band image. At best, it might be mistaken for a roadway. Once again, supplementary data would be required to identify it. By using the non-thermal bands of the sensor system to classify the surface cover types, one could generate an average, expected kinetic temperature for each cover type, and subtract this from the observed kinetic temperature. Any variations in the resultant image could be endogenetic in origin. A much higher resolution image would be required for this kind of analyses, to reduce the area of mixed pixels.

Thus, to clearly discriminate an endogenetic anomaly from surface clutter, supplementary information about the character of the surface cover is required. Depending on the environment, visible band images, multi-spectral images, radar images and topographic data may all be appropriate. If the study area is large enough that meteorological variation may occur across it, these factors must also be known and quantified. Ideally, a study image should contain an area with the same surface characteristics as the suspected endogenetic anomaly, but with normal endogenetic flux levels, to facilitate comparison. The image data must also be of reasonable resolution for the size of the thermal anomaly being sought. Thermal anomalies should be of a size comparable to or greater than the sensor pixel size, unless the surface is highly uniform and the sources are hot enough to facilitate mixed pixel detection.

13.4 THE UTILITY OF THE FINITE ELEMENT METHOD

The finite element method presented a number of advantages and disadvantages over previous published investigations using finite difference or analytical models.

The finite element method affords a number of considerable advantages over the finite difference method. Finite element meshes may be refined to give increased accuracy in areas of specific interest, and coarsened in less vital areas to reduce computational time. The finite element method solves the relevant equations of the elements for a continuum across each element, rather than just at the nodal points, as with the finite difference method. Finite element models are also applicable to certain niche areas, such as phase changes and radiative boundaries, where finite differences may not be as readily adaptable. In addition, relatively complex geometries can be analysed, if required.

Analytic solutions, while computationally inexpensive, are usually highly inflexible. It may be difficult to develop an analytic equation which takes into account reasonable complexities of a physical system. Therefore, analytic solutions require oversimplifications, and the results may be misleading rather than helpful. Finite element methods allow greater flexibility and as a consequence a more realistic physical system can be investigated.

In practice, however, the considerable advantages that the finite element method conveys can be swamped by limitations and uncertainties in the boundary conditions and physical parameters. At no point in this thesis was a difficulty encountered because the model results were not accurate enough. Uncertainty ranges in the finite element technique were usually an order of magnitude below the uncertainties in the thermal infrared images, and sometimes many orders of magnitude less than uncertainties in the physical properties of the system. The principle limitations encountered in performing the analyses were due to the variables in the physical system being insufficiently constrained.

Several software packages are available 'off the shelf', to facilitate finite element analyses. The software used in this thesis, Ansys, affords major advantages over other finite element modelling software in terms of ease of use. The Ansys software allows relatively rapid generation of new numerical models with only a relatively small amount of custom programming. Element sizes may be easily

changed and material properties may be readily modified and made temperature dependent.

13.5 THE EFFECT OF THE PHYSICAL SYSTEM ON THE MODELLED RESULTS

It was found that, in steady state models, the source depth, temperature and size have a dominant effect on the surface temperature. Figures 6.44, 6.45 show the marked effect of source depth variation. Figures 6.46 and 6.47 show the strong linear effect of source temperature variations. Figure 6.50 shows the relatively marginal effect of heat source geometry, showing how the size, rather than the shape, is the dominant geometric effect.

In addition to these factors, varying the surface properties has a significant effect. Certain factors, such as emissivity and bulk atmospheric temperature, tended to affect the peak temperature and background temperature equally and thus produced no net affect on the thermal anomaly. Other parameters principally the convection film coefficient, had a very marked effect on the thermal anomaly (see Figures 6.40 and 6.41). Variations in the physical properties of the rock were proportionally less important, but could still have significant effects. Figures 6.42 and 6.43 show a correlation between rock thermal conductivity and the expressed thermal anomaly.

Time dependent variation in the geothermal heat source takes a relatively long time to propagate to the surface. In the case of refilling of lava tubes, it was found that it took, at best, 24 hours for an injection of fresh, hot lava into a lava tube to produce a detectable temperature change at the surface. This is too long to be of predictive utility in most cases. Detection of such temperature changes could be useful in some cases, for example, lava tumuli formation, in conjunction with observations of deformation and gas emission.

Diurnal variations in the surface thermal boundary conditions could be easily modelled using the finite element method. Analyses carried out for terrestrial, Lunar and Martian situations found results of finite element models to be in good agreement both with published measured values, and with published results generated using finite difference and analytic techniques.

Phase change analyses carried out in *Chapter 9: Phase Change Models* for 2 examples, found that the effect of temperature dependent phase changing

materials was relatively marginal, compared to the effect of 'static' factors considered in *Chapter 6: Steady State Models*.

Studies of a heat source in cryolithosphere (Series 8.1.1) showed a marginal influence on the peak temperature, at best 1-2 degree reduction. The effect on thermal anomaly size was more marked, creating a reduction of 30-40%.

The second example of phase change effects on a reactivated lava tube (Series 8.1.2) had relatively subtle effects. The phase change enabled model showed a slightly delayed heating curve (due to energy loss in melting tube walls) and a slightly longer cooling curve (due to release of latent heat of crystallisation). Obviously, these results are valid only for the circumstances and boundary conditions considered, however, they can be taken to indicate a more general trend.

13.6 FURTHER WORK

As with all scientific investigations, this thesis is a work without end, and has in its course suggested far more avenues of investigation than one could ever hope to pursue. In addition recent technical advances and new datasets such as the ASTER dataset (Figure 13.3) or Galileo images (Figure 13.1,13.2) have opened up potential new areas of investigation, which would not have been available when the thesis was begun. Some of these are briefly outlined here.

FIELD INVESTIGATION OF ACTIVE LAVA TUBES

The work carried out in *Chapter 10:The Kilauea Lava Flow* could have lead to a much more precise characterisation of the lava tube system if there was sufficient supporting data to adequately constrain the model. It would be a most interesting exercise to investigate the thermal anomaly due to an active lava tube in the Kilauea system with adequate ground truth. Such a field investigation would involve the following:

- Systematic sampling of the basalt in a grid, and laboratory measurement of its thermal properties
- Coring to sample the basalt at shallow depth, to map the thermal properties in three dimensions, and determine the degree of anisotropy in the physical parameters
- Geophysical investigations to map the cross sectional area of active lava in the lava tube. Shallow seismic investigations to map out layers and porosity variations in the basalt could also be conducted.
- Measurement of the sensible heat transfer coefficient in the study area using Eddy Correlation equipment (3-d sonic anemometers and fine wire thermocouples).
- Monitoring of relative humidity, rainfall, and other meteorological factors.
- Systematic high-resolution emissivity mapping of the surface (using a handheld spectrometer).
- Mapping of the surface roughness, to determine the aerodynamic coefficient of the surface, to facilitate sensible heat flux calculations

- Placement of soil heat flux plates to quantify background geothermal fluxes.
- Placement of thermocouples at depth within the (solidified) lava flow, to map out the internal heat distribution
- Measurement of the temperature and value of outgassed material from over the lava tube, to determine if heat transfer by outgassing is important in the system
- Systematic measurement of solar insolation during the study period.
- Contemporaneous thermal infrared imaging at high resolution, supplemented by surface temperature measurements and radiometer transits across the study area.

Such a systemic instrumentation and quantification of the thermophysical properties of the physical system would allow comparison of numerical models of heat flow from the lava tube and the real, measured values, with a much higher degree of confidence than is presently available. This would the facilitate application of the technique to areas with poorer ground control data.

THERMAL MODELLING OF LAVA FLOW COOLING

The cooling and crystallisation of lava flows is a very complex process with considerable non-linearities and sharp thermal gradients. Complex processes like fluid flow, crystallisation and settling are beyond the capabilities of Ansys to model numerically. It would be an interesting exercise to custom write a finite element modelling application to address such situations.

THERMAL MODELLING OF GEOTHERMAL WATERS

In *Chapter 9: The Warm Springs of Southern Ireland*, it was noted that the thermal effects of geothermal groundwater are principally due to heat transfer by convection and fluid movements in fractures and pore space, rather than by conduction. It would be an interesting exercise to investigation the movement and effect of thermal groundwater, using commercial groundwater modelling software, to assess if existing conceptual models of the underlying hydrothermal systems are consistent with observed data.

MARTIAN GEOTHERMAL ANOMALY MAPPING

As noted in *Chapter 12: Mars*, geothermal heat sources on Mars are likely not to have a strong thermal infrared signature, due to the effect of the cryolithosphere. However, it would be an interesting exercise to examine some of the areas noted in the literature as potential geothermal sources. A detailed study of these regions in high-resolution visible band images could be carried out to look for evidence of recent collapse structures, alases (linear collapse features) and phreatic craters.

THE OUTER LIMITS: THERMAL ANOMALIES OF THE GALILEAN SATILLITES

A small but interesting thermal infrared dataset from the Galileo Spacecraft's Photopolarimeter-radiometer (PPL) shows some very interesting results from the moons of Jupiter. While the resolution of the images from the instrument is generally quite low (kilometer scale) it raises interesting questions about the unusual thermal geology of these exotic worlds.

Images from the Galileo probe in the 1990 confirmed Io as being the most volcanically active body known. Recently returned images of Io show shield volcanoes and tube fed lava flows. Given that there now exists a small dataset of moderate resolution thermal infrared images of the surface of Io, it would be an interesting exercise to calculate the expected surface thermal signature from endogenetic thermal anomalies on Io, for comparison with other planetary bodies.

Published work examining thermal images of Europa from the Galileo probe (Spencer et al 1999) suggests considerable complexity in the thermal geology of Europa. Considerable unexplained temperature variations were noted, which could be due to either endogenetic sources, or complex thermal inertia variations in the surface ices. Spencer et al did not observe any specific hot spots on Europas' night side within the resolution of the image. Despite the relatively small dataset and its low resolution (variable, but kilometer scale), there may be considerable application for thermal finite element models. Phase change models may also be useful to model cryovolcanic processes. Finite element thermal models could be used to investigate questions such as how long would a heat influx from a sub-ice volcanic eruption take to show an effect on the ice surface? Would it show an effect at all? What volume of melting could one expect from differing levels of volcanic activity on the

hypothetical Europan seafloor. The complex systems of fracturing and rifting observed in the ice surface (see Figure 13.2) would be most interesting to examine using phase change enabled finite element Models.

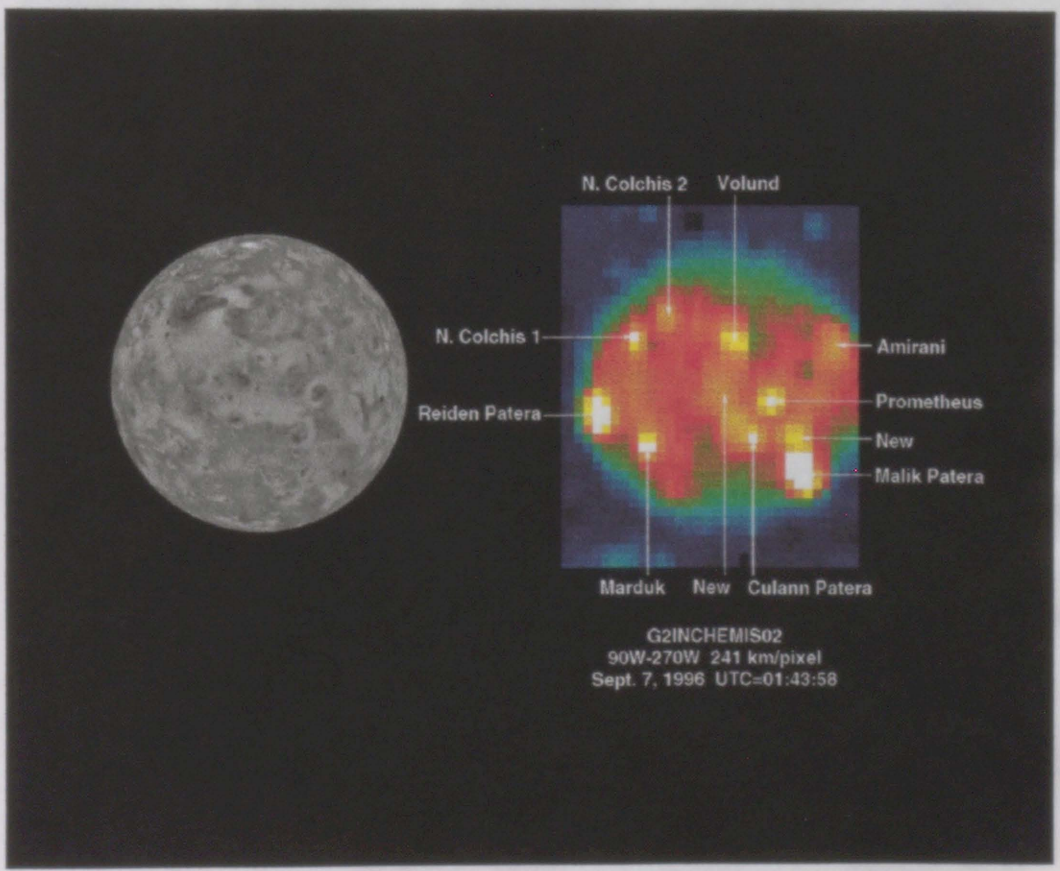


Figure 13.1 Image PIA00845. A hemispherical view of Io, showing visible and thermal infrared views. Image: NASA Jet Propulsion Laboratory.



Figure 13.2 Image PIA01127. Fractured ice surfaces on Europa. Image: NASA Jet Propulsion Laboratory.

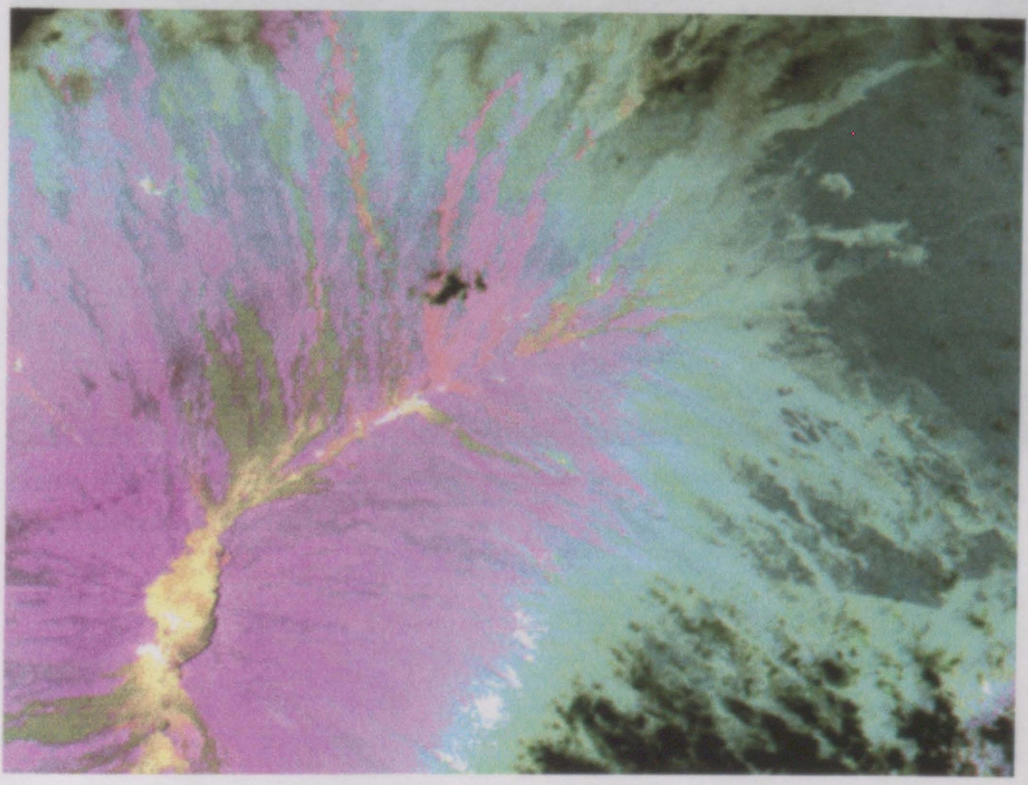


Figure 11.3 One of the First ASTER images, of Mauna Loa, Hawaii, April 18th 2000. Image is false colour thermal infrared showing different lava flow compositions. Image NASA Jet Propulsion Laboratory.

In final conclusion, examination of near surface thermal processes using a combination of finite element analyses and thermal infrared imaging is a useful technique, and has potential to be of greater use in the future. The technique should

not used in isolation, any analyses will benefit from availability of supplementary data. Continuing advances in the spatial, spectral and temporal resolution of thermal infrared datasets will make the technique more useful and widely applicable in the future than it is today.



Figure 13.4 Photo of Ape Cave, Washington. Empty lava tube with skylight. Photograph reproduced courtesy Gus Frederick, Oregon.

Appendix A: Symbols Used in the Text

A.1 ROMAN CAPITALS

Symbol	Meaning	Value/Units
A	Area	m^2
A_z	Cycle temperature amplitude at depth z	K
Bi	Biot number	
BR	Bowen ratio	
C	Capacitance matrix	
C_D	Drag coefficient	
C_p	Constant pressure specific heat	$Jkg^{-1}C^{-1}$
C_v	Constant temperature specific heat	$Jkg^{-1}C^{-1}$
E	Energy	J
E_{abs}	Radiative energy absorbed by the material	Wm^{-2}
E_{rad}	Radiative energy emitted by the material	Wm^{-2}
E_{geot}	Geothermal heat flux	Wm^{-2}
F	Radiation shape factor (defaults to 1)	
Fo	Fourier number	
G	Soil heat flux	Wm^{-2}
Gr	Grashof number	
H	Sensible heat flux	Wm^{-2}
H	Heat flux (unspecified)	Wm^{-2}
H_e	Enthalpy	Jm^{-3}
H_m	Heat loss per m of lava tube	Wm^{-1}

I	Thermal inertia	$Jm^{-2}s^{-1/2}K^{-1}$
J	Maximum heat flux at the surface	Wm^{-2}
K	Permeability	
K_{film}	Film Coefficient	$Wm^{-2}K^{-1}$
K_H	Eddy Diffusivity for heat	$m^{-2}s^{-1}$
K_v	Eddy Diffusivity for water vapour	$m^{-2}s^{-1}$
K_f	Effective Conductivity of a porous medium with immobile fluid in the pore spaces.	Wm^{-2}
K_{rad}	Linearised Radiation Coefficient	$Wm^{-2}K^{-1}$
$[K]$	Stiffness matrix	
LE	Latent heat flux	Wm^{-2}
L_I	Instrument scan rate	Lines/second
L_v	Latent heat of vaporisation of water	$2260kJkg^{-1}$
M_g	Mean atomic mass of a gas	
M_I	Spectral radiant exitance per m^2 of the Sun integrated across the spectral range.	Wm^{-2}
M_λ	Spectral radiant exitance of an object	$Wm^{-2}\mu m^{-1}$
N_u	Nussult number	
N_1, N_2	Shape functions for element	
P_a	Distance of pixel from the flight line centre	m
Pr	Prandtl number	
Q	Net heat transfer	Wm^{-2}
Ra	Rayleigh number	
Ra_c	Critical Rayleigh number	
R_m	Molar gas constant	8.31 $Jmol^{-1}K^{-1}$

R_d	Gas constant	287.04 $Jkg^{-1}K^{-1}$
Ri	Richardson number	
R_{dir}	Direct radiance absorbed.	Wm^{-2}
R_{dir}'	Direct radiance absorbed corrected for aspect	Wm^{-2}
R_{sky}	Background sky radiance absorbed	Wm^{-2}
R_{net}	Net radiation flux	Wm^{-2}
R	Radius of the Sun	$6.98x10^8$m
R_{ct}	Along-track resolution	m
R_{at}	Across-track resolution	m
S	Solar constant	1367 ±7 Wm^{-2}
S	Radiation shape factor	
S_{air}	Airspeed	ms^{-1}
S_e	Station elevation	m
T_1	Initial temperature	°C or K
T_a	Air temperature	°C or K
T_{anom}	Anomaly temperature	°C or K
T_b	Bulk temperature of the fluid (atmosphere)	°C or K
T_d	Elevated temperature of surface due to endogenetic heat	K
T_{surf}	Surface temperature	°C or K
T_{sky}	Sky temperature	°C or K
T(z,t)	Temperature at depth z, time t.	°C or K
T_n	Space node temperature	K
T_{sr}	Temperature of 'Space Node' for radiation	K

T_{∞}	Temperature of 'Space Node' for convection	°C or K
<U>	Average wind speed	ms^{-1}
V	Volume	m^3
W	Instantaneous vertical windspeed	ms^{-1}
Z	Height of measurement instruments over reference surface	m
Z_0	Surface roughness	

A.2 ROMAN SMALL

Symbol	Meaning	Value/Units
(a)	The set of the values of the free variable at each nodal point	
c	Speed of light in vacuum	$2.997x10^8$ ms^{-1}
c_a	Specific heat of air at constant pressure:	1010 $Jkg^{-1}K^{-1}$
c_p	Specific heat capacity of a material at constant pressure	Jkg^{-1} K^{-1}
d	Distance of the Earth from the Sun	$1.5x10^{11}m$
e	Flow thickness	m
g	Acceleration due to gravity (Earth Surface)	$9.81ms^{-1}$
h	Planck's constant	$6.626x10^{-34}$ Js
h_f	Film Coefficient	$Wm^{-2}K^{-1}$
h	Instrument height above the surface	m
k_a	Thermal conductivity of air	$Wm^{-2}K^{-1}$
k_b	Boltzmann constant	$1.38054x10^{-34}$ JK^{-1}
k	Thermal conductivity	$Wm^{-2}K^{-1}$
k_v	Von Karmans constant	0.4
k_p	Permeability of porous medium	m^2

n	Number of columns to the flight line centre column	
q_s	Specific humidity	$kg\ kg^{-1}$
q	Humidity of air	kgm^{-3}
t	Time	s
u	Horizontal windspeed	ms^{-1}
u^*	Effective water vapour content of the atmosphere: (total precipitable water in a cloudless atmosphere)	gcm^{-2}
z	Zenith angle of the sun as a function of time of the day and date of year.	Rad
z	Depth	m

A.3 GREEK

Symbol	Meaning	Value/Units
α	Albedo	$0<\alpha 1$
α_0	Atmospheric albedo	$0<\alpha 1$
α_g	Ground albedo	$0<\alpha 1$
β	Angle between the surface and the sun on the plane containing the sun	Rad
β	Coefficient of volume expansion	K^{-1}
β_a	Coefficient of thermal expansion of Air	$m^3kg^{-1}C^{-1}$
β	Coefficient of thermal expansion of the pore fluid	$m^3kg^{-1}C^{-1}$
ε	Emmissivity of surface	$0<\varepsilon<1$
ε_s	Shortwave emmissivity	$0<\varepsilon<1$
η_f	Viscosity of the pore fluid	$kgs^{-1}m^{-1}$
η_a	Viscosity of air	$kgs^{-1}m^{-1}$
τ	Atmospheric transmissivity.	$0<\tau<1$
ϕ	Radiation shape factor	ε

κ_d	Thermal diffusivity of the rock	m^2s^{-1}
κ_a	Thermal diffusivity of air	m^2s^{-1}
δ	Characteristic length.	m
$\delta T/\delta z$	Temperature gradient	Km^{-1}
$\delta q/\delta z$	Humidity gradient	
ν	Kinematic viscosity of the fluid	m^2s^{-1}
μ	Dynamic viscosity of the fluid	$kgm^{-1}s^{-1}$
χ	Specific heat ratio C_p/C_v	
δ	Solar declination	rad
φ	Local latitude	rad
ω	Phase angle	rad s^{-1}
ω	Phase angle of Earths' rotation	$7.292x10^{5}$ $rads^{-1}$
ψ	Instrument response	
σ	Stefan-Boltzmann Constant	$5.669x10^{-8}$ $Wm^{-2}K^{-4}$
ΔT	Temperature difference	°C or K
λ	Wavelength	m
ρ_a	Density of air.	$1.292kgm^3$
ρ_f	Density of the pore fluid	kgm^{-3}
$\Gamma_{1,2}$	System boundary regions	
Π	Energy integral, the Lagrangian Function	
ρ_s	Surface pressure	mbar
τ	Atmospheric transmissivity $(\exp(-\tau'))$	

θ	Angle between the normal to the surface and the solar zenith angle	rad
Ω	System domain	

Appendix B: Abbreviations and Acronyms

ABL	Atmospheric Boundary Layer
AOI	Area of Interest
ASTER	Advanced Spaceborne Thermal Emission and Reflection instrument
ATI	Apparent Thermal Inertia
AVIRIS	Airborne Visible/Infrared Spectrometer
AVHRR	Advanced Very High Resolution Radiometer
CFD	Computational Fluid Dynamics
DN	Digital Number
FEA	Finite Element Analysis
GOES	Geostationary Orbiting Environmental Satellite
HCMM	Heat Capacity Mapping Mission
HVNP	Hawaii Volcanoes National Park
IDL	Interactive Data Language
IRTM	Infra-Red Thermal Mapper
IFOV	Instantaneous Field Of View
MGS	Mars Global Surveyor
MOC	Mars Orbital Camera
MODIS	Moderate Resolution Imaging Spectral Radiometer
MSS	Multispectral Scanner
NASA	National Aeronautics and Space Administration
NCDC	National Climate Data Centre
NIR	Near Infra Red

NOAA	National Oceanography and Atmosphere Administration
RGB	Red-Green-Blue
SST	Sea Surface Temperatures
SBL	Surface Boundary Layer
SHC	Specific Heat Capacity
TLA	Three Letter Abbreviation
TES	Thermal Emission Spectrometer
TIMS	Thermal Infrared Mapping Spectrometer
TIR	Thermal Infra Red
TFEM	Thermal Finite Element Modelling
TIRS	Thermal Infrared Remote Sensing
TM	Thematic Mapper
UV	Ultraviolet
VTC	Virtual Thermal Conductivity

Appendix C: Properties of Selected Materials

C.1 THERMAL PROPERTIES OF ROCKS

Material	Thermal Conductivity K: $Wm^{-1}K^{-1}$	Specific Heat Capacity C: $Jkg^{-1}K^{-1}$	Density ρ: kgm^{-3}	Thermal Inertia I: $Jm^{-2}s^{-1/2}K^{-1}$	Thermal Diffusivity K_d $10^{-6}m^2s^{-1}$	Source
Sandy Soil						
Dry	0.3	800	1600	620	0.23	Garrett (1992)
η=0.2	1.9	1260	1800	2076	0.84	Garrett (1992)
η=0.4	2.2	1480	2000	2552	0.74	Garrett (1992)
Clay Soil						
Dry	0.25	890	1600	597	0.18	Garrett (1992)
η=0.2	1.1	1170	1800	1552	0.52	Garrett (1992)
η=0.4	1.6	1550	2000	2227	0.52	Garrett (1992)
Ices						
Water Ice I	2.5	2100	910	1828	1.3	Garrett (1992)
Water Ice (0°C,Pure)	2.24	2100	920		1.16	Oke (1978)
Snow						Garrett (1992)
Old	1	2090	640	1157	0.7	Garrett (1992)
Old	0.42	2090	480		0.3	Oke (1978)
New	0.1	2090	150	177	0.3	Garrett (1992)
New	0.08	2090	100		0.1	Oke (1978)
Water	0.6	4186	1000	1584.8	0.14	Garrett (1992)
Air*	2810	1007	1.292	1684	2.16	Garrett (1992)
Rocks						
Granite (max)	3.98	820	2640	2935	1.8	Holman (1990)
Granite (min)	1.73	820	2640	1935	0.8	Holman (1990)
Marble (max)	2.94	800	2700	2520	1.035	Holman (1990)
Marble (min)	2.07	800	2500	2035	0.59	Holman (1990)
Limestone (max)	1.33	900	2500	1730	0.56	Holman (1990)
Limestone (min)	1.26	900	2500	1684	0.56	Holman (1990)
Sandstone (max)	1.83	710	2300	1728.7	1.12	Holman (1990)
Sandstone (min)	1.83	710	2160	1675	1.19	Holman (1990)
Krafla Geothermal Reservoir	1.356	952	2650	1850	0.57	Tiab and Sigurdsson (1994)

* Dry air at 293K, 1013.25hPa. Values strongly variable see Garret (1992) Appendix 2.

C.2 STANDARD MATERIALS

For the purposes of facilitating modeling a series of "Standard Basalts" have been generated using the general relationships for physical properties of geologic material outlined in *Chapter 3: The Physical Model.*

C.2.1 BASALTS

C.2.1.1 Basalt1, Porous Permeable Basalt

Density 1080 kgm^{-3}
Vesicularity 60%
Permeability $10^{-7}m^{-2}$
Pore Fluid Air

Temperature (K)	273	400	600	800	1000	1200	1400
Thermal Conductivity (horizontal) ($Wm^{-1}K^{-1}$)	0.660	0.581	0.483	0.422	0.383	0.357	0.339
Thermal Conductivity (vertical) ($Wm^{-1}K^{-1}$)	4.226	4.026	3.758	3.57	3.45	3.373	3.31
Specific Heat Capacity ($Jkg^{-1}K^{-1}$)	321	373	410	428	439	447	452

C.2.1.2 Basalt2, Solid Impermeable Basalt

Density 2700 kgm^{-3}
Vesicularity 0
Permeability 0 m^{-2}
Pore Fluid Air

Temperature (K)	273	400	600	800	1000	1200	1400
Thermal Conductivity (horizontal) ($Wm^{-1}K^{-1}$)	2.08	1.812	1.47	1.25	1.11	1	0.934
Thermal Conductivity (vertical) ($Wm^{-1}K^{-1}$)	2.08	1.812	1.47	1.25	1.11	1	0.934
Specific Heat Capacity ($Jkg^{-1}K^{-1}$)	800	931	1024	1071	1099	1117	1131

Low Range

Temperature (K)	100	150	200	250	300	350
Thermal Conductivity (horizontal) ($Wm^{-1}K^{-1}$)*	2	2	2	2	2	2
Thermal Conductivity (vertical) ($Wm^{-1}K^{-1}$)*	2	2	2	2	2	2
Specific Heat Capacity ($Jkg^{-1}K^{-1}$)	91	460	650	760	830	891

*Temperature dependence of basalt thermal conductivity at low ranges is not known.

C.2.1.3 Basalt3, Solid Permeable Basalt

Density 2700 kgm^{-3}
Vesicularity 0
Permeability $10^{-7}m^{-2}$
Pore Fluid Air

Temperature (K)	273	400	600	800	1000	1200	1400
Thermal Conductivity (horizontal) ($Wm^{-1}K^{-1}$)	2.08	1.812	1.47	1.25	1.11	1	0.934
Thermal Conductivity (vertical) ($Wm^{-1}K^{-1}$)	6.74	5.88	4.81	4.14	3.7	3.39	3.16
Specific Heat Capacity ($Jkg^{-1}K^{-1}$)	800	931	1024	1071	1099	1117	1131

C.2.1.4 Basalt4, Porous Impermeable Basalt

Density 1080 kgm^{-3}
Vesicularity 60%
Permeability 10
Pore Fluid Air

Temperature (K)	273	400	600	800	1000	1200	1400
Thermal Conductivity (horizontal) ($Wm^{-1}K^{-1}$)	0.660	0.581	0.483	0.422	0.383	0.357	0.339
Thermal Conductivity (vertical) ($Wm^{-1}K^{-1}$)	0.660	0.581	0.483	0.422	0.383	0.357	0.339
Specific Heat Capacity ($Jkg^{-1}K^{-1}$)	321	373	410	428	439	447	452

C.2.2 LUNAR REGOLITHS

C.2.2.1 Regolith Type 1 Near Surface Fines.

Density= 1200kgm^{-3}

Temperature (K)	100	150	200	250	300
Thermal Conductivity (x10^{-3}Wm^{-1}K^{-1})	0.7	0.8	1	1.2	1.5
Specific Heat Capacity (Jkg^{-1}K^{-1})	360	460	560	670	770

C.2.2.2 Regolith Type 2 Subsurface Regolith

Density= 1800kgm^{-3}

Temperature (K)	100	150	200	250	300
Thermal Conductivity (x10^{-3}Wm^{-1}K^{-1})	8	8	8	8	8
Specific Heat Capacity (Jkg^{-1}K^{-1})	540	690	840	1005	1290

C.2.3 SANDSTONE-ICE MIXTURES

Temperature (K)	173	272	274	283	303
100% Sandstone					
Thermal Conductivity (Wm^{-1}K^{-1})	3	3	3	3	3
Enthalpy (Jm^{-3})	2.70e+8	4.24e+8	4.28e+8	4.42e+8	4.73e+8
80% Sandstone+20%Ice					
Thermal Conductivity (Wm^{-1}K^{-1})	2.8	2.8	2.4	2.4	2.4
Enthalpy (Jm^{-3})	2.55e+8	4.15e+8	4.86e+8	5.4e+8	6.86e+8
50%Sandstone+50%Ice					
Thermal Conductivity (Wm^{-1}K^{-1})	2.6	2.6	1.61	1.61	1.61
Enthalpy (Jm^{-3})	2.31e+8	3.99e+8	5.72e+8	5.81e+8	6.39+8

C.2.4 MARTIAN SOILS

C.2.4.1 VL1 Block

Temperature (K)	100	150	200	250	300
Density (kgm^{-3})	1150	1150	1150	1150	1150
Specific Heat Capacity (Jkg^{-1}K^{-1})	360	460	560	670	770
Thermal Conductivity (Wm^{-1}K^{-1})	0.01	0.01	0.01	0.01	0.01

C.2.4.2 VL1 Drift

Temperature (K)	100	150	200	250	300
Density (kgm^{-3})	1600	1600	1600	1600	1600
Specific Heat Capacity (Jkg^{-1}K^{-1})	360	460	560	670	770
Thermal Conductivity (Wm^{-1}K^{-1})	0.11	0.11	0.11	0.11	0.11

C.2.4.3 VL2 Clump

Temperature (K)	100	150	200	250	300
Density (kgm^{-3})	1400	1400	1400	1400	1400
Specific Heat Capacity (Jkg^{-1}K^{-1})	360	460	560	670	770
Thermal Conductivity (Wm^{-1}K^{-1})	0.06	0.06	0.06	0.06	0.06

C.2.4.4 MP Overall

Temperature (K)	100	150	200	250	300
Density (kgm^{-3})	1520	1520	1520	1520	1520
Specific Heat Capacity ($Jkg^{-1}K^{-1}$)	360	460	560	670	770
Thermal Conductivity ($Wm^{-1}K^{-1}$)	0.22	0.22	0.22	0.22	0.22

Appendix D: Description of Instruments

D.1 LANDSAT THEMATIC MAPPER

Band 6 of the Landsat Thematic Mapper (Landsat TM) instrument operates in the 10.4-12.5 μm bandwidth, at a 120m resolution and is the only channel of interest for low temperature anomalies aboard the Landsat instrument. The instrument was flown on both the Landsat 4 and 5 spacecraft. These two Landsat platforms are identical, and fly 99 minute sun synchronous orbits at 705km. Each satellite can provide repeat coverage every 16 days. The sun synchronous orbit means that each overflight is at the same time of day, 11.00AM and 11.00 PM approximately, depending on the latitude. This means that solar heating of the surface is a significant factor in interpreting Landsat band 6 images. Landsat is extensively available from archives, but as Eosat is a commercial company, it can be relatively expensive.

Band	Wavelength (μm)	Resolution (m)
1	0.45-0.52	30
2	0.52-0.6	30
3	0.63-0.69	30
4	0.76-0.9	30
5	1.55-1.75	30
6	10.4-12.5	120
7	2.08-2.35	30

Table D1 Landsat TM band Specifications

D.2 THERMAL INFRARED MAPPING SPECTROMETER

The Thermal Infrared Mapping Spectrometer (TIMS) is a Deadalus Corporation IR Multispectral imaging system flown by the U.S. Department of Energy aboard various aircraft, chiefly the medium altitude Cessna Citation and the high Altitude ER-2 (Palluconi and Meeks 1985)

Band	Wavelength (μm)
1	8.2-8.6
2	8.6-9.0
3	9.0-9.4
4	9.4-10.2
5	10.2-11.211.2-12.2
6	11.2-12.2

Table D2 TIMS Band specifications.

The system has a 2.5 mrad IFOV, but samples data every 2.094 mrad. The system resolution is dependent on the altitude of the flight line. Total swath width is 76.56° (638 pixels). The systems scan rate is variables to 7.3,8.7,12 or 25 scans per second. The system uses 6 element Mercury-cadmium-telluride detectors and has a thermal noise level of about 0.3°C. Data from TIMS is available from the Eros Data Centre on 8mm Exabyte tape, or via CD-ROM or FTP from other sources.

Data Formats:

Raw TIMS data uses an 8-bit digital number. However, it is usually not provided in raw format. Standard postprocessing using JPL's TIMSCAL software into 16-bit radiance values is usually carried out. All TIMS data used in this thesis has been processed in this way.

D.3 VIKING

The Viking 1 and 2 orbiters reached Mars in 1976 and carried an extensive suite of instruments. they performed the first thorough mapping of the Martian Surface. For thermal infrared studies, the Vikings carried an Infra-Red Thermal Mapper (IRTM) instrument. The instrument IRTM is a 28 channel 4 telescope radiometer operating on six spectral bands. Spatial resolution was quite low, varying from 170km to 8km per pixel. The data format is complex, as it is recorded as a series of readings, rather than in a classic raster style image format.

Channels per band	Spectral band, μm	Brightness Temperature Designation
7	0.3-3.0	Solar Band
3	6.1-8.3	T_7
3	8.3-12.5	T_9
7	9.8-12.5	T_{11}
1	14.56-15.41	T_{15}
7	17.7-24.0	T_{20}

Table D3: IRTM Band Specifications

D.4 TERMOSKAN

The TERMOSKAN instrument was flown aboard the ill-fated Soviet Phobos Mars probes in 1989. Phobos 1 was lost in transit, but a number of images were acquired using the instrument aboard Phobos 2 before that craft was also lost.

The TERMOSKAN instrument operated on two bands, a visual band (0.5-0.95 μm) and an infrared band (8.5-12μm). Instrument instantaneous field of view (IFOV) was 0.9 arcseconds, scan speed 1 line/second and scan angle 6.1°. At an altitude of 6300 km this gives a spatial resolution of 1.8km per pixel and a swath width of 650km (Betts 1994). Data output format is 8-bit.

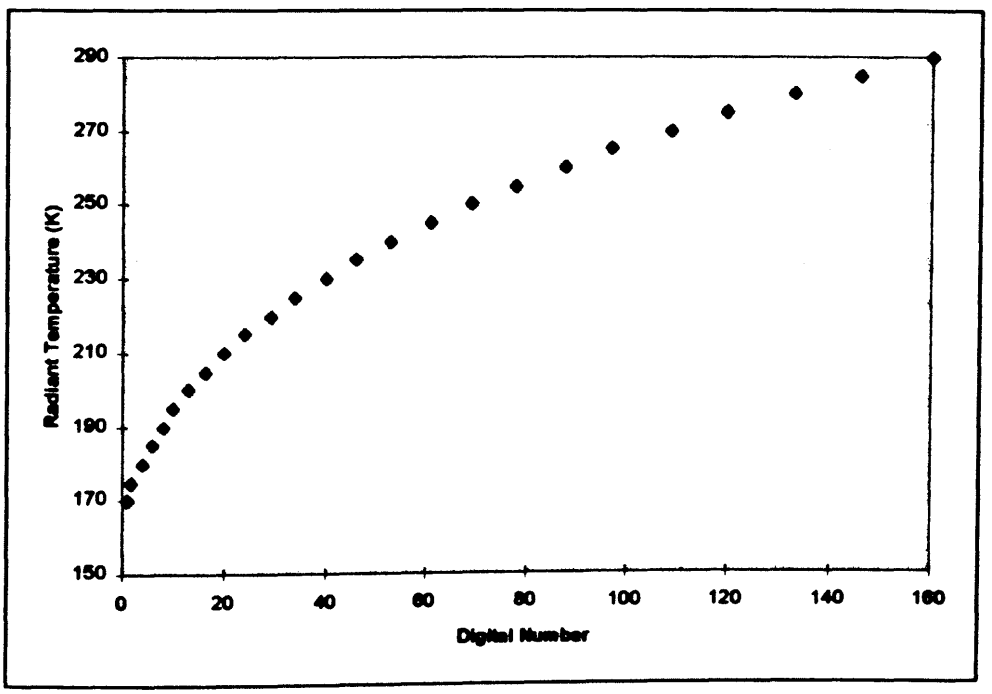


Figure D1 shows the response curve of the TERMOSKAN sensor to radiant temperature.

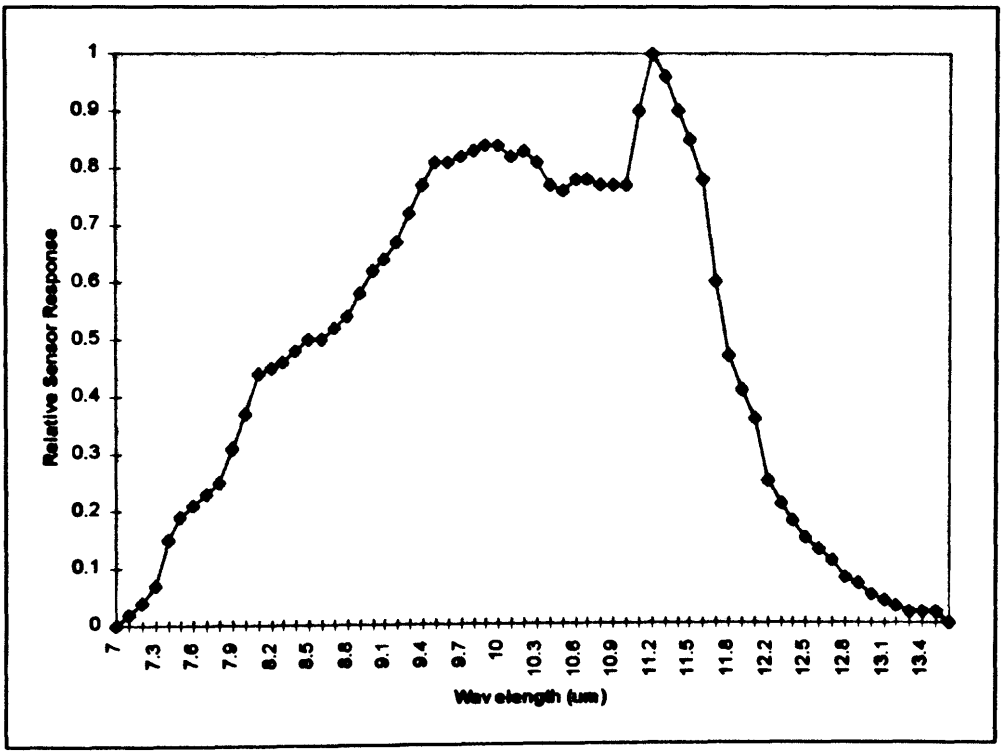


Figure D2 TERMOSKAN thermal infrared channel response curve. Note that the peak sensitivity (normalised to 1) is at about 11.2μm but that the instrument is sensitive to radiation between 7 and 13.5μm.

Appendix E: The Alpha and Bravo Models

E.1 ALPHA MODEL SCRIPT

```
/BATCH
/COM,ANSYS RELEASE 5.3   UP071096      15:24:24   09/08/1997
/input,menust,tmp   ,,,,,,,,,,,,,,,1
/PREP7
/input,start,ans   ,C:\PROGRA~1\ANSYS53\docu\,,,,,,,,,,,,,,,1
!Initial Static Thermal Model
!Initial Setup
! Setup as thermal problem
KEYW,PR_SET,1
KEYW,PR_STRUC,0
KEYW,PR_THERM,1
KEYW,PR_ELMAG,0
KEYW,PR_FLUID,0
KEYW,PR_MULTI,0
KEYW,PR_CFD,0
KEYW,LSDYNA,0
/PMETH,OFF
! Setup workplane
WPSTYL, STAT
/PREP7
! Setup elements
ET,1,PLANE77
!1st Keyopt set is default
KEYOPT,1,1,0
!For Planer axis of symettry chance keyopt 3 to 0
KEYOPT,1,3,0
DOF
! Establishing Variable Parameters
tair=0
thot=1000
thick=10
! Establishing Material properties
! The ABL
UIMP,1,DENS,,,1.172,
UIMP,1,KXX,,,2,
UIMP,1,C,,,1006,
! The SBL
UIMP,2,DENS,,,2700,
UIMP,2,KXX,,,2,
UIMP,2,C,,,800,
! The Rock
UIMP,3,DENS,,,2700,
UIMP,3,KXX,,,2,
UIMP,3,C,,,800,
!Setup Workplane
wpstyle,0.5,1,-10,100,0.003,0,0,,5
!Assemble and mesh component by component
!Create keypoints for model geometry
K,1,0,-thick,0
k,3,80,-thick,0
K,5,0,0,0,
K,6,0,1,0,
```

```
K,7,0,2,0,
K,8,80,0,0,
K,9,80,1,0,
K,10,80,2,0,
K,11,1,-thick,0,
!Create Lines connecting keypoints
LSTR,     1,     5
LSTR,     5,     8
LSTR,     8,     3
LSTR,     3,     1
LSTR,     5,     6
LSTR,     6,     7
LSTR,     7,    10
LSTR,    10,     9
LSTR,     8,     9
LSTR,     9,     6
!Create Areas from lines
!Area 1
FLST,2,4,4
FITEM,2,7
FITEM,2,10
FITEM,2,6
FITEM,2,8
AL,P51X
!Area 2
FLST,2,4,4
FITEM,2,5
FITEM,2,2
FITEM,2,10
FITEM,2,9
AL,P51X
!Area 3
FLST,2,4,4
FITEM,2,2
FITEM,2,4
FITEM,2,1
FITEM,2,3
AL,P51X
!Apply Loads
!
!Define Mesh parameters
FLST,2,4,4,ORDE,4
FITEM,2,2
FITEM,2,4
FITEM,2,7
FITEM,2,10
LESIZE,P51X,8, , ,1,
FLST,2,4,4,ORDE,4
FITEM,2,5
FITEM,2,-6
FITEM,2,8
FITEM,2,-9
LESIZE,P51X,1, , ,1,
FLST,2,2,4,ORDE,2
FITEM,2,1
FITEM,2,3
LESIZE,P51X,2, , ,1,
!Areas Attributes
CM,_Y,AREA
ASEL, , , ,     1
```

```
CM,_Y1,AREA
CMSEL,S,_Y
!*
CMSEL,S,_Y1
AATT,1,1,1,0,
CMSEL,S,_Y
CMDELE,_Y
CMDELE,_Y1
!*
CM,_Y,AREA
ASEL,,,,     2
CM,_Y1,AREA
CMSEL,S,_Y
!*
CMSEL,S,_Y1
AATT,2,1,1,0,
CMSEL,S,_Y
CMDELE,_Y
CMDELE,_Y1
!*
CM,_Y,AREA
ASEL,,,,     3
CM,_Y1,AREA
CMSEL,S,_Y
!*
CMSEL,S,_Y1
AATT,3,1,1,0,
CMSEL,S,_Y
CMDELE,_Y
CMDELE,_Y1
!Meshing Model
FLST,5,3,5,ORDE,2
FITEM,5,1
FITEM,5,-3
CM,_Y,AREA
ASEL,,,,P51X
CM,_Y1,AREA
CHKMSH,'AREA'
CMSEL,S,_Y
!*
AMESH,_Y1
!*
CMDEL,_Y
CMDEL,_Y1
CMDEL,_Y2
!Refining the Mesh
!Mesh Refinement1
/PREP7
FLST,2,3,4,ORDE,3
FITEM,2,1
FITEM,2,5
FITEM,2,-6
LREF,P51X,,,1,3,1
!Mesh Refinement2
FLST,2,4,2,ORDE,3
FITEM,2,81
FITEM,2,83
FITEM,2,-85
EREF,P51X,,,2,0,1
!*
```

```
!CM,_Y1,ELEM
!CHECK,ESEL,WARN
!CMSEL,S,_Y1
!CMDEL,_Y1
!*
!Refinement3
/PREP7
FLST,2,11,2,ORDE,7
FITEM,2,84
FITEM,2,175
FITEM,2,-177
FITEM,2,190
FITEM,2,-192
FITEM,2,201
FITEM,2,-204
EREF,P51X, , ,1,1,1
FLST,2,27,2,ORDE,15
FITEM,2,84
FITEM,2,175
FITEM,2,-176
FITEM,2,190
FITEM,2,-192
FITEM,2,201
FITEM,2,-204
FITEM,2,290
FITEM,2,301
FITEM,2,345
FITEM,2,348
FITEM,2,-353
FITEM,2,382
FITEM,2,385
FITEM,2,-391
EREF,P51X, , ,1,1,1
!*
!Load Nodes
!BottomLoad
/SOLU
/ZOOM,1,RECT,-0.934710,-0.161647,-0.830668,-0.066064
FLST,2,166,1,ORDE,72
FITEM,2,96
FITEM,2,116
FITEM,2,306
FITEM,2,569
FITEM,2,578
FITEM,2,686
FITEM,2,-687
FITEM,2,689
FITEM,2,-690
FITEM,2,711
FITEM,2,-712
FITEM,2,714
FITEM,2,-715
FITEM,2,865
FITEM,2,875
FITEM,2,-876
FITEM,2,1025
FITEM,2,1027
FITEM,2,-1028
FITEM,2,1030
FITEM,2,-1035
```

FITEM,2,1037
FITEM,2,-1038
FITEM,2,1040
FITEM,2,-1044
FITEM,2,1121
FITEM,2,1123
FITEM,2,-1124
FITEM,2,1126
FITEM,2,-1130
FITEM,2,1132
FITEM,2,1137
FITEM,2,-1140
FITEM,2,1158
FITEM,2,-1159
FITEM,2,1161
FITEM,2,1169
FITEM,2,-1174
FITEM,2,1191
FITEM,2,-1192
FITEM,2,1198
FITEM,2,-1199
FITEM,2,1250
FITEM,2,-1263
FITEM,2,1290
FITEM,2,-1301
FITEM,2,1443
FITEM,2,-1452
FITEM,2,1454
FITEM,2,-1459
FITEM,2,1461
FITEM,2,1463
FITEM,2,-1471
FITEM,2,1473
FITEM,2,-1482
FITEM,2,1484
FITEM,2,-1489
FITEM,2,1491
FITEM,2,1493
FITEM,2,-1501
FITEM,2,1571
FITEM,2,-1580
FITEM,2,1582
FITEM,2,-1585
FITEM,2,1591
FITEM,2,-1596
FITEM,2,1598
FITEM,2,1601
FITEM,2,-1606
FITEM,2,1621
FITEM,2,-1622
FITEM,2,1625
D,P51X,TEMP,thot,
FLST,2,28,1,ORDE,9
FITEM,2,1
FITEM,2,-21
FITEM,2,478
FITEM,2,481
FITEM,2,488
FITEM,2,491
FITEM,2,498

```
FITEM,2,501
FITEM.2,511
D,P51X,TEMP,tair,
!Solve
/STAT,SOLU
SOLVE
/POST1
PLNSOL,TEMP,,0
!Change window backround to white
/AUTO, 1
/REP
/COLOR,WBAK,WHIT,1
/COLOR,WBAK,BLAC,2
/COLOR,WBAK,BLAC,3
/COLOR,WBAK,BLAC,4
/COLOR,WBAK,BLAC,5
/REPLOT
!*
!Change contour values
/CVAL,1,1,05,10,025,50,100,500,1000
/REPLOT
!Define path
LPATH,    24,    22
!*
PDEF, ,TEMP, ,AVG
PRPATH,TEMP
!*
FINISH
```

E.2 BRAVO MODEL SCRIPT

```
/CLEAR,START
!BravoBasicLogfile
!LogFile to setup initial bravo model
!WorkplaneSetup
wpstyle,0.05,1,-10,100,0.003,0,1,,5
!SetupProblem
!SteadyStateThermal
KEYW,PR_SET,1
KEYW,PR_STRUC,0
KEYW,PR_THERM,1
KEYW,PR_ELMAG,0
KEYW,PR_FLUID,0
KEYW,PR_MULTI,0
KEYW,PR_CFD,0
KEYW,LSDYNA,0
/PMETH,OFF
/PREP7
!Definevariables
DEPTH  = 10
ROCKEMM=1
!ROCKK=2
!CONV=2
!Rock
UIMP,1,DENS, , ,ROCKDENS,
!Basalt1
ROCKDENS=1080
MPTEMP, ,273,400,600,800,1200,1400
MPDATA,KXX,1,1,0.66,0.581,0.483,0.422,0.357,0.339
MPDATA,KYY,1,1,4.226,4.026,3.758,3.57,3.45,3.373,3.31
MPDATA,C,1,1,321,373,410,428,447,452
UIMP,1,DENS, , ,ROCKDENS,
UIMP,1,EMIS, , ,ROCKEMM,
!ElementTypes
ET,1,PLANE55
KEYOPT,1,1,1
KEYOPT,1,3,0
KEYOPT,1,4,0
KEYOPT,1,8,0
KEYOPT,1,9,0
ET,2,SURF19
KEYOPT,2,1,1
KEYOPT,2,3,0
KEYOPT,2,4,1
KEYOPT,2,5,1
KEYOPT,2,6,0
!Changed from 5 to 0
KEYOPT,2,8,0
```

```
KEYOPT,2,9,1
KEYOPT,2,11,0
KEYOPT,2,12,0
DOF
!*
!Define SBConstant
R,1,1,5.67e-8,,,,
RMORE,,,
!*
!Establish Geometry
!*
!Keypoint number,x,y,z
K,1,0,0,0,
K,4,80,0,0,
K,5,80,-depth,0,
K,6,0,-depth,0,
!Lines
l,4,1
l,4,5
l,5,6
l,6,1
!Areas
FLST,2,4,4
FITEM,2,1
FITEM,2,2
FITEM,2,3
FITEM,2,4
AL,P51X
!Area Attributes
CM,_Y,AREA
ASEL,,,,     1
CM,_Y1,AREA
CMSEL,S,_Y
!*
CMSEL,S,_Y1
AATT,1,1,1,0,
CMSEL,S,_Y
CMDELE,_Y
CMDELE,_Y1
!*
!Create extra nodes
!RadiationNode
N,1,0,20,0,,,,
!Convection Node (not used)
N,2,10,20,0,,,,
!Mesh Size Controls
FLST,5,2,4,ORDE,2
FITEM,5,1
FITEM,5,3
CM,_Y,LINE
```

```
LSEL, , , ,P51X
CM,_Y1,LINE
CMSEL,S,_Y
!*
FLST,2,2,4,ORDE,2
FITEM,2,1
FITEM,2,3
LESIZE,P51X,1, , ,1,
FLST,2,2,4,ORDE,2
FITEM,2,2
FITEM,2,4
LESIZE,P51X,1, , ,1,
CM,_Y,AREA
ASEL, , , ,      1
CM,_Y1,AREA
CHKMSH,'AREA'
CMSEL,S,_Y
!*
AMESH,_Y1
!*
CMDEL,_Y
CMDEL,_Y1
CMDEL,_Y2
!*
!RefineZone
FLST,2,1,4,ORDE,1
FITEM,2,1
LREF,P51X, , ,1,1,1
FLST,2,1,4,ORDE,1
FITEM,2,1
LREF,P51X, , ,1,1,1
!*
!CM,_Y1,ELEM
!CHECK,ESEL,WARN
!CMSEL,S,_Y1
!CMDEL,_Y1
!*
!RefineTube
FLST,2,1,3,ORDE,1
FITEM,2,6
KREF,P51X, , ,1,3,1
FLST,2,1,3,ORDE,1
FITEM,2,6
KREF,P51X, , ,1,3,1
FLST,2,1,3,ORDE,1
FITEM,2,6
KREF,P51X, , ,1,5,1
FLST,2,1,3,ORDE,1
FITEM,2,6
KREF,P51X, , ,1,9,1
```

```
!*
!CM,_Y1,ELEM
!CHECK,ESEL,WARN
!CMSEL,S,_Y1
!CMDEL,_Y1
!*
!refineline again
FLST,2,1,4,ORDE,1
FITEM,2,1
LREF,P51X, , ,1,2,1
!RadiationElements
TYPE,2,
MAT,1,
REAL,1,
ESYS,0,
ESURF,1,
!Delete SurplusElements
FLST,2,161,2,ORDE,12
FITEM,2,6229
FITEM,2,-6327
FITEM,2,6329
FITEM,2,-6382
FITEM,2,6699
FITEM,2,6701
FITEM,2,6708
FITEM,2,6710
FITEM,2,7023
FITEM,2,-7024
FITEM,2,7027
FITEM,2,-7028
EDELE,P51X
EDELE,  6328
!Define constant variables
!Radiation
SPACE=270
!Sourcetemp
THOT=1400
Tinit=273
!FilmCoefficient
film=40
Bulktemp=273
!Open Output File
*CFOPEN,Curve,txt,
!Write Fileheader
*VWRITE,
(" Ansys Results File-Temperature Dependant ")
Number=1
*DO,N,1,5
      /input,bravol,txt                !Input Solution and Output Module
*ENDDO
```

```
!Write footer
*VWRITE
(" End of File ")
!Close output file
*cfclos
```

E.3.2 BRAVOL MODULE

```
!Solution and Output Module
/PREP7
LSCLEAR,ALL
!Loads
!Uniform initial temperature
FLST,2,5724,1,ORDE,2
FITEM,2,1
FITEM,2,-5724
IC,P51X,TEMP,tinit,
!Space Node
FLST,2,1,1,ORDE,1
FITEM,2,1
D,P51X,TEMP,space,
FLST,2,1,4,ORDE,1
FITEM,2,1
SFL,P51X,CONV,film, ,bulktemp, ,
FLST,2,213,1,ORDE,55
FITEM,2,84
FITEM,2,-85
FITEM,2,2339
FITEM,2,-2340
FITEM,2,234
FITEM,2,2386
FITEM,2,2389
FITEM,2,2391
FITEM,2,2393
FITEM,2,-2398
FITEM,2,2428
FITEM,2,-2429
FITEM,2,2434
FITEM,2,-2438
FITEM,2,2447
FITEM,2,-2454
FITEM,2,2456
FITEM,2,2458
FITEM,2,-2470
FITEM,2,2511
FITEM,2,-2518
FITEM,2,2520
FITEM,2,2531
FITEM,2,-2534
FITEM,2,2540
```

```
FITEM,2,2542
FITEM,2,2545
FITEM,2,-2554
FITEM,2,2563
FITEM,2,2565
FITEM,2,-2566
FITEM,2,2579
FITEM,2,-2603
FITEM,2,2608
FITEM,2,2610
FITEM,2,2612
FITEM,2,-2650
FITEM,2,2704
FITEM,2,-2726
FITEM,2,2730
FITEM,2,2732
FITEM,2,-2737
FITEM,2,2763
FITEM,2,-2765
FITEM,2,2767
FITEM,2,-2784
FITEM,2,2803
FITEM,2,-2812
FITEM,2,2815
FITEM,2,-2822
FITEM,2,2829
FITEM,2,-2832
FITEM,2,2837
FITEM,2,-2838
FITEM,2,2841
D,P51X,TEMP,thot,
!Solvit
/SOLU
FINISH
/SOLU
/STAT,SOLU
SOLVE
!Postproc path plot (off)
!/POST1
!LPATH,     4,     3
!*
!PDEF, ,TEMP, ,AVG
!PRPATH,TEMP
!Define Output Parameters
Temp1=TEMP(4)
temp2=TEMP(83)
Temp3=TEMP(82)
Temp4=TEMP(81)
Temp5=TEMP(80)
Temp6=TEMP(79)
```

```
Temp7=TEMP(78)
temp8=TEMP(77)
Temp9=TEMP(76)
Temp10=TEMP(75)
Temp11=TEMP(74)
Temp12=TEMP(73)
Temp13=TEMP(72)
temp14=TEMP(71)
Temp15=TEMP(70)
Temp16=TEMP(69)
Temp17=TEMP(68)
Temp18=TEMP(67)
Temp19=TEMP(66)
temp20=TEMP(65)
Temp21=TEMP(64)
Temp22=TEMP(63)
Temp23=TEMP(62)
Temp24=TEMP(61)
Temp25=TEMP(60)
temp26=TEMP(59)
Temp27=TEMP(58)
Temp28=TEMP(57)
Temp29=TEMP(56)
Temp30=TEMP(55)
Temp31=TEMP(54)
temp32=TEMP(53)
Temp33=TEMP(53)
Temp34=TEMP(51)
Temp35=TEMP(50)
Temp36=TEMP(49)
Temp37=TEMP(48)
temp38=TEMP(47)
Temp39=TEMP(46)
Temp40=TEMP(45)
Temp41=TEMP(44)
Temp42=TEMP(43)
Temp43=TEMP(42)
temp44=TEMP(41)
Temp45=TEMP(40)
Temp46=TEMP(39)
Temp47=TEMP(38)
Temp48=TEMP(37)
Temp49=TEMP(36)
temp50=TEMP(35)
Temp51=TEMP(34)
Temp52=TEMP(33)
Temp53=TEMP(32)
Temp54=TEMP(31)
Temp55=TEMP(30)
temp56=TEMP(29)
```

```
Temp57=TEMP(28)
Temp58=TEMP(27)
Temp59=TEMP(26)
Temp60=TEMP(25)
Temp61=TEMP(24)
temp62=TEMP(23)
Temp63=TEMP(22)
Temp64=TEMP(21)
Temp65=TEMP(20)
Temp66=TEMP(19)
Temp67=TEMP(18)
temp68=TEMP(17)
Temp69=TEMP(16)
Temp70=TEMP(15)
Temp71=TEMP(14)
Temp72=TEMP(13)
Temp73=TEMP(12)
temp74=TEMP(11)
Temp75=TEMP(10)
Temp76=TEMP(9)
Temp77=TEMP(8)
Temp79=TEMP(7)
Temp80=TEMP(6)
TEMP81=TEMP(3)
!Write paramaters
*VWRITE,number
(" Run Number ", 1F3.0)
*VWRITE,DEPTH,ROCKDENS,ROCKEMM
(" Depth " F6.0, " DENS ", F6.0, " EMM ", F3.1)
*VWRITE,space,thot,film,bulktemp,
(" SPACE " F5.0, " Thot " F5.0, " Film " F5.0, " bulktemp ", F5.0, )
!Write output
*VWRITE,Temp1,Temp2,Temp3,Temp4,Temp5,
(" Range0-4 ", 5F8.2)
*VWRITE,Temp5,Temp5,Temp7,Temp8,Temp9,
(" Range5-9 ", 5F8.2)
*VWRITE,Temp10,Temp11,Temp12,Temp13,Temp14,
(" Range10-14 ", 5F8.2)
*VWRITE,Temp15,Temp16,Temp17,Temp18,Temp19,
(" Range15-19 ", 5F8.2)
*VWRITE,Temp20,Temp21,Temp22,Temp23,Temp24,
(" Range20-24 ", 5F8.2)
*VWRITE,Temp25,Temp26,Temp27,Temp28,Temp29,
(" Range25-29 ", 5F8.2)
*VWRITE,Temp30,Temp31,Temp32,Temp33,Temp34,
(" Range30-35 ", 5F8.2)
*VWRITE,Temp35,Temp36,Temp37,Temp38,Temp39,
(" Range35-39 ", 5F8.2)
*VWRITE,Temp40,Temp41,Temp42,Temp43,Temp44,
(" Range40-44 ", 5F8.2)
```

```
*VWRITE,Temp45,Temp46,Temp47,Temp48,Temp49,
(" Range45-49 ", 5F8.2)
*VWRITE,Temp50,Temp51,Temp52,Temp53,Temp54,
(" Range50-54 ", 5F8.2)
*VWRITE,Temp55,Temp56,Temp57,Temp58,Temp59,
(" Range55-59 ", 5F8.2)
*VWRITE,Temp60,Temp61,Temp62,Temp63,Temp64,
(" Range60-64 ", 5F8.2)
*VWRITE,Temp65,Temp66,Temp67,Temp68,Temp69,
(" Range65-69 ", 5F8.2)
*VWRITE,Temp70,Temp71,Temp72,Temp73,Temp74,
(" Range70-74 ", 5F8.2)
*VWRITE,Temp75,Temp76,Temp77,Temp78,Temp79,
(" Range75-79 ", 5F8.2)
*VWRITE,Temp80,Temp81
(" Value 79,80 ", 2F8.2)
!
!Define incrementing variable
FILM=FILM+10
Number=Number+1
FINISH
```

Appendix F: IDL Programme Scripts

This appendix lists a selection of the IDL programme scripts used for data processing in this thesis. A Semicolon indicates a comment line.

G.1 KIN

Calculates the kinetic kemperature from the radiance array

```
;PART 1:Reading In Data
;1.1Read in TIMS data
;Required input- Signed 16 bit BSQ export file from Imagine, filename input.dat
;Required alterations to modify, adjust filename and related array sizes
;ArraySizes
A=21
B=51
file = FILEPATH('input.dat',SUBDIR=['idltims'])   ;Open Filepath
OPENR, lun, file, /GET_LUN                                                    ;Assign
LUN
tims1 = INTARR(A,B)
        ;Define Array Band1
tims2 = INTARR(A,B)
        ;Define Array Band1
tims3 = INTARR(A,B)
        ;Define Array Band3
tims4 = INTARR(A,B)
        ;Define Array Band4
tims5 = INTARR(A,B)
        ;Define Array Band5
tims6 = INTARR(A,B)                                                           ;Define
Array Band6
READU, lun, tims1,tims2,tims3,tims4,tims5,tims6
;ArraySizes
FREE_LUN, lun
;1.2 Read in TIMS lookup tables provided by Ron Alley, JPL.
file = FILEPATH('tims.lut',SUBDIR=['idltims'])
                ;Open Filepath
OPENR, lun, file, /GET_LUN
        ;Assign LUN
lut1 = INTARR(32767,1)
        ;Define LUT Array Band1
lut2 = INTARR(32767,1)
lut3 = INTARR(32767,1)
lut4 = INTARR(32767,1)
lut5 = INTARR(32767,1)
lut6 = INTARR(32767,1)
READU, lun, lut1, lut2, lut3, lut4, lut5, lut6                    ;Reading Arrays
FREE_LUN, lun
BYTEORDER, lut1, lut2, lut3, lut4, lut5, lut6              ;Flip byte order to Intel
;
;Part 2 Convert radiances to Temperatures
;Convert Radiance values in TIMS data to radiant temperatures
;Band 1
X=0.0
Temp1=FLTARR(A,B)
        ;Establish temperature array
X = tims1(*,*)
```

```
Temp1(*,*)=float(lut1(X,0))/100
;Band 2
Temp2=FLTARR(A,B)
        ;Establish temperature array
X = tims2(*,*)
Temp2(*,*)=float(lut2(X,0))/100
;Band 3
Temp3=FLTARR(A,B)
        ;Establish temperature array
X = tims3(*,*)
Temp3(*,*)=float(lut3(X,0))/100
;Band 4
Temp4=FLTARR(A,B)
        ;Establish temperature array
X = tims4(*,*)
Temp4(*,*)=float(lut4(X,0))/100
;Band 5
Temp5=FLTARR(A,B)
        ;Establish temperature array
X = tims5(*,*)
Temp5(*,*)=float(lut5(X,0))/100
;Band 6
Temp6=FLTARR(A,B)
        ;Establish temperature array
X = tims6(*,*)
Temp6(*,*)=float(lut6(X,0))/100
;Merge all temperature data into a single temperature array
;Warning-May need to code around this array if using larger input arrays (>265*256/6)
TEMPALL=FLTARR(A,B,6)
TEMPALL(*,*,0)=TEMP1(*,*)
TEMPALL(*,*,1)=TEMP2(*,*)
TEMPALL(*,*,2)=TEMP3(*,*)
TEMPALL(*,*,3)=TEMP4(*,*)
TEMPALL(*,*,4)=TEMP5(*,*)
TEMPALL(*,*,5)=TEMP6(*,*)
;Convert TEMPALL to kelvin-Duh!
TEMPALL(*,*,*)=TEMPALL(*,*,*)+273
;Radiant Temperatures to Kinetic Temperatures Conversion
;Radiant Temperature
KINTEMP=FLTARR(A,B,6)
EMM =FLTARR(6,1)
;Check Emmisivity array
EMM =[(0.92),(0.92),(0.90),(0.96),(0.96),(0.94)]
;EMM =[(0.94),(0.93),(0.885),(0.965),(0.96),(0.95)]
KINTEMP(*,*,0)=TEMPALL(*,*,0)/(EMM(0)^0.25)
KINTEMP(*,*,1)=TEMPALL(*,*,1)/(EMM(1)^0.25)
KINTEMP(*,*,2)=TEMPALL(*,*,2)/(EMM(2)^0.25)
KINTEMP(*,*,3)=TEMPALL(*,*,3)/(EMM(3)^0.25)
KINTEMP(*,*,4)=TEMPALL(*,*,4)/(EMM(4)^0.25)
KINTEMP(*,*,5)=TEMPALL(*,*,5)/(EMM(5)^0.25)
;Average the derived kinetic temperatures
TEMPAVG=FLTARR(A,B)
TEMPAVG(*,*)=(KINTEMP(*,*,0)+KINTEMP(*,*,1)+KINTEMP(*,*,2)+KINTEMP(*,*,3)+KIN
TEMP(*,*,4)+KINTEMP(*,*,5))/6
;Convert Tempavg back to degree C
TEMPAVG(*,*)=TEMPAVG(*,*)-273
TEMPDIFF=FLTARR(A,B)
TEMPDIFF=KINTEMP(*,*,0)-KINTEMP(*,*,5)
;Write output
```

```
file = FILEPATH('output61.dat',SUBDIR=['idltims'])
                              ;Open Filepath
OPENW, lun, file, /GET_LUN
                                                    ;Assign LUN
WRITEU, lun, TEMPAVG
FREE_LUN,lun
tvscl,kintemp
;Some output for the talk through...
;Radiant temperatures for Erdas
;file = FILEPATH('radtemp.dat',SUBDIR=['idltims'])
                              ;Open Filepath
;OPENW, lun, file, /GET_LUN
                                                    ;Assign LUN
;WRITEU, lun, TEMPALL(*,*,*)
;FREE_LUN,lun
;Radtemp differences for Excel
file = FILEPATH('diff61.dat',SUBDIR=['idltims'])
                    ;Open Filepath
OPENW, lun, file, /GET_LUN
                                                    ;Assign LUN
WRITEU, lun, TEMPDIFF
FREE_LUN,lun
;plot,kintemp(10,10,*)-293
;Write radiant temperatures
file = FILEPATH('rad61.dat',SUBDIR=['idltims'])
                    ;Open Filepath
OPENW, lun, file, /GET_LUN
                                                    ;Assign LUN
WRITEU, lun, TEMPALL
FREE_LUN,lun
```

G.2 GEOMETRIC CORRECTION

Performs Geometric Correction and resampling of image arrays.

```
;Geometric correction module
;Read in Kintemp array
;Define Array Size, can delete this if running modules sequentially
A=21
B=51
;Elevation over target, in metres dummy! Target 680m asl
ELEV=1694
;How many rows from left edge of the swath is the left edge of the image?
STARTROW=69
;How many rows from the left edge of the image is the row containing the main fumarole?
FUM=7
;Read in array, again, can delete this if running modules sequentially
kintemp=FLTARR(A,B)
file = FILEPATH('output61.dat',SUBDIR=['idltims'])        ;Open Filepath
OPENR, lun, file, /GET_LUN
        ;Assign LUN
READU, lun, kintemp
FREE_LUN, lun
;Define Along track Resolution
YRES=8.24
;Calculate Correct Y ordinate
kintempA=FLTARR(3,A,B)
;YVAL=0
YPOS=0.0
PRINT,'oksofar1'
XLOOP, kintempA, kintemp,  A, XVAL, XPOS, STARTROW, PHI, ELEV
PRINT,'oksofar2'
XVAL=0
PHI=0
XPOS=0.0
YLOOP,  kintempA, kintemp, B, YPOS, YRES, YVAL
PRINT,'oksofar3'
;For image coregistration
;Set the zerovalue to
Zeroval=kintempa(1,FUM,0)
;Need to ensure that the row containing the fumarole maps in to row forty of outarray
kintempa(1,*,*)=Zeroval-kintempa(1,*,*)+30
;DefineOutputArray
OUTARRAY=FLTARR(120,540)
;Need to ensure that the row containing the fumarole maps in to row forty of outarray
;Convert position information to integars using BYTE Command in fillet routine
Q=0
V=0
TEX=0
TY=0
FILLET, outarray, kintempa, A, B, Q, V, TEX, TY
PRINT,'oksofar4'
;test output
tvscl,outarray
tvscl,kintemp
;Next Job-need to populate complete array
;Not working yet
;zeros are data points!
;need to delete zeros and then replace, Nan?
N=0
M=0
```

```
BIX=0.0
BIXO=0.0
NIX=0.0
NIXO=0.0
POPULATE2,Outarray, N, M, BIX, BIXO, NIX, NIXO
Outarray = SMOOTH(Outarray, 3)
tvscl,outarray
;Write outarray to a file
file = FILEPATH('seg61.dat',SUBDIR=['idltims'])
                    ;Open Filepath
OPENW, lun, file, /GET_LUN
;120 cols, 540 rows. Standard IDL import
                                                    ;Assign LUN
WRITEU, lun, OUTARRAY
FREE_LUN,lun
```

G.4 POPULATE

Submodule of geometric correction programme to populate arrays

```
PRO Populate2, Outarray, N, M, BIX, BIXO, NIX, NIXO
        FOR N=0,498 DO BEGIN
                FOR M=0,118 DO BEGIN
                        BIX=OUTARRAY(M,N)
                        BIXO=OUTARRAY(M+1,N)
                        IF BIX NE 0 THEN IF BIXO EQ 0 THEN BIXO=BIX
                        OUTARRAY(M+1,N)=BIXO
                ENDFOR
        ENDFOR
        FOR M=0,118 DO BEGIN
                FOR N=0,428 DO BEGIN
                        NIX=outarray(M,N)
                        NIXO=OUTARRAY(M,N+1)
                        IF NIX NE 0 THEN IF NIXO EQ 0 THEN NIXO=NIX
                        OUTARRAY(M,N+1)=NIXO
                ENDFOR
        ENDFOR
END
```

G.5 EXTRACTOR

Calculates the median, maximum and anomaly limits.

```
PRO EXTRACTOR, array1fa, array2, array3, array4, array5, array6, array7fa, array8fa,
res
BIG=0.0
BACK=0.0
;Do it for one array, then worry about looping or copying
;Assign a number into the first position of each array.
RES(0,*,*)=1
RES(1,*,*)=2
RES(2,*,*)=3
RES(3,*,*)=4
RES(4,*,*)=5
RES(5,*,*)=6
RES(6,*,*)=7
RES(7,*,*)=8
;Slot 0
;Find Background Value for each image-just use median value for each images, into slot 0
RES(0,*,0)=MEDIAN(array1fa)
RES(1,*,0)=MEDIAN(array2)
RES(2,*,0)=MEDIAN(array3)
RES(3,*,0)=MEDIAN(array4)
RES(4,*,0)=MEDIAN(array5)
RES(5,*,0)=MEDIAN(array6)
RES(6,*,0)=MEDIAN(array7fa)
RES(7,*,0)=MEDIAN(array8fa)
        ;Array1fa
        FOR N=0,539 DO BEGIN
                        ;Slot1
                        ;Find Maximum Value of Each Row, into slot 1
                        ROW=N
                        RES(0,N,1)=MAX(array1fa(*,N))
                        TEST=[MAX(array1fa(*,N),I),I]
                        ;Slot2
                        ;Find Peak Position, slot 2
                        TEST=[MAX(array1fa(*,N),I),I]
                        RES(0,N,2)=I
                        ;Slot3
                        ;Find left position, space 3
                        Y=I
                        FOR Y=I,0,-1 DO BEGIN
                                THRESH=(RES(0,N,0))+1
                                IF array1fa(Y,N) LT THRESH THEN IF RES(0,N,3) EQ 1
                                THEN RES(0,N,3)=Y
                        ENDFOR
                        ;Slot4
                        ;Right position, space 4
                        Y=I
                        FOR Y=I,119 DO BEGIN
                                THRESH=(RES(0,N,0))+1
                                IF array1fa(Y,N) LT THRESH THEN IF RES(0,N,4) EQ 1
                                THEN RES(0,N,4)=Y
                        ENDFOR
ENDFOR
plot,res(0,*,2)
oplot,res(0,*,3)
oplot,res(0,*,4)
```

```
Y=0
I=0
TEST=0
THRESH=0
;
;Repeat for each array

;Test Sequence outputs
plot,res(7,*,2)
oplot,res(7,*,3)
oplot,res(7,*,4)

;test=fltarr(120,540)
;test(*,300)=array1fa(*,300)-RES(0,300,1)
END
```

Appendix G: The Finite Element Method

The following discussion broadly outlines the mathematics of the finite element method for one dimensional, steady state problems, and is based in its entirely on Cambell (1996).

G.1 THE PHYSICAL MODEL

To construct a finite element model, or indeed any mathematical model, the user must first define a mathematical formulation of the physical process under investigation, together with the geometry of the object being modelled and the physical properties of the component materials. The physical model is continuous, it is not divided into subregions beyond those required to describe the it adequately. The boundary conditions must also be known and mathematically represented.

For example, for a one-dimensional conductive problem, the physical process can be described mathematically by the equations:

$$D(u)=\delta k_t/\delta x\ \delta u/\delta x+q \qquad x\in\Omega \qquad \text{G.1 24}$$

$$b_1(u)=u-u_p=0 \qquad x\in\Gamma_1 \qquad \text{G.2 25}$$

$$b_2(u)=k_t\delta u/\delta x-q_p=0 \qquad x\in\Gamma_2 \qquad \text{G.3 26}$$

Where:

k_t Thermal Conductivity ($Wm^{-1}K^{-1}$)

u Temperature Function

q Heat source or sink

Ω The domain of the physical system

Γ_1,Γ_2 The boundaries of the physical system

Equation G.1 describes the temperature within the system. Equation G.2 describes the boundary condition at boundary b_1, which has a fixed temperature u_p (a Diriclet boundary condition). Equation G.3 describes the boundary condition at b_2, which has a thermal flux q_p (A Van Neumann boundary condition).

By calculus of variations the system equations can be rewritten as integral equations instead of as differentials. Rewriting the equations in this form gives:

G.2 MESH DISCRETISATION

For finite element modelling a user must break the continuous model into small mathematically manageable units, or finite elements. The distribution of the function being modelled (in this study, temperature) can be described by an element shape function. Element 'meshes' in one, two or three dimensions, can be created, with values for given physical constants such as conductivity or Youngs' Modulus transferred onto each element in the mesh. Elements need not be of uniform size, and so elements can be made smaller in areas of interest and much larger in less interesting parts of the problem.

For a one dimensional conductive problem, the set of degrees of freedom (i.e. variables), for each element is:

$$\mathbf{a}^{\bullet} = \begin{pmatrix} a_1^{\bullet} \\ a_2^{\bullet} \end{pmatrix} = \begin{pmatrix} u(x_1^{\bullet}) \\ u(x_2^{\bullet}) \end{pmatrix} \qquad \text{G.5}$$

The variable is the nodal temperature. The spatial variation of the temperature between these nodes can be prescribed by an interpolation function. The values at the nodes will be known precisely and the values between the nodes estimated by the interpolation function, which is in this case linear (see Figure G.1) but may be quadratic or quartic.

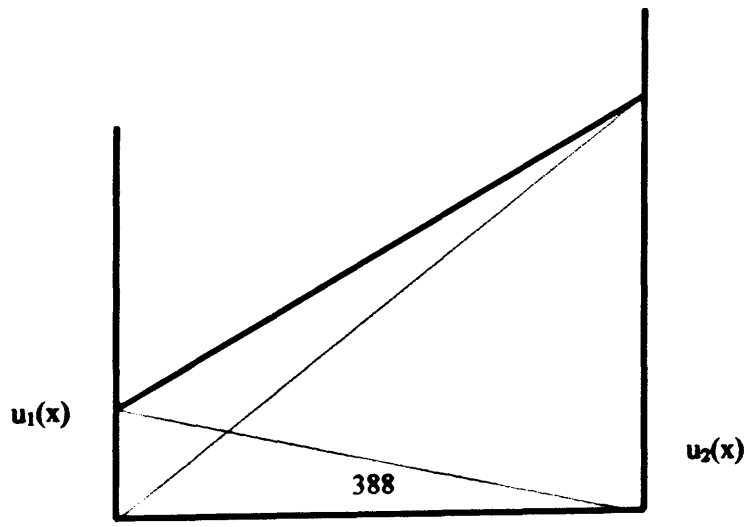


Figure G.1 Finite Element Linear Interpolation Function for an element Ω_e

Note that:

$$u(x)=\alpha_1+\alpha_2 x \qquad \text{G.6}$$

Where:

u(x)	Value of variable (Temperature, K)
α_1,α_2	Constants
x	Position (m)
Ω_e	Element Domain

Equation G.6 describes the interpolated function (heavy line) which is a linear combination of functions describing the dashed lines. There are two of these expressions, one for each node. They are sometimes referred to as pyramid functions, as the functions on each side of a node will graph as a triangle or pyramid.

Equation G.6 can be rewritten in matrix form:

$$u(x) = \langle 1 \quad x \rangle \begin{pmatrix} \alpha \\ \alpha \end{pmatrix} \qquad \text{G.7}$$

Or:

$$u(x) = \langle P(x) \rangle \alpha \qquad \text{G.8}$$

At node 1:

$$u(x_1) = a_1^e = \langle 1 \quad x_1^e \rangle \alpha \qquad \text{G.9}$$

At node 2:

$$u(x_2) = a_2^e = \langle 1 \quad x_2^e \rangle \alpha \qquad \text{G.10}$$

This can itself be expressed in matrix form:

$$ae = \begin{pmatrix} 1 & x_1^e \\ 1 & x_2^e \end{pmatrix} \alpha = [C]\alpha \qquad \text{G.11}$$

$$\alpha=[C]^{-1} a^e \text{ where } ae = \begin{pmatrix} 1 & x_1^e \\ 1 & x_2^e \end{pmatrix} \alpha = [C]\alpha \qquad \text{G.12}$$

If we substitute G.12 back into G.7 we get:

$$u(x) = \langle P(x) \rangle [C]^{-1} a^e \qquad \text{G.13}$$

Which can be recast as:

$$u(x) = N_1^e(x)a_1^e + N_2^e(x)a_2^e \quad \text{G.14}$$

$$= [N_1^e(x)\ N_2^e(x)]\ a^e \quad \text{G.14.1}$$

N_1 and N_2 are the shape functions describing the shape of the interpolation function for a given element

$$N_1(x) = (x_1 - x) / h_e \quad \text{G.15}$$

$$N_2(x) = (x_2 - x) / h_e \quad \text{G.15.1}$$

Finally, if we differentiate the equation G.6

$$\delta u(x)/\delta x = [B_x]\ a^e \quad \text{G.16}$$

Where $[B_x]$ is the derivative with respect to x of the shape function in square brackets in G.14.1

G.3 MINIMISING THE ENERGY INTEGRAL

Equation G.4 is an energy integral related to the concept of the Lagrangian in classical mechanics. The system energy integral will be the sum of the element energy integrals, i.e.:

$$\Pi(u) = \Sigma\, \Pi^e(u) \quad \text{G 17}$$

Where:

$$\Pi^e(u) = \int_{\Omega e} 1/2\ {}_{uT}\partial_{xu}{}_{Tx} - u^T q d\Omega - \int_{\Gamma 2} u^T q d\Gamma \quad \text{G 18}$$

Now, substituting in the element shape functions from equations G.15 and G.17

$$\Pi^e(u) = \int_{\Omega e} 1/2\ a^{eT}[B]^T [B]\ a^e d\Omega - \int_{\Omega e} a^{eT}[N]^T q\, d\Omega - \int_{\Gamma 2} a^{eT}[N]\, q d\Gamma \quad \text{G.19}$$

By finding a minimum of the curve of $\Pi(u)$ the true solution to the system can be found. This can be calculated by setting the differential equal to zero:

$$\delta\Pi(u)/\delta a^e = 0$$

Thus:

$$\Sigma \int_{\Omega e} [B]^T [B]\, d\Omega\, a^e = \Sigma \int_{\Omega e} [N]^T q\, d\Omega - \int_{\Gamma} [N]\, q d\Gamma \quad \text{G.20}$$

Or:

$$\Sigma[K^e]a^e = \Sigma(f_\Omega^e + f_\Gamma^e) \qquad \text{G.21}$$

Which after summation reduces to:

$$[K]a = f \qquad \text{G.22}$$

Which is the finite element equation.

G.4 DERIVATION OF ELEMENT MATRICES

After writing the basic finite element equations all that remains is to derive from them the actual components of the matrices.

For the element stiffness matrix $[K]^e$, remember:

$$N_1^e(x) = (x_1 - x)/h^e$$

$$N_2^e(x) = (-x_2 - x)/h^e \qquad \text{G.23}$$

Let:

$$S = (x - x_1)/h^e \qquad \text{G.24}$$

Thus:

$$N_1(x) = N_1(s) = 1 - S \qquad \text{G.25}$$

$$N_2(x) = N_2(s) = S$$

This rescales so that $dx = h^e ds$.

$$dN_1/dx = 1/h^e \qquad \text{G.26}$$

$$dN_2/dx = 1/h^e \qquad \text{G.27}$$

Therefore:

$$B = \langle -1/h^e \;\; 1/h^e \rangle \qquad B^T = \begin{pmatrix} -1/h^e \\ 1/h^e \end{pmatrix} \qquad \text{G.28}$$

But from G.20

$$[K]^e = \int_{\Omega e} [B]^T [B]\, dx \qquad \text{G.29}$$

$$= \int_{\Omega e} [B]^T [B]\, h^e ds \qquad \text{G.30}$$

$$= \int_0^1 \begin{pmatrix} -1/h^e \\ 1/h^e \end{pmatrix} k_t \langle -1/h^e \quad 1/h^e \rangle h^e ds \qquad \text{G.31}$$

No S term is present in the equation so the integral vanishes. Multiplying out the terms gives:

$$[K]^e = hk_t \begin{pmatrix} 1/h^2 & -1/h^2 \\ -1/h^2 & 1/h^2 \end{pmatrix} \qquad \text{G.32}$$

The boundary conditions and forcing functions for the elements must also be described. From G.20:

$$f_\Omega^e = \int_{\Omega e} [N]^T q\, d\Omega \qquad \text{G.33}$$

$$d\Omega = A\, h^e ds \qquad \text{G.3}$$

$$f_\Omega^e = Ah^e q \int_{\Omega e} [N]^T ds \qquad \text{G. 35}$$

Substituting in the shape functions [N] from G.25 we get:

$$f_1 = Ah^e q \int_0^1 (1-S)\, ds \qquad \text{G.35}$$

$$f_2 = Ah^e q \int_0^1 (S)\, ds \qquad \text{G.36}$$

Both of which reduce after integration to:

$$f_n = Ah^e q/2 \qquad \text{G.37}$$

Thus

$$f_\Omega^e = Ah^e q/2 \begin{pmatrix} 1 \\ 1 \end{pmatrix} \qquad \text{G.38}$$

For the boundaries:

$$f_\Gamma = \int_\Gamma [N]\, q_n \Gamma \qquad \text{G.39}$$

$$\int_\Gamma d\Gamma = \text{Area A} \qquad \text{G.40}$$

Therefore:

$$\begin{pmatrix} f_1 \\ f_2 \end{pmatrix} = A\, q \begin{pmatrix} N_1 \\ N_2 \end{pmatrix} \qquad \text{G.41}$$

Which, after substitution reduces to:

$$\begin{pmatrix} f_1 \\ f_2 \end{pmatrix} = \begin{pmatrix} Aq_1 \\ Aq_2 \end{pmatrix} \qquad \text{G.42}$$

This produces an element stiffness matrix:

$$hk\begin{pmatrix} 1/h^2 & -1/h^2 & u_1 \\ -1/h^2 & 1/h^2 & u_2 \end{pmatrix} - \begin{pmatrix} Ah^e c/2_1 \\ Ah^e C/2_2 \end{pmatrix} + \begin{pmatrix} Aq_1 \\ Aq_2 \end{pmatrix} \qquad \text{G.43}$$

G.5 ASSEMBLY OF GLOBAL MATRICES

The loss of the summation after equation G.21 denotes assembly of the element matrices, denoted by the superscript e into a global matrix. This assembly is carried out utilising network theory. The resulting stiffness matrices will always be sparse (i.e. most entries will be zero) and symmetric about the diagonal. The complete matrix equation can them be solved by computer, using any one of a number of appropriate algorithms, such as the Gauss-Siedel method.

It should be noted that the above example is for a non-transient problem, that is, the system is in equilibrium, as the energy functional has been minimised. A more complex approach, similar in theory, will be required to consider transient modelling.

BIBLIOGRAPHY

ABRAMS, M.J., KAHLE, A.B., PALLUCONI, F.D., SCHIELDGE, J.P., 1984, Geologic mapping using Thermal Images, *Remote Sensing of Environment*, **16**:13-33

ANDERSON, M.C., NORMAL, J.M., DIAK, G.R., KUSTAS, W.P., MECIKALSKI, J.R., 1997, A Two-source Time Integrated Model for Estimating Surface Fluxes Using Thermal Infrared Remote Sensing, *Remote Sensing of Environment*, **60**:195-216

ANSYS ELEMENT MANUAL, 7th Edition, 1996, Ansys, Houston PA.

BAKER, V.R. ,CARR M.H., GULICH, V.C. WILLIAM, C.R., MARLEY, M.S. 1988, Channel and valley networks in *Mars* edited by H.H,. Kieffer (University of Arizona Press).

BETTS, B.H. ,1994, Thermal and Visible Studies of Mars Using the Termoskan Data Set. PhD thesis. Unpublished. (University of Arizona Press)

BIRD, R.B., STEWART, W.E., LIGHTFOOT, E.N., 1960, Transport Phenomena, John Wiley and Son, New York.

BONNEVILLE, A., KERR, Y., 1987, A Thermal forerunner of the 28th March 1983 Mount Etna Eruption from Satellite thermal Infrared Data. *Journal of Geodynamics* , **7**,1-31.

BONNEVILLE, A., VASSEUR, G., KERR, Y., 1984, Satellite thermal infrared observations of Mount Etna after the 17th March 1981 Eruption. *Journal of Volcanology and Geothermal Research*, **24**, 293-313.

BONNEVILLE, A., GOUZE, P., 1992, Thermal survey of Mount Etna volcano from space, *Geophysical Research Letters*, **19**:725-728.

of Geophysical Research, **82** No 28.

CARSLAW, H.S., JAEGER, J.C., 1959, *Conduction of Heat in Solids, 2nd Edition* Oxford University Press (New York)

CASSINIS, R., TOSI, N., LECHI, G.M., BRIVIO, P.A., ZILIOLI, E., MARINI, A., 1984, Thermal inertia of rocks- an HCMM experiment on Sardinia, Italy, *International Journal of Remote Sensing*, **5**:79-94.

ÇENGEL, Y.A., 1997, Introduction to Thermodynamics and Heat Transfer, McGraw-Hill.

CHRISTENSEN, P.R., H.J.MOORE. 1992. The Martian Surface Layer in: *Mars*, H.H. Kieffer, B.M. Jakosky, C.W. Snyder, M.S. Matthews eds, University of Arizona Press. Tucson.

CHENG, P., MINKOWYCZ, W.J. ,1977, Free Convection About a Vertical Flat Embedded in a Porous Medium With Application to Heat transfer From a Dike, *Journal of Geophysical Research,* **82**: 2040-2044.

CHENG, P.,1985, Natural Convection in a Porous Medium: External Flows, in *KAKAC, S., AUNG, W., VISKANTA, R., (editors) Natural Convection: Fundamentals and Applications,* Springer Verlag, Berlin.

CLIFFORD, S.M., BARTELS C.J., RUBENSTEIN E.P., 1987, The Mars Thermal Model (MARSTHERM): A Fortran 77 Finite-difference program designed for general distribution, Lunar and Planetery Institute, Houston.

CLOUGH, R.W., 1960, The Finite Element Method in Plane Stress Analysis. *Journal of Structural Division ASCE, Proceedings of 2nd Conference on Electronic Computation*, pp345-378.

COOPER, H.J., SMITH, E.A., 1995, Limitations in estimating surface sensible heat fluxes from surface and satellite radiometric skin temperatures, *Journal of Geophysical Research,* **100D12**:25419-25477.

CRACKNELL, A.P., XUE Y., 1996, Thermal Inertia determination from space-a

tutorial review, *International Journal of Remote Sensing*, **17**:431-461

CRAGO, R., SUGITA, M., BRUTSAERT, W, 1995, Satellite-derived surface temperature with boundary layer temperatures and geostropic winds to estimate surface energy fluxes, *Journal of Geophysical Research*, **100D12**:25447-25451

CREMERS, C.J., BIORKEBAK, R.C., DAWSON, J.P., 1972, Thermal conductivity of Fines from Apollo 11 . Proceedings of the Apollo 11 Lunar Science Conference, *Geochimica et Cosmochimica Acta*, Supplement 1, Volume 3 pp 2045-2050.

CREMERS, C.J., 1972, Thermal conductivity of Apollo 14 Fines. Proceeding Third Lunar Science Conference, *Geochimica et Cosmochimica Acta*, Supplement 3 pp 2611-2617 MIT Press.

CRISP, J.A., KAHLE, A.B., ABBOTT, E.A., 1990, Thermal infrared spectral character of Hawaiian basaltic glasses. *Journal of Geophysical Research*, **95**: 21657-21667.

CLIFFORD, S.M., 1987, Mars: Evolution of its Climate and Atmosphere, editors V. Baker, M.H. Carr F. Fanale, R. Greeley, R. Haberle.

CLIFFORD, S.M., BARTELS, C.J., RUBENSTEIN, E.P. 1987 The Mars thermal model (MARSTHERM): A FORTRAN 77 Finite-Difference program designed for general distribution, Lunar, Planetary Institute, Houston.

CLIFFORD, S.M.,1984, A model for the climatic behaviour of water on Mars, PhD thesis, Unpublished, University of Mass.

DAVIS, S.N., 1969, *in* Flow through Porous Media, edited by DeWeist, R.J.M., Academic Press, New York.

DAVIES, G.F., ARVIDSON, R.E., 1981, Martian Thermal History, core segregation and tectonics *Journal of Geophysical Research*, **46**:339-346.

DEACON, E.L.,1953, Vertical Profiles of Mean Wind in the Surface Layers of the Atmosphere, *Geophysical Memoirs* **91**, The Meteorological Office, Bracknell, U.K.

DEROIN, J.P., COCHRANE, G.R., MONGILLO, M.A., BROWNE, P.R.L., 1995, Methods of remote sensing in geothermal regions: The geodynamic setting of the Taupo Volcanic Zone (North Island, New Zealand), *International Journal of Remote Sensing*, **16**: 1663-1667

DIAK, G.R., WHIPPLE, M.S., 1995, Note on estimating surface sensible heat fluxes using surface temperatures measured from a geostationary satellite during FIFE 1989, *Journal of Geophysical Research*, **100D12**:25453-25461

DOZIER, J., 1981, A Method of Satellite identification of surface temperature fields of subpixel resolution. *Remote Sensing and Environment*, **11**:221-229.

DUFFIE, J.A., BECKMAN, W.A., 1974, Solar Energy Thermal Process, John Wiley and Son.

FELDMAN, W.C., MAURICE, S., BINDER, A.B., BARRACLOUGH, B.L., ELPHIC, R.C., LAWRENCE, D.J., 1998, Fluxes of Fast and Epithermal Neutrons from Lunar Prospector: Evidence for Water Ice at the Lunar Poles. *Science* **281**:1496-1500.

FANALE, F.P, 1976, Martian Volatiles: their degassing history and Geochemical fate, *Icarus*, **28**:179-202.

FERREIRA, L.G.; and. MENESES, P.R., 1994, Discrimination of hydrothermally altered Zones through Visible Near Infrared Spectrometry and Multispectral Image Processing. in *Proceedings of the 10th Thematic Conference on Geologic Remote Sensing 9-12 May 1994, San Antonio, Texas* (Environmental Research Institute of Michigan).

FRIEDMAN, J.D., WILLIAMS R.S.., PALMASON G., MILLER C.D., 1969, Infrared Surveys in Iceland-Preliminary Report, U.S. Geological Survey Professional Paper 650-C pp C89-C105.

FRIEDMAN, J.D., FRANK D., 1978. Thermal Surveillance of active volcanoes using the LANDSAT-1 data collection system, Part 3-Heat discharge from Mount St. Helens, Washington: U.S. Geological Survey Open-File Report 77-541 30pp.

FLASER, F.M., GOODY, R.M., 1976, Diurnal behaviour of water on Mars, *Planetery and Space Science*, **24**:161-181.

GARRETT, J.R.1977, Aerodynamic Roughness and mean monthly surface stress over Australia, Technical Paper No. 29, 19pp (CSIRO Division of Atmospheric Physics).

GARRETT, J.R., 1977, Review of drag coefficients over oceans and continents, Monthly Weather Review **105** 915-29.

GARRETT, J.R.,1992, The Atmospheric Boundary Layer, Cambridge Atmospheric and Space Science Series.

GOETZ, S.J., HALTHORE R.N., HALL, F.G., , MARKHAM, B.L., 1995, Surface temperature retrieval in a temperate grassland with multi-resolution sensors. *Journal of Geophysical Research*, **102(D12)**:25397-25410.

GIVRI, J.R., 1997, The extension of the split window technique to passive microwave surface temperature assessment, *International Journal of Remote Sensing*, **18**: 335-353

HABERLE, R.M., JAKOSKY, B.M., 1992, Atmospheric effects on the remote determination of thermal inertia on Mars, *Icarus* , **90**:197-204

HALLIDAY, D., RESNICK, R., WALKER, J; 1996, *Fundamentals of Physics, 5th Edition*, John Wiley and Sons.

HAMAL, R.A., CONRAD B.J., HAIS, W.A. KUNDE, V.G., LOWMAN, P.D, PEARL, J.C., PRABHAKARA, C.,. SCHLACHMAN, B, LREVIN, G.V.,1972, Infrared Spectroscopy experiment on the Mariner 9 Mission: Preliminary report. *Science*, **175**, 305-308.

HARRIS, A.J.L., BLAKE, S., ROTHERY, D.A., 1997, A chronology of the 1991 to 1993 Mount Etna eruption using advanced very high resolution radiometer data: Implications for real-time thermal volcano monitoring., *Journal of Geophysical Research*, **102(B4)**:7985-8003.

HARRIS, A.J.L, BUTTERWORTH, A.L., CARLTON, R.W., DOWNEY, I, MILLER, P., NAVARRO, P., ROTHERY, D.A., 1997, Low Cost volcano surveillance from space: case studies from Etna, Krafla, Cerro Negro, Fogo, Lascar and Erebus. *Bulletin of Volcanology*, **59**:49-64.

HEALD, E.E., JOHNSON, D.H., ROTH, D.E., 1995, Heat transfer: Users Guide for Revision 5.1, Ansys Inc Houston PA.

HEIKEN, G., VANIMAN, D., FRENCH, B.M., 1991, Lunar Sourcebook: A users Guide to the Moon, Cambridge University Press.

HIESER, M.D., SELLER, P.J., 1995, Production of a filtered and standardised surface flux data set for FIFE 1987, *Journal of Geophysical Research*, **10(D12)**:25631-25643.

HEMINGWAY, B.S., ROBIE, R.A., WILSON, W.H., 1973, Specific Heat of lunar soils, basalt and breccias from the Apollo 14, 15 and 16 landing sites between 90 and 350K. Proceedings of the Fourth Lunar Science Conference, Supplement 4, *Geochimica et Cosmochimica Acta*, . **3** :2481-2487.

HILLEL, D., 1982, Introduction to Soil Physics, (Academic Press.)

HOLMAN, J.P., 1990, Heat Transfer, 7th Ed. (McGraw Hill.)

HON, K., KAUAHIKAUA, J, DENLIGER, R., MACKEY, K., 1994, Emplacement and inflation of pahoehoe sheet flows: Observations and measurements of active lava flows on Kilauea Volcano, Hawaii, *Geological Society of America Bulletin*, **106**:351-370

HOOK, S.J., KARLSTROM, K.E., MILLER, C.F., McCAFFREY, K.J.W., 1994, Mapping the Piute Mountains, California, with Thermal Infrared Multispectral Scanner (TIMS) images, *Journal of Geophysical Research*, **99B**:15605-15622

HORAI, KI-ITI, 1991, Thermal Conductivity of Hawaiian Basalt: A New Interpretation of Robertson and Peck's data, *Journal of Geophysical Research*, **96B3**:4125-4132

HöSKULDSSON, A., SPARKS, R.S.J., 1997, Thermodynamics and fluid dynamics of effusive subglacial eruptions, *Bulletin Volcanolique*, **59**:219-230

HRENIKOFF, A., 1941, Solution of Problems in Elasticity of the Framework Method. *Transactions of the ASME Journal of Applied Mechanics*, **8**:169:175

HUGHES, P.A., MCCOMB, T.J.L., RIMMER, A.B., TURVER, K.E., 1993, A mathematical model for the prediction of temperature of man made and natural surface, *International Journal of Remote Sensing*, **14**:1383-1412

INCROPERA, F.P., DEWITT, D.P., 1990, Fundamentals of Heat and Mass Transfer, Wiley, New York.

IZUMI, Y., 1971, 1968 Field Program Data Report, Air Force Cambridge Research Papers No. 379, (USAF Cambridge Laboratory)

JAEGER, J.C., 1953, Conduction of heat in a solid with periodic boundary conditions, with an application to the surface temperature of the moon, *Proceedings of the Cambridge Philisophical Society*, **49(2)**:355-359

JENTOFT-NILSON, M., ALLEY, R.E., 1996, Algorithm Theoretical basis Document for Brightness Temperature v2.3 JPL D-13913, Jet Propulsion Laboratory, Pasadena CA.

JOSEPH, J.H., 1966, Calculation of radiative heating in numerical general circulation models, Numerical Simulation of Weather and Climate, *Technical Report 1*, (Department of Meteorology, University of California, Los Angeles).

JOSEPH, J.H., 1971, On the calculation of Solar radiation fluxes in the troposphere, *Solar Energy*, **13**:251-261

KAHLE , A.B.,1977, A Simple thermal model of the Earth's Surface for geologic mapping by remote sensing, *Journal of Geophysical Research*, **82**: 1673-1680

KAHLE, A.B.,GOETZ, A.F.H., 1983, Mineralogic Information from a new

Airborne Thermal Infrared Multispectral Scanner, Science, **222**:24-27

KALLURI, S.N.V., DUBAYAH, R.O., 1995, Comparison of atmospheric correction models for thermal bands of the Advanced Very High Resolution Radiometer over FIFE, *Journal of Geophysical Research*, **100D2**: 25411-25418

KESZTHELYI, L., 1994, On the Thermal Budget of Pahoehoe lava tubes, PhD Thesis, Unpublished, California Institute of Technology.

KESZTHELYI, L., 1995, A Preliminary thermal budget for lava tubes on the Earth and planets, *Journal of Geophysical Research*, **100B10**: 20411-20420

KESZTHELYI, L., 1995, Measurements of the cooling at the base of Pahoehoe flows, *Geophysical Research Letters* **22:16**-2195-2198.

KEALY, P.S., HOOK, S.J., 1993, Separating Temperature and Emissivity in Thermal Infrared Multispectral Scanner Data: Implications for Recovering Land Surface Temperatures, IEEE Transactions on Geoscience and Remote Sensing, **31**:1155-1164

KIEFFER, H.H., JAKOSKY, B.M., MARTIN, T.Z., MINER, E.D., PALLUCONI, F.D., PETERFREUND, A.R.,1977, Thermal and Albedo Mapping of Mars during the Viking Primary Mission, *Journal of Geophysical Research*, **82**: No 28

KIEFFER, H.H., FRANK D., J.D., FRIEDMAN, 1982, Thermal infrared Surveys of Mount St. Helens-Observations prior to the eruption of May 18th, in *The 1980 Eruptions of Mount St. Helens*, USGS Washington D.C.

KIEFFER, H.H. (ed), 1992 , Mars. (University of Arizona Press)

KIEFFER, H.H.,1997, Personal Communication

KNEIZYS, P.X., SHETTLE, F.P., ANDERSON, G.P. ABREW, I.W., CHETWYND, J., SHELBY, F.A., GALLERY W.O., 1987, Atmospheric transmittance/Radiance computer code, LOWTRAN 7, Air Force Geophysical Laboratory, Hanscom AFB.

KSANFOMALITY, L.V., MOROZ, V.I., BIBRING, J.P., COMBOS, M., SCUFFLOT, A., GANPANTZEROVA, O.F., GOROSKOVA, N.V., ZHARKOV, A.V., NIKITIN, G.E., PETROVA, E.V., 1989, Spatial Variations in the Thermal and Albedo properties of the surface of Phobos, *Nature*, **341**.

LAGOURDE, J.P., MCANENEY, K.J., 1991, Daily Sensible heat Flux estimation from a single measurement of Surface Temperature and Maximum air temperature, *Boundary Layer Meteorology*, **59**:340-363

LANGSETH, M.G., CLARK S.P., CHUTE, J.L. jr, KEIHM, S.J., WECHSLER A.E., 1972, Heat-Flow Experiment, in Apolo 15 Preliminary Science Report NASA SP-289

LANGSETH, M.G., KEIHM, S.J. 1977, In-situ measurements of lunar heat flow. *In Soviet-American Conference on geochemistry of the Moon and Planets*, pp 283-293, NASA SP 370

LANGSETH, M.G, KEIHM, S.J., PETERS, K., 1976, Revised Lunar heat flow values, *Proceedings of the 7th Lunar Science Conference*, pp3143-3171.

LANGSETH, M.G, KEIHM, S.J., CHUTE, J.L. jr, 1973, Heat-Flow experiment. *in Apollo 17 Preliminary Science Report*, pp9-1,9-24, NAS SP-330

LIN, J.D., 1980, On the Force-Restore Method for Prediction of Ground Surface Temperature, *Journal of Geophysical Research*, **85C**:3251-3254

LINACRE, E., 1992, Climate Data and Resources: A Reference and Guide (Routledge)

LUCHITTA, B.K.,1987, History of the Valles Marineris, *Lunar and Planetary Science* **XVIII**:572-573.

LUCHITTA B.K., 1987, Recent Mafic volcanism on Mars, *Science*, **235**:565-567

MATSUNAGA T., ROKUGAWA S., ISHII y., 1992, Application of Split Window technique to TIMS data, in Summaries of the Third Annual JPL Airborne Geoscience Workshop June 1-5 1992, Vol 2, pp16-18 edited by Vincent J. Realmuto.

MALARET M., 1995, *Photogrammetric Engineering and Remote Sensing* **51**:1407-1416

MALLON, A., 1998, Personal Communication

MANDL, F., 1991, Statistical Physics, 2nd Edition, John Wiley and Sons.

MARSDEN, R., 1997, Personal Communication.

MARTIN, T.Z., 1997, Personal Communication.

MAXWELL, J.C., 1892, A treatise on Electricity and Magnetism,Vol1 3rd Edition, Clarendon, Oxford.

MENDELL, W.W, 1976, Degradation of large, Period II craters, *Proceedings of the 7th Lunar Science Conference*, pp2705-2716

MOORE, H.J., JAKOSKY, B.M. 1989. Viking Landign Sites, Remote Sensing Observations, and Physical Properties of Martian Surface Materials, *Icarus*, **81**:164-184, 1989.

MOUGINIS-MARK, P.J., WILSON, L, HEAD, J.W., 1982, Explosive volcanism of Hecates Tholus, Mars: investigation of eruption conditions. *Journal of Geophysical Research* **87**:9890-9904

MOUGINIS-MARK, P.J., GARBEIL, H., FLAMENT, P., 1994, Effects of Viewing geometry on AVHRR Observations of Volcanic Thermal Anomalies, *Remote Sensing of Environment*, **48**:51-60

MOXHAM, R.M., 1970, Thermal features at volcanoes in the Cascade range, as observed by aerial infrared surveys, *Bulletin Volcanologique*, **34**: pp77-106

MUHLEMANN, D.O, BUTLER, B.J., GROSSMAN, A.W., SLADE, M.A., 1991 Radar images of Mars, *Science*, **253**:1508-1513

NASA ,1978, HCMM Users Guide. Goddard Space Flight Centre.

NASH, D.B., 1988, Detection of a Buried Horizon with a High Thermal Diffusivity using Thermal Remote Sensing, *Photogrammetric Engineering and Remote Sensing*, **54**::1437-1446

NELLIS, M.D., 1982, Application of Thermal Infrared Imagery to Canal leakage Detection, *Remote Sensing of Environment*, **12**:229-234

NOZETTE, S., RUSTAN, P., PLEASANCE, L.P., HORAN, D.M., REGEON, P., SHOEMAKER, E.M., SPUDIS, P.M., ACTON C.H., BAKER, D.N., BLAMONT, J.E., BURATTIT, B.J., CORSON, M.P., DAVIES, D.N., DUXBURY, T.C., ELIASON, E.M., JAKOSKY, B.M., KORDAS, J.F., LEWIS, I.T., LICHTENBERG, C.L., LUCEY, P.G., MALARET, E., MASSIE, M.A., RESNICK, J.H., ROLLINS, C.J., PARK, H.S., McEWAN, A.S., PRIEST, R.E., PIETER, C.M., REISSE, R.A., ROBINSON, M.S., SMITH, D.E., SORENSON, T.C., VORDER BREUGGE, R.W., ZUBER, M.T., 1995, The Clementine Mission to the Moon: A Scientific Overview, *Science*, **1226**:1835-1839.

NOZETTE, S. P., LICHTENBERG, C.L. SPUDIS, P., BONNER, R., ORL, W., MALARET E., ROBINSON, M., , SHOEMAKER, E.M., 1996, The Clementine Bistatic Radar Experiment, *Science* **274**

O'BRIEN, M.,1987, The Development of Geothermal Resources in the Mallow Area for heating purposes MSc, Unpublished. Shelf No. DM2028 University College Cork.

OKE, 1978 ,Boundary Layer Climates, Methuen (London)

OPPENHEIMER, C, ROTHERY, D.A., 1997 Remote sensing of heat, lava and fumarole emissions from Erta 'Ale Volcano, Ethiopia. *International Journal of Remote Sensing* **18**:1661-1692.

OPPENHEIMER, C., ROTHERY, D.A., PIERI, D.C., ABRAMS, M.J., CARERRE V. 1993, Analysis of Airborne Visible/Infrared Imaging Spectrometer (AVIRIS) data for volcanic hot spots, *International Journal of Remote Sensing* **14**:2919-2934.

PALLUCONI, F.D. MEEKS, G.R., 1985, An investigators Guide to TIMS data, JPL Publication 85-32 32pp

PECK, D.L., 1978, Cooling and vesiculation of Alae Lava Lake, Hawaii, *USGS Professional Paper* **550-B**, 59p.

PIERI, D.C., GLAZE L.S., ABRAMS M.J., 1990, Thermal radiance observations of an active lava flow during the June 1984 eruption of Mount Etna, *Geology*, **18**:1018-1022

PIERI, D.C., KHRENOV, A.P., MILLER, T.P., ZHARINOV, S.E., REALMUTO, V., ABRAMS, M., GLAZE, L.S., KAHLE, A.B., DROZNIN, V., DVIGALO, V., KIRIANOV, V., ABBOTT, E., CHERNOBIEFF, S., 1997, Joint Effort Results in First TIMS Survey of Kamchatka Volcanoes, *Eos* **78**:125-128.

PLANCK, M., 1901, On the Distribution of Energy in the Spectrum, *Annals of Physics* **4**:553:563

POHN, H.A., OFFIELD, T.W., WATSON, K., 1974, Thermal Inertia Mapping from Satellite Discrimination of Geologic Units in Oman, *Journal of Research of the U.S. Geological Survey*, **2**:147-158.

PRATT, D.A., ELLYETT, C.D., 1979, The Thermal Inertia Approach to Mapping of Soil Moisture and Geology, *Remote Sensing of Environment* **8**:151-168

PRATT, D.A. FOSTER, S.J. , ELLYETT, C.D., 1980, A calibration procedure for Fourier series thermal inertia models. *Photogrammetric Engineering and Remote Sensing* **46**:529-538

PRICE, J.C.,1977, Thermal Inertia mapping: A New View of the Earth, *Journal of Geophysical Research*, **82**: 2582-2590

PRICE, J.C.,1982, On the Analysis of Thermal Infrared Imagery: The Limited Utility of Apparent Thermal Inertia. *Remote Sensing of Environment* **18**:59-73

RAZNJEVIC, K., 1976, Handbook of Thermodynamic Tables and Charts, Hemisphere Publishing, London.

REALMUTO, V.J., HON K., KAHLE A.B., ABBOTT, E.A., PIERI, D.C.,1992, Multispectral thermal infrared mapping of the 1 October 1988 Kupaianaha flow field, Kilauea volcano, Hawaii. *Bulletin of Volcanology*, **55**:33-44.

REDDY, J.N., 1993, *An Introduction to the Finite Element Method*, 2nd Edition, McGraw-Hill, Inc.

ROBERTSON, E.C., PECK, D., 1974, Thermal Conductivity of vesicular basalt from Hawaii, *Journal of Geophysical Research* **79**:4875-4888

ROSSE, L. 1869, On the Radiation of Heat from the Moon, *Proceedings of the Royal Society of London*, Vol. 27 pp436-441.

ROTHERY, D.A., BONNEVILLE, A., OPPENHEIMER, C.,1995,Thermal monitoring, in: *Monitoring Active Volcanoes, Strategies, Procedures* (University College London).

ROVER TEAM , 1997, Characterisation of the Martian Surface Deposits by the Mars Pathfinder Rover, Sojourner, *Science*, **278**:1765-1770

ROWLAND, S.K., 1992, The use of TIMS for mapping different Pahoehoe surfaces :Mauna Iki, Kilauea, in: *Summaries of the Third Annual JPL Airborne Geoscience Workshop, June 1-5, 1995 Volume 2:TIMS Workshop* edited by V.J. Realmuto. JPL Pubs 92-14 Vol 2.

SAARI, J.M.,1969, Lunar Thermal Anomalies and Internal Heating, *Astrophysics and Space Sciences*, Volume 4 January 1969.

SARAF, A.K., PRAKESH, A., SENGUPTA, S., GUPTA, R.P.,1995, Landsat TM data for estimating ground temperature and depth of subsurface coal fire in the Jharia coalfield, India. *International Journal of Remote Sensing* **16**:2111-2124.

SASS, J.H., MUNROE, R.J.,(editors), 1974, U.S. Geological Survey Open Files Report, 74-9, Sections 2-7.

SCHIELDGE, J., KAHLE, A.B., ALLEY, R.E., GILLESPIE, A.R.,1980, Use of thermal-inertia properties for material identification, *SPIE Image Processing for Missile Guidance*, **238**:350-357

SCHIELDGE, J.,1997, Personal Communication.

SCHOTT, J.R., 1982, Comparison of Techniques for Atmospheric Correction of Thermal Infrared Satellite Imaging Systems *in*: Remote Sensing and the Atmosphere-Proceedings of the Annual Technical Conference of the Remote Sensing Society, Liverpool, **198**:100-107

SCHOFIELD, J.T., BARNES, J.R.,CRISP, D., HABERLE, R.M.,LARSEN.S., MAGALHAES, J.A., MURPHY, J.R., SEIFF, A., WILSON, G. 1997, The Mars Pathfinder Atmospheric Structure Investigation/Meteorology (ASI./MET) Experiment, *Science* **278**:1752-1757

SCHULTZ, P.H., MENDELL, W.W., 1978, Orbital infrared observations of lunar craters and possible implications for impact ejecta emplacement, *Proceedings of the 10th Lunar Science Conference*, pp2899-2918.

SCOTT, D.H., 1982, Volcanoes and Volcanic Provinces: Martian Western hemisphere *Journal of Geophysical Research* **87**:9839-9851.

SEKIOKA, M., 1985, Geothermal observations by Use of a Helicopter-Borne Remote Sensing System, *Remote Sensing of Environment*, **18**:193-203.

SELIVANOV, A.S., NARAEVA, M.K., GORNY, V.I., KOLESNIKOV, V.I., SHILIN, B.V., TRONIN, A.A., 1992, Preliminary results from the Termoskan Instrument, *International Journal of Remote Sensing* **13**:3391-3393

SHORT, N.M., STUART, L.M., 1982, The Heat Capacity Mapping Mission (HCMM) Anthology, NASA SP-465, NASA, Washington D.C.

SHORTHILL, R.W., 1972, The Infrared Moon: A Review, *in Thermal*

Characteristics of the Moon, Lucas J.W. (editor) MIT Press.

SHUTTLEWORTH, W.J., 1989 , Micrometeorology of temperate and tropical forest, *Philosophical Transactions of the Royal Society of London.* **b324**, 299-334.

SIMPSON, J.A., WEINER, E.S.C. 1989, The Oxford English Dictionary, 2nd Edition, Clarendon Press, Oxford.

SMITH, P.H, BELL J.F., BRIDGES, N.T., BRITT, D.T., GADDIS, L.,GREELEY, R., KELLER, H.U., HERKENHOFF, K.E., JAUMANN, R., JOHNSON, J.R., KIRK R.L., LEMMON, M., MAKI, J.N., MALIN, M.C., MURCHIE, S.L., OBERST, J., PARKER, T.J., REID, R.J., SABLOTNY, R., SODERBLOM, L.A., STOKER, C., SULLIVAN,R., THOMAS, N., TOMASKO M.G., WARD, W., WEGRYN,E. 1997, Results from the Mars Pathfinder Camera, *Science* **278**:1758-1764.

SPUDIS, P., GREELEY, R., 1976, Surficial Geology of Mars: A study in support of a penetrator mission to Mars. NASA, Washington D.C.

SQUYRES, S.W., CLIFFORD, S.M., KIZMIN, R.O., ZIMBELMAN, J.R., COSTARD, F.M., 1992, Ice in the Martian Regolith in *Mars* edited by H.H. Keiffer (University of Arizona Press)

SUTTON, O.G., 1953, Micrometeorology. McGraw Hill.

SWINBANK, W.C., 1963, Long Wave radiation from clear skies, *Quarterly Journal of the Royal Meteorological Society* **89**:339-348

TANAKA, K.L, ISBELL, N.K., SCOTT, D.H., GREELEY, R., GUEST, J.E., 1988, The Resurfacing history of Mars: a synthesis of digitized, Viking based Geology. *Proceedings of the Lunar and Planetery Science Conferences.* **18**:665-678

THOM, A.S.,1971, Momentum absorption by vegetation, *Quarterly Journal of the Royal Meteorological Society*, **97**:414-28

THOMPSON, G.A., WHITE, D.E.,1964, Regional Geology of the Steamboat

Springs, Washoe CO. Nevada, USGS Prof Paper 458-A-54 (USGS)

THOMPSON, O.E., PINKER, R.T., 1975, Wind and temperature profile characteristics in a tropical evergreen forest, *Tellus* **27**:562-73

TIAB, D., SIGAURDSSON, O., 1994, Analysis of pressure pulses resulting from magmatic activity in the vicinity of the Krafla Geothermal field in Iceland, *Geothermal Science and Technology*,**4(1)**:1-18

TOSI, N., 1983, A Simulation Model supporting HCMM investigations on Geological Objectives, *International Journal of Remote Sensing* **4**:353-369

TOULOUKIAN, Y.S., JUDD, W.R., ROY, F., 1989, Physical Properties of Rocks and Minerals, Hemisphere Publishing,

TURCOTTE, D.L., SCHUBERT, G., 1982, Geodynamics, application of continuum physics to Geological problems, Wiley, New York.

TRONIN, A.A., 1996, Satellite thermal survey- a new tool for the study of seismoactive regions. *International Journal of Remote Sensing* **17**:1439-1455

VAN WIJK, W.R., 1963, Sinusoidal temperature variations in layered soils, in *Physics of Plant Environments*, (pp109-123) edited by Van Wijk, W.R., John Wiley. New York.

WARNER, T.A., LEVANDOWSKI, D.W.,1992, Atmospheric Corrections for TIMS estimated Emittance, in Summaries of the Third Annual JPL Airborne Geoscience Workshop June 1-5 1992, Vol 2, pp16-18 edited by Vincent J. Realmuto.

WEAVER, H.L., 1990, Temperature and Humidity Flux-variance Relations Determined by one Dimensional Eddy Correlation, Boundary Layer meteorology **53**:77-91

WILLIAMS, R.S. Jr, FRIEDMAN, J.D., 1970, Satellite observations of effusive volcanism, *Journal of the British Interplanetary Society*, **23**:441-450

WOOD, J.A., LASSERE, M., FEDOSEJEVS, G., 1990, Analysis of Mid Infrared Spectral Characteristics of Rock outcrops and an evaluation of the Kahle model in predicting Outcrop Thermal Inertias, *Remote Sensing and Environment*, **30**:169-195

WOODSIDE, W., MESSMER, J.H., 1961a, Thermal Conductivity of porous media, I Unconsolidated sands, *Journal of Applied Physics* **32**:1688-1698.

WOODSIDE, W., MESSMER, J.H., 1961b, Thermal Conductivity of porous media, II: Consolidated sands, *Journal of Applied Physics* **32**:1699-1706.

XUE, Y., CRACKNELL, A.P.,1992, Thermal inertia mapping: from research to operation, *Proc of the 18th Annual Conference of the Remote Sensing g Society, University of Dundee*

XUE, Y., CRACKNELL, A.P., 1993, Advanced thermal inertia modelling and its application to modelling the emissivity of the ground, *Proceeding of the 25th Symposium on Remote Sensing and global environmental change, Graz Austria 4-8 April 1993* (Ann Arbor Michigan ERIM) **II**:121-122

XUE, Y., CRACKNELL, A.P., 1996, Advanced Thermal Inertia Modelling, *International Journal of Remote Sensing*, **16**:431-446

ZENT A.P., FANALE F.P., SALVAIL J.R., POSTAWKO S.E. 1986, Distribution and State of H_2O in the High Lattude Shallow Subsurface of Mars, *Icarus* **67**:19-36.

ZHAN, X., KUSTAS.,W.P., HUMES K.S.,1996, An Intercomparison Study on Models of Sensible heat Flux over Partial Canopy Surface with Remotely Sensed Surface Temperature, *Remote Sensing and Environments*, 58:**242-256**

ZIENKIEWICZ O.C., 1971, The Finite Element Method in Engineering Science. McGraw Hill, London.

ZIENKIEWICZ O.C., MORGAN, 1985, Finite Elements and Approximation. John Wiley and Sons.

ZILIOLI, E., GOMARASCA, M.A., TOMASONI, R., 1992, Application of terrestrial Thermography to the detection of Waste-Disposal Sites, *Remote Sensing of Environment*, **40**:153-160

ZIMBELMAN J.R., 1986, Note: The Role of Porosity in Thermal Inertia Variations on Basaltic Lavas, *Icarus*, **68**:366-369

ZUBER, M.T. SMITH, D.E. LEMOINE, F.G., NEUMANN G.A., 1994, The Shape and internal Structure of the Moon from the Clementine Mission, *Science* **266**:1839-1843